Detection, Localization and Quantification of Non-Calcified Coronary Plaques in Contrast Enhanced CT Angiography

Muhammad Moazzam Jawaid

Department of Electrical and Electronic Engineering

City, University of London

A thesis submitted in partial fulfilment of the requirement for the degree of

Doctor of Philosophy

City, University of London October 2017

Declaration

I hereby declare that except where specific reference is made to the work of others, the contents of this dissertation are original and have not been submitted in whole or in part for consideration for any other degree or qualification in this, or any other university. This dissertation is my own work and contains nothing which is the outcome of work done in collaboration with others, except as specified in the text and Acknowledgements. I hereby grant powers of discretion to the University Librarian to allow this thesis to be copied in whole or in part without further reference to the author. This permission covers only single copies made for study purposes, subject to normal conditions of acknowledgement.

Muhammad Moazzam Jawaid

October 2017

Acknowledgements

This thesis could not be completed without the support I have received from many people during my time as a PhD student at City University London. First, I would like to thank my PhD advisers, Dr. Greg Slabaugh and Dr. Constantino Carlos Reyes-Aldasoro for your invaluable guidance throughout my study and research at City, University of London. It has been a privilege to be a student of yours, to learn from you and to be inspired by you. I am so grateful to have had such great advisers who not only have incredible foresight and view of the big picture, but also guided me through numerous technical details. I would like to thank my thesis examiners Dr. Xujiong Ye and Dr. Dympna O'Sullivan for helpful comments and suggestions, which improved my thesis in many aspects.

I also would like to acknowledge the support of Erasmus Mundus INTACT project, which enabled this research through the award of a PhD studentship. In addition I acknowledge the support of my lab colleagues including Alena Uus, Atif Riaz, Muhammad Asad, Nathan Olliverre and Adriana Danilakova for their technical assistance through out my research. I am also thankful to our collaborators at Guy's and St Thomas' Hospital, London and Semmelweis University Budapest for the provision of the CTA datasets and their invaluable advice in a clinical context.

Moreover, I would like to mention the support of my wife and children, who have borne many difficult times alone in these three years at the cost of my PhD My last words go to my parents, who always give me unconditional support, love and reassurance. I lost my father in the middle of this long journey; however, I owe my life and every achievement to him.

Abstract

State-of-the-art imaging equipment has increased clinician's ability to make non-invasive diagnoses of coronary heart disease (CHD); however, high volumes of imaging data make manual abnormality detection cumbersome in practice. In addition, the interpretation of CTA heavily relies upon the previous knowledge of the clinician. These limitations have driven an intense research in the context of automated solutions for fast, reliable and accurate diagnosis. Accordingly, in this thesis, we present an automated framework for detection, localization and quantification of the non-calcified coronary plaques in cardiac computed tomography angiography (CTA).

The first contribution of the thesis is a coronary segmentation algorithm that is adaptive to the contrast agent and employs a hybrid energy incorporating local and global image statistics in a segmentation framework using partial differential equations (PDEs). Accordingly, we illustrated with the help of experimental evidence that a volume-specific intensity threshold leads to an improved segmentation in CTA. In the subsequent step, we employed a hybrid region-based energy for improved segmentation in CTA imagery. The hybrid energy couples an intensity-based local term with an efficient discontinuity-based global model of the image for optimal segmentation. The proposed method is less sensitive to the local optima problem and helps in reducing false positives, as well as it allows a certain degree of freedom for the initialization. Moreover, we employed an auto-correction feature for improved segmentation, as an auto-corrected mask captures the emerging peripheries of the coronary tree during the curve evolution. The effectiveness of the proposed model is demonstrated with the help of both qualitative and quantitative results, with a mean accuracy of 80% across the CTA dataset.

The capability to address the variations in initial mask and localization radii simultaneously, makes our algorithm a feasible choice for coronary segmentation.

The second contribution of the thesis is an automatic approach to analyse the segmented coronary tree for the presence of non-calcified plaques. The specific focus of this work is detection of non-calcified plaques in CTA, as intensity overlap between blood, fat and non-calcified plaques make the detection challenging. Non-calcified plaques are identified based on mean radial profiles that average the image intensities in concentric rings around the vessel centreline. Subsequently, an SVM classifier is applied to differentiate the abnormal coronary segments from normal ones. A total of 32 CTA volumes have been analysed and a detection accuracy of 88.4% with respect to the manual expert has been achieved. For plaque-affected segments, we further proposed a derivative-based method to localize the position and length of the plaque inside the segment. The plaque localization accuracy has been around 83.2%. Moreover, the proposed model has been tested on three different CTA datasets and has produced consistent results, demonstrating its reproducibility for generic CTA data.

The final contribution of the thesis is a method to segment and quantify the non-calcified plaque. After evaluating the vessel wall thickness, posterior probability based voxel classification has been performed to quantify the lumen and plaque, respectively. Both qualitative and quantitative results demonstrate that the proposed model shows a good agreement with three independent experts. To optimize the processing time, we employed sparse field method in a level-set based active contour evolution.

Table of contents

List of figures

List of tables

Nomenclature

I_o	X-ray attenuation without obstruction
I_t	X-ray attenuation with structural obstruction
μ_L	Linear transform coefficient to map attenuation value
μ_{water}	Intensity transformation coefficient for water
μ_{air}	Intensity transformation coefficient for air
Ω	Image domain
S_k	Set of pixels comprising k^{th} object
Im	Two dimensional image
∇Im_i	Partial derivative in horizontal direction
∇Im_j	Partial derivative in vertical direction
$\nabla Im_{(i,j)}$	Gradient vector of a two dimensional image
T	Edge strength threshold
E_{map}	Edge-map for a two dimensional image
C_s	Parametric curve, parametrized with respect to s
E	Total energy of the deformable curve

E_{int}	Internal energy of the curve
E_{ext}	External energy of the curve
E_{cons}	Constraint based energy of the curve
α	Constant weight regulating curve elasticity
η	Constant weight regulating curve stiffness
Φ	Level set representation of parametric curve
t	Evolution time to track the level set-based deformation
ϕ_t	Updated curve at time t
$\phi(x(t),t) = 0$	Initial boundary formulation or zero level set representation
$distt$	Distance representation in signed distance function
κ	Curvature of evolving surface
Δt	Change in time
ϕ_x, ϕ_y	First derivative of ϕ with respect to x and y, respectively
ϕ_{xx}, ϕ_{yy}	Second derivative of ϕ with respect to x and y, respectively
ϕ_{xy}	Mixed derivative of ϕ with respect to x and y
$\{i, j\}$	Coordinates of spatial point in in image domain Ω
$\Delta^{+x}(i, j)$	Right side finite difference at spatial location (i,j)
$\Delta^{-x}(i, j)$	Left side finite difference at spatial location (i,j)
$\{\mathbf{x}, \mathbf{y}\}$	Discrete spatial points in image domain
c_1	Mean intensity value inside curve

c_2	Mean intensity value outside curve
F	Generic force function regulating the growth of curve C
$F_{(c_1,c_2,C)}$	Chan-Vese functional for region-based segmentation
I	Three dimensional CTA volume
$\lambda_1, \lambda_2, \lambda_3,$	Hessian-based eigenvalues for vesselness computation
$V_o(\mathbf{x})$	Multiscale vesselness response for an image
$\alpha_t, \beta_t, \gamma_t$	Regularization constants used to optimize vesselness computation
R_A, R_B	Shape discriminator to identify tubular structures
R_C	Noise penalty in vesselness computation
μ_I	Volume-specific Gaussian mean in HU, reflecting aorta-based intensity average
σ_I	Volume-specific standard deviation in HU, reflecting aorta-based intensity variability
R_I	Volume-specific intensity range, reflecting the impact of the contrast medium
R_{index}	Reference slice index
C_r	Reference slice index factor
N_{planes}	Number of axial planes in volumetric image
$V_c(\mathbf{x})$	Cylindrical geometry-based vesselness response for image
$Seed_o(\mathbf{x})$	Seed detection response for reference slice
$Seed_o^{'}(\mathbf{x})$	Improved seed detection response for reference slice

T_f	Vesselness threshold for multiscale filter response $V_o(\mathbf{x})$
T_{gf}	Vesselness threshold for cylindrical geometric filter response $V_c(\mathbf{x})$
γ	Constant weight for regularization of the curve length
H	Heaviside function to compute internal and external regions in level set surface ϕ
δ	Dirac Delta function to identify curve in level set surface ϕ
$B(\mathbf{x},\mathbf{y})$	Localization mask to select spatial points **y** around **x**
R_{Local}	Radius for selecting localized neighbourhood
F_{Local}	Localized image-based force
F_{global}	Global image-based force
F_{hybrid}	Hybrid image-based force
β	Constant weight regulating the influence of global component
$d = I(\mathbf{x})$	Image intensity at spatial location **x**
$\mathcal{N}\{\mu_k, \sigma_k\}, k = 1...3$	Gaussian approximation for three peaks of image histogram
$p(d)$	Gaussian Mixture Model for three class image
$Pr(x \in c_k), k = 1...3$	three class posterior probability(s) at spatial location **x**
Pr^{Smth}	three class smoothed posterior probability
I_{global}	Posterior-based image discontinuity map
n_{xyz}	Normal to the plane
c_{xyz}	Centre of the plane
N_s	Number of cross-sections in coronary segment

r	Sampling radius for mean radial profile
q_k	k^{th} Cross-section of the coronary segment
θ	Angle of projecting rays for radial profile
$p[r,k], \{r = 1,...,6mm, k = 1,...,Ns\}$	Mean radial profiles along the length of segment
$v[ii,k], \{ii = 1,...,8,, k = 1,...,Ns\}$	Customized radial profiles using discrete radii along the length of segment
L	Number of projected rays on cross-section
θ_t	Customized angle for projecting rays to obtain discrete radial profile
$S[k], \{k = 1,...,Ns\}$	Discrete mean representation of the coronary segment
Sz	Size of kernel in moving average operation
μ_s	Smoothed mean representation of the coronary segment
σ_s	Smoothed standard deviation-based representation of the coronary segment
S_{rad}	Cross-sectional radius profile along the length of segment
$\mu_s^{'}, \sigma_s^{'}, S_{rad}^{'}$	Fixed length characteristics function defining mean, deviation and radius, respectively
m	Number of subsets in segment approximation
f_μ, f_σ, f_{rad}	Subset-based approximation of segment mean, deviation and radius, respectively
f_{mid}	Subset-based approximation of segment mid-lumen intensity
N	Total number of samples in SVM classification model

$X_n, \{n = 1, ..., N\}$	Feature-based inputs for SVM classifier
$Y_n, \{n = 1, ..., N\}$	Ground truth label for SVM classifier
$D = \left\{(X_n, Y_n) \mid X_n \in \mathbb{R}^{dims}, Y_n \in \{0,1\}\right\}_{n=1}^{N}$	Collective dataset representation for SVM classifier
$dims$	Feature vector dimensions
ε	Slack variable for realistic solutions in SVM classification
$\hat{Y}$	Predicted output label of SVM classifier
f_s'	First derivative of segment profile
f_s''	Second derivative of segment profile
$T_{mod}(CP, \theta_{cs}^{'})$	Tubular model for coronary segment
CP	Centreline of the coronary segment
$\theta_{cs}^{'}$	Array defining cross-section parameters
$C_{xyz}(i)$	Centre of a 3D ellipse
$[a(i), b(i)]$	Major and minor axis length for i^{th} ellipse in the segment
$R_{xyz}(i)$	Orientation information for i^{th} 3D ellipse
$t^{'}$	Angular parameter varying between 0 - 2π
$P = [p_x p_y p_z]$	An arbitrary point on a 3D plane
B	Set of the points defining the lumen boundary
$E_{xyz}(i) = [C_{xyz}(i), a(i), b(i), R_{xyz}(i)]$	Parametric model for i^{th} ellipse
$[a(s), b(s)]$	The major and minor axis lengths for the upper normal ellipse
$[a(e), b(e)]$	The major and minor axis lengths for the lower normal ellipse

f	Parametric function for computing elliptical axes lengths in the plaque affected region
Ω_s	The manually annotated lumen object
xx	An arbitrary point around the lumen boundary
$\partial\Omega_s$	Manually annotated lumen boundary
$F_{label}(i,j,k)$	Voxel-wise customized fuzzy label
μ_p	Bimodal histogram-based intensity peak for the plaque
μ_l	Bimodal histogram-based intensity peak for the lumen

Chapter 1

Introduction

1.1 Introduction

The heart is the most important organ of the cardiovascular system that is responsible for the continuous supply of blood to all body parts. In order to operate continuously, the heart muscles, i.e. myocardium, require an uninterrupted supply of oxygenated blood, which is accomplished through a complex vascular network known as the coronary tree. In a biological context, the main trunk artery (aorta) filled with the oxygenated blood comes out of the left ventricle chamber and splits into arterial network. This arterial network is clinically divided into two structures namely left and right coronary arteries (LCA and RCA), respectively. The two coronary structures are responsible for routing the oxygenated blood from the aorta to myocardium tissues of the heart in respective dimensions.

Any obstruction in the supply of oxygenated blood to the myocardium may result in severe clinical abnormalities. The most common abnormality based on reduced blood supply is termed as "coronary atherosclerosis" or the Coronary Heart Disease (CHD). CHD is related to an accumulation of calcium, cholesterol and fatty materials inside the coronary arteries. The growth of non-blood depositions leads to deformation of the vasculature that supplies blood to the heart tissues. Consequently, the heart muscles become oxygen starved which may result in cardiac consequences including angina, heart failure and arrhythmias.

From a clinical point of view, an early detection of arterial plaque can help physicians to start preventive measures to avoid or at least delay the worst cardiac events. This can be achieved by addressing behavioural risk factors, diet control and preventive medication as proposed in [24]. The conventional methods used to detect coronary obstruction include: catheter guided X-ray angiography [25], optical coherence tomography (OCT) [26] and intravascular ultrasound (IVUS) [27, 28]. However, the invasive nature of these techniques makes them time-consuming and impose a relative patient risk. In contrast, recent advancements in non-invasive imaging have significantly improved the diagnostic accuracy in terms of high temporal and spatial resolution [29]. An example is the clinical use of cardiac computed tomography angiography (CTA) that enables three dimensional imaging of the heart with sub-millimetre accuracy. This precision makes CTA a feasible substitute to cardiac catheterization for detecting coronary obstructions [30]; however, the composition of the coronary plaques poses a difficult challenge in the effective diagnosis.

In a three-dimensional (3D) CTA image, different organs can be visually identified based on the characteristic intensity response i.e. blood-filled vessels appear brighter than the surroundings in CTA [31, 32]. However, the atherosclerotic plaques can be divided into two categories based on the intensity response in CTA: *calcified plaques* and *non-calcified plaques*. The calcified plaques (also termed as hard plaques) are easily discernible in conventional imaging due to high intensity values, whereas detection of the non-calcified plaques (also termed as soft plaques) is difficult due to the ambiguous intensity values, i.e. the intensity range for soft plaques often overlaps with the intensities of blood and nearby muscles.

From a clinical point of view, non-calcified plaques are more threatening due to unexpected rupturing phenomena that occurs without any early symptoms [33, 34]. The main limitation of existing plaque diagnostic methods is the inability to provide information about deformations of the vessel wall. Consequently, there is an ultimate need of advanced imaging techniques for early identification of non-calcified plaques in coronary vasculature. Accordingly, this work is focused on the detection, localization and segmentation of the non-calcified plaques in cardiac CTA.

Plaques are normally classified with clinical gradings to measure the severity of the plaque [4]. Mild or immature plaques are considered less-threatening as well as difficult to detect in a computational framework as they lack the characteristic features of plaques. In contrast, developed or mature plaques can be detected using a computational framework as demonstrated in this research.

1.2 Motivation

Coronary heart disease (CHD) has become a major cause of death worldwide. The mortality rate of CHD has dramatically increased in the last decade around the globe. According to the fact sheet of the World Health Organization [35], CHD was the prevailing cause of death globally in 2014-15, resulting in 8.14 million deaths (16.8% of total deaths) compared to 5.74 million deaths (12%) in 1990. Moreover, recent statistics of the National Health Service, United Kingdom [36] reveal that over 2.3 million people in the United Kingdom are suffering from CHD and annual death toll is approximately 73,000 (on average, one death every seven minutes). These substantial levels of ongoing morbidity and mortality have led to heightened interest in new methods to identify coronary abnormalities. Consequently, clinicians are interested in early detection of CHD methods to effectively predict and control possible cardiac events in the future.

The gold standard method used for coronary abnormality detection in recent years has been the cardiac angiography [25, 37]; however, it involves a certain amount of risk to the patient due to the invasive nature of the procedure. In addition, the conventional angiography process demands a certain amount of time and the outcome depends heavily on the expertise of the clinician. These limitations have driven intensive research for non-invasive diagnosis of coronary heart disease, resulting in highly sophisticated imaging procedures for accurate diagnosis. The clinical use of computed tomography angiography is a prominent example of non-invasive diagnosis, in which blood-filled vasculature can be easily discriminated from the background based on high intensity.

High spatial and temporal resolution of CT scanners produces a large quantity of data that is very useful for revealing internal information; however, it becomes cumbersome and time-consuming for the clinician to explore a large number of 2D axial slices to track the coronary vasculature. Moreover, the facts that coronary vasculature represents about 2% of imaged data and there is a wide inter-patient variability in coronary architecture [38], make diagnosis much challenging. In addition, the "manual" interpretation of the complex CTA imagery is prone to inter-observer error as well as it remains subjective because it employs the previous knowledge of radiologist. Hence, an automated system is required to help clinicians in fast and reliable diagnosis of coronary heart disease.

1.3 Aims and objectives of this work

In a broader view, the aim of this work is to develop an automated framework for detection, localization and quantification of the non-calcified plaques in cardiac CTA imagery. The objectives for this thesis can be defined as follows:

1. To derive an adaptive intensity threshold for improved segmentation using aorta-based intensity statistics.

2. To formulate a hybrid energy model, which couples local intensity with global edges for the improved segmentation of coronary vasculature in a 3D CTA volume.

3. To detect non-calcified plaques on per-segment basis in the segmented coronary tree, with a good agreement to ground truth manually labelled by a human expert.

4. To quantify the vessel wall, lumen and detected non-calcified plaque in an abnormal segment with a good agreement to ground truth manually labelled by three human experts.

Accordingly, a brief summary of research objectives is given below.

1.3.1 Adaptive threshold based on contrast medium diffusion

Non-vascular structures found in CTA volume should be suppressed in a pre-processing step to effectively delineate coronary vasculature. In this context, geometric shape characteristics are combined with intensity based constraints to extract the vascular tree in CTA imagery. Hessian matrix-based eigenvalue analysis is used for detection of the tubular objects; however, an intensity threshold constraint is often used from literature without employing the impact of the contrast medium in the respective CTA volume. We aim to derive an adaptive intensity threshold for optimal segmentation in the respective volume.

1.3.2 Hybrid energy based efficient coronary segmentation

Based upon the coronary seed points, a region based active contour model is applied for delineation of the coronary vasculature. The inherent problem of intensity inhomogeneity in medical images is generally addressed using localized intensity information in a curve evolution. However, the localized energy based active contour model often suffers from erroneous segmentation due to the local optima problem. We aim to formulate a hybrid energy model for optimal segmentation of the coronary vasculature in CTA. The hybrid energy model couples the localized intensity with the global discontinuity model of the image for optimized segmentation.

1.3.3 Detection and localization of non-calcified plaques

In the subsequent step, we aim to employ a machine learning technique to detect the non-calcified plaques in the segmented coronary tree. A support vector machine evaluates individual coronary segments and plaque affected segments are identified accordingly. Moreover, the plaque affected segments are evaluated using a second order derivative to identify the precise location of non-calcified plaque in respective segments.

1.3.4 Segmentation and quantification of non-calcified plaques

In the final stage of this work, we aim to segment and statistically quantify the non-calcified plaques present in the respective coronary segments. Moreover, we aim to perform the vessel wall thickness analysis in this context as it directly reflects the amount of non-calcified plaque. In the subsequent step, we aim to validate the quantified lumen and plaque with respect to segmentations produced manually by three independent human experts.

1.4 Organization of the thesis

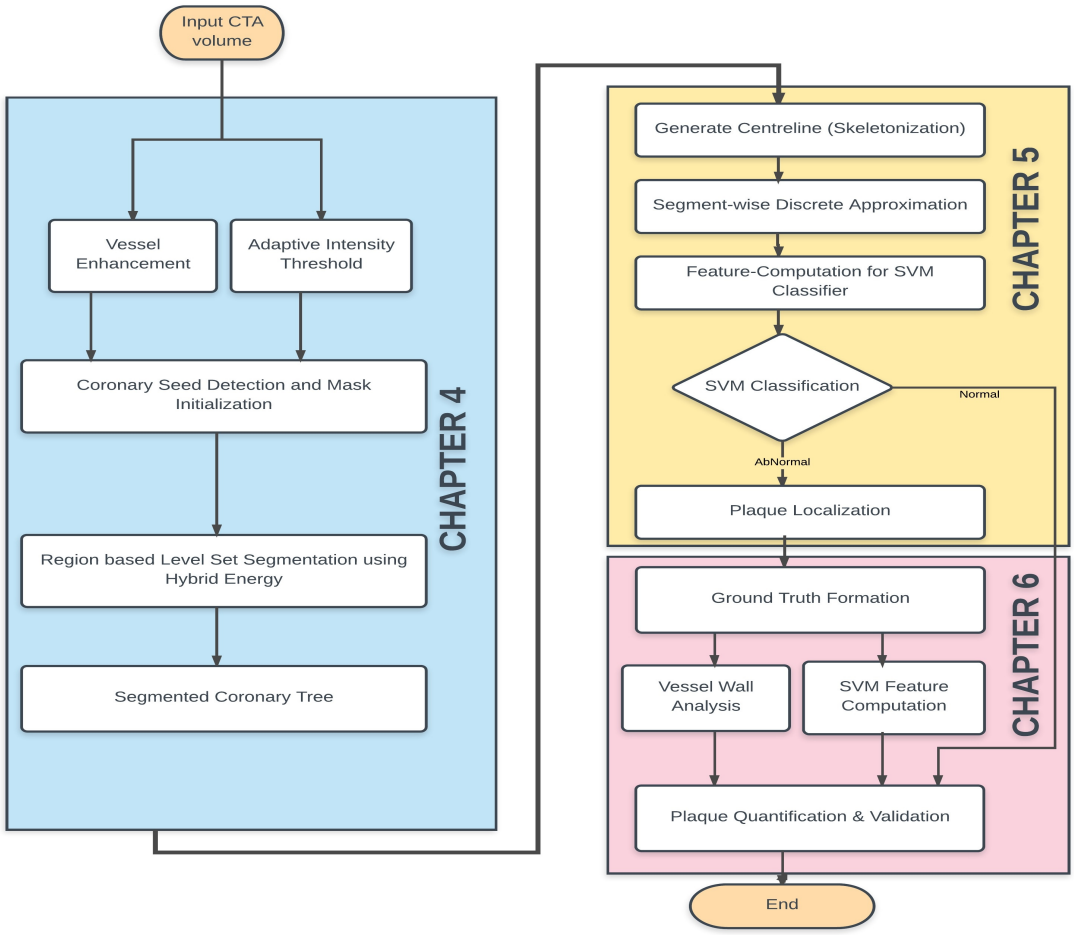

Fig. 1.1 Flowchart for the plaque segmentation framework. Chapter-wise processing is illustrated using three different colours.

The main flowchart reflecting the structure of this thesis is represented in Fig. 1.1. It is important to mention that the initial three chapters address the background and the relevant literature for this research, whereas Chapters 4 - 6 explain the implementation details and relevant results for this work. Moreover, the limitations and possible future extensions for this work are discussed in the last chapter. For a greater appreciation of this thesis, a brief description for individual chapters is presented below.

Chapter 1 introduces the basic theme of this work with a short introduction followed by the aims and objectives of the thesis. Moreover, the importance of the research problem is highlighted with the help of disease incidence statistics in this chapter.Subsequently, Chapter 2 defines the clinical context of this work for the general audience. Starting with heart anatomy, we explain the cardiovascular diseases with a specific emphasis on coronary heart disease (CHD) and associated non-calcified plaques (NCP). This is followed by an overview of medical imaging techniques (invasive versus non-invasive diagnosis methods). We conclude this chapter with a focus on CTA based acquisition and interpretation methodologies in context of CHD diseases.

Chapter 3 addresses the basic problem of image segmentation. We start with an overview of simple edge and region-based methodologies and extend our discussion to complex PDE based parametric segmentation models. In the following section, we explore the explicit curve representation in terms of level set formulation and the image based energy for curve evolution. In the last section of this chapter, we provide a literature based detailed review for vessel segmentation, and non-calcified plaque detection / segmentation.

Chapter 4 starts with the details of clinical CTA data used in this work, followed by the ground truth construction of vessel boundaries for comparative purposes. In the subsequent section, we explain the contrast medium modelling phenomena followed by the hybrid energy based coronary segmentation. In the last section of this chapter, we illustrate the efficiency of the proposed adaptive intensity threshold and the hybrid energy model with the help of both qualitative and quantitative results.

In Chapter 5, we address the problem of detection and effective localization of non-calcified plaques in the segmented coronary vasculature. Starting with the coronary skele-

tonization details, we explain the idea of a discrete radial profile for the representation of a coronary segment. This is followed with the SVM based formulation for the detection of abnormal segments. Next, we explain the plaque localization method in the context of abnormal segments. In the last section of this chapter, we discuss the efficiency of the plaque detection and localization methods.

Chapter 6 explains the method for computing segment-wise non-calcified plaque. We start with a description of our Matlab based coronary analysis tool, which allows an evaluation as well as expert-based manual demarcations for coronary lumen and plaques. In the subsequent step, we explain the voxel-wise ground truth formulation for non-calcified plaque based on the work of Rotterdam experts [18]. Next, we explain the inter-observer variability statistics to justify the complexity of the NCP segmentation problem and derive a range of accuracy for our proposed model output. This is followed by the vessel wall analysis to establish a reference for healthy arteries as non-calcified plaque directly affects the vessel wall geometry. Next, we derive hand-crafted features for SVM based classification of plaque voxels by exploiting intensity distributions. In the last section of this chapter, we present both visual and statistical results in context of the plaque segmentation.

In Chapter 7, we conclude our work and explain some of the limitations of this work. Moreover, we discuss some of the future directions in which this work can be extended for an improved clinical diagnosis.

1.5 Contributions and Publications

The contributions of this research, i.e., those that form the basis of the thesis, are to be found in two main areas, associated with the segmentation of the coronary vasculature and quantitative plaque analysis in the segmented tree, described in Chapters 4, 5 and 6, respectively. Specifically, the contributions of this thesis are summarised as follows:

We demonstrated that adaptive modelling of the contrast medium intensity can considerably improve the accuracy of the coronary segmentation. The usefulness and originality of these contributions is reflected in the promising results validating a significant improvement

in segmentation accuracy which have produced two journal publications [39, 40]. Moreover, we introduced a hybrid energy formulation that integrates the local intensity and a probability based global discontinuity map of the image. The proposed hybrid energy based model captures object boundaries accurately as the hybrid energy is less attracted to the local optima solutions. Consequently, this chapter leads to a quality journal publication [41]. After coronary tree segmentation, we extended our work for detection and localization of the non-calcified plaques using discrete radial profiles in clinical CTA. In this work, we employed a machine learning framework (support vector machine) for detecting non-calcified plaque affected coronary segments from normal sections. This chapter leads to two quality publications [42, 43].

In the final phase of this work, we proposed the framework for voxel-wise computation in the plaque affected coronary segments. The experimental results show a good correlation with respect to three human experts, which will lead to an additional journal publication. In addition, our contribution in this work is the design of an automated tool (Coronary Artery Evaluation Framework CAEF) for analysis and investigation of the segmented coronary tree. CAEF framework allows user to visualize the segmented coronary tree both in 2D and 3D space for a detailed investigation. Moreover, it allows user to construct customized visualization using maximum intensity projection, re-sampled oblique cross-section and multi-planar reformations for individual coronary segments. Furthermore, the notable feature in CAEF is the provision of manual annotation facility, in which user can manually annotate the vessel components i.e. lumen and the plaque. It should be mentioned that CAEF can be used efficiently to construct expert based manual ground truth, which is the most important step of any clinical study.

Chapter 2

Coronary Heart Disease - A Clinical Context

2.1 Anatomy of Human Heart

The human heart is located between two lungs in the centre of the chest. Anatomically, it is divided into four chambers: upper left and right atria; and lower left and right ventricles [44, 45], each performing a specific task in the blood circulation in the body. The strongest chamber of the heart is left ventricle, which is responsible for pushing blood through aortic valve towards different organs of the body. In a cardiovascular system, the heart works as a pump that moves nutrient rich blood to different organs of human body. In addition, the deoxygenated blood is collected and routed to heart. This transportation of the blood is accomplished through a complex network of vessels around the heart. According to the purpose, vasculature is termed as arteries (moving purified blood away from the heart) or veins (responsible for routing deoxygenated blood to the heart).

Being the centre of cardiovascular system, the heart is responsible for performing uninterrupted operation throughout the life of every person. For a continuous operation, a rich supply of oxygen and nutrients is required to the heart itself so that muscles can perform required contraction operations effectively. This is achieved through a vessel network (coronary artery tree) over the external surface of the heart. Moreover, the constant motion of the heart is

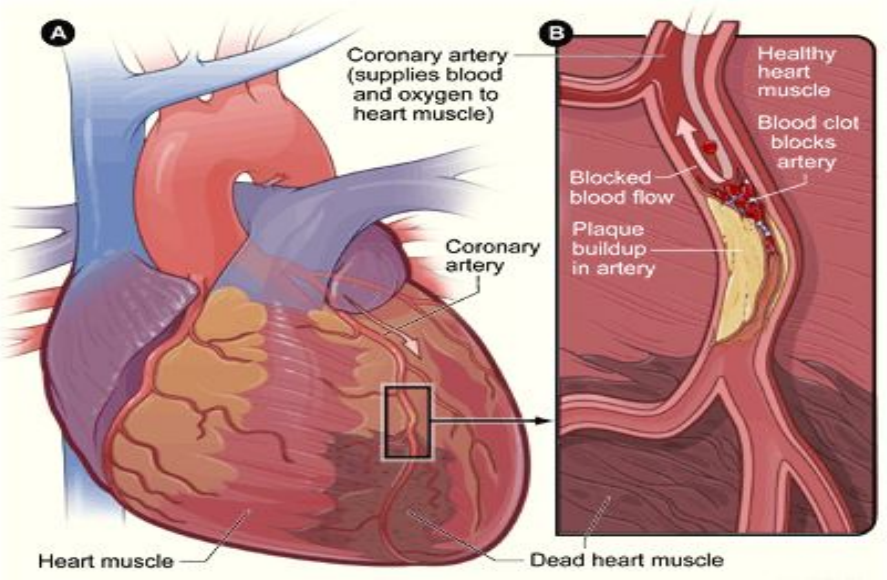

Fig. 2.1 Illustration for external surface of human heart [1]. The left image shows the muscular surface of the heart with an overlaid network of arterial vessels for blood supply. The right image shows a possible obstruction in the blood flow and resultant damage to the heart muscle. It can be observed that reduced blood flow to a particular muscle/tissue results in destruction of the respective region, which increases the chance of myocardial infarction and ischaemia.

accommodated in terms of a "vaso-constriction" phenomena, a process of cyclic peaks and troughs of coronary circulation. It allows coronary arteries to adjust blood flow according to the requirement of the heart tissue and muscles.

In contrast to other organs, smaller branches of coronary arteries are very refined and do not offer interconnections for blood flow diversions. This makes the coronary blockage a severe threat leading to the myocardial infarction and ischemia. Cardiac ischemia often results in an "angina" attack, i.e. reduced blood flow to heart muscles causing tissue damage as illustrated in Fig. 2.1. The patient undergoing angina attack needs immediate restoration of blood flow, otherwise the affected muscles begin to die which ultimately results in cardiac morbidity.

The coronary network in humans comprises of two (left and right) arteries that originate from the root of the aorta, where the aorta is the main vessel coming out of the left ventricle filled with oxygenated blood. The Left Coronary Artery (LCA) supplies oxygenated blood to the left chambers of the heart, whereas the right and posterior muscles of the heart are

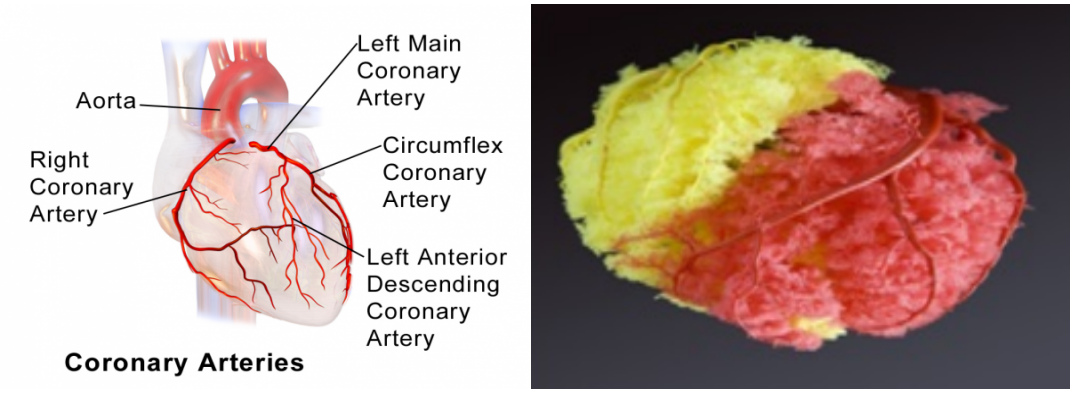

(a) coronary tree (b) Muscle nourishment using two coronaries

Fig. 2.2 Coronary Nomenclature and heart muscle nourishment [2]. (a) The heart surface is overlaid with two coronary arteries, and the major branches are labelled in a clinical context. The contribution of the respective coronary arteries (RCA, LCA) in the heart muscle nourishment is presented in (b), where red and yellow shows the heart region dependent upon left and right coronary arteries respectively.

nourished through the Right Coronary Artery (RCA) and the Posterior Descending Artery respectively. For a meaningful clinical evaluation and diagnosis of the coronary vasculature, two main arteries are further divided into branches as illustrated in Fig. 2.2 - 2.3. For Left Coronary Artery, the initial segment from the aorta to the first bifurcation point is termed as Left Main (LM) section. Subsequently, two bifurcated branches are named as the Left Anterior Descending (LAD) and Left Circumflex (LCX) arteries. Likewise, the Right coronary artery generally splits into few marginal arteries (OM1, OM2) and posterior descending arteries (PDA).

Instead of a standard coronary architecture applicable to all human beings, a wide inter-patient variability has been observed in clinical studies as defined in [46]. In a clinical context, side dominance is used to classify subjects according to coronary behaviour. Dominance is determined by identifying the oxygenated blood route to posterior muscles of the heart. Almost 70% of the population is right dominant where posterior tissues are nourished by right coronary artery. For 10% cases, the left coronary artery is dominant, whereas the remaining 20% are identified as co-dominant where both left and right arteries are feeding the PDA. Moreover, the Sinuatrial nodal artery arises from the RCA in 55% of the population, whereas for remaining 45% it comes out of the LCA [47].

This inter-patient variability in coronary architecture has made coronary investigation a challenging problem, as individual experts interpret the coronary tree without employing a common terminology. In this context, the American Heart Association (AHA) [4] formulated a standard for systematic interpretation and reporting compilation of coronary structural diagnosis. Accordingly, the standard AHA coronary model divides two coronary arteries (LCA and RCA) into 17 discrete segments as illustrated in Fig. 2.3. The clinical diagnosis is reported in terms of quantitative coronary analysis (QCA) report based on a per-segment basis. Likewise, the lumen - plaque quantification in advanced analysis tools is performed on a per-segment/per patient basis to accurately represent the clinical threat. In a general interpretation, segments close to the aorta are normally referred as proximal or major, whereas segments away from the aorta are termed as distal or minor.

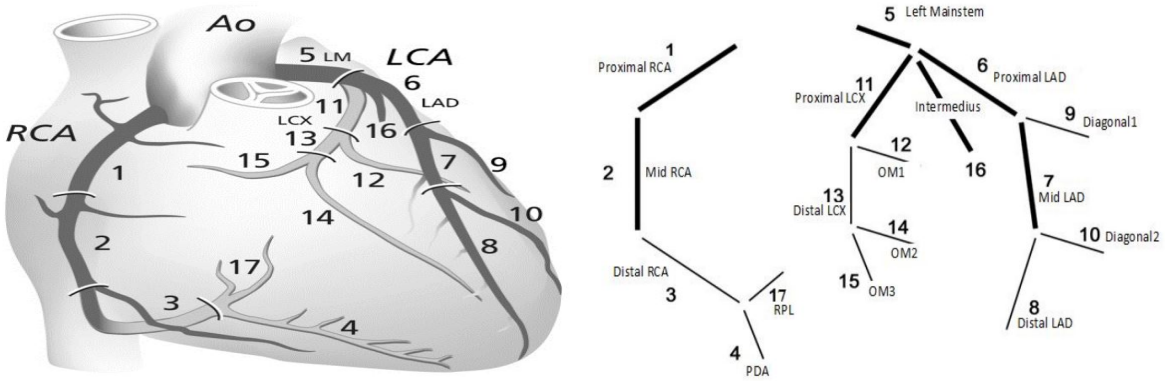

(a) coronary tree on heart surface (b) coronary tree schematic

Fig. 2.3 The 17-segment coronary model from [3]. (a) shows the heart surface overlaid with two coronary arteries, with individual segments numbered according to the 17-segment coronary model, (b) shows the coronary model schematic as proposed in [4].

2.2 Cardiovascular Diseases

The term cardiovascular disease (CVD) refers to all abnormalities that involve the heart and the blood vessels, i.e. coronary artery diseases (CAD), stroke, heart failure, hypertensive heart disease, cardiomyopathy, heart arrhythmia, congenital heart disease, aortic aneurysms [20, 47]. In general, the underlying mechanism for cardiovascular diseases involves some

chronic issues like high blood pressure, high blood cholesterol, Diabetes, as well as many lifestyle habits including lack of exercise, smoking, obesity, poor diet and excessive alcohol consumption among others [48, 35]. In recent years, CVDs have become the leading cause of death globally; combined they resulted in 17.9 million deaths (32.1%) in 2015 up from 12.3 million (25.8%) in 1990 [24]. Developed counties have been affected severely by CVDs in recent years. Approximately 40% of total deaths per year in the Unites States are related with cardiovascular diseases [49]. Likewise, according to National Health Services (NHS) United Kingdom statistics, over 1.6 million men and around 1 million women suffer from cardiovascular diseases in United Kingdom [36]. In the UK each year, CVDs are responsible for 88,000 deaths (an average of one death every six minutes), and around 276,000 attacks (heart and stroke) occur every year leading to thousands of mortalities. The contribution of individual diseases in the total death toll of CVDs is presented in Table 2.1. It can be observed from the table that coronary heart disease is the most threatening condition as it alone contributes to almost 50% of total CVD related deaths.

Table 2.1 Percentage breakdown of the death toll due to cardiovascular diseases world wide. [20]

Disease Nature	Contribution Ratio (%)
Coronary Heart Disease	49.9
Stroke	16.5
High Blood Pressure	7.5
Congestive Heart Failure	7
Diseases of Arteries	3.4
Other	15

2.2.1 Coronary Heart Disease

Coronary heart disease (CHD) is a state in which calcium and fatty material builds up inside the coronary arteries as shown in Fig. 2.4. These depositions (also termed as plaques) normally reside inside the lumen or vessel wall causing an obstruction in the flow of oxygenated blood to the heart muscles. Clinically, the development of plaques inside coronary arteries is termed as “atherosclerosis” and it takes many years before it posses an acute risk. In case of

calcium depositions (calcified plaque), the blood supply to heart tissues is almost terminated leading to the symptomatic myocardial infarction and angina. However, the fatty depositions (non-calcified plaque) makes the patient prone to arterial rupture due to its fragile nature which results in unexpected casualties. Moreover, coronary heart disease can also weaken the heart muscles leading to "arrhythmias" or heart failure, i.e. the heart cannot pump blood to the body organs.

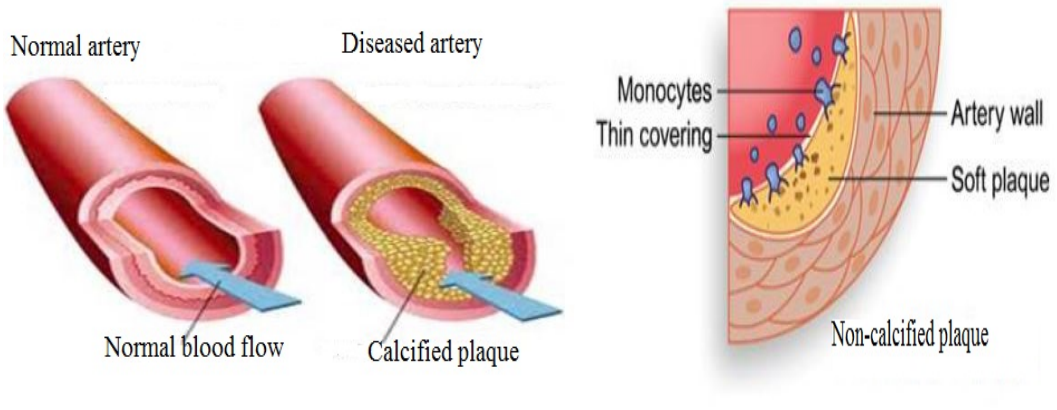

Fig. 2.4 Plaque present in a coronary artery. (a) calcified plaque deposition inside the lumen, (b) non-calcified plaque deposition inside the vessel wall. It can be observed that calcified plaque reduces the blood flow which leads to disease symptoms, whereas non-calcified plaque generally exhibits positive remodelling, i.e. the expansion of the vessel [5].

As coronary heart disease has emerged as the most significant threat, it is essential to diagnose coronary artery atherosclerosis at early stages to minimize the possible impact. This is based on the fact that medication and surgical procedures can avoid or at least delay the worst cardiac events in the future. Consequently, specialized medical examinations have been designed for detection and diagnosis of coronary heart disease; however no single investigation can draw final conclusions and multiple tests are advised for confirmation. Electrocardiogram and stress testing are two simple methods to diagnose initial symptoms of CHD, such that electrocardiogram monitors electrical activity of the heart, and the stress test records blood flow, heart and breathing rate in the excited state to identify possible abnormalities. Similarly, an echocardiography test uses sound waves for imaging the beating heart such that poor blood flow can be identified. Based on the initial results, clinicians advise

for coronary angiography that is an advanced, reliable but invasive test for CHD diagnosis. Accordingly, coronary angiography injects a contrast medium (dye) in suspected arteries followed by x-ray imaging. The injected contrast medium during cardiac catheterization process makes the respective coronaries prominent in the X-ray imagery, which allows clinicians to trace blood flow passage and identify any potential blockages therein.

2.2.2 Calcified versus Non-Calcified Plaques

Referring to the plaque depositions inside coronary arteries, atherosclerosis can be classified into two categories depending upon the composition and plaque location as illustrated in Fig. 2.5. The first type is "calcified" plaque, which is made up of calcium and normally resides within the lumen. With the passage of time, the build-up can narrow the vessel lumen and reduce blood supply to heart tissues, leading to clinical symptoms. These large plaques remain relatively stable, and due to the hard calcified covering, these are less prone to rupture or cracks. Moreover, the clinical symptoms reflect the presence of the calcification well before fatal events, allowing medication and precautionary measures.

The second type is "non-calcified" plaque, which is made up of fatty materials, lipids and cholesterol. This plaque normally resides inside the vessel walls, hence the lumen reduction is not always the case in non-calcified plaques. However, these dynamic, less stable soft plaques are much more likely to suddenly rupture through the arterial lining. As the body forms a clot to try to heal such a rupture, the result is normally a total blockage of blood flow; i.e. a severe heart attack. It is important to mention that these non-calcified plaques remain hidden inside the walls of the artery and often causes no obvious arterial blockage until, the fatal rupture occurs. This is the reason that clinically non-calcified plaques are treated more threatening as they do not provide any early symptoms, i.e. in many cases, death is the first symptom of non-calcified plaques [50].

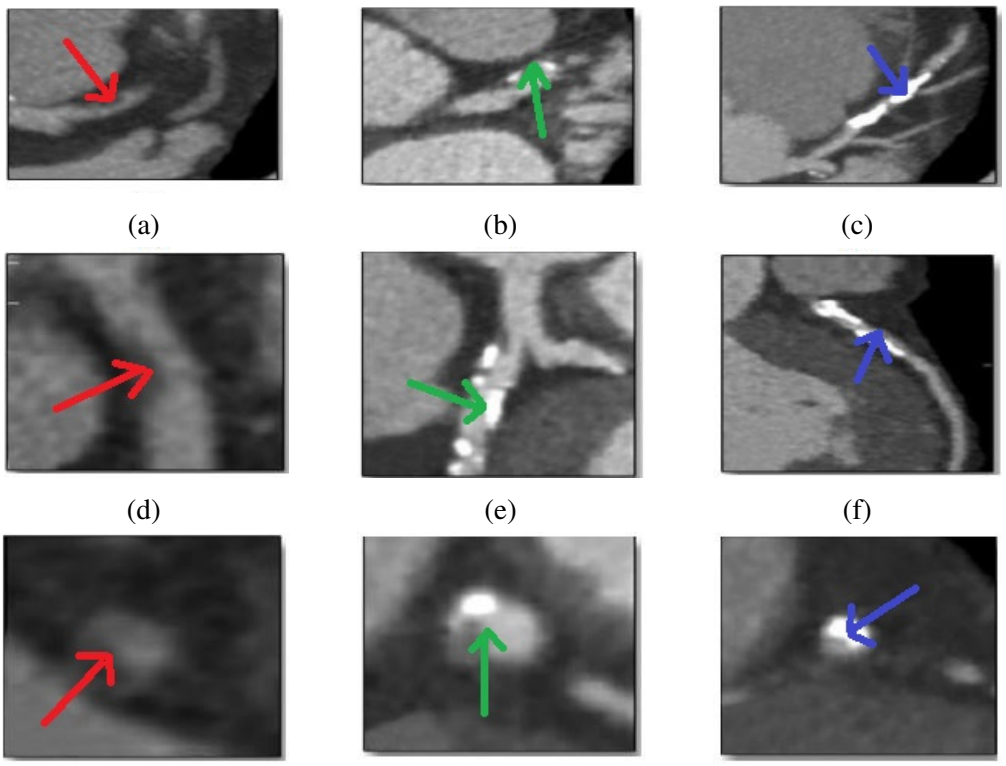

Fig. 2.5 Different types of plaques highlighted using different types of visualizations. (Top row) three axial slices, (middle row) three multi-planar reformatted images, (bottom row) three cross-sectional orthogonal images. The left column represents non-calcified plaques (red arrow), the middle column shows mixed-plaque (green arrow) and the right column shows calcified plaques(blue arrow).

2.3 Imaging based CHD Diagnosis

Medical imaging refers to the process of recording details of inside the body for visual interpretation, medical analysis and possible intervention. By combining radiology with imaging technologies, internal body structures are revealed for detailed clinical investigations. Accordingly, state-of-the-art imaging techniques have been developed for imaging the cardiac region in context of efficient diagnosis of cardiovascular diseases. In general, coronary imaging methods are divided into invasive and non-invasive categories depending upon the procedural and operational requirements.

2.3.1 Invasive Imaging

Invasive imaging refers to procedures involving the insertion of an apparatus into the body cavities. Some examples include X-ray angiography, optical coherent tomography (OCT) and intra-vascular ultrasound (IVUS). These methods are catheter-guided techniques they carry a sensor to the desired locations inside vessels. An example 2D angiogram obtained from X-ray angiography is shown in Fig. 2.6. The ability to reflect luminal diameter and occlusion points are the strengths of this method and it has remained as the gold standard for coronary disease diagnosis for years. However; the 2D representation is the inherent limitation of this method which can underestimate the plaque burden due to the loss of the third dimension of 3D arteries. For effective 3D reconstruction of vessels, different variations of X-ray angiography have been proposed including rotational systems for acquiring 2D angiograms at different angles. The obtained image sequence is used to create a 3D volume representing vascular structures. However, the rotational mechanism involved in this technique makes image quality inferior to a real CT scan.

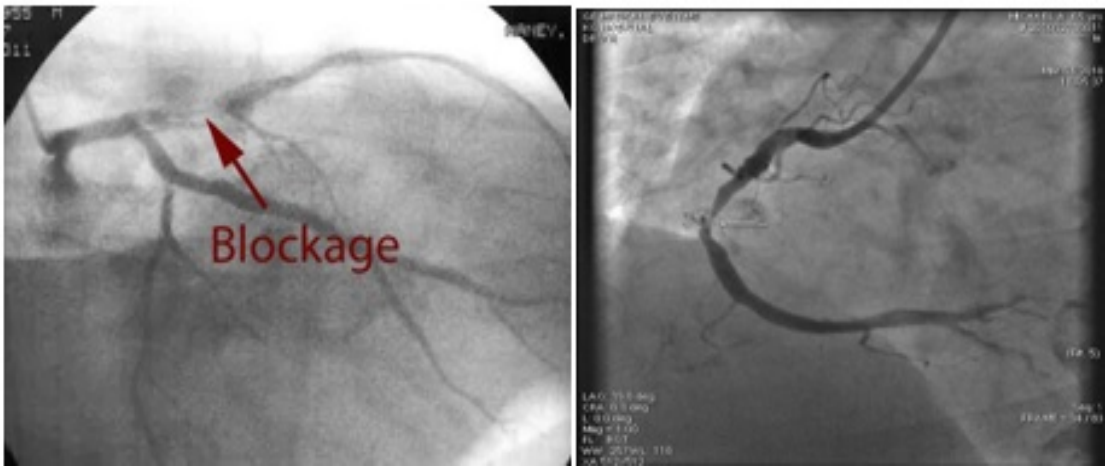

Fig. 2.6 An angiogram obtained from invasive angiography. In an optimal case, the arterial blockage can be identified visually in this 2D image, as illustrated by the arrow. In general, information relating to the third dimension is lost [6].

Catheter-guided IVUS is used for imaging vessel walls with high accuracy. This techniques allow direct and real time imaging of vessel occlusions by providing cross sectional views. Image acquisition is performed by recording signals from reflected laser beams (OCT)

or ultrasound beams (IVUS) respectively. Generally OCT is capable of providing more accurate images because of higher spatial resolution (around 10 micrometers); however, OCT suffers from a problem of low penetration as the laser beams are attenuated quickly in arterial walls. The main limitation associated with these methods are difficulty in reconstruction of 3D structures from 2D cross sections. Besides, these methods are applied to small segments of vessels to reduce the complications of catheterization procedure, so it is not possible to trace all the important branches of the arterial tree. For additional details, a comprehensive review of IVUS, OCT can be found in [51].

2.3.2 Non Invasive Imaging

Despite the fact that invasive imaging acquires valuable coronary information, the main drawback is complicated clinical procedures and associated risk to the patient. This becomes a time consuming clinical procedure and requires expertise from clinician. In particular, if the progress of the disease is to be tracked in routine examinations on regular basis, this invasive methodology is not suitable at all. Advancements in the technology have turned 3D non-invasive imaging of the human body into a reality in recent years. Two state-of-the-art imaging modalities being used to record internal organ details include CTA and magnetic resonance imaging (MRI). MRI is preferably used to image the muscular tissues, whereas CTA is used for recording blood structures in clinical practice. A variant of MRI used for non-invasive imaging of blood vessels is magnetic resonance angiography (MRA) but due to less spatial resolution and high slice thickness, this modality is used for imaging larger vessels only.

The advantage of these imaging modalities is that besides being non-invasive, these methods reveal information in terms of 3D volume rather than 2D projections as recorded in conventional angiograms. CTA is used clinically to record 3D behaviour of different organs including the head, neck, abdomen and heart with precise details (sub millimetre resolution in all three dimensions). Especially for cardiac imaging, CTA is a valuable technique as contrast medium affected blood can be traced visually due to their high intensity value as illustrated in Fig. 2.7. Along with blood filled coronaries, calcified plaques (if any) that

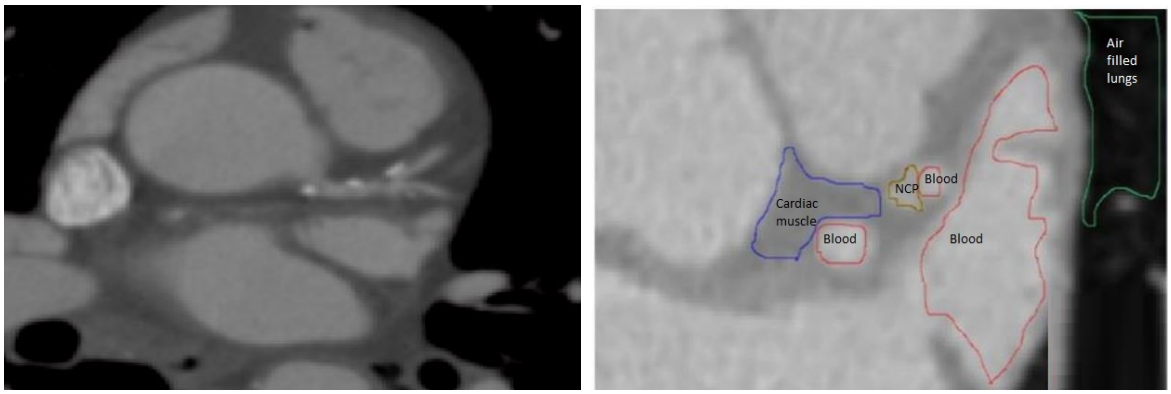

(a) axial slice

(b) zoomed version

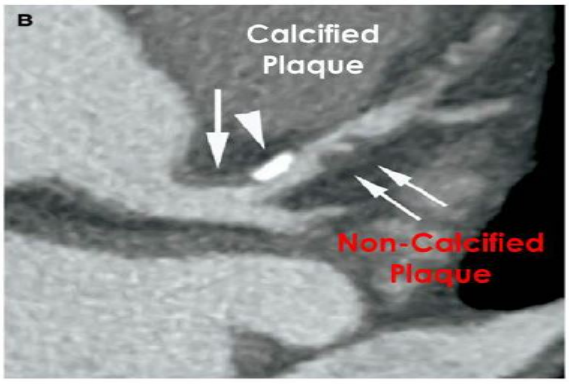

(c) Plaque identification

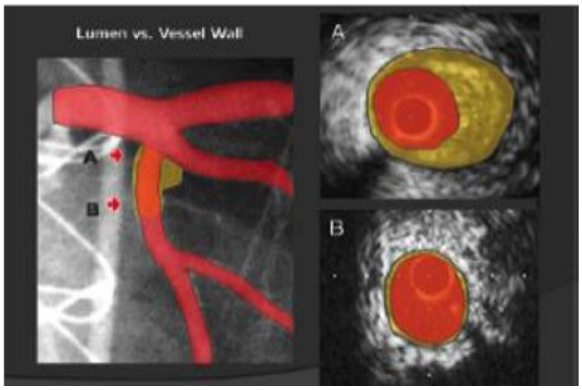

(d) Ultrasound analysis

Fig. 2.7 Non-invasive imaging for coronary analysis. (a) the intensity response (axial plane) showing different components inside the field of view of a cardiac CTA image, (b) zoomed version from an axial plane with annotations for different intensity responses. (c) shows the plaque visualization in CTA imagery, whereas (d) shows an ultrasound based appearance for the coronary vessel. It can be observed from (c) that calcium based plaque appears brighter in CTA due to high intensity, whereas lipid based non-calcified plaque appears relatively dull. Moreover, the IVUS based representation for the lumen and plaque can be visualized in (d).

are not seen in traditional angiograms can be visualised easily in CTA images. Moreover, based on the fact that CTA leads to 3D volumetric data, the cross sectional images can be constructed in 3D space to replicate the information captured by OCT and IVUS. Using vessel medial axis, a direction vector can be used for extracting orthogonal 2D cross sectional images to allow the analysis of the lumen and vessel wall. As the 2D oblique plane is constructed by interpolating intensities in 3D space, the quality is inferior to OCT but still useful for evaluating luminal changes. Digital subtraction angiography (DSA) is an extended visualization procedure used to capture blood filled vessels by subtracting normal CTA image

from a contrast enhanced version. Practically this procedure becomes difficult because it requires collecting two CTA datasets, leading to additional exposure to radiation. Moreover, it is difficult to obtain identical images of coronary arteries due to the constant motion of the heart. Therefore despite of the advantages DSA offers, it is not widely used for cardiac imaging and visualization.

2.4 Computed Tomography Angiography

2.4.1 Basics of Computed Tomography

Computed Tomography (CT) imaging combines specialized X-ray equipment with sophisticated digital geometry processing for generating 3D images of internal organs of the body. 3D re-construction is done from a sequence of 2D images acquired around a single axis of rotation, i.e. a number of images of same area are recorded from different angles and placed together to produce a 3D image. An ability to provide precise internal details has made the CT exam the preferred choice for clinical diagnosis of internal body organs like the head, neck, abdomen etc.

In clinical practice, CT is used as a diagnostic imaging test to create detailed images of internal organs, bones, soft tissue and blood vessels. The cross-sectional images generated during a CT scan can be reformatted in multiple planes, and used to produce3D visualizations that can be viewed on a computer monitor, printed on film or transferred to electronic media. CT scanning is often the best method for detecting many different cancers since the images allow the clinician to confirm the presence of an anomaly and determine its size and location. To conclude, CT is a fast, painless, non-invasive and accurate method for clinical diagnosis. In emergency cases, it can reveal internal injuries and bleeding to quickly help save lives. However, excessive use of CT leads to increased exposure to radiation.

As illustrated in Fig. 2.8, a modern CT scanner, in general, consists of a tunnel-like structure with an X-ray tube on one side and the detector on the other side. A motorized table moves the patient through a circular opening in the CT imaging system. As the patient passes through the CT imaging system, a source of X-rays rotates around the circular opening. In

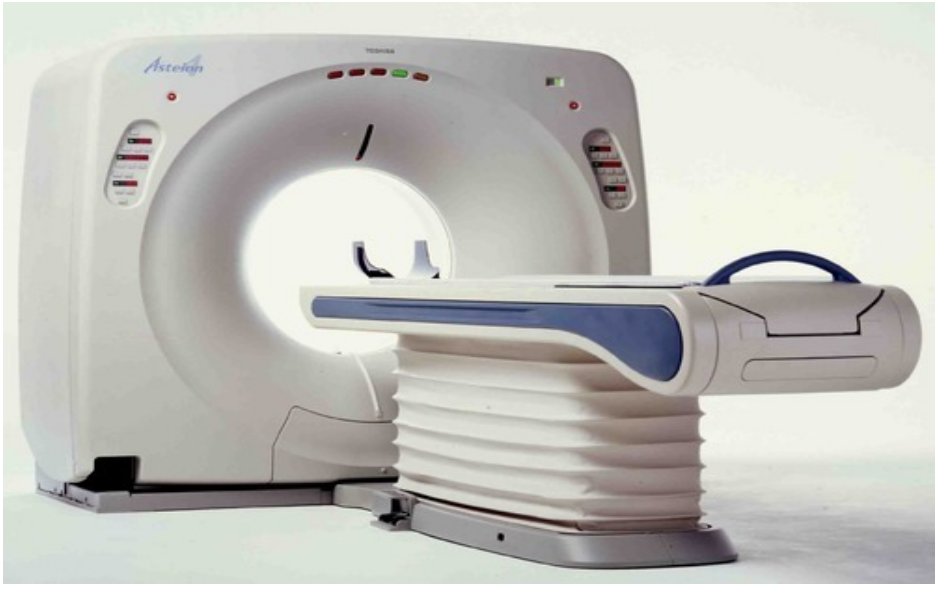

Fig. 2.8 A modern multiple slice computed tomography machine. The patient is placed on the table, moving through the ring unit, which is comprised of the X-ray source and the detector. [7].

typical examinations there are several phases; each made up of 10 to 50 rotations of the x-ray tube around the patient in coordination with the table moving through the circular opening. Detectors on the exit side of the patient record the x rays exiting the section of the patient's body being irradiated as an x-ray "snapshot" at one position (angle) of the source. Many different "snapshots" (angles) are collected during one complete rotation. The data are sent to a computer to reconstruct all of the individual "snapshots" into a cross-sectional image (slice) of the internal organs and tissues for each complete rotation of the source of x-rays. Moreover, CTA uses an injection of iodine-rich contrast material to help visualize and evaluate blood vessel disease or related conditions, such as aneurysms or blockages.

Despite the impressive results, CTA scan has not been used widely for imaging the cardiac system in the last decade because of the motion of the fast beating heart. High temporal resolution is required to capture the dynamic heart in an instant in time. Moreover, coronary arteries being very refined structures with a diameter in the sub-millimetre range demands high spatial resolution acquisition. State-of-the-art advancements in medical imaging have resolved this problem by introducing sub-second rotation combined with CT to achieve high speed and high resolution at same time. Similarly, dual source technique employing

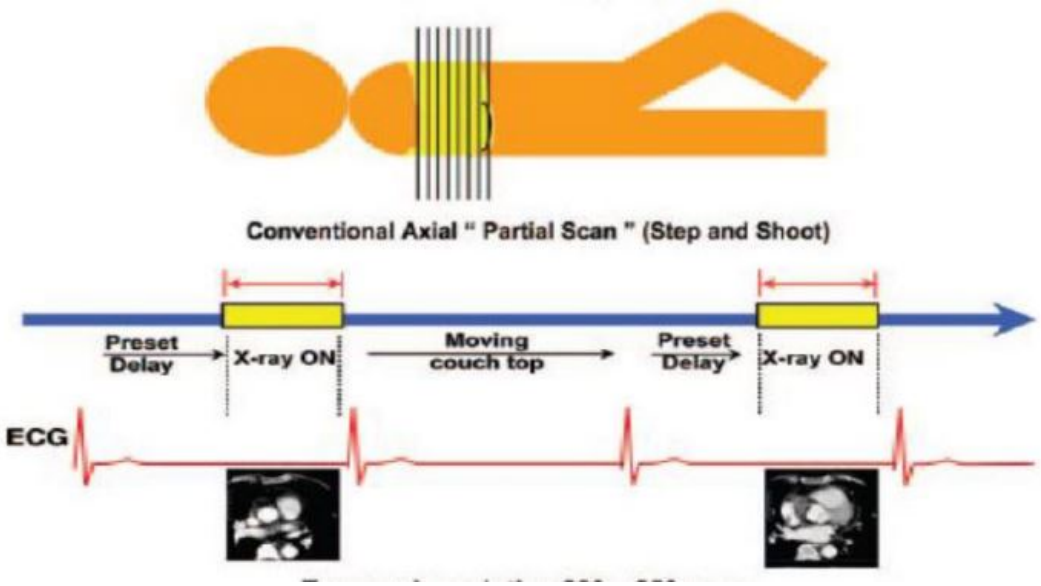

Fig. 2.9 ECG triggered CT scan for compensation of the heart motion. In order to minimize the impact of heart motion, each slice is scanned during same ECG phase [6].

double x-ray sources has reduced the acquisition time by imaging data in half a rotation, whereas the multi-detector approach has increased the spatial resolution. This makes CTA a clinical reality for assessment of the cardiac vascular system (i.e. imaging the dynamic heart for coronary analysis). In addition, ECG gating is used during the CT scan process to achieve synchronization between heart motion and image acquisition/reconstruction. Every detail of the heart is imaged multiple times along with ECG traces. In the subsequent step, corresponding phases of cardiac contraction are correlated by using ECG data. After correlation, systole related data is discarded and images are constructed using static phase (diastole) data. Fig. 2.9 represents the acquisition process of CT data showing compensation of heart motion during scan.

2.4.2 Interpretation of Computed Tomography Imagery

According to the imaging principle of x-rays, the anatomical organ images are obtained on the basis of their ability to block x-rays, termed as radiodensity. Radiodensity refers to the relative inability of electromagnetic radiation (x-rays) to pass through a particular material. Accordingly, materials that inhibit the passage of electromagnetic radiation are

called radiodense, while those that allow radiation to pass more freely are referred to as radiolucent. As the CT imaging employs x-rays, the CT scanner records the x-ray attenuation of the patient through a plane with a finite cross-sectional thickness, and these attenuation measurements are then reconstructed using a dedicated computerised system to produce a 3D volumetric image dataset of the body.

Every component (pixel) of a planar cross-section image represents the mean attenuation value of the segment. The mathematical formulation for pixel attenuation is expressed as follows:

$$I_t = I_o e^{-\mu_L \Delta x}, \tag{2.1}$$

where I_t is the structure (pixel) attenuation value, I_o represents intensity measured in the beam path without obstruction and μ is the linear transformation coefficient for a specific material. Three dimension information for volumetric objects can be incorporated by adding all attenuation values along the beam path according to Eq. 2.2.

$$I_t = I_o e^{-\Sigma_{i=1}^{k} \mu_L(i) \Delta x}. \tag{2.2}$$

A linear transformation coefficient or narrow beam attenuation coefficient of the volume of a material characterizes how easily it can be penetrated by a beam of light, sound, particles, or other energy or matter. A large attenuation coefficient means that the beam is quickly "attenuated" (weakened) as it passes through the medium, and a small attenuation coefficient means that the medium is relatively transparent to the beam.

The pixel attenuation value is represented in terms of the Hounsfield unit (HU) scale with a standardized range of [-1024 to +3071] HU. The HU scale transforms intensity values into a normalised scale where distilled water at standard temperature and pressure is assigned *zero* HU, whilst the air is defined as -1000 HU. Accordingly, the HU value for a particular structure is derived using Eq. 2.3. For a robust medical investigation, certain HU values are expected according to the behaviour/structure of the anatomical organs as presented in Table 4.4. These expected values are used in the clinical diagnosis of structural abnormalities i.e. investigation of calcified plaques and abnormal tumours.

$$HU = 1000 * \frac{(\mu - \mu_{water})}{(\mu - \mu_{air})}. \tag{2.3}$$

Table 2.2 Standard intensity in Hounsfield unit for different anatomical structures [21, 22]

Structure	HU Range
Air.	-1000
Lung.	-700 to -600
Fat.	-120 to -90
Chyle.	-30
Water.	0
Urine.	-5 to +15
Bile.	-5 to +15
Kidney.	+20 to +45
Blood.	+30 to +45
Muscle.	+35 to +55
Soft tissue.	+50 to +100
Bones.	+700 to +3000

2.4.3 CTA processing and interpretation

In addition to the radiation dose, the major limitation of the non-invasive CTA imaging is the amount of recorded data. Accordingly, the high volume of imaged data makes the manual investigation difficult and the interpretation is dependent on the previous knowledge of the clinician. Accordingly, a number of image-processing techniques are applied in clinical practice to extract the required information from a 3D CTA volume. This includes the use of customized window/level setting in visualization, application of maximum intensity projection, re-construction of multi-planar reformatted images from 3D CTA volumes, and volume rendering [52, 53, 38].

The basic concept behind window/level is to apply a linear grey-scale transform function, in the form of a lookup table (LUT) specified by two parameters, window and level. The end result is that pixel intensities corresponding to a subset of the entire dynamic range are highlighted, at the expense of pixels not in the subset falling outside the specified range. Fig. 2.10 shows a LUT where input pixels of intensity less than 73HU are mapped to 0, pixels of

intensity greater than 198HU are mapped to 255, and pixels within the range [74,...,197] HU are scaled appropriately depending on the slope of the transform function in the bracketed region of Fig. 2.10.

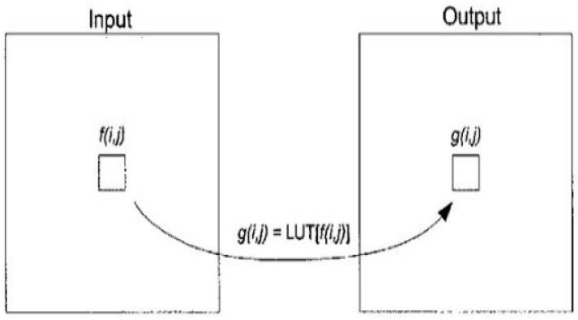

(a) Look-up table processing

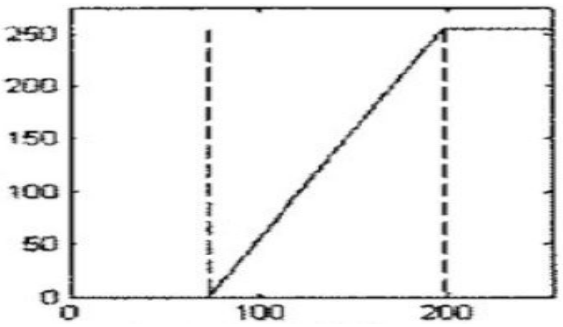

(b) Window transformation

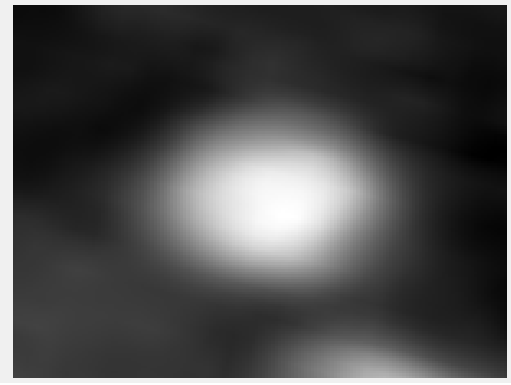

(c) Cross-sectional view using maximum intensity

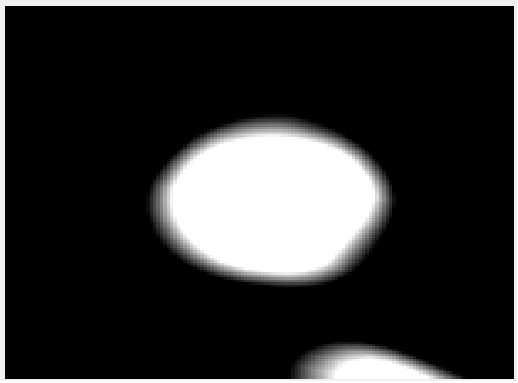

(d) Cross-sectional view using window [74 197]

Fig. 2.10 Table look-up based processing for image. (a) shows that a pixel-to-pixel mapping is performed using a pre-defined transformation criteria, (b) defines a window for investigating a particular intensity range [74-197] HU.

A standard way of specifying a linear grey-scale transform function of Fig. 2.10 is to define the width of the LUT where the slope is non-zero (window) and the centre of that same segment of the LUT (level). Accordingly, holding the window constant while adjusting the level has the effect of moving the non-zero slope portion of the transform to the left or to the right. Likewise, altering the window parameter either broadens or narrows the pixel intensity range to be highlighted. From a clinical point of view, standardized window/level settings have been formulated to evaluate different anatomical structures from the CT image as presented in Table 2.3. Accordingly, the object of the interest can be quickly isolated from the background for a detailed investigation.

Table 2.3 Standard window-level setting for visualization of different anatomical structures in CTA [23]

Structure	Window	Level	Grey-scale Range
Posterior fossa (P.F).	150	35	[-40 110]
Brain	70	35	[0 70]
Internal auditory canal	4095	600	[1448 2648]
Bone	2000	800	[-200 1800]
Lung	1600	-600	[-1400 200]
Abdomen	350	60	[-115 235]
Liver A	200	100	[0 200]
Liver B	220	25	[-85 135]
Spine.	300	60	[-90 210]
Fat	270	-35	[-170 100]
Coronary vasculature	800	300	[-100 700]

In addition to the window/level display settings, the CTA volume can be investigated using a maximum intensity projection technique. Maximum intensity projection (MIP) is a sophisticated method to project the voxels with maximum intensity from the 3D volume to a visualization plane. Accordingly, the voxels with maximum intensity that falling in the way of parallel rays traced from the viewpoint to the plane of projection are recorded. This technique is used in CT imagery for the detection of lung nodules in lung cancer screening programs which utilise computed tomography scans. Similarly, MIP is often used in cardiac CTA to trace any existing high-intensity calcified plaques as illustrated in Fig. 2.11a. Multi-planar/ curved-planar reformation is another possible technique which makes CT imaging very effective in clinical context. Based on the medial axis of the segmented coronary tree, a 2D image can be sampled in 3D space to follow the progression of the curvilinear vessel as shown in Fig. 2.11b.

The real strength of the CT imaging is illustrated in Fig. 2.12, in which a segmented coronary structure is presented. Based on the fact that CT equipment records three dimensional details, the segmented artery tree can be evaluated in all three directions. This is a significant advantage over conventional 2D angiogram based imaging, in which the third dimension is often lost. Moreover, the segmented coronary tree can be investigated for lumen and vessel wall analysis by sampling 2D orthogonal cross sections as shown in Fig. 2.12b. Hence,

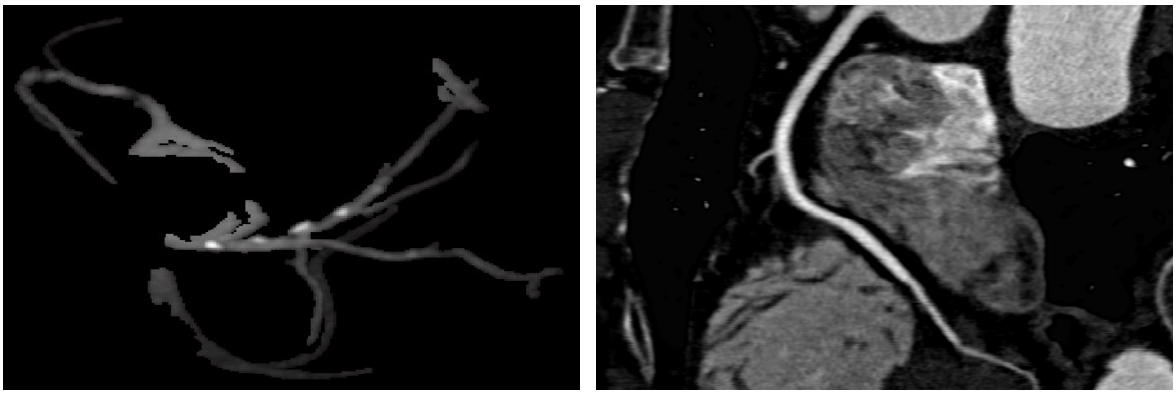

(a) MIP (b) CPR

Fig. 2.11 Interpretation of a CTA image for effective diagnosis in clinical practice. (a) Maximum intensity projection (MIP) representing the coronary vasculature and calcified plaques. (b) Curved-planar reformatted (CPR) image representing right coronary artery in a 3D CTA volume.

the non-invasive nature and three dimensional data availability makes the CTA feasible for clinical diagnosis of coronary heart disease.

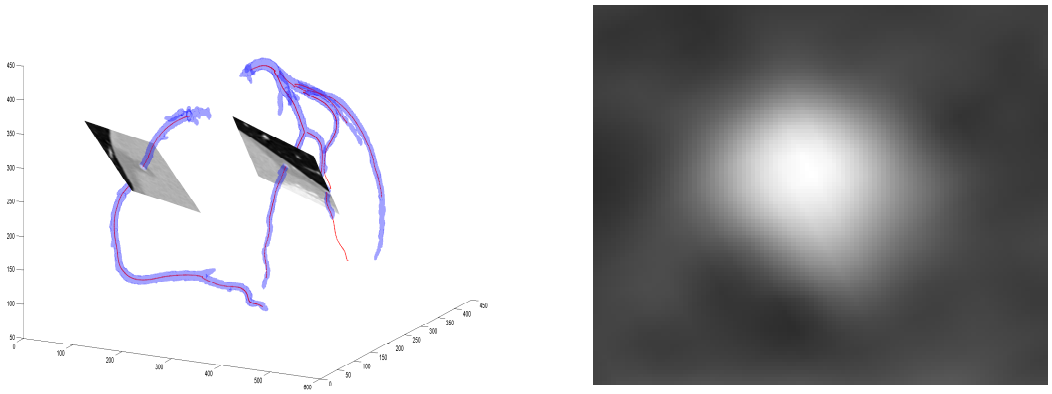

(a) 3D surface (b) Orthogonal

Fig. 2.12 Interpretation of a CTA image for effective diagnosis. (a) surface re-construction of the 3D arterial tree, with overlaid oblique planes, (b) Cross-sectional slice defining the coronary lumen. It can be observed that the 3D surface can be investigated in all three dimension using rotation.

Chapter 3

Image Segmentation: Background and Related Work

3.1 Introduction

Based on high temporal and spatial resolution, the latest imaging scanners are capable of recording sub-millimetre details of internal body organs. However, the manual analysis of recorded image data becomes time consuming, and interpretation often depends upon the knowledge of the expert. Therefore, fast and precise segmentation of the object of interest is important for reliable clinical diagnosis.

In computer vision, image segmentation is the process of assigning a label to every pixel in an image such that pixels having the same label belong to one object. The result is a set of segments that collectively cover the entire image where adjacent segments differ significantly with respect to certain features. For effective analysis of the local features, segmentation is necessary i.e. to extricate region of interest by suppressing the unwanted background of the image. The concept of segmentation has been widely applied for image analysis in several areas such as conception and visualization, intelligent transportation systems, satellite imaging and biomedical diagnosis. One of the most important application domain is medical imaging where it can be used as an effective tool to assist computer aided surgery, tumour detection and the identification of vascular abnormalities.

From a clinical point of view, a cardiac CTA image contains multiple anatomical organs exhibiting similar visual appearance on the screen; however, a clinician is interested in the coronary vasculature for abnormality detection. Here segmentation techniques can effectively differentiate coronary vasculature from the remaining organs for a focused diagnosis. It is important to mention that coronary vasculature comprises around 2 - 3% of the total CTA volume [38]. Hence, it is extremely important to discard the irrelevant background and delineate the object of interest for a focused investigation. Moreover, in context of this research, the ultimate theme is detection and segmentation of the non-calcified plaques in CTA. The presence of background structure can significantly affect the performance of plaque detection algorithm, since the intensity value of non-calcified plaques and heart muscles often overlap. Once, the object of interest is delineated successfully, a number of image processing technique (contrast enhancement, image sharpening etc.) can be employed further for optimal visualization and interpretation.

Generally, texture homogeneity and spatial connectivity is used to extract different objects in an image [54, 55]; however, for complex medical data, a combination of features (intensity and geometric) is often required for effective delineation. For a mathematical representation of the segmentation problem, let Ω represent the image domain, and S_k represent a set of connected pixels (discrete object). Accordingly, segmentation can be interpreted as process of identifying non-overlapping setsS_k such that the union is the image domain and intersection is the /null set as expressed by Eq. 3.1.

$$\Omega = \bigcup_{k=1}^{NumObjects} S_k, \qquad (3.1)$$
$$where \quad S_k \bigcap S_j = \phi, \forall k \neq j.$$

In some cases, one of these objects is called *background* and it includes all the regions not covered by the objects of interest. For complex medical images, where there exist multiple objects of the interest in the image, normally associated with organs, tissues or cells, the classical segmentation process is replaced by pixel segmentation. Pixel segmentation is a relaxed version of classical segmentation where the connectivity constraint between regions is

removed; as a result disconnected regions belonging to the same tissue class can be delineated. However, it is difficult to determine the total number of classes (sets) in pixel segmentation at the beginning. Consequently, the domain specific knowledge is usually employed to make the segmentation process robust and realistic in terms of expected number of classes in the image.

A number of segmentation algorithms have been proposed in the literature with a basic difference in the boundary detection principle. Simple algorithms employ the image characteristics including predetermined cut-off intensity value for threshold based segmentation, gradient strength for edge based segmentation and regional intensity characteristics for region based segmentation [56, 57, 55, 58, 59]. In addition, sophisticated algorithms employ partial differential equations (PDEs) to detect object boundaries [60, 61], i.e. an initial guess is evolved under constraints to detect the object boundaries. Starting with simple edge and region based segmentation techniques, we explain the classic active contour models, the geometric deformation and the level set formulation in this section. In the subsequent section, we present a review of the literature in the context of vascular segmentation. The last section presents a comprehensive review of the state-of the-art literature for non-calcified plaque detection/segmentation in CTA.

3.2 Classification of the segmentation algorithms

Apart from simple threshold and clustering techniques, the recent sophisticated algorithms employ partial differential equations (PDEs) to detect object boundaries, i.e. an initial guess is evolved under constraints to detect the object boundaries. Commonly used formulations include the *parametric snake model* and the *level set formulation*. The parametric snake i.e. active contour model [62] leads to a fast and computationally efficient segmentation but shows greater sensitivity to the topological changes, whereas the level set representation [60], [63] provides inherent split and merge mechanisms to accurately detect complex structures at the cost of processing time. It should be noted that for both formulations, the evolution of the initially placed curve is regulated by underlying image characteristics in terms of

an energy functional. Methods reported in [62] and [63] approximate the image-based energy in terms of the intensity gradient strength (edge-map), whereas techniques proposed in [64] and [65] employ regional intensity statistics for the energy approximation. The region-based methods show robust performance in general as the gradient strength often leads to over segmentation for weak edges. However, the conventional region-based methods fail to address the intensity inhomogeneity problem of medical images due to the underlying piecewise constant assumption. Consequently, localized statistics have been frequently reported to regulate the curve growth in medical images for minimizing the impact of the intensity inhomogeneity Li *et. al.* [66] and Lankton *et al.* [16].

3.2.1 Edge-based Segmentation

The basic idea behind edge-based segmentation is that a closed shape object in a binary image can be fully represented by its edges. Accordingly, edge detection often helps in substantial evaluation of image contents by delineating individual components. In general, the edge detectors are formulated to capture (respond to) image discontinuity in terms of gradient strength. From a practical point of view, edge-based segmentation can be defined as a multi-stage process starting with edge map generation in an image. In the subsequent step, the identified edges are investigated for closed shape measures as segmentation aims to delineate the closed boundary object(s). In the final step of edge-based segmentation, intelligence-based operations are generally required to bridge small gaps and remove false edges.

Mathematically, the gradient computation is the most effective way of detecting discontinuities in an image intensity values. In a pre-processing step, image noise is often normalized using smoothing filters to avoid detection of false edges. Subsequently, differentiation is applied using finite differences to record spatial intensity variations as defined in Eq. 3.2. The finite difference approximation of Eq. 3.2 represents the derivative for a continuous function; however, a discrete approximation implementable on a computer is achieved by substituting the minimum step distance $\Delta i = \Delta j = 1$ pixel accordingly.

$$\nabla Im_i = \frac{Im(i+\Delta i, j) - Im(i,j)}{\Delta i}, \qquad \nabla Im_j = \frac{Im(i, j+\Delta j) - Im(i,j)}{\Delta j}. \tag{3.2}$$

For two-dimensional images, the intensity variation is calculated in both directions to obtain the gradient vector $G\left(\nabla Im_i, \nabla Im_j\right)$ for respective pixels, where ∇Im_i and ∇Im_j represents the partial derivatives in two directions. The effective gradient strength for the pixel is computed using Eq. 3.3 , whereas the edges are established by comparing the gradient magnitude with an application dependent threshold T according to Eq. 3.4.

$$|\nabla Im(i,j)| = \sqrt{\left(\nabla Im_i^2 + \nabla Im_j^2\right)}. \tag{3.3}$$

$$E_{map}(i,j) = \begin{cases} 1 & \text{if } |\nabla Im(i,j)| > T, \\ 0 & elsewhere. \end{cases} \tag{3.4}$$

Different operators [67, 68] have been proposed in literature employing horizontal, vertical and diagonal computations. However, gradient-based edges usually results in frequent gaps or false edge identification which require intelligent post-processing. If prior shape information is available, a Hough transformation [69, 70] can be applied in the post-processing step to track objects in edge map. Another method for linking nearby pixels is the neighbourhood search, which can lead to closed boundary edges. Constraints imposed on linking criteria ensure the linkage on right path at the cost of computational complexity.

3.2.2 Region-based Segmentation

Edge-based segmentation isolates individual objects by delineating outer boundaries, whereas region-based segmentation interprets individual objects as consolidated regions. The region-based segmentation starts from a single reference (seed) point, and the object shape is adopted gradually by including all the pixels that satisfy predefined similarity criteria in terms of

texture, intensity or shape constraints as illustrated by Fig. 3.1. It can be observed that the neighbouring voxels that satisfy the similarity criteria iteratively becomes the part of the larger vessel in the proposed region based segmentation.

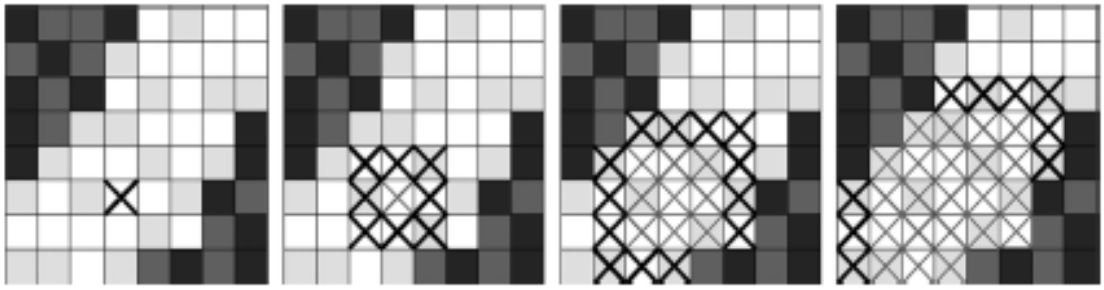

Fig. 3.1 Region growing algorithm for vessel segmentation. Based on the connectivity criteria, the adjacent pixels are merged to form an object.

Region-based segmentation has shown potential to overcome the limitations of the edge based theory, especially noise induced images are handled more effectively by region-based processing with minimum leakage. The core idea of the region-based processing employs "split" and "merge" operations for image pixels. Pixel merging operation begins with the assumption of over segmentation in an image. Subsequently, it starts fusing adjacent pixels having similarity until no more merging is possible. The similarity criteria used is important and often relies on intensity value similarity. The region growing technique is a practical implementation of merging segmentation. Starting with a set of pixels (seed values), the neighbourhood is scanned for pixels that fulfil the similarity criteria and consequently added to object. In contrast, splitting is based on the assumption of under segmentation, as it starts splitting image regions having dissimilarity into distinct regions until no more splitting is possible. The combination of these two operations produces accurate segmentation; however the computational cost is often increased.

3.2.3 Parametric Active Contour Models

Active contours have been a popular choice for medical image segmentation in recent years [71]. A comprehensive review of deformable models in image segmentation can be found in [72]. The motivation for the active contour model is the seminal work of Kass *et*

al. [62] in which the object segmentation was posed as an energy minimization problem. According to this model, the object boundaries can be captured in an image with the help of a parameterized contour, where the evolution (the propagation speed and the direction of growth) of the contour is regulated by a complex energy function as expressed in Eq. 3.5.

$$E = \int_0^1 E_{int}\left(C_s\right) + E_{ext}\left(C_s\right) + E_{cons}\left(C_s\right) ds, \tag{3.5}$$

where $C(s) = \left(x(s), y(s)\right), \quad 0 < s < 1$ denotes the evolving curve (also called as snake) parameterized by arc-length s, such that intermediate values of s define the curve control points representing deformable snake. The internal energy E_{int} penalizes the bending and stretching of the curve to ensure smoothness, E_{ext} represents an image based energy (intensity statistics) and E_{cons} refers to explicit constraints imposed by the user. Accordingly, image based energy E_{ext} pushes the finite length evolving curve towards the object boundaries, whereas E_{con} based on prior knowledge is often employed to speed up the computation.

The internal energy E_{int} reflecting the snake behaviour can be modelled according to Eq. 3.6. The norm of the first derivative$\frac{\partial C(s)}{\partial s}$ represents elasticity and second derivative $\frac{\partial^2 C(s)}{\partial s^2}$represents curvature measure. Two constants α and η in Equation 3.6 assign weights controlling the importance of individual factors (elasticity and stiffness) in the overall cost calculation. Setting $\alpha = 0$ may lead to infinitely long snake, whereas low values of η will allow sharp twists in the curve. However, sharp twists and lengthy spans increase the internal energy, so an appropriate combination of two values (α) and (η) is obtained after experimentation for minimization of the curve energy.

$$E_{int} = \alpha(s)\left|\frac{\partial C(s)}{\partial s}\right|^2 + \eta(s)\left|\frac{\partial^2 C(s)}{\partial s^2}\right|. \tag{3.6}$$

E_{ext} represents the external energy (derived from the image) that pushes the snake towards specific features of image including line and corners. The energy value decreases as the evolving curve comes closer to a particular feature of interest in the image. To emphasize a particular feature, the respective weights can be assigned in terms of significance in the cost function of Eq. 3.7, i.e. often edges are the most important features in images. To

detect edges inside an image, the external energy is often represented using gradient strength $E_{ext} = -w\|\nabla Im\|^2$. Accordingly, highest gradient locations (edges) will attain minimum energy and forces the moving snake to stick therein. E_{cons} represents external constraints by the user for explicit control of snake movement. This can be used to penalize the snake if it moves too away from the initial position, or into some undesired region. For many applications constraints are not imposed, which means this energy is set equal to *zero* and snake moves under influence of internal and external energy only.

$$E_{ext} = w_{line}E_{line} + w_{edge}E_{edge} + w_{term}E_{term}. \tag{3.7}$$

The energy optimization is achieved not by direct minimization of snake energy functional of Equation 3.5, but solving a numerical model based on Euler-Lagrange formulation as expressed by Eq. 3.8.

$$-[\frac{\partial\left(\alpha\left|\frac{\partial C(s)}{\partial s}\right|^2\right)}{\partial s} + \frac{\partial^2\left(\eta\left|\frac{\partial^2 C(s)}{\partial s^2}\right|^2\right)}{\partial s^2}] + \nabla\left(E_{ext}\right) = 0. \tag{3.8}$$

The parametric snake has been used effectively for years in image segmentation [72]. Being an intuitive method, it directly moves the control points of the evolving curve; however certain limitations are also associated with the snake model. Firstly, the convergence of the snake depends upon an initial estimation of curve, i.e. the curve may fall to identity the object accurately if initialization is done away from the object. Moreover, as the snake grows or shrinks, the number of control points may require adjustment for precise estimation.

3.3 Level set Processing

The classical snake model of Kass et al. [62] is implemented using a parametric representation for object segmentation, i.e. the underlying cost function (snake energy) reaches a minimum at the object boundaries [73]. Unfortunately, this parametric model is not capable of handling the topological changes as illustrated in Fig. 3.2. Another drawback is, the cost function (i.e. the snake energy) depends upon the curve parametrization instead of related object geometry

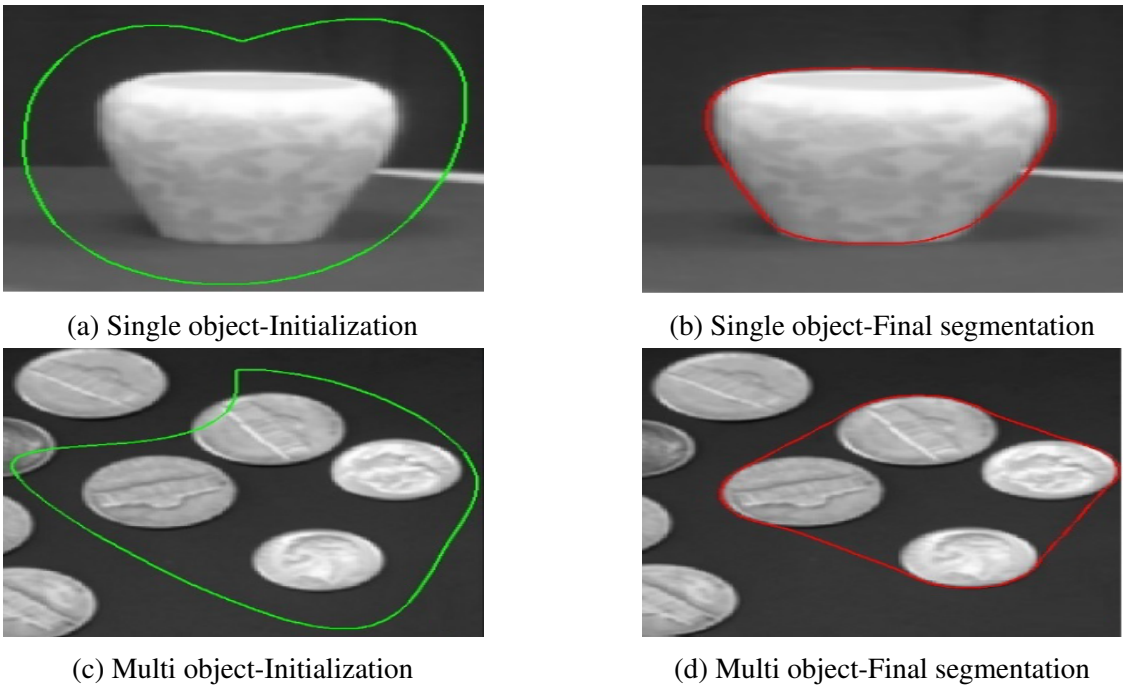

(a) Single object-Initialization

(b) Single object-Final segmentation

(c) Multi object-Initialization

(d) Multi object-Final segmentation

Fig. 3.2 Segmentation based on active contours (parametric snake models). Green is the initial contour and red shows the final segmentation. It can be observed from (b) that the evolving curve successfully segments a single object of interest, whereas (d) shows that the snake model lacks split and merge capability, leading to an erroneous segmentation.

and shape information. These limitations were addressed by Caselles *et al.* [74–76] in terms of "geometric contours," that are capable of addressing topological variations. The curve growth of the geometric contour is regulated by a speed function consisting of two terms (first is the curve regularization term and the second is an image based energy responsible for expansion or shrinkage towards the object boundary). Moreover, the curve deformation is this work was achieved using a method called the level-set representation (a mathematical formulation initially proposed to track the front propagation [60, 61, 8]).

According to the level set formulation, the evolving curve is represented as an iso-contour embedded into a higher dimensional space, such that merge and split operations are handled naturally by the surface motion. However, there are certain limitations for using a level set formulation in practice. The main drawback is the required computational resources and processing time, as the complete surface is evolved in every iteration. Consequently, different algorithms have been proposed [77] to optimize the computational time with minimal

impact on the segmentation completeness. The most important technique is "narrow-band" processing that focusses the computation only at a specific region around the moving curve for upcoming iterations, as sudden jumps in the object boundaries are not practical.

3.3.1 Level set Formulation

The level set formulation [61] has become a standard framework for complex medical image segmentation in recent years. The idea of level set processing is to evolve a surface (ϕ) instead of a curve (C), such that the curve is defined to be all points where the surface has no height i.e. $\phi = 0$. The curve is then represented implicitly using the zero level set $\phi = 0$ as shown in Fig. 3.3a. It should be noted that there occurs numerous structural changes leading to cusps and valleys. The ability to handle these structural changes using the level set is illustrated in Fig. 3.3b-3.3e, where the the intersection of the surface ϕ with the plane z=0 creates the implicit contour.

For mathematical representation of the level set, let us assume that a point $\mathbf{x} = (x, y)$ belongs to a moving curve, such that $\mathbf{x}(t)$ is the position of the point over time. According to the definition of the level sets, at any time t, for each point $\mathbf{x}(t)$ on the curve, the surface has no height as expressed by Eq. 3.9.

$$\phi(\mathbf{x}(t), t) = 0. \tag{3.9}$$

Here $\phi(\mathbf{x}(t), t)$ can actually be any arbitrary function as long as its zero level set gives us the contour. The surface height in level set formulation is equal to the distance from $\mathbf{x}$ to the closest point on the contour, so that $\phi(\mathbf{x}, t = 0) = \pm distt$, with distance $distt$ negative outside the contour, and positive inside. So the initial ϕ can actually be any arbitrary signed distance function as long as its zero level set matches the initial mask. Subsequently, the motion equation $\frac{\partial \phi}{\partial t}$ can be employed to track the evolving curve based on the fact that the initial ϕ at time $t = 0$ is available. Accordingly, the chain rule leads to the following computations:

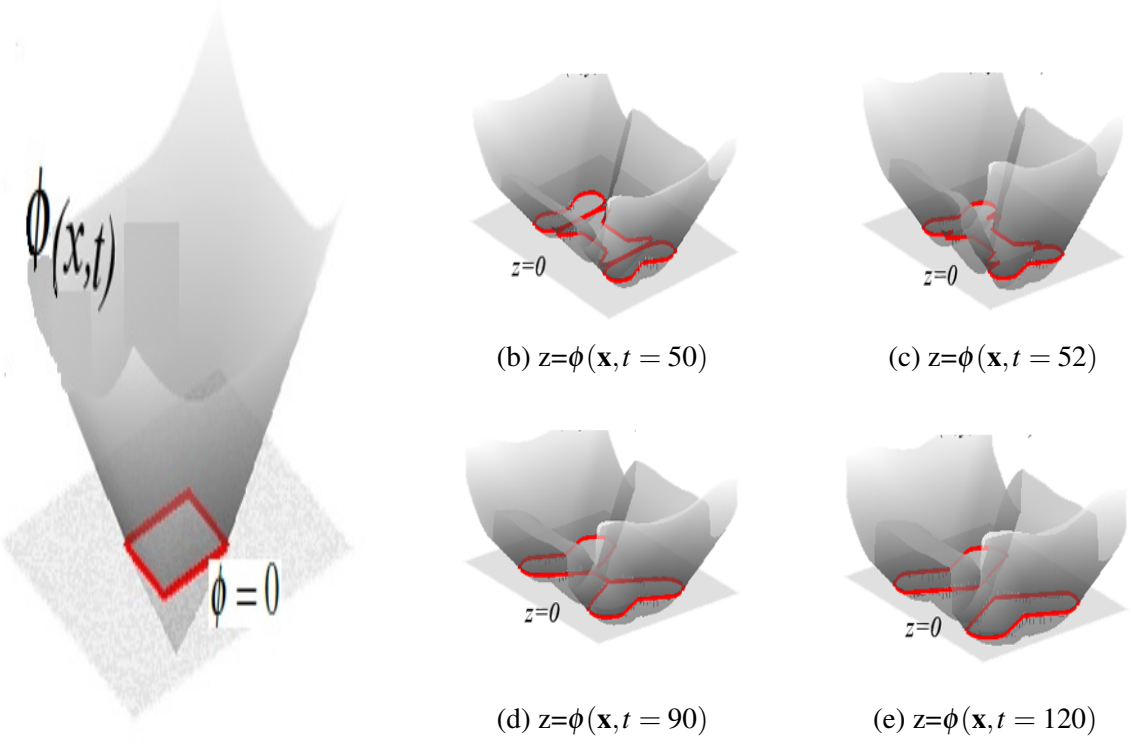

(a) Surface evolution

(b) z=$\phi(\mathbf{x},t=50)$ (c) z=$\phi(\mathbf{x},t=52)$

(d) z=$\phi(\mathbf{x},t=90)$ (e) z=$\phi(\mathbf{x},t=120)$

Fig. 3.3 Illustration of the implicit contour representation [8]. (a) shows how the contour is extracted from the evolving surface, whereas (b-e) illustrate the level set evolution with respect to time. (b) beginning of merging at t=50, (c) end of merging at t=52, (d) beginning of splitting at t=90, and (e) end of splitting at t=120.

$$\begin{aligned} \frac{\partial \phi(\mathbf{x}(t),t)}{\partial t} &= 0, \\ \frac{\partial \phi}{\partial \mathbf{x}(t)} \frac{\partial \mathbf{x}(t)}{\partial t} + \frac{\partial \phi}{t} \frac{t}{t} &= 0, \\ \frac{\partial \phi}{\partial \mathbf{x}(t)} \mathbf{x}_t + \phi_t &= 0. \end{aligned} \tag{3.10}$$

Here, we substitute $\frac{\partial \phi}{\partial \mathbf{x}}$ with $\nabla \phi$, whereas the propagation speed $\mathbf{x}_t$ is given by a force F normal to the surface, so we redefine the propagation speed as $\mathbf{x}_t = F\left(\mathbf{x}(t)\right).\mathbf{n}$ where $\mathbf{n} = \frac{\nabla \phi}{|\nabla \phi|}$.

Accordingly, motion equation of 3.10 can be rewritten as follows:

$$\begin{aligned} \phi_t + \nabla\phi \mathbf{x}_t &= 0, \\ \phi_t + \nabla\phi F.\mathbf{n} &= 0, \\ \phi_t + F\nabla\phi.\left(\frac{\nabla\phi}{|\nabla\phi|}\right) &= 0, \\ \phi_t + F\,|\nabla\phi| &= 0. \end{aligned} \tag{3.11}$$

Eq. 3.11 defines the evolution of ϕ with respect to time, i.e. given ϕ at time t=0, and its motion over time, it is now possible to track $\phi(\mathbf{x}(t),t)$ by evolving the initial $\phi(\mathbf{x}(t),t=0)$ over time using force F. This force can depend on a variety of physical effects as it is application dependent. For instance, the problem of tracking a boundary of a melting ice block in a warm liquid derives the force from the temperature difference, whereas tracking a heavy liquid spreading into a lighter one (honey against water) derives F using a mix of gravity, fluid density ratio and surface tension between the two liquids. Moreover, in context of the curve regularization, the surface curvature κ can be computed directly from the evolving surface ϕ as expressed by Eq. 3.12.

$$\kappa = \nabla.\frac{\nabla\phi}{|\nabla\phi|} = \frac{\phi_{xx}\phi_y^2 - 2\phi_{xy}\phi_x\phi_y + \phi_{yy}\phi_x^2}{(\phi_x^2+\phi_y^2)^{3/2}}. \tag{3.12}$$

3.3.2 Level Set Discrete Implementation

Implementation of the level set formulation for image segmentation requires a bit of additional processing as images have pixels and functions must be discretized. Accordingly, we can compute ϕ_t at a spatial pixel $\{i,j\}$ as expressed by Eq. 3.13, where the gradient will be evaluated using finite difference scheme of Eq. 3.14.

$$\phi_t = \frac{\phi(i,j,t+\Delta t) - \phi(i,j,t)}{\Delta t}, \tag{3.13}$$

$$\nabla^{+x}(i,j) = max[0,\Delta^{-x}\phi(i,j)]^2 + min[0,\Delta^{+x}\phi(i,j)]^2, when \qquad F > 0,$$
$$\nabla^{-x}(i,j) = max[0,\Delta^{+x}\phi(i,j)]^2 + min[0,\Delta^{-x}\phi(i,j)]^2, when \qquad F < 0. \tag{3.14}$$

Here, $\Delta^{-x}\phi$ or $\Delta^{+x}\phi$ is the left or the right side finite difference for a given point. The gradient is computed differently depending on the front direction and a finite difference scheme takes account of that. Accordingly, we redefine the motion equation of 3.11 by substituting the discrete approximations for gradient and the force terms as expressed by Eq. 3.15

$$\frac{\phi(i,j,t+\Delta t) - \phi(i,j,t)}{\Delta t} + max[F,0]\nabla^{+x}(i,j) + min[F,0]\nabla^{-x}(i,j) = 0. \tag{3.15}$$

From Eq. 3.15, the update equation for surface $\phi(i,j)$ is derived as expressed by Eq. 3.16, whereas the curvature regularization is computed for respective point (i,j) using Eq. 3.17. When computing the curvature, it depends only on the surface ϕ, so central differences can be used accordingly.

$$\phi(i,j,t+\Delta t) = \phi(i,j,t) - \Delta t[max[F,0]\nabla^{+x}(i,j) + min[F,0]\nabla^{-x}(i,j)]. \tag{3.16}$$

$$\kappa(i,j) = \frac{\phi_{xx}\phi_y^2 - 2\phi_y\phi_x\phi_{xy} + \phi_{yy}\phi_x^2}{(\phi_x^2 + \phi_y^2)^{3/2}}, \tag{3.17}$$

where

$$\phi_x(i,j) = \frac{1}{2}(\phi(i+1,j) - \phi(i-1,j)),$$
$$\phi_y(i,j) = \frac{1}{2}(\phi(i,j+1) - \phi(i,j-1)),$$
$$\phi_{xx}(i,j) = (\phi(i+1,j) - \phi(i,j)) - (\phi(i,j) - \phi(i-1,j)),$$
$$\phi_{yy}(i,j) = (\phi(i,j+1) - \phi(i,j)) - (\phi(i,j) - \phi(i,j-1)),$$
$$\phi_{xy}(i,j) = \frac{1}{4}[(\phi(i+1,j+1) - \phi(i-1,j+1)) - (\phi(i+1,j-1) - \phi(i-1,j-1))].$$

3.4 Image-Based Energy

For effective segmentation of objects using level set formulation, the curve driving force for Eq. 3.11 (Eq. 3.16 in discrete approximation form) is derived from the image in context of the particular application. For instance, the gradient strength is often used as image characteristic to detect the object boundaries as expressed in Eq. 3.18.

$$F = \frac{1}{1 + |\nabla Im|}, \tag{3.18}$$

where $|\nabla I|$ represents the magnitude of the image gradient and explicit *one* is added in denominator to avoid division by zero. Based on the fact that the gradient magnitude is an effective indicator of object separation, the conventional segmentation methods [62, 75, 63, 78] approximate the image based curve driving force in terms of gradient strength as expressed in Eq. 3.18 with an expectation to stop the curve growth at object boundaries. Despite being intuitive method, the major disadvantage of the gradient driven active contour is that the initial curve should be placed near the objects to be segmented for a high quality delineation. However, the complex medical imagery often contains multiple objects and usually the inter-object border is comparatively weak due to the similar intensity of different

anatomical structures. Consequently, the curve evolution does not stop at weak object edges, resulting in oversegmentation or "leakage". Moreover, the performance of these methods is very sensitive to image noise due to dependence on the image gradient. In general, Gaussian smoothing is applied in a preprocessing step to filter the noise, but smoothing widens the boundary of the objects and leads to under segmentation, i.e. the curve evolution may stop before realistic edges of the objects.

In contrast, a region based image force can be used for more effective segmentation as it employs the neighbourhood statistics for detecting the object boundaries. The regional statistics make the region based segmentation resistant to image noise and weak edges. Based on the assumption of homogeneous intensity for the object and background region, Chan-Vese [79] approximated two regions with their global mean intensities as expressed by Eq. 3.19. This method seeks to minimize the intraclass variance by optimizing the fitting term $F_1(C)+F_2(C)$.

$$F_1(C)+F_2(C)=\int_{inside(C)}|I_m(\mathbf{x})-c_1|^2\,d\mathbf{x}+\int_{outside(C)}|I_m(\mathbf{x})-c_2|^2\,d\mathbf{x}, \tag{3.19}$$

where C is the evolving contour, c_1 and c_2 represent the mean intensity value inside and outside the contour respectively. The use of a fitting term for optimal segmentation is illustrated in Fig. 3.6 with the help of four different cases. It can be observed from Fig. 3.4a - 3.4b that if the curve C is outside the actual object, then $F_1(C)$>0 and $F_2(C)=0$, whereas if the curve C lies inside the object bounds then two fitting components show opposite behaviour i.e. $F_1(C)=0$ and $F_2(C)>0$. Moreover, in a case when the initial curve is both inside and outside the object bounds, both components of the fitting term assume significant values i.e. $F_1(C)>0$ and $F_2(C)$> 0 as shown in Fig. 3.4c. In the last scenario, when the curve C exactly lies on the actual boundaries of true object, it can be observed that both fitting components approaches to zeros leading to overall fitting term $F_1(C)+F_2(C)$=0 i.e. the fitting term becomes optimal (minimal) when the curve captures the true boundaries of the object (see Fig. 3.4d). Similarly, the energy formulation of Yezzi *et al.* [65] employed

the idea of maximal separation between two mean intensities of a piecewise constant image. According to these models, the image based force $F(c_1, c_2, C)$ becomes minimal at the object boundaries leading to the optimal segmentation.

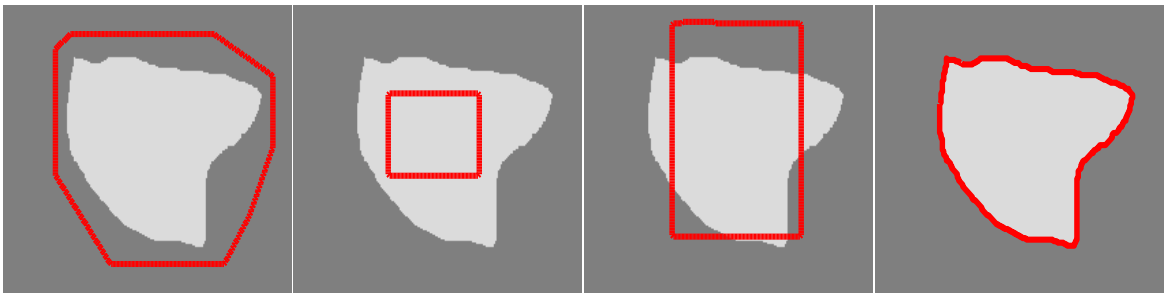

(a) Fitting>0 (b) Fitting>0 (c) Fitting>0 (d) Fitting=0

Fig. 3.4 Four different cases (curve positions) to illustrate the efficacy of Chan-Vese fitting term in region based segmentation. It can be observed that the fitting error becomes minimal for (d), where the curve captures the object boundaries accurately.

3.5 Related Work

Depending upon the underlying imaging modality (DSA, CT or MR), numerous techniques have been proposed to investigate the blood filled structures in imaged data. In the conventional DSA and MRA angiograms, the blood pool can be traced due to its distinctive behaviour in the global histogram of the image, as blood voxels are assigned very low or high intensities. Hence, the direct visualization of DSA data is possible with maximum intensity projection (MIP) or volume rendering. In contrast, the precise segmentation of specific anatomical structures in CTA is quite challenging due to the overlapping intensity distribution. The blood-filled vessels in CTA data have intensity values that fall in the middle of the global histogram (between intensity of lungs and bones). Consequently, application of maximum intensity projection (MIP) or direct volume rendering does not yield reasonable results for visual diagnosis. For instance, a MIP view is obstructed by bones and large blood filled regions (left ventricle of the heart) resulting in hiding thin tubular vessels. In this scenario, advanced visualization techniques like contrast adjustment and window levelling are applied for visual emphasis of specific features. For a detailed analysis, the object of interest

must be segmented in a first step, and focused investigation is performed subsequently. In this section, we give a brief review of the literature addressing medical image diagnosis, with a focus on the vessel and plaque segmentation in clinical CTA data.

3.5.1 Vessel Segmentation

Despite active research in the last decade, 3D vascular segmentation remains a challenging task due to several reasons. The inter-patient variability is one of the most important factors, and even for a specific patient, vessels are generally surrounded by complex anatomical organs that makes segmentation very challenging. Moreover, due to the complexity of medical data, like cardiac CTA or brain MRI, a particular segmentation method may not produce very effective results and a mix of segmentation techniques are often applied to extract the required structures, i.e. coronary vasculature in cardiac CTA. In this context, a number of methods can be found in the literature addressing the vascular segmentation, however automatic frameworks are least reported because of the complexity of problem. We provide here a brief review of the vessel segmentation literature with a focus on CTA based processing.

In literature, the majority of the CTA based vessel segmentation studies are related with carotid artery segmentation. In contrast to the coronary vasculature, the carotid arteries are larger vessels as well as their static nature leads to good image quality in CTA that makes segmentation comparatively easier. Geodesic active contour curve evolution has been used by Antiga *et al.* [80] for carotid arterial segmentation from CTA images. For efficient implementation, sparse field representation [77] was used in curve evolution. Based on initial seed points, surface grows iteratively like balloon as the curve evolves, whereas artefacts in segmented surface due to collateral vessels were removed by applying a smoothing filter. Andel *et al.* [81] proposed a medial axis extraction method for carotid arteries based on gradient and image derivatives. The Canny edge filter in combination with a Hessian filter was used to design the cost function. In the following stage, a minimal cost path search mechanism was used for extracting the lumen centreline defining the progression of carotid vasculature; however, surface extraction was not reported in this work. Based on the intensity

similarity in CT imagery, a challenging task in evaluation of brain related CTA data is to separate blood filled vessels from bones, both having high intensity values. In this context, Harnandez *et al.* [82] used a combination of pixel segmentation and active contour based evolution. In the first step, pixels were classified into bone and vessel based on a probability density function. In the following stage, active contour deformation was applied to extract the carotid vasculature.

Cheng *et. al.* [83] proposed a novel idea of 2D cross-section based boundary detection of 3D vessels. According to the proposed method, the vessel axis was computed in the first stage using multi-scale Hessian analysis. In the following step, an active contour model was evolved to detect the vessel boundaries under shape and size constraints for improved accuracy; however, the main limitation of the method is the circular shape approximation of the vessels. Consequently, the pathological lesions, vessel bifurcations and morphological abnormalities may lead to inaccurate segmentation in this method. Boskamp *et al.* reported the use of a region growing algorithm for vessel segmentation in CT and MR images. Initialized with one or more manual seed points within the vessel, region growing segmentation was used to delineate the complete vessel structure.

The criteria used for region growing mechanism was traditional intensity thresholding, which leads to segmentation leakage in for noisy and weak boundary regions; however, to minimize the impact of nearby non-vascular objects, connectivity-based pre-processing was used. Likewise, Metz *et al.* [84] described a semi-automatic approach for tracking a vessel centreline in CT data. Consequently, the proposed region growing method was used in combination with bifurcation and leakage detection scheme. Accordingly, the proposed method successfully minimizes the leakage problem in segmentation that usually occurs at bifurcation points; however, provision of the manual seed points still poses a challenge for automated segmentation.

Model based methods simplify the vessel extraction and representation problem by fitting the shape of the vessel to a certain geometric model. These can be fast and intuitive but the model usually has limitations in representing all possible shapes such as bifurcations and irregular cross sections, which is often the case for diseased vessels. The construction

of such models remains a difficult task as it is quite difficult to obtain the required training data representing all possible variations. Feng *et al.* [85] applied a two-phase modelling approach to segment the entire vascular structures from volumetric data. In the first stage, a model deformed to fit the medial axis of the vessels, and the radius of the vessel was estimated in a second stage of deformation. By interpreting the tubular structures as the assembled cylindrical branches, their method can be used to segment the vessel with multiple bifurcations. Similarly, Florez *et al.* [86] also presented a deformable cylindrical model based algorithm to extract the vascular lumen from 3D MR images. They firstly applied a fast skeleton method to estimate the centreline of the vessels in a coarse resolution, and then, the model was initialized near the medial axis of the vessels. The model was evolved in terms of the geometric constraints combined with image forces to capture the boundary of the vessels. In a similar fashion, Worz *et al.* [87] employed a cylindrical model for the vessel segmentation problem. In order to capture vessels of different vessel sizes, a parametric intensity model was proposed in their work. However, the main limitation of this work is approximation of vessel cross sections with a circle, which is not valid especially for abnormal vessels showing some extent of remodelling.

Other researchers have explored the use of minimal cost paths as an alternative to vessel segmentation. [88, 89] presents the application of this technique for extraction of vessels in 2D and 3D images. The cost function generally incorporates image gradient (intensity based information) or additional constraints for smoothness of the surface. By interpreting the vessel size as 4th dimension, Li and Yezzi [90] adjusted the centreline position in an augmented space. The additional constraint lead to an aligned and more accurate centre point. However, the intrinsic nature of the minimal path technique which requires at least two manual points for path calculation, makes it less automatic as initialization depends upon the user input. Moreover, in the case of the left coronary artery, multiple seed points are required for detection of complete arterial tree.

Wink *et al.* [91] reported a simple vessel extraction approach based on 2D contour segmentation. An iterative process of determining centre point and corresponding vessel boundary was performed to generate final segmented surface. Based on the centre point,

3D data was re-sampled and 2D orthogonal cross sectional slices were obtained in the direction of the vessel. The achieved segmentation is not very effective due to the inherent limitations of gradient based approaches i.e. sensitivity to noise. To address the gradient based leakage of geometric contours, Nain *et al.* [92] proposed to integrate a shape prior into the geometric active contours. Accordingly, they proposed to apply a local shape filter representing geometric constraints. The shape filter was defined as a ball structure centred at each point along the contour to be evolved with radius "*r*". The filter calculates the percentage of the voxels that are both within the ball and the region inside the contour. The output of the shape filter becomes high if the current point resides inside a widening region. On the other hand, the lower value of the filter's output indicates that the current point is within the vascular region. By combining the filter response with the level set formulation, the proposed method was able to penalize leaks during curve evolution.

Yim *et al.* [9] employed tubular deformable model to reconstruct the vessel surface from MRA images. The surface deforming process was carried on within a tubular coordinate system, thus giving a convenient measure of the cross-sectional area of the vessels. However, re-parametrization and vertex merging are needed to avoid problems of self-intersection of the surface. In addition, this method only models single branches of the vessels, so in the case of bifurcation, two branches are needed to be merged to form a Y-shaped structure as illustrated in Fig. 3.5.

The conventional region based active contours models [65, 79] reported successful image segmentation for weak gradient images; however, the intensity inhomogeneity associated with medical images often lead to a problem of segmentation leakage. Intensity inhomogeneity often occurs in medical images due to the acquisition hardware artefacts, partial volume effect and different types of noise. In other cases, it also appears due to the nature of data i.e. the non-uniformity of tissues leads to an increased inhomogeneity [93]. An effective way to overcome the inhomogeneity problem is to approximate the image based energy E_{ext} using a fairly small region, so that image based curve evolving force can be derived using a local intensity distribution. In this context, numerous algorithms have been proposed to employ localized intensity statistics for an improved and realistic segmentation. The incorporation of

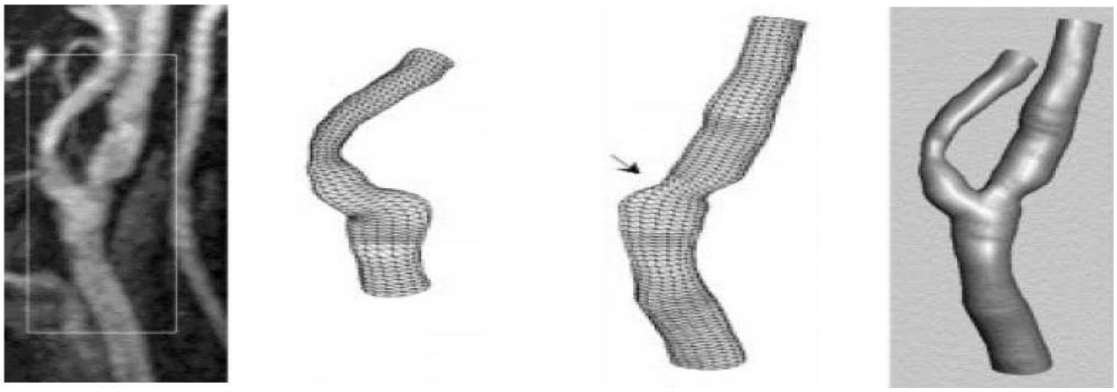

(a) (b) (c) (d)

Fig. 3.5 Reconstruction of the vessel surface using a tubular deformable model from contrast enhanced MRA images in [9]. (a) Original image of a carotid artery, (b) re-constructed branch of the external carotid artery (ECA), (c) re-constructed branch of the internal carotid artery (ICA). (d) the ECA and ICA are merged into a complete carotid model.

localized statistics in the image segmentation was first proposed by Brox and Cremers in [94], where the piecewise smooth model of Mumford-Shah [95] was approximated by the local means. As a solution to handle intensity inhomogeneity of medical images, Li *et al.* [66, 96] proposed to utilize the localized regional information to segment the objects effectively. In their method, the local intensity information was extracted by a Gaussian kernel function. The fitting energy (local statistics) was then calculated at the each point of contour (falling within the kernel) to compute an image based force; however, the main limitation of their work is sensitivity to the initialization mask.

Yi *et al.* [97] proposed solution of leakage problem by a localized region growing algorithm. Accordingly, a region grows in a local cube where the size of the cube was determined dynamically with the help of an estimated diameter. A similar scheme of controlled region growing was adopted by Tschirren *et al.* [98] as they incorporated fuzzy connectivity criteria to minimize the leakage. Another related method was reported by Lankton and Tannenbaum [16] which presented a framework that allowed localizing region based energy functions for effective delineation of the object of interest. Accordingly, this work proposed a novel method for localized region based segmentation by introducing a radius-based kernel to define the localization scope. Successful results were presented for

both 2D segmentation [16] and 3D coronary segmentation [99]; however, the initialization sensitivity was explicitly emphasized. We have observed from experimentation that the selection of the localization radius plays a critical role in this method. A large radius leads to a global approximation resulting in erroneous segmentation, whereas a small radius makes the evolving contour vulnerable to spurious local minima as illustrated in Chapter 4. Another limitation of this method is the requirement for intelligent placement of the initial mask to avoid converging to a local optima far from the desired solution.

More recent work has explored the use of hybrid energies (which combine local and global image statistics) for vessel segmentation. Xu *et al.* [100] proposed the use of local intensity statistics in a hybrid model for an improved segmentation. Accordingly, the authors used global approximation of the image intensities in Chan-Vese energy model and the local approximation in the mean separation energy model of [65]. An improved segmentation was achieved by using a weighted contribution of two terms; however, the computational cost increases two-fold. Moreover, the method was quantitatively evaluated only on 2D images and no results were reported for complex 3D multi-scale images. Yin and Liatsis [101, 102] proposed a hybrid energy model by integrating the global image behaviour in the coronary evolution. In a pre-processing stage, voxels representing the air in the CTA volume were normalized to obtain a two class representation. Next, using the assumption of a constant background, a bimodal histogram was approximated with a Gaussian Mixture Model. In the final stage, an explicit label image was derived using a cumulative distribution function of the histogram to represent the global model of the CTA image. This method works efficiently for images with a bimodal intensity histogram; however, it fails to handle the significant variations in CTA data encountered in practice. For instance, the intensity variation in the background makes this approach vulnerable as the label image misguides the evolving contour. Another limitation is the pre-processing required for individual volumes as the acquisition dependent parameters affect the quality of the CTA differently.

3.5.2 Plaque Segmentation Review

The state-of-the-art imaging modalities (MRI, DSCT, MDCT) have emerged as promising tools for description of atherosclerotic plaques [103, 104], both in terms of the shape quantification and intensity composition. Based on the fact that calcified plaques are easily discernible in CTA, numerous methods have been proposed to automatically detect calcified plaques with a reasonable accuracy [105–107, 13, 32, 108–111]. However, the detection and segmentation of the non-calcified plaques in CTA is still a challenging problem, mainly because of similar appearance (HU intensity values) to nearby blood and muscle tissues. Consequently, there is limited literature [99, 10, 112, 11, 113] addressing the complex problem of non-calcified plaque detection, out of which the majority of papers have been clinical pilot studies.

An automated framework for the quantification of manually identified soft plaques in CTA was proposed by Clouse *et al.* [10]. From a dataset of 40 CTA volumes, a total of 49 major coronary segments (41 normal and 8 abnormal) were investigated to validate the proposed quantification method. For precise quantification of the soft plaques, the authors established correspondence between normal cross sections at the terminal sites of the plaque region to approximate the outer boundary of the vessel. In the subsequent step, the mean intensity value for the lumen was approximated using the intensity response in the mid of the vessel. In a final step, all voxels having intensity value equivalent to lumen intensity, were subtracted and those left over were labelled as non-calcified plaque.

The results demonstrated that CTA based soft plaque quantification was possible; however the outcomes were based on a high degree of manual input i.e. intelligently selected coronary segments were investigated in the study as illustrated in Fig. 3.6. Moreover, the prior knowledge of plaque locations was an additional requirement as the quantification method required information about normal cross sections on terminal sites for computing the plaque volume.

An extension of this pilot study reported successful correlation between CTA analysis and intravenous ultrasound (IVUS) plaque quantifications [114]. A total of 20 soft plaque effected segments were identified from 12 multi-detector CT (MDCT) volumes for comparative

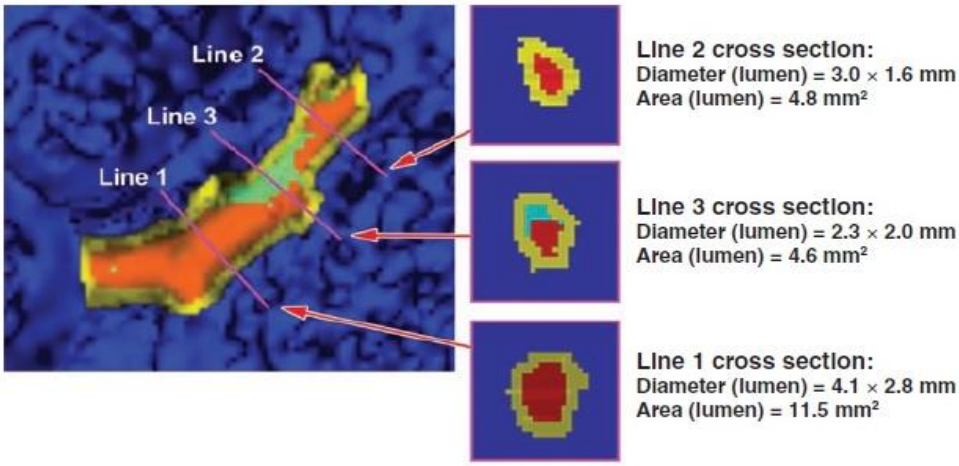

Fig. 3.6 Non-calcified plaque quantification using manual detection of the plaque region as proposed in [10]. Left shows an arterial segment with marked positions at different points along the segment, the right shows the cross sectional views for three positions with corresponding lumen-plaque annotations

.

Table 3.1 Distribution of 49 cross-sections used in [10]

Arterial segment	Normal cross sections	Abnormal cross sections
Proximal right coronary	10	0
Mid right coronary	7	1
Left main	4	1
Proximal left anterior descending	8	4
Mid left anterior descending	4	2
Proximal left circumflex	8	0

quantification. However, the main limitation of this work was the manual identification of plaque lesions as the aim of the study was to correlate quantitative metrics of two imaging modalities rather than the detection and segmentation of non-calcified plaques.

Renard and Yang [11] proposed a computationally efficient method that integrated the plaque detection problem in the vessel segmentation framework. A coronary skeleton based on eigenvalue analysis was used to segment the vessel (lumen and wall) in the first step. To ensure the minimal impact of image local features on the centreline extraction process, substantial pre-processing is done to suppress features like myocardial cavities and calcified plaques i.e the high intensity calcified plaques voxels were manually normalized by

assigning a low intensity value. The non-calcified plaques were detected in the second step by comparing effective cross-sectional area of the lumen against vessel wall as illustrated in Fig. 3.7. Encouraging visual results were presented for this computationally efficient method, but no clinical validation was discussed in the paper. Moreover, the outcomes were reported for a very small data sample (2 CTA volumes only) which makes the reproducibility difficult. In addition, this method requires substantial pre and post-processing of the volumetric data. Another concern is that results were only reported on an isolated vessel branch and no hint was provided for treatment of multi-branch arterial tree containing several bifurcations.

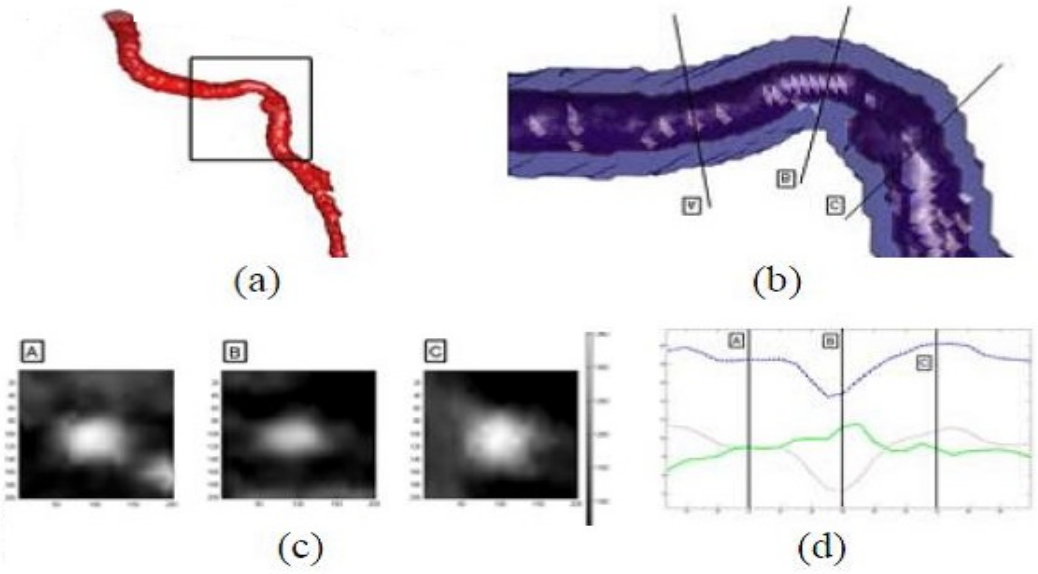

Fig. 3.7 Plaque detection results for the first CTA volume of [11]. (a) extracted vessel of the LAD artery in which a soft plaque is present, (b) cross sectional view showing lumen and vessel wall for a segment of this artery, (c) corresponding intensity images of different cross sections in (b), with the middle plane showing soft plaque, (d) effective cross sectional area of the lumen (dotted-red), vessel wall (dashed-blue) and their difference (solid green). The unexpected area metrics for middle plane indicates the presence of soft plaque.

Lankton *et al.* [99] proposed a novel method in which the soft plaque detection was posed as an active contour segmentation problem. In this two stage detection process, the coronary tree was extracted from the CTA volume in the first stage using mean separation energy model [79]. In the subsequent step, two explicit surfaces derived from the original segmentation (using erosion and dilation) were evolved simultaneously to encompass low density soft plaques using the mean separation energy model of Yezzi *et al.* [65]. The

novel aspect of this work is the idea of simultaneous segmentations using localized intensity information. Initially the interior region of the inside surface contains only the bright voxels. As the contour is allowed to deform, it expands to capture more voxels containing blood but does not expand into a bit darker non-calcified plaque voxels. Similarly the external contour contains myocardium voxels initially, and it does not contract to accommodate the soft plaque voxels from the boundary during evolution. This way soft plaques can be captured in between two contours as neither will move into plaque voxels when driven by localized means-separation energy. Simply, in case of absence of soft plaque (no inhomogeneity in intensity values) these two evolving contours meet on the vessel wall, whereas deposition of the plaque inside wall will stop contours at the boundary of vessel and they will remain separate from each other. Moreover, this method casts the problem in a variational active contour framework i.e. level set framework that operates directly on the raw imagery that naturally handles branching vessels and benefits from the geometric properties of active contours. Hence, this technique does not require any pre or post-processing of CTA data. A total of 8 CTA volumes were investigated in this work and a detection rate of 88% against manual annotations was reported; however, a requirement for the careful initialization of the evolving surfaces has reduced the practicality of this method as illustrated in Fig. 3.8.

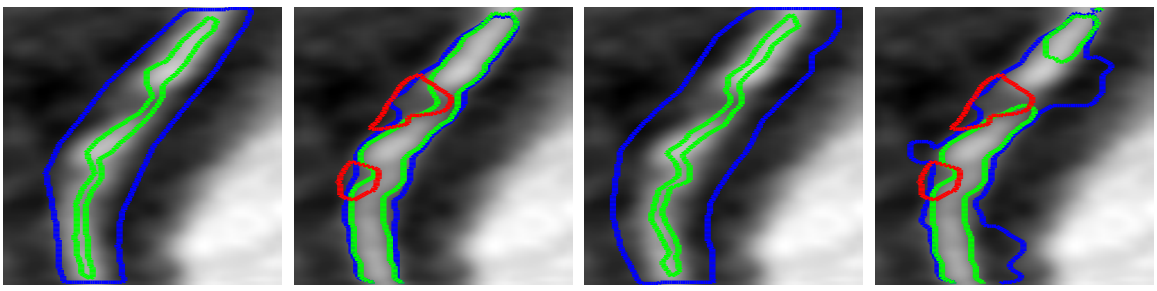

(a) Good initialization (b) Detection success (c) Different initialization (d) Detection failure

Fig. 3.8 Soft plaque segmentation using mean separation energy in bi-directional curve evolution. (a, c) represents two explicit initializations (blue and green) based on morphological operations, (b, d) shows corresponding plaque segmentations. Moreover, red annotations show the expert based manual ground truth. It can be observed that an intelligent initialization of (a) leads to good segmentation in (b), whereas a vague initialization of (c) leads to segmentation leakage in (d).

The use of machine learning in soft plaque detection was first reported by Wei *et al.* [112] where a linear discriminant analysis (LDA) was used to reduce the false positives in a set of 120 pre-selected soft plaque candidates. This is a multi-stage process where the detection of coronary vasculature is followed by a series of geometric analysis. The initial segmentation of arterial tress is achieved by using MSCAR-RBG algorithm [115] which extracts about 86% correct arteries with respect to standard 17-segment AHA coronary model [4]. Subsequently, the incorrect arterial branches were eliminated / inserted interactively, to ensure that accurate coronary arteries are to be passed to the plaque detection phase. In the second stage, the plaque candidates were selected based on a combination of intensity and geometric features. In the final stage, features including radius differential, mean, standard deviation and skewness of the plaque candidates were used in a LDA classifier for soft plaque detection. A total of 120 plaque candidate regions were chosen from 83 CTA volumes in this study and a sensitivity of 92.5 percent was reported; however, the accuracy of the classifier was mainly dependent upon NCP candidate selection criteria and machine learning was employed only to optimize performance by suppressing false candidates.

Likewise, Tessman [113] proposed a learning based method for the classification of coronary stenosis. In the first step, the pre-extracted coronary centreline was used to map the vessel segment with a series of multi-scale overlapping cylinders to identify the sampling points inside the segment. In the following step, the authors extracted image based features at the sampled points including intensity, gradient magnitude, and the first order derivatives to detect the high intensity calcifications. Moreover, global features including image mean, entropy and variance were used in combination with Haar-like features to detect the low intensity soft plaques. Accordingly, the detection accuracies reported were 94% and 79% respectively for the calcified and non-calcified plaques, along with a high number of false positives. The low detection rate for the soft plaques illustrate the fact that low-density based soft plaques demand a more sophisticated system i.e. beyond stenosis based computations are required to handle low intensity and the positive remodelling of the vessels. Another interesting method for the automatic detection of vascular abnormalities was proposed by Zuluaga *et al.* [116]. In this work, the authors formulated an unsupervised learning system

for detecting abnormal cross-sections in a vascular tube using “density level detection-DLD" technique of Steinwart [117]. Accordingly, the cross sectional images were discretely sampled around the tube centreline in a first step to derive the feature set for discriminating outliers from normal cross sections. In the second step, an unsupervised one-class SVM model trained on normal cross sections was used to detect the outliers i.e. the cross sections which violate the intensity pattern of normal class. The authors reported promising results for 9 clinical CTAs with non-calcified plaque detection accuracy of 79.62%, however; the correct selection of ρ (parameter identifying the anomaly concentration) is important for the optimal results. Moreover, due to the one class unsupervised learning, a large number of normal cross sections with identical intensity pattern are required to train the SVM classifier, which is relatively difficult to achieve from clinical CTAs. Furthermore, the presence of nearby structures severely affect the classification performance in this one-class abnormality detection model.

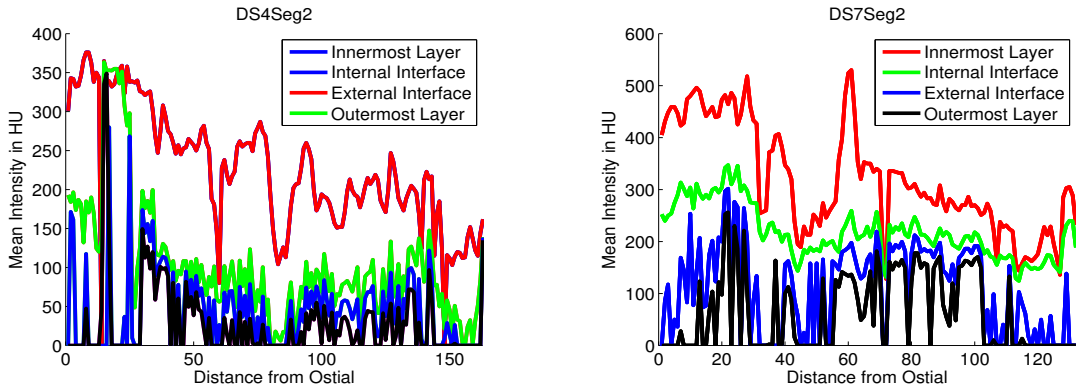

(a) CTA volume4-segment1 (b) CTA volume7-segment2

Fig. 3.9 Vessel wall based voxel map analysis used in [12]. (a, b) represents the intensity based gradient at four layers of the vessel wall (from innermost to outermost layer) for plaque effected segments of two CTA volumes. The abnormality of the gradient can be used as plaque indicator at respective locations.

One automated method for the detection of non-calcified plaques was reported by Li *et al.* [12] in which region growing coronary segmentation was followed with voxel based detection analysis. Based on the assumption that lumen voxels have intensity value greater than 160 HU, the region growing segmentation was used to segment the coronary vasculature

in the first step. Subsequently, in the plaque detection step, the authors constructed a voxel map of the vessel wall using morphological dilation and erosion. After generation of the voxel map (dilation and erosion is done), the vessel wall was divided into four layers with labels -1, 1, 2, 3 (from outer border of lumen to the outer border of wall). Next, the mean intensity gradient at the internal and external interface of the vessel wall was computed and all the abnormal fluctuations were associated with soft plaques as illustrated in Fig. 3.9. This detection was based on the experimental evidence that the inner lumen intensity value increases sharply as approaches close to the aorta (due to the high concentration), whereas the intensity remains stable through out the vessel length at the outer vessel wall. Hence, the violations of the intensity at vessel wall layers were associated with the non-calcified plaques; however, no statistical data was provided for the plaque detection in the paper as well as morphological erosion often leads to discontinuities in plaque affected segments.

Mirunalini *et al.* [13] reported fully automated framework for identification of coronary artery plaques with a success rate of 97%. Accordingly, the plaque detection was achieved by exploiting the discontinuities in the vessel; however, the paper did not explicitly mention statistics for the non-calcified plaques which often remains significantly low in a comparison to the calcification detection. Starting with the aorta localization in Gaussian convolved image, the inter-branch connectedness was improved using the Sobel operator. In the final step, the stenosis regions were detected by identifying the discontinuities in the centreline of the segmented coronary tree as shown in Fig. 3.10b. Although the authors reported 97% success rate for this approach, but the research was focused on stenosis detection problem as well as based upon several manually selected thresholds.

3.6 Summary

It can be summarized that CTA based vessel segmentation and plaque quantification have been challenging problems for the research community in recent years. A number of algorithm have been reported in literature for vascular segmentation, with a basic difference in the boundary detection principle. [80] employed seed based region growing method to

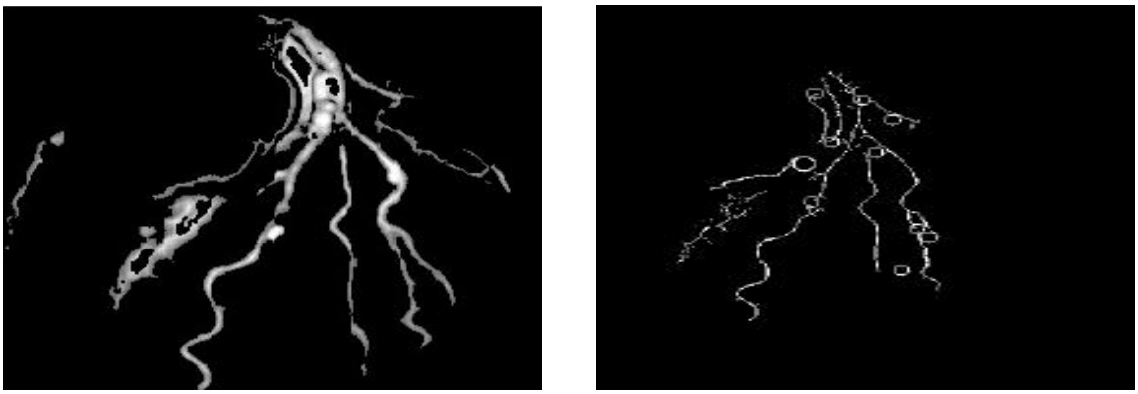

(a) Segmented tree (b) Centreline skeleton

Fig. 3.10 Detection of plaques in coronary vasculature as proposed in Mirunalini *et al.* [13]. (a) Segmented coronary tree, (b) centreline representing plaque based discontinuities. The nature of the plaque (calcified or non-calcified) can be identified using intensity threshold in segmented tree of (a).

segment carotid arteries in CTA, whereas [82] proposed a 2-stage method in which pixel-based classification is combined with region growing active contour. Likewise, Cheng [83, 91] proposed the idea of 2D cross section-based boundary detection for construction of 3D vasculature in CTA. The cross-section boundary detection was based upon constrained active contour; however, the circular approximation leads to erroneous segmentation for bifurcation and lesion regions. In addition, [85–87] used cylindrical model to delineate vessels in 3D volumes; however, the cylindrical model fails to handle the natural bifurcations in the coronary vasculature. The intensity inhomogeneity problem was addressed in terms of localized region growing segmentation in [94, 16, 96, 97]; however, the performance of the segmentation algorithm heavily relies upon manually selected localization scope. For improved segmentation, recent studies have reported the use of hybrid energy [100, 6, 102] to overcome intensity inhomogeneity artefacts.

CTA-based non-calcified plaque quantification has been reported in the literature;however, majority of the studies show segmentation over small datasets. Renard *et al.* [11] proposed a 2-stage plaque detection method using lumen area statistics; however, results were reported for two CTA volumes only. A similar geometrical method for plaque segmentation and quantification was reported in [10, 114];however, the non-calcified plaque was manually

selected in first stage and algorithm validates the quantification capability. A novel method alleviating the need of geometrical analysis was proposed by Lankton *et al.* in which plaque detection was achieved using energy minimization;however, the explicit initialization reduced the applicability. Moreover, the results were reported for 8 CTA volumes and no-quantification was performed. The use of machine learning was reported by Tessman *et al.* [113], Zuluaga *et al.*[116] and Wei *et al.* [112]. Tessman and Zuluaga employed One-class support vector machine to exploit intensity abnormalities; however, no radius information was investigated. In contrast, Wei *et al.* stressed upon intensive pre-processing in terms of topological soft gradient computation to optimal detect plaque affected patches using Adaboost classifier.

To conclude, we presented a detailed background and the relevant literature in this chapter. Starting with the basic image segmentation problem, we explored sophisticated methods used for segmentation of anatomical structures in medical imagery. In addition, we compared the parametric representation and implicit level set formulation in context of image segmentation in this chapter. This is followed by a brief review of the vessel segmentation techniques reported in literature, to familiarize the reader as this issue is investigated in Chapter 4. The last section of this chapter presents a detailed review for state-of-the-art non-calcified plaque detection methods to set the background for Chapters 5 and 6 of this thesis.

Chapter 4

Coronary Image Segmentation using a Hybrid Image Energy

4.1 Introduction

In this chapter, we address the problem of coronary tree segmentation in a CTA volume. The segmented tree is used subsequently in Chapters 5 and 6 for the detection and quantification of non-calcified plaques, respectively. This chapter starts with the specifications of the clinical dataset used in this work, followed by the manual ground truth construction.We then explain the coronary segmentation process with an emphasis on geometrical vessel enhancement and the intensity-based adaptive threshold computation. Next, we highlight the limitations of the conventional localized energy-based segmentation model, which is followed by the explanation of the proposed hybrid model. In the last section, we demonstrate the efficacy of the proposed model with the help of both qualitative and experimental validation.

The first contribution in this chapter is the use of an adaptive intensity threshold for improving the segmentation quality. The influence of the contrast medium in a CTA volume was modelled by approximating the intensity histogram of the descending aorta with a Gaussian-based approximation. We demonstrate the need of a volume-wise adaptive intensity threshold using statistical and visual results. The second contribution of this chapter is the formulation of a hybrid energy metric that couples an intensity-based local term with

a discontinuity-based global model of the image for optimal segmentation. The proposed hybrid energy-based model captures object boundaries accurately as the hybrid energy is less attracted to the local optima solutions. Moreover, we demonstrate with the help of experimental results that the hybrid energy provides robustness against the initialization and localization radius simultaneously. After demonstrating the usefulness of the hybrid energy on generic imagery, we apply the proposed model to solve an important clinical problem of 3D coronary segmentation. The segmentation is achieved using a level set formulation for computational robustness, and a mask auto-correction feature was introduced for tracking the emerging peripheries during the curve evolution for completeness of the coronary tree in a 3D CTA volume. Finally, the proposed model is evaluated by comparing the segmentation performance against the coronary segmentation model of Yang *et al.* [17]. The qualitative and quantitative results demonstrate the effectiveness of the proposed framework with a consistent mean sensitivity and specificity measures of 80% across the CTA dataset. Moreover, the high degree of agreement with respect to the inter-observer differences demonstrates the proposed algorithm has similar performance to expert clinicians.

4.2 Clinical Data

From a broader perspective, three different datasets have been investigated in this research. The first dataset, which consists of 18 CTA volumes has been downloaded from the publicly available database of the Rotterdam Coronary Artery Evaluation framework [18, 118]. The Rotterdam CTA data comes from different sources and is based on different vendors as illustrated in Table 4.1, whereas remaining two datasets are obtained from our clinical partners.

The Second dataset, consisting of 12 CTA volumes was obtained from Guy's and St. Thomas' Hospital, London which was acquired using a Philips iCT256 scanner. The image was acquired using 256 slice/rotation with Ultravist370 contrast medium. In order to overcome the heart motion, a perspective ECG gating technique was used, whereas a medium soft re-construction kernel *XCB* was used in the filtered back-propagation slice reconstruction

Table 4.1 CTA data specifications.

CTA Datasets	Semmelweis	Guy's & Thomas	Rotterdam dataset		
Vendor	Philips	Philips	Siemens	Toshiba	Philips
Vol Count	2	12	6	6	6
Institution	Semmelweis Uni.(HN)	City Uni. (UK)	Erasmus Uni. (NL)	Leiden Uni. (NL)	Utrecht Uni. (NL)
CT Scanner	Brilliance256	Brilliance256	Somatom Def.	Aquillion One 320	Brilliance 64
Slice/Rotation	256x1	256x1	32x2	320x1	64x1
ECG Gating	Perspective	Perspective	Retrospective	Retrospective	Retrospective
Reconstruction Kernel	XCC	XCB	b26f	b26f	b26f
Contrast Medium	Ultravist 370	Ultravist 370	Ultravist 370	Ultravist 370	Ultravist 370

algorithm. The mean resolution for this data set is $512 * 512 * 290$, the inter-voxel distance is 0.39 mm with slice thickness equal to 0.43 mm. Likewise, the third dataset consisting of *two* CTA volumes was obtained from Semmelweis University Budapest, Hungary. The CT scanning equipment for these two CTA volumes remain the same i.e. Philips iCT256; however, the reconstruction kernel XCC was used in filtered back projection algorithm to produce sharp images. The mean resolution for this data set is $512 * 512 * 300$, the inter-voxel distance is 0.41 mm with slice thickness equal to 0.40 mm.This multi-platform dataset makes the segmentation problem challenging as a CTA volume reflects the acquisition differences in terms of acquisition time and amount of contrast medium injected; however, this serves as a great platform to ensure generalization of the proposed method.

It is important to mention that the Rotterdam dataset provides ground truth for both the vessel boundary and plaque inside individual segments of the coronary tree. The boundary ground truth is provided in terms of 3D discrete contours (manual annotations representing the vessel boundary) from start to end of the segment, whereas the plaque information is provided in terms of plaque type and the precise position inside the coronary segment. In contrast, the remaining two datasets do not provide information regarding vessel boundary; however, they provide the adequate information regarding plaque in terms of plaque type and the precise position of the plaque in abnormal segments.

4.2.1 Rotterdam CTA Data

Based on the fact that the focus of this chapter is effective segmentation of the coronary vasculature in CTA volume, we explored only first dataset in this chapter. The motive behind

using Rotterdam dataset in this chapter is the availability of the vessel boundary in terms of 3D discrete contours. Accordingly, the performance of the vessel segmentation algorithm is assessed with respect to the manual boundary contours. However, for the subsequent chapters addressing plaque detection and localization problem, we evaluated all three datasets as plaque related ground truth information is available for all three datasets.

The detailed specification of the Rotterdam dataset is provided in Table 4.2 indicating the important parameters including spatial resolution, the in-plane resolution and the slice thickness. In order to make accurate computations of the lumen radius and area using oblique slices in 3D space, we performed standard pre-processing to convert the input CTA data into isotropic volumes such that the voxel size becomes identical in all three dimensions (see Table. 4.2). This is achieved by using tri-cubic interpolation [119]. This means that axial, coronal, and sagittal sections are equal in terms of spatial resolution. The isotropic dimensions can lead to accurate quantification of lumen and plaque using 2D oblique cross-sections in 3D space. It should be mentioned that isotropic conversion employing downsampling can lead to fast computation [120]; however, it leads to loss of useful information. Accordingly, we performed up-sampling to retain the minimal voxel dimensions of input data.

4.2.2 Ground Truth Construction

The segment-wise [121] reference ground truth is provided in terms of 3D discrete contours defining the lumen boundary along the length of the segment. Fig. 4.1 shows the lumen boundary annotations from three independent experts who manually delineated the lumen for two different coronary segments. It can be observed from Fig. 4.1a-4.1c that there occurs a significant inter-observer mutual agreement for normal/healthy segments, whereas the abnormal/diseased segments leads to a significant variation among the three observers (Fig. 4.1d-4.1f). This reduced inter-observer agreement in abnormal segments is associated with the poor blood flow in the respective segments as the reduced concentration of the contrast medium in the blood makes visual interpretation challenging even for expert radiologists. This inter-observer variability is further explored in Chapter 6, in context of voxel-wise plaque quantification. It should be mentioned that the main theme of the Rotterdam framework

Table 4.2 Input Data CTA-Specifications

Serial #	Input Data			Isotropic Data	
	CTA Title	Dimensions	Voxel Size (mm^3)	Dimensions	Voxel Size (mm^3)
01	DS00	512*512*304	0.40*0.40*0.45	513*513*342	0.40^3
02	DS01	512*512*296	0.28*0.28*0.40	592*592*473	0.25^3
03	DS02	512*512*299	0.30*0.30*0.40	524*524*399	0.30^3
04	DS03	512*512*297	0.40*0.40*0.45	513*513*334	0.40^3
05	DS04	512*512*279	0.40*0.40*0.45	513*513*314	0.40^3
06	DS05	512*512*324	0.40*0.40*0.45	513*513*365	0.40^3
07	DS06	512*512*261	0.35*0.35*0.40	600*600*348	0.30^3
08	DS07	512*512*313	0.30*0.30*0.40	517*517*418	0.30^3
09	DS08	512*512*286	0.36*0.36*0.45	471*471*322	0.40^3
10	DS09	512*512*336	0.35*0.35*0.40	600*600*448	0.30^3
11	DS10	512*512*253	0.40*0.40*0.45	513*513*285	0.40^3
12	DS11	512*512*289	0.39*0.39*0.40	667*667*385	0.30^3
13	DS12	512*512*560	0.39*0.39*0.25	504*504*351	0.40^3
14	DS13	512*512*560	0.42*0.42*0.25	550*550*351	0.40^3
15	DS14	512*512*640	0.38*0.38*0.25	493*493*401	0.40^3
16	DS15	512*512*512	0.36*0.36*0.25	673*673*458	0.28^3
17	DS16	512*512*480	0.42*0.42*0.25	512*512*480	0.42^3
18	DS17	512*512*560	0.42*0.42*0.25	673*673*458	0.28^3

[118, 18] is computation of lumen stenosis which often leads to vessel constriction; however, the provision of the segment-wise lumen boundary (manual ground truth) makes this dataset suitable for coronary segmentation problems.

4.3 Enhancement of Tubular Structures

The image segmentation process can be improved by employing prior medical knowledge in the pre-processing stage. For multi-object images, shape priors are often used to track specific objects having a known geometry. Accordingly, a shape constraint can speed up the computation process by suppressing irrelevant objects quickly. For instance, to detect circular objects in an image, it is suitable to suppress all the voxels that violate the circular shape model in a first step followed by a level set-based segmentation for precise detection of boundaries. This idea of suppressing irrelevant structures has been used effectively in

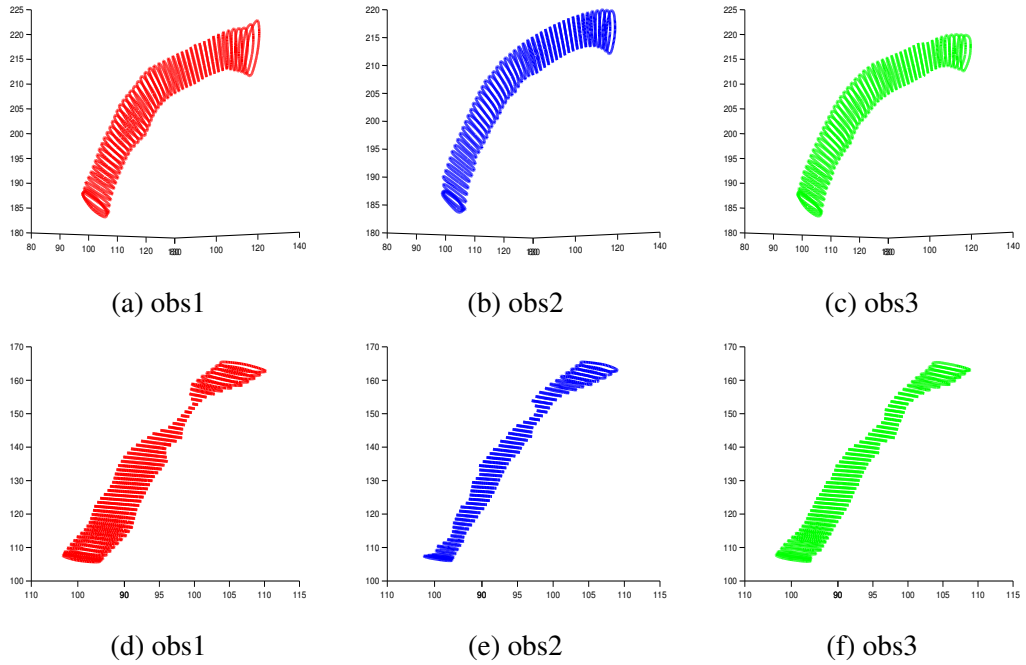

(a) obs1 (b) obs2 (c) obs3

(d) obs1 (e) obs2 (f) obs3

Fig. 4.1 Manual ground truth for coronary segmentation based on three independent experts. (Top) good agreement between the three observers for normal segment, (bottom) reduced agreement for diseased segment.

medical images, with a focus on detection of a particular structure for clinical analysis. An example in clinical context is the use of geometric shape features of tubular structures to compute pixel-wise (voxel-wise in 3D space) vesselness for robust segmentation of the vascular objects in an image.

A number of algorithms [15] have been proposed in the literature to enhance curvilinear structures in medical images. These methods compute a vesselness response for each pixel to measure the likelihood of the pixel to be a vascular structure, and they are usually operated in a scale space to respond to vessels of different sizes. The core idea of the vessel enhancement filter is eigenvalue analysis of the Hessian matrix, as eigenvalues can effectively reveal the local geometric information of objects present in the image. In context of the coronary tree segmentation in a 3D CTA volume, we performed eigenvalue analysis of the 3D Hessian matrix [15] to exploit the local shape and geometric information as presented in Table 4.3. The Hessian matrix is often used in structural analysis as it efficiently reveals the local curvature using second order partial derivative of the image.

Table 4.3 Different combinations of eigenvalues ($|\lambda_1| < |\lambda_2| < |\lambda_3|$) with respective patterns. (H=high, L=low, N=noisy, usually small, +/- indicate the sign of the eigenvalue).

Eigenvalues				Interpretation
S no.	λ_1	λ_2	λ_3	Shape
1	N	N	N	Noise
2	L	L	H-	(bright) Plate-like structure
3	L	L	H+	(dark) Plate-like structure
4	L	H-	H-	(bright) Tubular structure
5	L	H+	H+	(dark) Tubular structure
6	H-	H-	H-	(bright) Blob-like structure
7	H+	H+	H+	(dark) Blob-like structure

For enhanced visualization of the coronary vasculature, a contrast agent is often injected intravenously before the cardiac CTA exam. Consequently, the background in the CTA image comprising of air-filled lungs appears darker, whereas the blood vessels appear significantly brighter due to the effect of the contrast medium. Referring to the combination (4) of Table 4.3, where λ_1 is approximately zero and remaining two eigenvalues are negative numbers with high magnitude $0 \approx |\lambda_1| \ll |\lambda_2| \leqslant |\lambda_3|, \forall \lambda_2, \lambda_3 < 0$, we computed the vesselness response for individual voxels using Eq. 4.1.

$$V_o(\mathbf{x}) = \begin{cases} 0 & \text{if } \lambda_2 \; or \; \lambda_3 > 0, \\ \left\{ 1 - exp\left(-\frac{R_{\alpha_t}^2}{2\alpha_t^2} \right) exp\left(-\frac{R_{\beta_t}^2}{2\beta_t^2} \right) \left(1 - exp\left(\frac{R_{\gamma_t}^2}{-2\gamma_t^2} \right) \right) \right\} & \text{otherwise ,} \end{cases} \tag{4.1}$$

where term R_{α_t} distinguishes plate-shaped structures from tubular vessels and R_{β_t} discriminates blobs from other irregular shapes, and the term R_{γ_t} is used as a penalty to serve the background noise in CTA. Moreover, α_t, β_t and γ_t are constants that control the weights in the overall vesselness measurement. The selection of these tuning parameters is generally application dependent and requires a search to determine the optimal values. Moreover, the variable size vasculature in the CTA volume is addressed with the multi-scale processing, i.e.

the voxel-wise vesselness response is computed at different scales and the strongest response is selected to generate the final vesselness measure as expressed in Eq. 4.2.

$$
\begin{aligned}
R_{\alpha_t} &= \frac{LargestCrossSectionArea/\pi}{(LargestAxisSemiLength)^2} = \frac{|\lambda_2|}{|\lambda_3|}, \\
R_{\beta_t} &= \frac{Volume/(4\pi/3)}{(LargestCrossSectionArea/\pi)^{3/2}} = \frac{|\lambda_1|}{\sqrt{|\lambda_2\lambda_3|}}, \\
R_{\gamma_t} &= \sqrt{\sum_{1\leq i\leq 3} \lambda_i^2}.
\end{aligned}
\tag{4.2}
$$

The multi-scale approach refers to the application of the convolution kernel to identify variable size structures in the image. In image processing, a kernel, convolution matrix, or mask is a small matrix, which is often used for blurring, sharpening, embossing and edge detection. For effective detection of variable-size objects, this work employs a Gaussian convolution kernel which handles CTA noise effectively. After a series of experiments, we computed the optimal values for the tuning parameters α_t, β_t and γ_t equal to 0.5, 0.6 and 220 respectively, whereas the multi-scale vesselness is computed at scale range of [1,...,6] to address vessels of different sizes. Accordingly, the input image is convolved with a Gaussian kernel at specific scales (standard deviation of the Gaussian kernel) to enhance potential tubular structure of corresponding size. Readers are referred to [15] for detailed mathematical model and optimization of the tuning parameters of multi-scale eigenvalue analysis.

It should be noted that application of the vesselness filter leads to detection of potential tubular voxels, which can be further employed in active contour-based evolution for accurate segmentation of the coronary vasculature. The justification of the multi-scale filter across the complete CTA volume is visually illustrated in Fig. 4.2, which shows a rendering for actual CTA volume and corresponding vesselness. It can be observed from Fig. 4.2b that the multi-scale filter effectively suppress the non-vascular structure across CTA volume. Accordingly, an active contour-based segmentation employing a subset of the image (see Fig. 4.2b) can lead to fast and accurate segmentation of the coronary vasculature. Moreover, the response of the vesselness filter for 2D axial slices of a CTA volume is shown in Fig.

4.2d. The efficacy of vesselness filter is evident from the figure as the tubular structures are well identified, whereas the surrounding tissues have been assigned a fairly low vesselness measure.

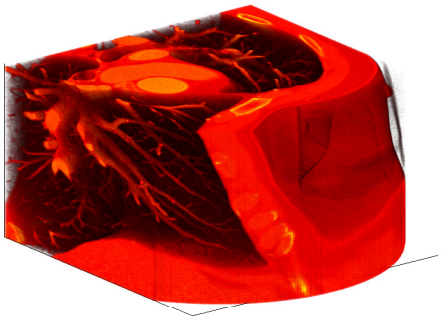

(a) 3D CTA volume

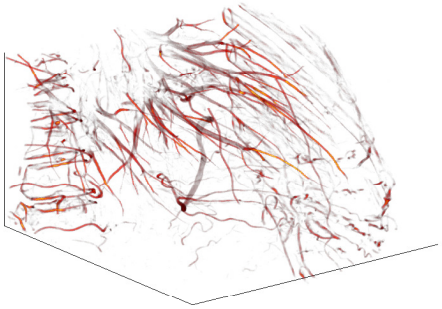

(b) 3D multi-scale vesselness

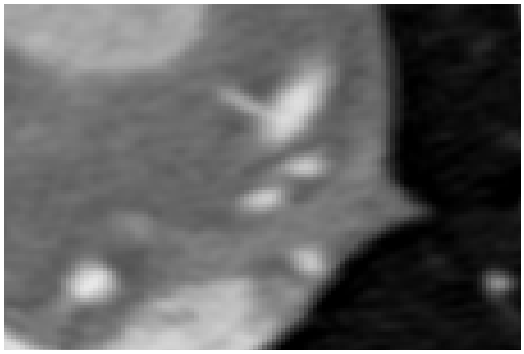

(c) 2D axial slice

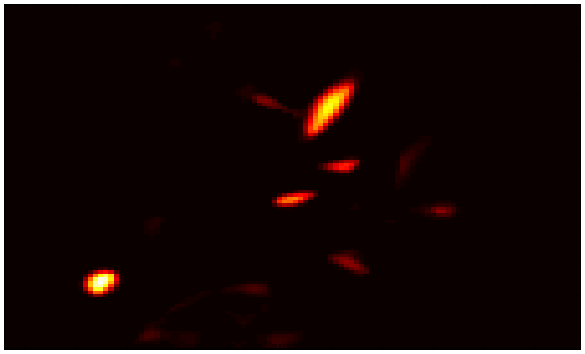

(d) 2D multi-scale vesselness

Fig. 4.2 Hessian-based vessel computation. (a) shows the complete CTA volume before application of multi-scale vesselness filter, (b) represent the vesselness measure for the complete 3D volume. (c) shows a 2D axial slice from the CTA volume, (d) represents the 2D vesselness measure for the respective slice. It can be observed that use of the multi-scale vesselness filter results in background suppression and enhanced tubular structures across the CTA volume.

Multi-scale computation has ensured that all the tubular instances are tracked irrespective of the size as evident in the 3D vesselness figure. It can be observed from Fig. 4.2b (3D) and Fig. 4.2d (2D) that the tubular structures have been assigned high vesselness in comparison with the background; however, an inherent limitation of the Hessian-based multi-scale filter is misclassification of the edges, i.e. edges are often assigned comparatively high vesselness as well. These unwanted responses negatively affect accurate vessel segmentation in terms of

segmentation leakage and increased false positive rate. This limitation becomes problematic in cardiac CTA due to a number of step edges (heart chamber boundaries). This problem is visually evident in Fig. 4.2b where it becomes extremely complex to delineate the coronary vasculature solely on the basis of the vessel enhancement response. Consequently, we derive additional intensity-based constraints to be employed in an active contour model for accurate segmentation of the coronary tree.

4.4 Contrast Medium Approximation

The contrast affected (high intensity) blood appears brighter in the CTA volume which allows a clinician to distinguish the coronary vasculature from the background as shown in Fig. 4.3a - 4.3c. However, the diffusion of the contrast medium is non-homogeneous across patients as it depends upon several factors including the type and amount of contrast medium, the total scan time and the heart rate. Therefore, despite similar visual appearance of the blood filled coronaries, there exists a significant difference in the blood intensity values for different CTA volumes. Consequently, we proposed to improve the coronary segmentation process by suppressing the non-coronary structures using intensity-based constraints in a pre-processing step.

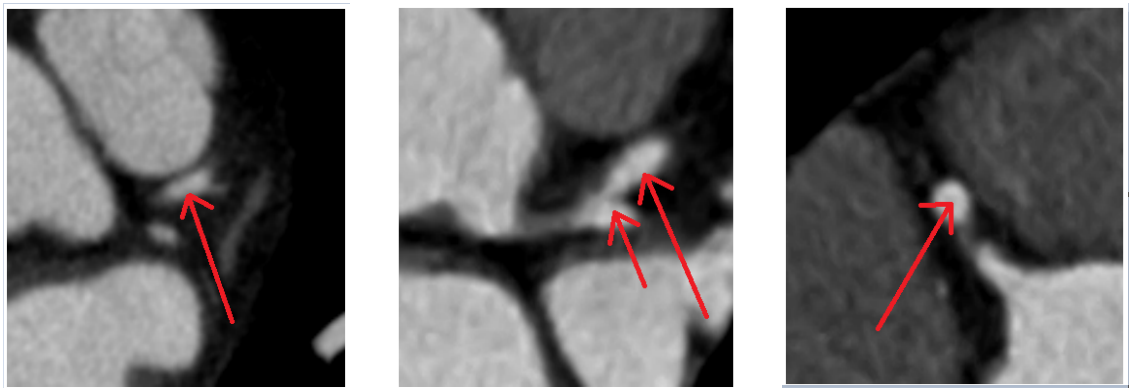

(a) LCA (b) LCA (c) RCA

Fig. 4.3 Coronary visualization with respect to the background on axial planes for three different CTA volumes. It can be observed that due to the contrast filled blood, the coronary vasculature appears brighter than the background for all three volumes.

It is notable that choosing a fixed intensity threshold to differentiate blood voxels from other structures in a CTA volume (low intensity tissues or high intensity calcifications) often leads to inaccurate results as the fixed threshold lacks local image characteristics. The selection of an appropriate intensity threshold become critical, especially when the segmented coronary tree is to be evaluated for plaque analysis. For instance, Isgum *et al.* [122] proposed an automated system for coronary calcification detection, in which all the connected components of intensity value greater than 220 HU were interpreted as potential calcified plaques. Similarly, Hong *et al.* [123] proposed a fixed threshold of 350 HU for the segmentation of coronary calcified plaques in the contrast enhanced CTA. Accordingly images with strong concentration of contrast medium will lead to increased false positives, whereas a low concentration of the contrast medium may lead to missed calcifications for these methods. Moreover, the segmentation of the blood-filled vasculature in CTA has been reported by Harnandez *et al.* [82], Mohr *et al.* [124], Szymczak *et al.* [125], Yin *et al.* [101], Yang *et al.* [126] and Cheng *et al.* [83]; but the impact of the externally injected contrast medium has been little employed in the coronary segmentation process, as computing a generic intensity threshold across patients is non-realistic. Consequently, we propose to adaptively model the response of the contrast agent to derive the volume-specific intensity range (HU range) for respective CTA volumes.

4.4.1 Aorta Segmentation

Since the blood flows into coronaries from the descending aorta, we segmented the aorta in the first step to investigate the impact of contrast medium. The bright appearance of the aorta in Fig. 4.4b reflects the presence of the contrast medium. For aorta segmentation, we first applied an intensity threshold of 100 HU [127] to enhance the visualization of blood voxels (i.e. to suppress the background consisting of lungs and soft tissues) as shown in Fig. 4.4a. Based on the circular appearance of the aorta in initial axial planes on caudal-cranial axis, we applied a circular Hough Transform [69] based shape analysis in the subsequent step to segment the aorta from the blood volume as shown in Fig. 4.4b. Iteratively, 2D

segmentation is performed through axial slices until the aorta changes shape in terms of circular deformations (see Fig. 4.4c), which reflects the origin of the coronary vasculature.

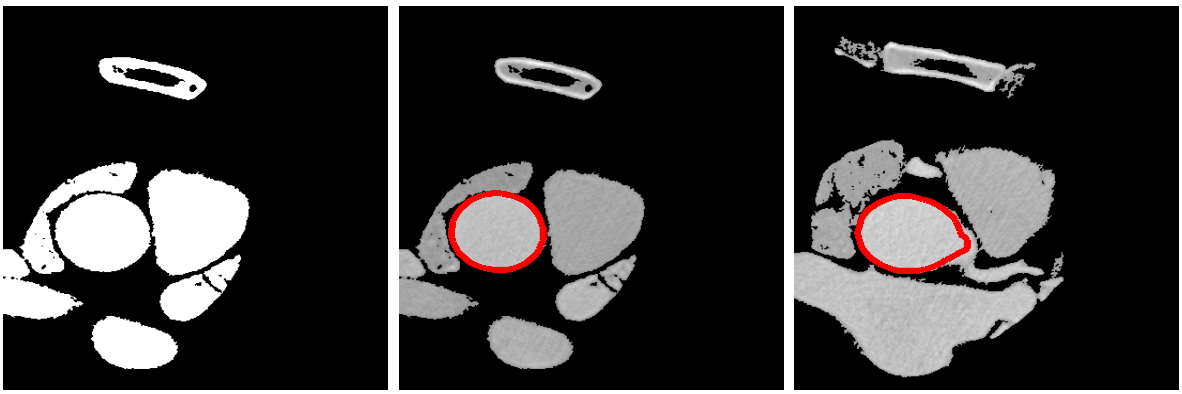

(a) Blood Mask (b) Circular Aorta (c) Shape Change

Fig. 4.4 Contrast medium approximation in a CTA volume. (a-b) background suppression mask and initial aorta segmentation using an intensity threshold of 100 HU and circular Hough transform. Aorta shape-change due to emerging coronary structure is illustrated in (c).

4.4.2 Gaussian Fitting

Next, we computed the intensity histogram of the segmented aorta and the contrast medium response is modelled using a Gaussian fitting. Fig. 4.5 shows the Gaussian approximation for five CTA volumes where a significant variation in the mean values emphasizes the need of an adaptive intensity threshold for accurate segmentation of coronary vasculature.

It should be noted that the Gaussian mean represents the intensity for blood-filled aorta; however, the concentration of the contrast medium decreases as the blood flows towards distal segments of coronary tree. Moreover, the vessel narrowing towards the distal end points often result in the less diffusion and poor contrast. Thus, to take into account the intensity drop towards distal segments, we estimate the adaptive intensity range R_I for respective CTA volume I as expressed in Eq. 4.3.

$$R_I = \{\mu_I \pm 3\sigma_I\}\,. \tag{4.3}$$

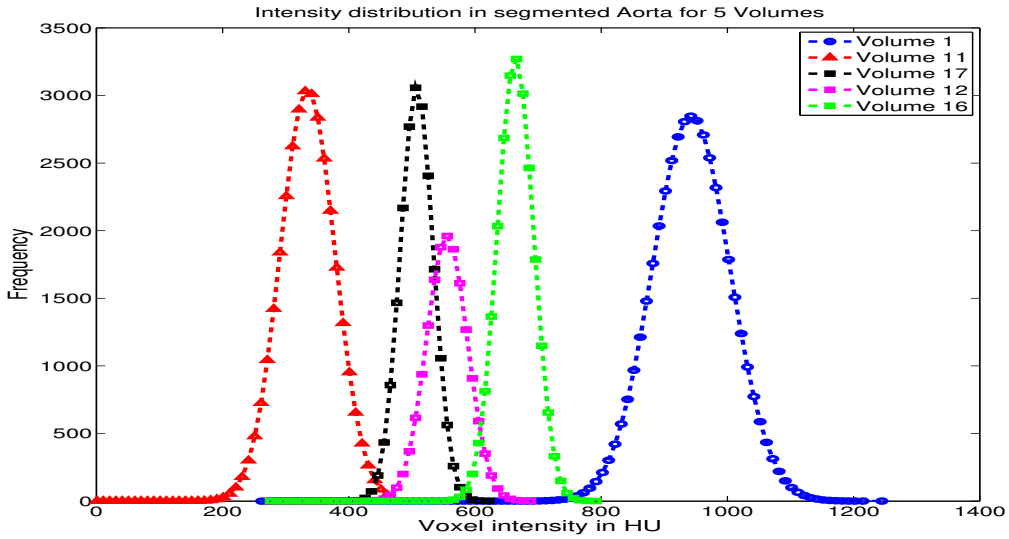

Fig. 4.5 Intensity distribution approximation for four CTA volumes. A significant variation in the mean value validates the need of an adaptive intensity threshold.

where μ_I and σ_I represent the aorta-based mean HU and standard deviation for the respective CTA volume. For a quantitative comparison, the Gaussian distribution parameters and the derived intensity range for 18 clinical CTA volumes are presented in Table 4.4. A significant variation in the Gaussian mean across CTA dataset validates the need of volume-wise exclusive intensity threshold for accurate coronary segmentation. Moreover, the lower boundary of adaptive intensity range is meant for suppressing the non-coronary voxels and the upper boundary can be used to segment the calcified plaques (if any) in the arterial tree.

To overcome the limitations of the Hessian-based vessel enhancement, the CTA volume I is filtered using constraints of Eq. 4.4 (intensity and vesselness combined) with T_f set equal to 10^{-3} to identify potential candidates of the coronary vascular tree.

$$I(\mathbf{x}) = \begin{cases} I(\mathbf{x}) & \text{if } V_o(\mathbf{x}) > T_f \, and \, I(\mathbf{x}) \in R_I, \\ 0 & \text{otherwise .} \end{cases} \tag{4.4}$$

Table 4.4 Volume-specific intensity range for CTA volumes

CTA Volume	Gaussian model		Coronary intensity range (HU)	
	mean	SD	minimum	maximum
DS00	418	27	337	499
DS01	942	62	756	1128
DS02	492	24	420	564
DS03	325	23	256	394
DS04	370	22	304	436
DS05	542	60	362	722
DS06	460	31	367	553
DS07	663	53	504	822
DS08	370	35	265	475
DS09	499	22	433	565
DS10	370	50	220	520
DS11	335	45	200	470
DS12	556	32	460	652
DS13	532	25	457	607
DS14	426	26	348	504
DS15	454	25	379	529
DS16	665	28	581	749
DS17	507	26	429	585

4.5 Coronary Seed Detection

The seed detection process employed in this thesis is based on the work of Han *et al.* [14], in which the authors combined the Hessian-based vesselness with a localized geometric measure for accurate detection of the seed points. The localized geometric measure was proposed to overcome the limitation of the Hessian-based vesselness against step edges in a CTA volume and are often associated with the heart chambers. We further improved the efficiency of the seed detection method by employing the adaptive intensity constraint for minimizing the false positive detections. This additional processing in terms of geometrical measure and the adaptive intensity constraint is necessary for the accurate seed detection, as the subsequent arterial segmentation is based upon the seed points.

The first stage in seed selection is to select appropriate reference slice that contains both left and right coronary arteries. This can be selected from a wide range of axial slices centred on the middle of the CTA volume. This reference slice index (*RSI*) can be can be modelled according to Eq. 4.5, where C_r is the constant and N represents the total number of slices in given CTA image. Generally, the values of Cr ranging [0.4,...,0.6] ensure that the selected slice contains all major branches of the coronary tree. In the following step, the potential regions of interest (ROIs) are detected on the identified reference slice by discarding open boundary objects. Subsequently, the potential seed point candidates are identified for localized geometrical analysis by obtaining the centroid values of all ROIs.

$$R_{index} = C_r * N_{planes}. \tag{4.5}$$

The localized geometrical analysis starts with the assumption that coronary arteries appear as tubular structures along the patient axis (z dimension) in CTA volume and the arterial geometry remains collateral through the consecutive slices for major segments i.e. (LCA, LCX, LAD and RCA) appear as bright elliptic objects in axial slices. To test this assumption mathematically, the vessel direction at potential candidate seed points was computed in the first step using Hessian eigenvalues. In the subsequent step, three consecutive planes orthogonal to the vessel direction are extracted as shown in Fig. 4.6a. Next, the

shape similarity was computed by correlating shapes through these consecutive planes. In this process, ray casting is performed on each plane in 16 uniformly sampled directions based on respective centre points and boundary was detected using radial gradient. The distance between the border point and the centre of the plane is interpreted as ray length in corresponding direction. After sorting 16 ray lengths, highest and the lowest three measures were discarded to avoid outliers. The remaining 10 ray lengths are arranged for every plane in a 2D data structure representing the $[plane][ray]$ index. For each ray index ray = [1,...,10], the minimum values $B_{min}[ray]$ and the maximum values $B_{max}[ray]$ among the three ray lengths plane are calculated. Accordingly, the normalized local vesselness measure $V_c(\mathbf{x})$ of Eq. 4.6 is computed such that *one* defines an ideal tubular structure.

$$V_c(\mathbf{x}) = \prod_{ki=1}^{10} \frac{1}{B_{max}[ray(ki)] - B_{min}[ray(ki)] + 1} \tag{4.6}$$

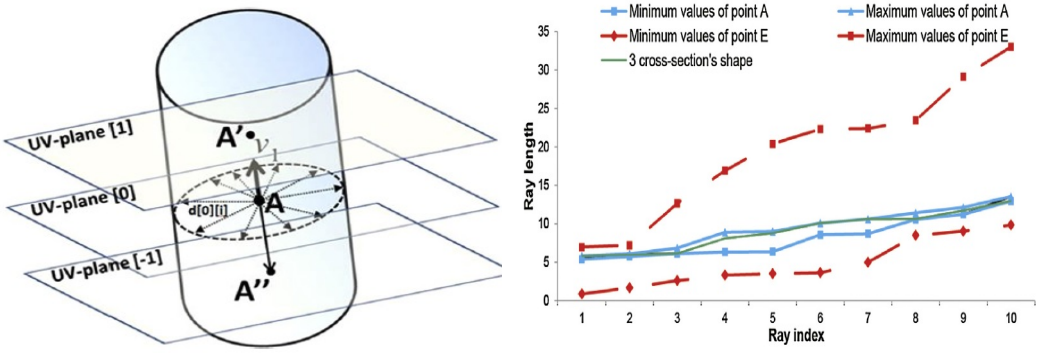

(a) Consecutive Orthogonal planes (b) Raywise Boundary distance

Fig. 4.6 Coronary seed detection as proposed in [14]. (a) Three consecutive planes orthogonal to vessel direction used in cylindrical modelling of the vessel. Centre plane UV [0] passes through point "A" i.e. the centroid of the region of interest, whereas two consecutive planes (forward UV [1] and backward UV [-1]) are parallel to plane UV [0] at a parametric distance of D units. (b) shows the plot for ray-wise boundary distance. It can be observed that for a coronary structure, the min-max distance remains stable (blue), whereas as non-coronary structure leads to unexpected distance values (red).

Fig. 4.6 shows the capability of the local geometric measure to distinguish vasculature from non–tubular structures by investigating minimum and maximum value profiles for two objects. For a vessel-based seed point, the radial border on three consecutive cross

sections shows a stable change in radius in all directions i.e. minimum values remain closer to maximum values. This small difference will lead to a high value assigned to geometric feature $V_c(\mathbf{x})$ in Eq. 4.6. In contrast, the non-vessel seed points will undergo through a significant difference in minimal and maximal ray lengths, resulting in a small value of $V_c(\mathbf{x})$ approaching towards zero. In the subsequent step, the authors combined the response of the local cylindrical model with the multi-scale vesselness to identify the potential coronary segments. To avoid erroneous seed detection, the paper used a threshold-based classification to label the candidates voxels $\mathbf{x}$ according to Eq. 4.7, where $seed_o(\mathbf{x})$ denotes the seed label i.e. *one* denotes coronary seed and *zero* otherwise.

$$seed_o(\mathbf{x}) = \begin{cases} 1 & \text{if } V_o(\mathbf{x}) \geq T_f \text{ and } V_c(\mathbf{x}) \geq T_{gf}, \\ 0 & \text{otherwise.} \end{cases} \tag{4.7}$$

As proposed in [14] algorithm, we had chosen fairly small values for multi-scale vesselness $T_f = 10^{-3}$ and cylindrical response $T_{gf} = 10^{-4}$ thresholds to ensure that all potential tubular candidates are investigated in the seed detection process. It can be observed from Fig. 4.8b that seed the detection process based on Eq. 4.7 incurs a number of false positives. This is due to the fact that both geometrical filters had taken into account the shape features only. As a result, the elongated heart muscles and the surrounding non-coronary vasculature have been marked as the coronary segments which resulted in numerous false positive seeds. To suppress the non-coronary seed points, we posed our intensity-based constraint in the seed detection process and redefine Eq. 4.7 to obtain improved seed label $seed_o^{'}$ as expressed in Eq. 4.8. Equation 4.8 ensures that only those candidates seed points are retained in the final set $seed_o^{'}$ which satisfy the HU intensity criteria R_I of the respective CTA volume. Fig. 4.8c illustrates the efficacy of intensity-based constraint R_I as the majority of the false positives

has been eliminated.

$$seed_o^{'}(\mathbf{x}) = \begin{cases} 1 & \text{if } V_o(\mathbf{x}) \geq T_f \text{ and } V_c(\mathbf{x}) \geq T_{gf} \text{ and } I(\mathbf{x}) \in R_I, \\ 0 & \text{otherwise.} \end{cases} \tag{4.8}$$

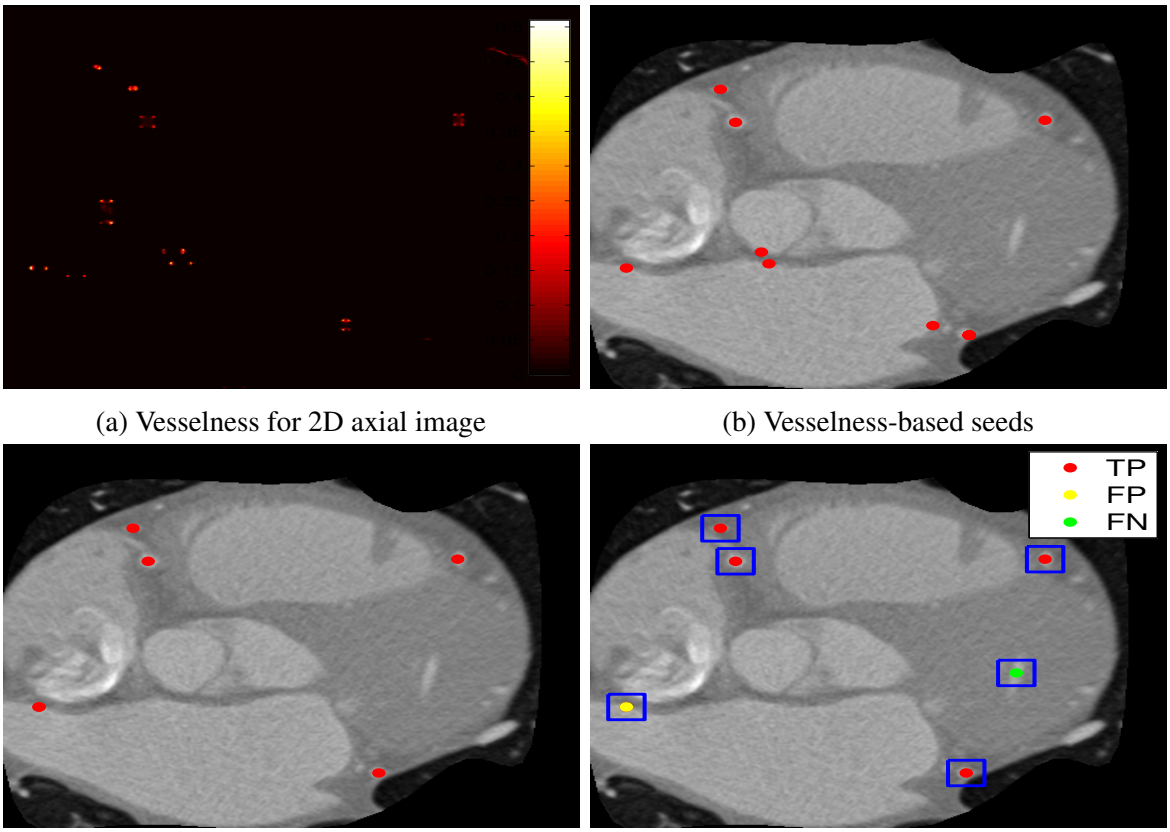

(a) Vesselness for 2D axial image

(b) Vesselness-based seeds

(c) Seed points using [14]

(d) Improved seeds based on adaptive threshold

Fig. 4.7 Coronary seed detection and mask initialization. (a) shows that the multi-scale model [15] has assigned considerable vesselness to image edges. (b) represents the consequent seed points with numerous false positives. (c) and (d) shows improved seed points and the associated initialization mask for the region-based segmentation.

Next, we initialize a localized mask spanning over the region of 6 millimetres around the detected coronary seed points as shown in Fig. 4.8d. A 6 millimetre neighbourhood is selected as the coronary segments are well encompassed within the mask area on the axial slice of a CTA image [128–131]. It is remarkable that if the reference slice is exactly the axial cross section where respective coronary originates from the aorta, the complete tree can

be segmented efficiently. But due to the condition that same reference slice to be used for both seed points (Left & Right coronary artery), usually middle of CTA volume is chosen as reference slice. The resultant reference slice ensures the seed produced works with for both arteries; however, arterial information exists in both directions on the caudal-cranial axis (towards aorta as well as arterial end points). This mid volume seed detection is apportioned with the provision of bi-directional evolution mechanism i.e. the seed based initial mask is evolved in both directions starting from the aorta to distal endpoints. In addition, false positive seed points lead to disconnected structures which are removed using connectivity filter in the final step.

4.6 Coronary Segmentation using Localized Energy

Once the CTA volume is effectively filtered (as expressed in Eq. 4.4) and the coronary seed points are identified, the coronary tree is segmented using a 2D level set evolution based on the localized version of the Chan-Vese [64] energy model. The initial mask, which is centred on the seed point, evolves under the influence of image-based localized Chan-Vese energy to capture the true boundary of the coronary structures. Because of the 2D nature of the level set evolution, the evolved mask serves as an initialization to the adjacent axial slices on the caudal-cranial axis to capture the respective coronary structures. The choice of the image-based curve evolution energy in the level set formulation plays a decisive role in the context of segmentation accuracy. For sharp images having significant object borders, the edge strength is employed in a level set-based energy minimization process, whereas the complex imagery with weak inter-object boundaries is often segmented using regional intensity statistics for optimal object delineation. The conventional region-based active contour models of Chan and Vese [79] and Yezzi *et al.* [65, 132] reported successful object segmentation using region-based intensity statistics on a global scale; however, these methods show poor performance for complex medical imagery due to underlying assumption of piecewise constant intensity. This is further explained later in this section in the context of the localized formulation for Chan-Vese energy model.

To explain the coronary segmentation model used in this work, we start with the basic Chan-Vese [64] segmentation model, in which image segmentation was interpreted as energy minimization problem. Accordingly, the boundary fitting error was defined using image-based energy functional $F(c_1,c_2,C)$ in context of an energy minimization problem as expressed in Eq, 4.9.

$$F(c_1,c_2,C) = \int_{inside(C)} [I(\mathbf{x}) - c_1]^2 d\mathbf{x} + \int_{outside(C)} [I(\mathbf{x}) - c_2]^2 d\mathbf{x} + \gamma length(C), \tag{4.9}$$

where I is an input image, C is the evolving contour (based on the initial mask), c_1, c_2 represent the global mean intensity for two regions (i.e. inside and outside the curve) and γ is the regularization weight term to enforce contour smoothness. Eq. 4.9 defines the image segmentation problem as mapping two regions (foreground and the background) by their mean intensity values; hence, the optimal segmentation is achieved when the two regions are best approximated with their global mean values. The mathematical formulation for this energy minimization problem can be expressed by Eq. 4.10.

$$\inf_{c_1,c_2,C} F(c_1,c_2,C). \tag{4.10}$$

The energy minimization problem expressed in Eq. 4.10 can be redefined using the level set formulation as expressed by Eq. 4.11. In the level set representation, the unknown curve C has been replaced with a signed distance function $\phi(\mathbf{x})$, such that the evolving curve C is represented as zero level set $C = \{\mathbf{x} \mid \phi(\mathbf{x}) = 0\}$. The detailed formulation, evolution and discrete implementation of level sets is explained in Section 3.3.

$$F(c_1,c_2,\phi) = \int_\Omega H\phi(\mathbf{x}) (I(\mathbf{x}) - c_1)^2 d\mathbf{x} + \int_\Omega (1 - H\phi(\mathbf{x})) (I(\mathbf{x}) - c_2)^2 d\mathbf{x} + \gamma \int_\Omega \delta\phi(\mathbf{x}) |\nabla\phi(\mathbf{x})| d\mathbf{x} \tag{4.11}$$

Based on the signed distance representation, we used the Heaviside function $H\phi(\mathbf{x})$ to select the interior of the curve C, whereas the exterior region is selected using the complementary equation $(1-H\phi(\mathbf{x}))$. Moreover, the interface at the zero level set is obtained by using Dirac delta function $\delta(\phi)$. The $\delta(\phi)$ is the derivative of the $H(\phi)$, which is 1 when $\phi(\mathbf{x}) = 0$ and 0 far from the interface. The mathematical representation for the Heaviside and Dirac delta function is expressed by Eq. 5.5.

$$H\phi(\mathbf{x}) = \begin{cases} 1 & \text{if } \phi(\mathbf{x}) \geq 0, \\ 0 & \text{if } \phi(\mathbf{x}) < 0. \end{cases}, \ \delta\phi(\mathbf{x}) = \begin{cases} 1 & \text{if } \phi(\mathbf{x}) = 0, \\ 0 & \text{otherwise .} \end{cases} \tag{4.12}$$

Results for conventional Chan-Vese formulation are presented in Fig. 4.8a and 4.8c, where it can be observed that the initial mask evolved using intensity statistics on a global scale fails to capture the object boundaries successfully. This failure is based on the fact that the medical data often suffers from intensity inhomogeneity due to the acquisition dynamics and patient related movements. Accordingly, the global intensity statistics-based methods result in significant leakage as shown in Fig. 4.8a and 4.8c.

To overcome the intensity inhomogeneity problem in medical imagery, a number of improvements [66, 16, 96, 133] have been proposed for the Chan-Vese model with the basic idea of "localized or constrained" regional intensity statistics for curve evolution. Likewise, we employed the localization statistics in the energy minimization process by using a neighbourhood selection mask. Accordingly, we use here a radius controlled (6 mm in this work) mask $B(\mathbf{x},\mathbf{y})$ to select the localized neighbours as expressed in Eq. 4.13. According to the equation, the selection kernel will be 1 when a spatial point $\mathbf{y}$ lies within a region of radius R_{Local} centred at $\mathbf{x}$, and 0 otherwise. The use of the localized regional intensity statistics in the curve evolution avoids leakage outside the neighbours and pushes the curve in a local context towards the boundaries of the object. The interaction of the localization kernel with the evolving curve is graphically illustrated in Fig. 4.9, whereas the mathematical equation for computing the localized mean intensity inside and outside the curve (c_1, c_2 respectively) is expressed in Eq. 4.14. Moreover, the advantage of employing

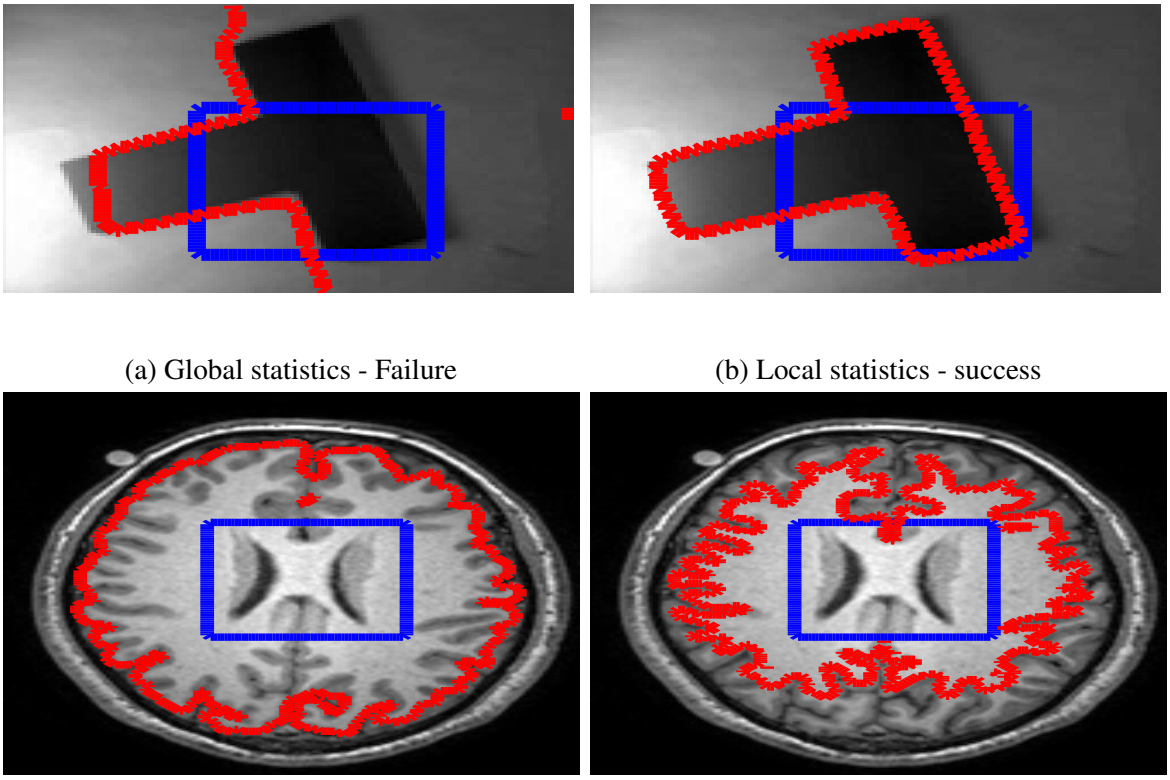

(a) Global statistics - Failure (b) Local statistics - success

(c) Global statistics - Failure (d) Local statistics - success

Fig. 4.8 Advantage of using localized region-based statistics over global intensity metric. (a, c) shows over segmentation associated with the global mean values of two regions, whereas (b, d) represents successful segmentation accomplished using localized intensity-based deformation.

the localized intensity statistics is visually illustrated in Fig. 4.8b and 4.8d, where it can be observed that object of the interest can be segmented precisely using localized evolution.

$$B(\mathbf{x},\mathbf{y}) = \begin{cases} 1 & \text{if } |\mathbf{x}-\mathbf{y}| < R_L, \\ 0 & \text{otherwise.} \end{cases} \tag{4.13}$$

$$c_1(\phi) = \frac{\int_{\Omega_y} B(\mathbf{x},\mathbf{y}) I(\mathbf{y}) H\phi(\mathbf{y}) d\mathbf{y}}{\int_{\Omega_y} B(\mathbf{x},\mathbf{y}) H\phi(\mathbf{y}) d\mathbf{y}},\ c_2(\phi) = \frac{\int_{\Omega_\mathbf{y}} B(\mathbf{x},\mathbf{y}) I(\mathbf{y}) (1-H\phi(\mathbf{y})) d\mathbf{y}}{\int_{\Omega_y} B(\mathbf{x},\mathbf{y}) (1-H\phi(\mathbf{y})) d\mathbf{y}}. \tag{4.14}$$

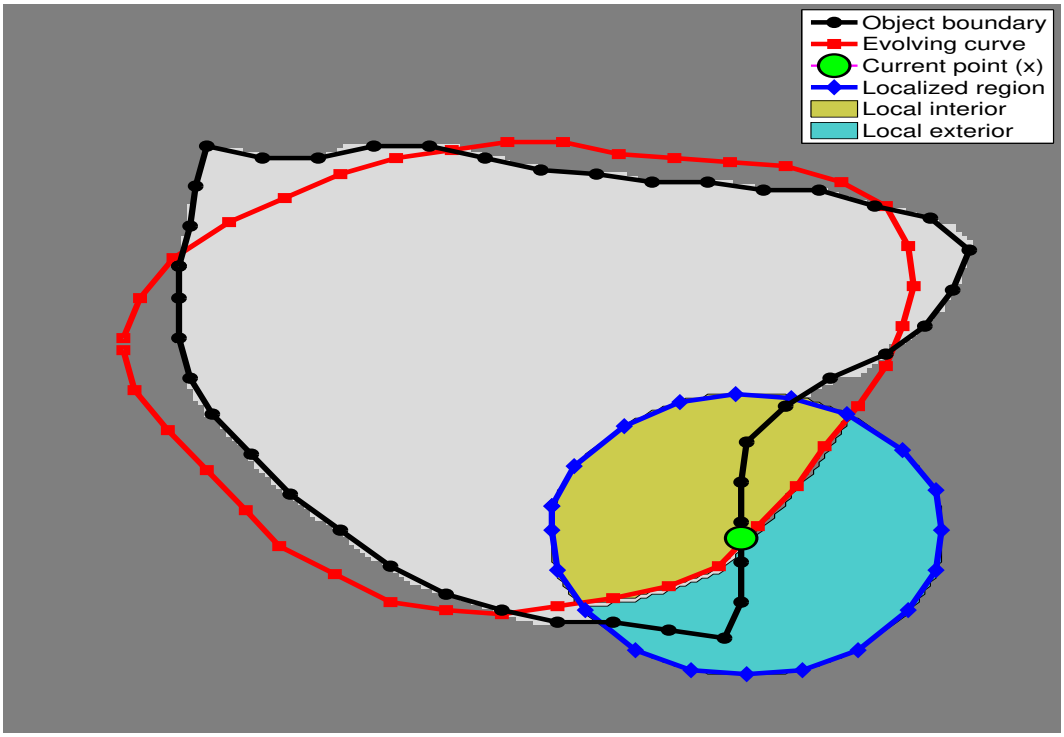

Fig. 4.9 Kernel function to illustrate the localized intensity model. Red shows the evolving curve, whereas the blue represents the localized ball region $B(\mathbf{x},\mathbf{y})$. For the current point (green), the localized interior and exterior are shown as yellow and cyan.

The minimization problem expressed in Eq. 4.11 can be solved using Euler-Lagrange formulation as derived in [64, 16]. The subsequent application of the gradient descent method for an optimal deformation leads to Eq. 4.15.

$$\begin{aligned}\frac{\partial \phi}{\partial t}(\mathbf{x}) =& \delta\phi(\mathbf{x}) \int_{\Omega\,\mathbf{y}} \phi(\mathbf{y}) B(\mathbf{x},\mathbf{y}) \left\{ (I(\mathbf{y}) - c_1)^2 - (I(\mathbf{y}) - c_2)^2 \right\} d\mathbf{y} \\ &+ \gamma\delta\phi(\mathbf{x}) div \left\{ \frac{\nabla\phi(\mathbf{x})}{|\nabla\phi(\mathbf{x})|} \right\}, \end{aligned} \tag{4.15}$$

where γ is the weight assigned to regularization term and c_1, c_2 represents the localized interior and exterior intensity mean values as expressed in 4.14. For a simple interpretation, the image-based force responsible for the curve evolution can be identified by discarding the regularization term of evolution Eq. 4.15. Accordingly, the localized curve driving force can

be written as expressed by Eq. 4.16.

$$F_{local} = \delta\phi(\mathbf{x}) \int_{\Omega_\mathbf{y}} \phi(\mathbf{y}) B(\mathbf{x},\mathbf{y}) \left\{ (I(\mathbf{y}) - c_1)^2 - (I(\mathbf{y}) - c_2)^2 \right\} d\mathbf{y}. \tag{4.16}$$

The localized energy handles the intensity inhomogeneity problem of medical data successfully as illustrated in Fig. 4.8; however, the practical efficiency of F_{local} depends upon several factors including careful selection of the localization radius and the intelligent placement of the initial mask. The sensitivity to the initialization makes this method fragile as small perturbations in the initialization may lead to an undesirable solution. Fig. 4.10 presents two simple cases for synthetic images where the localized curve evolution fails to handle small perturbations in the initial mask. To overcome the limitations of the localized energy-based evolution, we propose to integrate the global model of the image in terms of a discontinuity map for improved accuracy and robustness against initialization.

In the subsequent section, we explain the mathematical approach for a global model (discontinuity map) and the formulation of the hybrid energy for improved segmentation. Accordingly, we will show that the hybrid energy-based curve evolution will make the segmentation process robust i.e. less sensitive to the initial placement of the mask and more flexible against the localization scale.

4.7 Hybrid Energy Model for Improved segmentation

The localized model computes the image-based energy E_{ext} from a radius constrained region, which often leads to convergence to a local optimum. Thus, to achieve the desired segmentation, it requires a careful initialization, which is not always straightforward in the case of complex medical structures. Consequently, we propose to overcome the limitation of the localized energy model by integrating a global model of the image represented by the discontinuity map in the segmentation process as expressed by Eq. 4.17. The integration of the image global model in the curve evolution process will allow a certain amount of flexibility in the placement of initial contour. In the case of a poor/far initialization, the global term will push the contour towards the object boundary by suppressing the influence of local

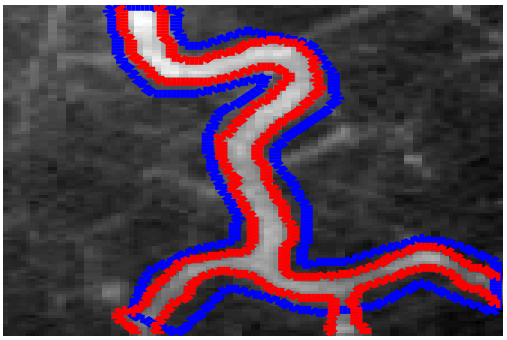

(a) Intelligent Initialization

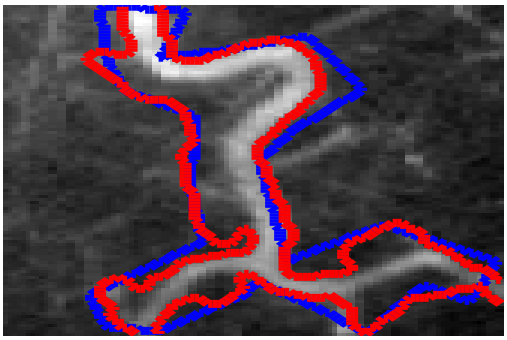

(b) Perturbations in Initialization

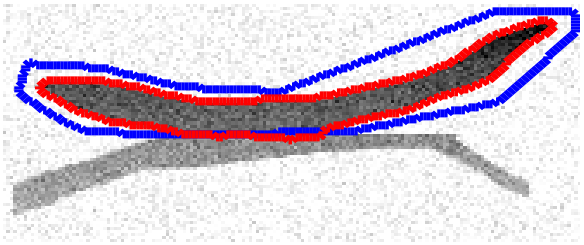

(c) Intelligent Initialization

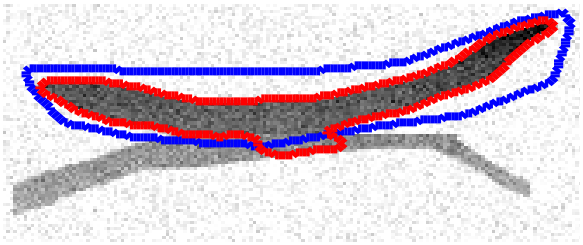

(d) Perturbations in Initialization

Fig. 4.10 The sensitivity of the localization model against the initial mask. (a) and (c) show the segmentation result for a cautious initialization, that is, very close to the object boundaries. On the other hand (b) and (d) shows the result when perturbations are introduced in the initial mask. Blue is the initial mask and red is the final segmentation result.

optima. Moreover, a scalar weight β regulates the influence of the global term to achieve the desired segmentation. A higher weight of the global term will push contour rapidly towards the salient features derived from the global image, whereas a lower weight will allow the localized statistics to fine tune the object boundaries.

$$
\begin{aligned}
F_{hybrid} &= \left\{ F_{local} + \beta F_{global} \right\}, \\
F_{hybrid} &= \delta\phi(\mathbf{x}) \int_{\Omega \mathbf{y}} \phi(\mathbf{y}) B(\mathbf{x},\mathbf{y}) \left\{ (I(\mathbf{y}) - c_1)^2 - (I(\mathbf{y}) - c_2)^2 \right\} d\mathbf{y} + \beta F_{global}.
\end{aligned} \tag{4.17}
$$

The global model of the image is based on the intensity discontinuities in the image. Conventionally the gradient strength is used for defining an edge-map of an image; however,

the gradient generally thickens the object boundary as shown in Fig. 4.11b. Thus, the quality of the segmentation is compromised as the evolving contour stops away from the true borders of the object. One possibility is the use of smaller gradient scale; however, the selection of the optimal scale directly influences the segmentation quality. In contrast, the Bayesian framework leads to sharp inter-class distinctions [17] inside an image as presented in Fig. 4.11c. In this work, the Bayesian approach is preferred for the coronary segmentation problem as the cardiac CTA data is generally approximated using a three class assumption [17, 134, 102].

Based on the clinical interpretation of the cardiac CTA, we start with the assumption that the histogram of the CTA volume can be well approximated using three classes (air filled lungs, heart tissues and the blood filled structures). However, we applied a precautionary normalization to suppress the calcifications (if any) in the CTA volume by clamping the intensity against the upper threshold value of the respective R_I intensity range. Next, we approximated the individual peaks of the image histogram to obtain the Gaussian approximation for three individual classes using Eq. 4.18.

$$p\left(I\left(\mathbf{x}\right) \mid \mathbf{x} \in c_k\right) = N\left(d, \mu_k, \sigma_k\right) = \frac{1}{\sigma_k\sqrt{2\pi}} exp^{\frac{-(d-\mu_k)^2}{2\sigma_k^2}}, \tag{4.18}$$

where $d = I(\mathbf{x})$ denotes the intensity levels in the volume I at position $\mathbf{x}$, c_k is the class identifier and (μ_k, σ_k) represent distribution parameters of the respective class. In the subsequent step, the overall histogram of the CTA is represented using a Gaussian mixture model where individual peaks are mapped to a weighted Gaussian distribution as expressed in Eq. 4.19.

$$p(d) = \sum_{k=1}^{3} a_k N(d; \mu_k, \sigma_k). \tag{4.19}$$

Next, the expectation maximization [135] algorithm is iteratively applied to determine the optimal distribution parameters for each class where the prior probability is set equivalent for all three classes at the start. In the final step, Bayes' rule is applied to obtain the voxel-wise posterior probabilities (i.e. probabilities of a single voxel $\mathbf{x}$ with intensity value d, for three

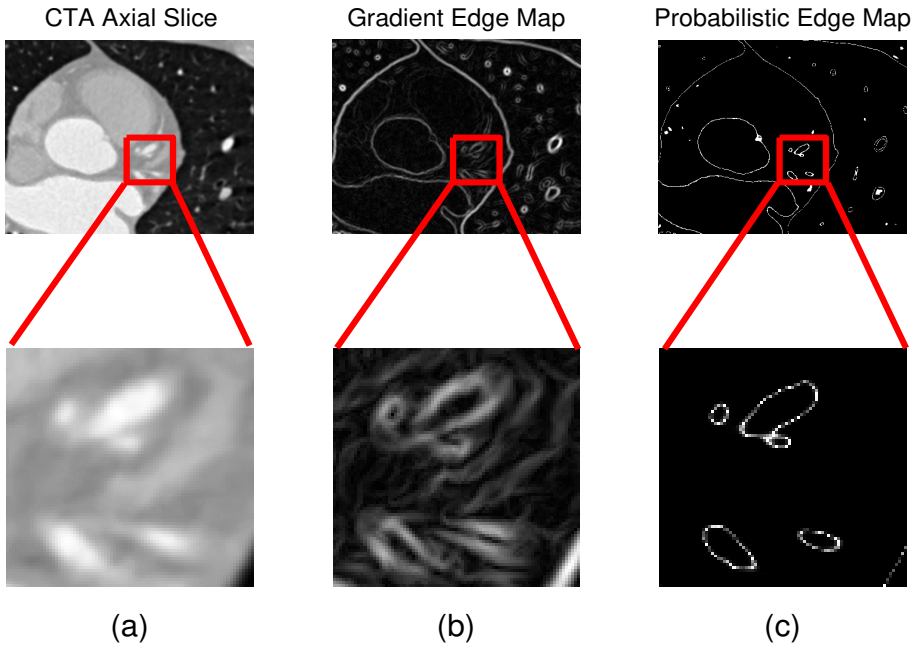

Fig. 4.11 Image discontinuity modelling based on two methods. (a) shows the 2D axial slice with coronary segments. (b) shows the edge map obtained using gradient strength which leads to thicker edges. (c) presents shows the probabilistic difference-based discontinuity map with sharp edges.

different classes).

$$Pr(\mathbf{x} \in c_k \mid I(\mathbf{x}) = d) = \frac{Pr(I(\mathbf{x}) = d \mid \mathbf{x} \in c_k) Pr(\mathbf{x} \in c_k)}{\sum_{\tau=1}^{n} Pr(I(\mathbf{x}) = d \mid \mathbf{x} \in c_\tau) Pr(\mathbf{x} \in c_\tau)}. \tag{4.20}$$

where $Pr(I(\mathbf{x})|c_k)$ and $Pr(\mathbf{x} \in c_k)$ represent the likelihood and the prior probability function for three individual classes. To reduce the effect of noise, we applied anisotropic diffusion as proposed by Perona and Malik [136]. A total of five iterations are applied to achieve smoothed posteriors Pr^{Smth} with gradient modulus (Kappa) set equal to 30. In the subsequent step, we derive the global model of the image as the squared difference of the two largest posteriors for every pixel as expressed in Eq. 4.21. This encoding significantly enhances the boundary between two classes as presented in Fig. 4.11c.

$$I_{global} = \left\{ Pr^{smth}(\mathbf{x} \in c_{k1}) - Pr^{smth}(\mathbf{x} \in c_{k2}) \right\}^2. \tag{4.21}$$

Computation in Eq. 4.21 is based on the assumption that the boundary between two objects can be detected using squared difference of two posterior probabilities [17]. Let us assume that we have a bimodal image with class q_{in} representing the object to be segmented, and class q_{out} representing the background. Then the boundary between object and background can be computed as the squared difference of two posteriors. For our tri-modal CTA image, the first peak represents the dark background, second peak defines the heart muscles and the last peak represents blood filled structures. The dark background represents air-filled lungs in CTA which is often located in outer field of view, whereas our discontinuity model aims to separate blood-filled structures from the heart muscles. Accordingly, the posterior probability for two higher classes is employed in the discontinuity computation.

By substituting the global force into Eq. 4.17, we obtain the hybrid curve driving force as expressed in Eq. 4.22.

$$F_{hybrid} = \delta\phi(\mathbf{x}) \int_{\Omega\mathbf{y}} \phi(\mathbf{y}) B(\mathbf{x},\mathbf{y}) \left\{ (I(\mathbf{y}) - c_1)^2 - (I(\mathbf{y}) - c_2)^2 + \beta \left(\frac{1}{I_{global}(\mathbf{y})} \right) \right\} d\mathbf{y}. \tag{4.22}$$

Here β acts as a regularization constant, regulating the influence of the global component in the overall evolution process. The selection of the global weight β is important as the true boundary will be surpassed in distal segments due to a high influence of the global force. On the other hand, segmentation obtained with very low values of β will produce results similar to localization model of [16] due to less influence of the global term. Accordingly, we evaluated different values for β in the normalized range [0, 0.01, 0.05, 0.10, 0.15, 0.25, 0.50, 0.75, 1.0] to determine the best global weight. Subsequently, experimental evidence shows that the segmentation obtained with β less than 0.1 produces results similar to localization model of [16], whereas setting β greater than 0.25 results in suppression of distal segments due to very high influence of global term. This makes $\beta = 0.15$ a feasible choice for effective segmentation of the coronary tree for our CTA dataset.

4.8 Iterative Mask Adjustment

The proposed model uses a self-adjusting model to handle the coronary segmentation in the 3D CTA volume; however, this is not required for simple 2D images (synthetic and the clinical CPR imagery used in validation tests). According to the self-correction approach, the algorithm reconstructs the evolving contour after every iteration to follow the arterial progression more precisely. This is based on the fact that the coronary tree comes out from the descending aorta in general and splits into branches along the caudal-cranial axis. Hence all the segments are well captured in the level set-based active contour evolution; however, due to the wide inter-patient variability and 2D axial slice-based data acquisition in CTA, some distal branches emerge away from the main trajectory and become a part of the tree as axial slices are navigated. To address this issue, one possible solution is using a 3D level set segmentation but it increases the complexity in terms of computational resources and processing time. In contrast, we introduced an auto-correction feature in the mask to capture the emerging peripheries during active contour-based evolution. The proposed method reconstructs the mask in every iteration by scanning the neighbourhood of the trajectory on a 2D axial slice. All the individual peripheries that satisfy the constraints (tubular shape

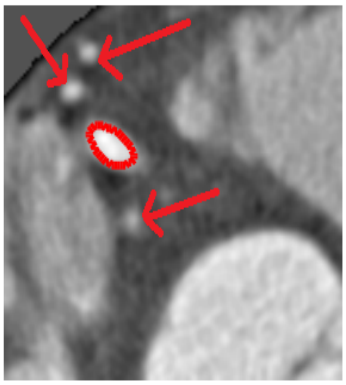

(a) Peripheries pointed by arrows

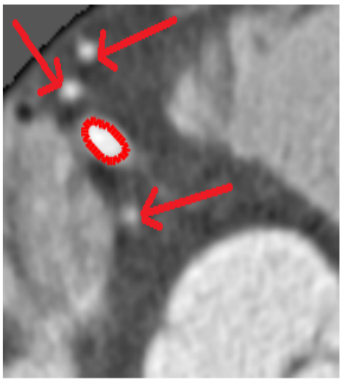

(b) Emerging peripheries missed

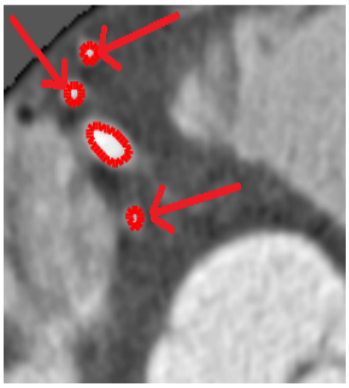

(c) Emerging peripheries captured

Fig. 4.12 Auto-correction feature of the mask to capture nearby emerging peripheries during evolution. (a), emerging peripheries as pointed by arrows, (b) peripheries missed during evolution before introducing the auto-correction feature. (c), emerging peripheries are captured for complete tree extraction with the help of the auto-correction feature.

and adaptive intensity validation) are captured as shown in Fig. 4.12c -4.12c. This self-adjustment feature offers improved accuracy and the computational robustness, whereas the non-connected structures are automatically discarded using connected component analysis.

A primary drawback associated with the level set evolution is the processing time as the curve evolution in a 2D space using signed distance functions require a large number of computations. However, the key to minimize the processing time is to exploit the fact that the curve changes position smoothly. Consequently, the area around the evolving curve is to be evaluated for new position i.e. only a narrow band is to be investigated. For a fair processing time, we employed the sparse field method of Whitaker [77] *et al.* to evolve the curve as it promises an accurate but minimal representation of the evolving curve. In addition to self-correction of the mask, we employed bi-directional evolution in this work to extract the complete coronary tree. This is based on the fact that the coronary seed points lie in the mid of the CTA volume. Accordingly, the initial mask is constructed and evolution is performed in both directions of the caudal-cranial axis to capture proximal and distal segments, respectively. Accordingly, the average time for segmentation of coronary vasculature of a Matlab R2014b [137] on an Intel 3.4 GHz machine is 80 seconds.

4.9 Results

4.9.1 Efficacy of the adaptive threshold

In this section, we demonstrate experimentally that adaptive modelling of the contrast medium intensity can considerably improve the accuracy of the coronary segmentation, whereas the use of a fixed intensity threshold across the dataset may decrease precision by capturing the nearby non-coronary segments or missing the distal parts of the coronary tree. Accordingly, the hybrid energy-based coronary segmentation was performed using two different intensity thresholds. The comparative results reveal that the use of a fixed threshold i.e. 350HU [123] leads to an erroneous coronary tree in terms of under/over segmentation, whereas the proposed adaptive threshold ensures accurate segmentation by employing the influence of contrast medium in the segmentation process. Moreover, the proposed segmentation shows a greater corroboration with the manual annotations in the cross sectional analysis as explained below.

CPR Based Analysis

Fig. 4.13 shows the segmented right coronary artery (RCA) of DS 01 (CTA volume 1) using two different thresholds. It can be observed from Fig. 4.13b that the volume-specific threshold (756HU) precisely tracks the main progression of the RCA from the aorta to the distal endpoint with minimal peripheries, whereas the use of a literature-based [123] fixed threshold 350 HU results in numerous side branches for the RCA (see Fig. 4.13a). The efficacy of the adaptive intensity threshold is further investigated by constructing the curve planar reformatted (CPR) images along three different axes as shown in Fig. 4.13c - 4.13e. CPR visualization from three different views helps to evaluate if there exist any intermediate peripheries for the segmented RCA. It can be observed that distinct views along three different axes substantiate the fact that the right coronary artery is well segmented from the aorta to the distal points using the adaptive intensity threshold. Moreover, it becomes evident that the peripheries which appear to be a part of the coronary structure in Fig. 4.13a,

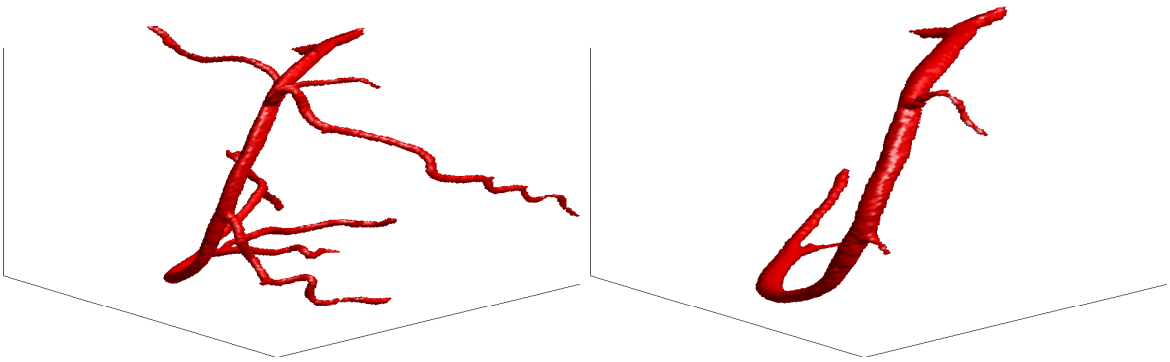

(a) Use of fixed HU threshold (b) Use of adaptive HU threshold

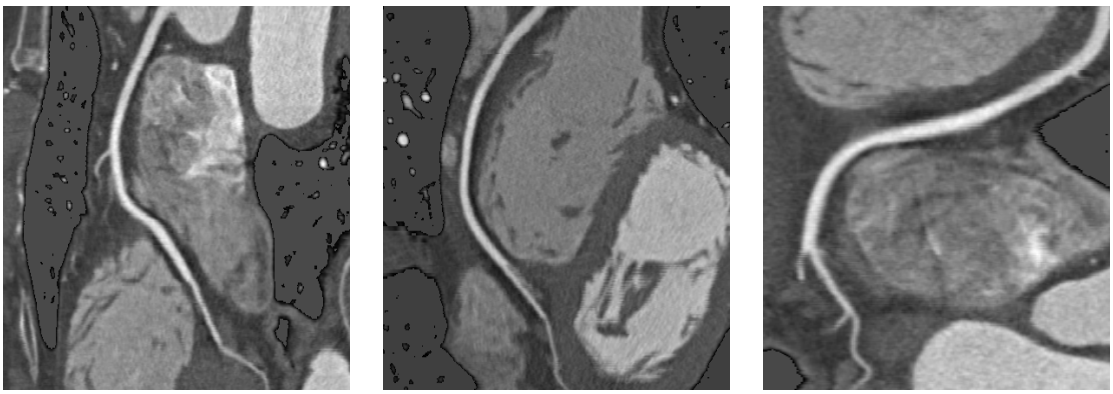

(c) CPR along X-axis (d) CPR along Y-axis (e) CPR along Z-axis

Fig. 4.13 Visualization of segmented RCA of CTA volume1. (a) RCA obtained using fixed intensity threshold of 350HU, (b) RCA obtained using adaptive threshold. (c-e) represent CPR image along three axes to confirm the efficacy of adaptive threshold. It can be observed from CPR images that RCA does not contain a large number of side peripheries as reflected by fixed-threshold segmentation.

are not true coronaries but the "kissing" vasculature in close proximity which was captured mistakenly by active contour during the evolution as illustrated in Fig. 4.15.

Cross-Sectional Analysis

The efficacy of the adaptive intensity threshold is also illustrated by comparing the two segmentations in 3D space. Fig. 4.14a - Fig. 4.14b shows a zoomed version of the segmented Left circumflex artery (LCX) branch of CTA volume 1 obtained using two thresholds. It can be observed that the adaptive threshold (756 HU) results in a smooth segmentation (see Fig. 4.14a), whereas the fixed threshold (350 HU) leads to over-segmentation in terms of

expansion through disconnections of the LCX (see Fig. 4.14b). This is based on the fact that the high concentration of the contrast medium misleads the evolving curve to capture the nearby structures. This over-segmentation is further demonstrated using the orthogonal planar analysis as shown in Fig. 4.14c. The impact of the over-segmentation can be clearly observed by viewing the boundary points, as the fixed threshold-based segmentation shows incorrect expansion of the vessel in a transparent cross sectional plane, in contrast to the response of adaptive threshold-based segmentation. Moreover, five consecutive cross sectional planes are shown in Fig. 4.14d -4.14f with the segmented boundary overlaid. It can be observed that the adaptive threshold precisely captures the true boundary of the vessel by suppressing the nearby vasculature, whereas the fixed threshold-based segmentation captures the adjacent non-coronary structures that result in increased false positives.

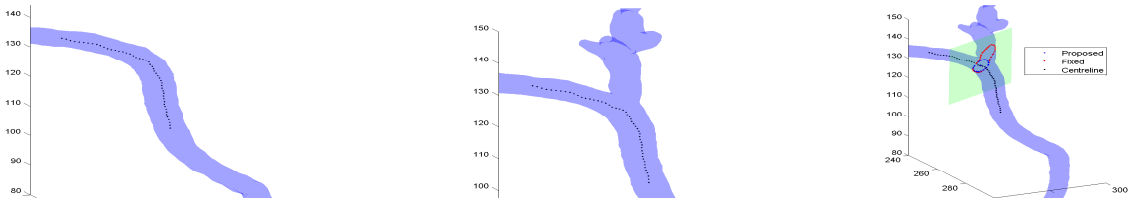

(a) Normal LCX (b) Disconnected expansion (c) Planar Visualization

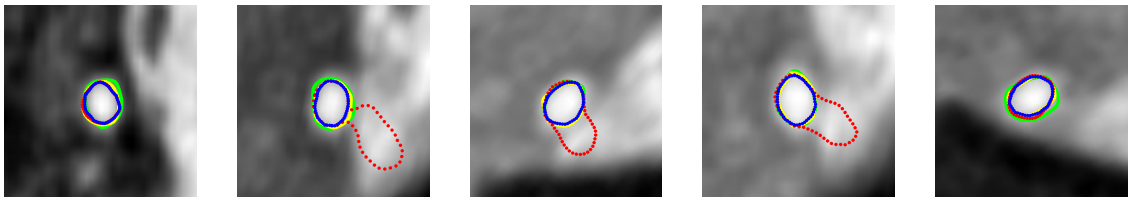

(d) Normal (e) Expanded (f) Expanded (g) Expanded (h) Normal

Fig. 4.14 Analysis for LCX branch of CTA volume 1. (a-b) LCX segmentation using adaptive (756HU) and fixed (350HU) threshold values respectively. (c) illustrates the efficacy of adaptive threshold as planar boundary points show over-segmentation for fixed threshold. (d-h), 5 consecutive cross sections of LCX illustrating the over segmentation associated with fixed threshold. Red is the fixed threshold segmentation contour and green is the adaptive threshold result. Blue and yellow represent manual annotations.

The kissing vessel phenomena is further illustrated in Fig. 4.15 where it can be observed that use of adaptive intensity threshold leads to true coronary vasculature segmentation by suppressing non-coronary objects in close proximity.

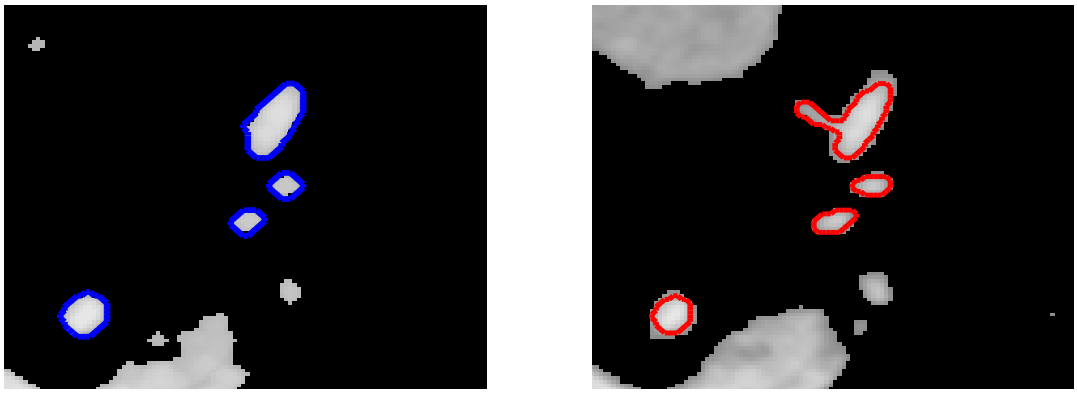

(a) Normal LCX (b) Expanded LCX

Fig. 4.15 Kissing vessel suppression. (a and b) represents an orthogonal slice in the middle of LCX artery. It can be observed from (a) that true coronary peripheries are captured using adaptive intensity threshold based segmentation (blue contours), whereas a fixed threshold (red contours in b) captures nearby non-coronary vasculature leading to disconnected expansion and increased false positives.

4.9.2 Statistical Quantification Metrics

We designed a Matlab-based framework to compare the obtained segmentation with respect to the manual ground truth. For individual contours of the ground truth lumen, we computed the plane normal (perpendicular to the medial axis) in the first stage. In the subsequent stage, we extracted the corresponding orthogonal planes from the segmented tree and the lumen boundary contours are identified as shown in Fig. 4.16. The first stage of the quantification process is illustrated in Fig. 4.16a, in which 3D segmented contours are plotted against the manual ground truth. Next, we projected the 3D contours on a 2D plane where two polygons are interpreted as binary images as shown in Fig. 4.16b. In the final stage, we computed the statistical measures including true positive, false positive, false negative with respect to the reference contours. For a meaningful evaluation of the obtained segmentation statistics, we employed efficiency metrics including sensitivity, specificity and Jaccard similarity index [138] to compute the overlap between two segmentations (reference and the obtained). The mathematical equation for obtaining the efficiency metrics are expressed by Eq. 4.23.

$$
\begin{aligned}
Sensitivity &= \frac{TP}{(TP+FN)}, \\
Specificity &= \frac{TN}{(TN+FP)}, \\
Jaccard\,index &= \frac{TP}{(TP+FP+FN)},
\end{aligned} \tag{4.23}
$$

where TP denotes the true positive i.e. an intersection between two images, FP represents the false positive i.e. part of the segmented image not present in the ground truth and FN denotes the false negative i.e. part of the ground truth missed in the obtained segmentation. The Jaccard index for ideal overlapping segmentation approaches to *one*, whereas two dissimilar images results in Jaccard index of *zero*. It is important to mention that the Jaccard index (or Intersection of Union) is preferred over the standard accuracy measure, as the latter includes true negatives, which are abundant in vessel segmentation and can result in an artificially high accuracy measure.

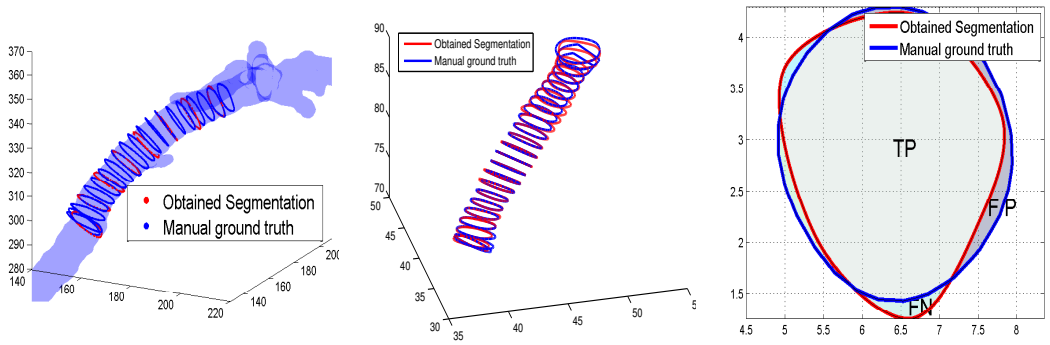

(a) 3D surface with overlaid contours

(b) 3D contours

(c) Jaccard overlap

Fig. 4.16 Segmentation evaluation against the manual ground truth of Rotterdam dataset. (a) shows the ground truth and the obtained segmentation contours overlaid on a 3D coronary surface in the voxel coordinate system. (b) presents a visual comparison of obtained segmentation with ground truth in the world coordinate system, whereas (c) shows the Jaccard overlap computation for the corresponding 2D contours based on TP, TN and FN.

4.9.3 Hybrid Segmentation Performance for 2D Images

As demonstrated in Fig. 4.10, the localization model successfully detect objects of interest when the initialization is fairly close to the object boundary, whereas it fails to handle perturbations because of the local optima problem. This shortcoming is further highlighted in Figs. 4.17 - 4.18 to illustrate the effectiveness of the proposed hybrid method over the localization model of [16] for 2D images (synthetic and clinical CPR respectively). It can be observed that the localization model is trapped in a local optima leading to erroneous segmentation for different initializations, whereas the hybrid method results in successful segmentation for different initializations. Moreover, the weight regulating the influence of the global term can be adjusted to obtain the desired segmentation according to the nature of the image data or the initialization.

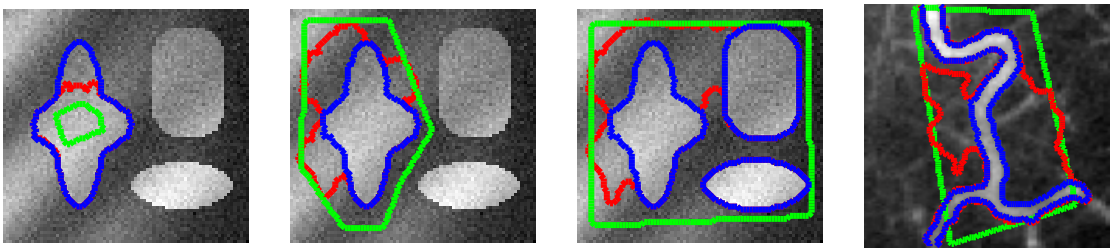

(a) (b) (c) (d)

Fig. 4.17 Performance of two segmentation methods for synthetic images. Blue and red show the hybrid and localization segmentation respectively, whereas green represents the initializations. The localization radius used for these results is 8 pixels.

We also investigated the robustness of proposed model against the localization radius. Figs. 4.19 - 4.20 shows the response of the two methods when localization radius is decreased from 8 to 4 pixels. It is evident that change in the radius degrades the performance of the localized model leading to incorrect segmentation, whereas the proposed model successfully delineates the object for the updated radius. We observed that there exists an inverse relationship between localization radius and the global weight β. The smaller radius results in less information for the energy optimization process requiring more influence of the global term, whereas a large radius offers adequate intensity information, hence; less stimulus from

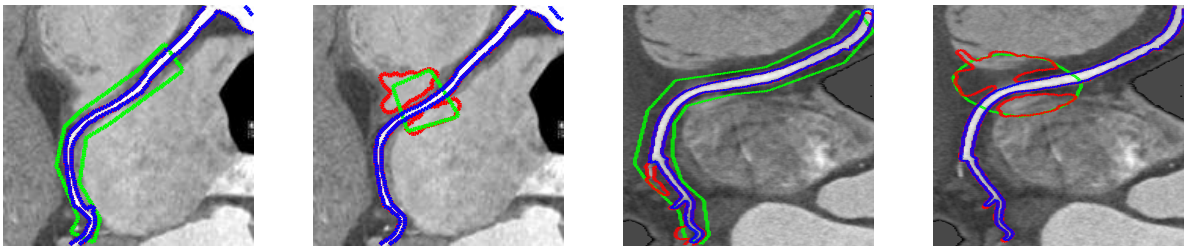

(a) (b) (c) (d)

Fig. 4.18 Performance of two segmentation methods for clinical images. (a) and (b) show right coronary of CTA volume 01 for two different initialization. (c) and (d) show right coronary of CTA volume 02 for two different initializations. Green denotes the initialization, whereas blue and red represent the hybrid and localized segmentation, respectively. The localization radius used for these results is 8 pixels.

the global term is required. This correlation is to be investigated in a future study to make the weight β adaptive against the localization radius and to define an image-based threshold for the localization radius, as a very large radius leads to a global approximation of image which is not suitable for medical data.

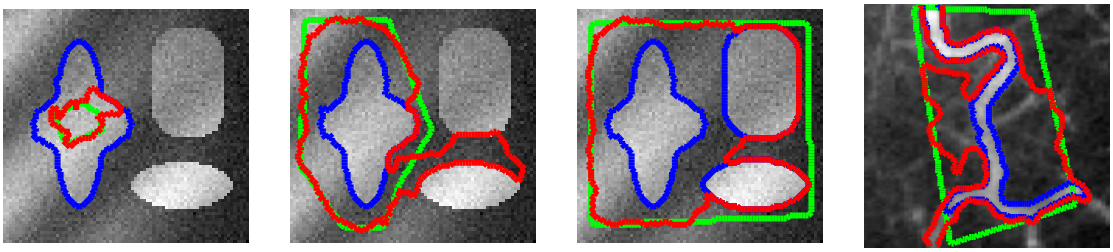

(a) (b) (c) (d)

Fig. 4.19 Performance of two segmentation methods for synthetic images. Blue and red show the hybrid and localization segmentation respectively, whereas green represents the initialization. The localization radius used for these results is 4 pixels.

4.9.4 Hybrid Segmentation Performance for 3D images

It becomes challenging to visually evaluate the segmentation quality in 3D space due to viewing angle limitations as shown in Fig. 4.21a. Thus, we extracted 2D slices orthogonal to the segment centreline at different points across the length of the vessel to illustrate the effectiveness of the hybrid energy model over the localization method. Consequently, the

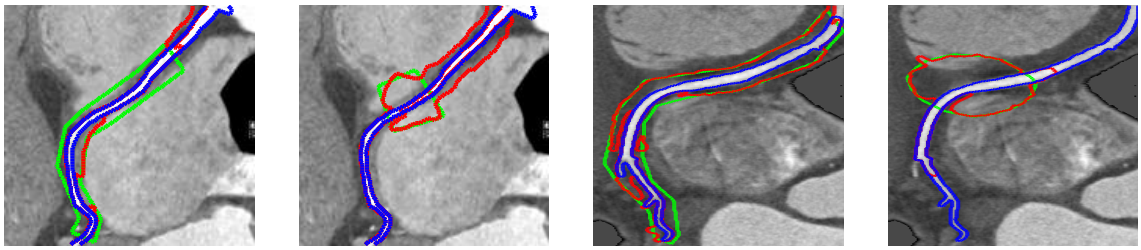

(a) (b) (c) (d)

Fig. 4.20 Performance of two segmentation methods for clinical images. (a) and (b) show right coronary of CTA volume 01 for two different initialization. (c) and (d) show right coronary of CTA volume 02 for two different initialization. Green denotes the initialization, whereas blue and red represents the hybrid and localized segmentation respectively. The localization radius used for these results is 4 pixels.

lumen boundary based on orthogonal cross sections is compared with the manual ground truth contour as illustrated in Fig. 6.8b - 6.8i. It is apparent from the figure that the curve moving under the influence of localized energy (red) gets trapped away from the real lumen, whereas the integration of the global force pushes the contour further to attain a more accurate approximation (blue). The explicit push of the contour towards the lumen reduces the false positives and leads to an improved accuracy of the segmentation.

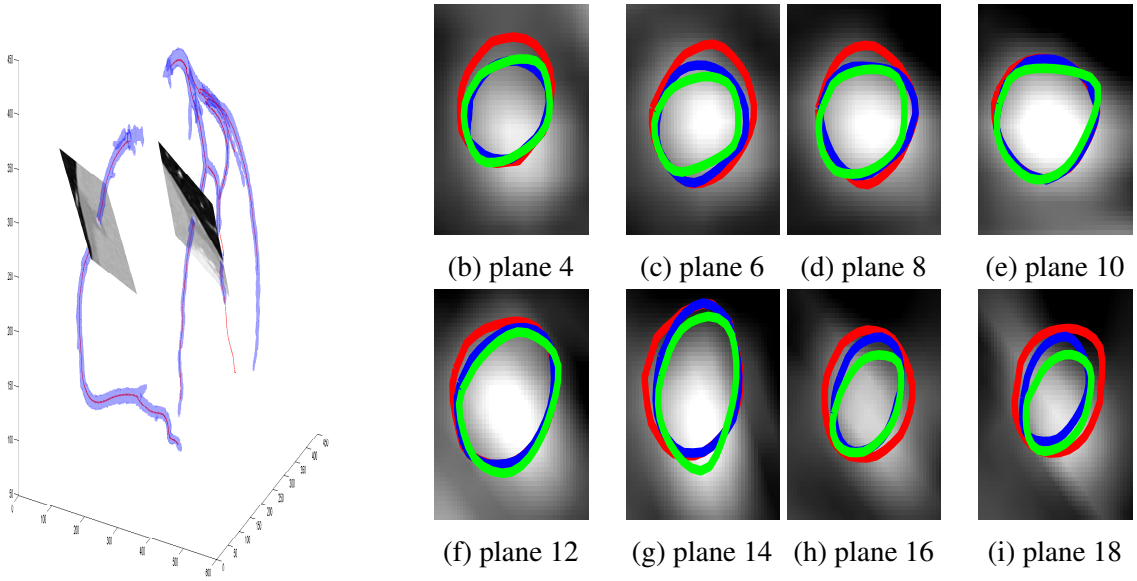

(a) 3D surface with cross sectional intensity planes

(b) plane 4 (c) plane 6 (d) plane 8 (e) plane 10

(f) plane 12 (g) plane 14 (h) plane 16 (i) plane 18

Fig. 4.21 Coronary segmentation visualization. (a) shows the segmented 3D coronary tree with overlaid centreline and two oblique cross sections. (b-i), Consecutive cross-sectional planes for segment-12 of CTA volume 01. Green is the expert's manual ground truth, blue represents the hybrid energy segmentation and red shows the segmentation for localized model [16].

Moreover, the statistical comparison of the two segmentation methods is presented in Fig. 4.22, where we plotted the respective false positive rate and the Jaccard index with respect to the ground truth annotations for three representative volumes. To avoid bias towards a particular expert, we compared the response of the two methods with three manual observers individually and it can be observed that the hybrid model consistently achieves higher Jaccard index in comparison to localization method of [16]. The mean results of complete dataset reflecting the comparative performance of hybrid energy model with respect to the localized segmentation are presented in Table 4.5.

4.9.5 Hybrid Segmentation Performance in clinical context

Before presenting the mean performance of the two segmentation methods for the complete Rotterdam dataset, we evaluated the performance of the hybrid segmentation in a clinical context. From a clinical point of view, the coronary segments are divided into two classes namely major and minor segments. The major class refers to proximal sections close to the descending aorta, whereas the minor class refers to distal segments of the coronary tree. Any abnormality or occlusion in the major segments is treated as a severe clinical threat as the dependent branches are simultaneously affected resulting in considerable damage to the heart tissues. In contrast, the abnormality associated with the minor segments are less threatening as these segments do not affect other downstream segments. Fig. 4.23a shows the mean performance of the hybrid energy model for Rotterdam dataset in the context of major-minor segment classification. The box plot is used based on the fact that distributional characteristics of different groups can be compared effectively. The high median value and the compact distribution reflects that the overall accuracy is fairly high and consistent for the major segments, whereas the reduced diffusion, poor contrast and narrower diameter in minor segments results in reduced accuracy and high variability.

This relationship between the segmentation accuracy and segment position is further investigated as shown in Fig. 4.24. It can be observed from Fig. 4.24a that the high concentration of the contrast medium in the major segment of the coronary tree leads to a good inter-observer agreement. Consequently, both segmentation models achieve an adequate quality segmentation and the Jaccard index shows a marginal superiority of hybrid model over the localization method in Fig. 4.24b. In contrast, a lower concentration of the contrast medium in the minor segments results in the ambiguous appearance, which leads to a significant inter-observer disagreement as shown in Fig. 4.24c. This results in an increased false positive ratio for the localization model, whereas the hybrid energy moderates false positives due to the influence of global term in curve evolution (see Fig. 4.22). Consequently, the hybrid model shows a considerable improvement in the Jaccard index as plotted in Fig. 4.24d.

Similarly, Fig. 4.23b shows the performance of the hybrid energy model using "healthy versus diseased" criteria. It can be observed that the segmentation accuracy for the healthy segments is high in comparison to the diseased segments. The variability observed for the healthy class is unexpected, however this can be related to the immature plaques/lesions present in different segments. As the ground truth classification (healthy versus diseased) is done on the basis of visual inspection of the coronary tree, so there is a chance that segments with insignificant abnormalities were placed in healthy class; however, it affects the segmentation accuracy. On the other hand, the performance for the diseased class is persistent as this class contain significantly abnormal segments.

The mean results for the two segmentation methods are presented in Table 4.5. The Jaccard index (with respect to the manual annotations) shows that the hybrid energy achieves better segmentation over the localization model of [16] for all types of coronary segments. A considerable difference for the minor segments is related with the reduced false positive (%) due to the increased push of global term in hybrid segmentation, whereas lower Jaccard index value for the diseased segments reflect the complexity of segmentation. To validate the statistical significance of the hybrid energy model, we performed a paired $t-$test by employing results of the two segmentation methods. Accordingly, the null hypothesis is rejected which indicates a significant difference in the mean of the two distributions. Moreover, we obtained p values equal to 0.0014 for the false positive rate and 0.0001 for the Jaccard index which indicates a statistically significant difference.

Table 4.5 Segment class-based Jaccard Similarity (%) for the two segmentation methods.

Segment type	Radius	Local model	Hybrid model		
		Jaccard%	β	T_f	**Jaccard%**
Major	4	73.48	0.15	10^{-3}	**76.5**
Minor	4	58.26	0.15	10^{-3}	**68.65**
Healthy	4	68.21	0.15	10^{-3}	**71.62**
Diseased	4	57.79	0.15	10^{-3}	**65.56**

4.9.6 Comparison with Existing Method

After validating the superiority of hybrid energy over the localized [16] segmentation, we compared the performance of the hybrid model with the coronary segmentation algorithm of Yang *et al.* [17], which implements an edge-based conformal factor in the curve evolution. For comparative purpose, we start with the assumption that observer 2 of the Rotterdam CTA framework is the typical ground truth representing the "true" lumen. Accordingly, the segmentation statistics (sensitivity, specificity and Jaccard index) with respect to the ground truth observer are computed in the first step. In the subsequent step, we evaluated the segmentation accuracy of the two models with respect to the ground truth in relation with remaining manual observers as shown in Fig. 4.25. It can be observed from Fig. 4.25a that the higher true positive rate of the hybrid energy model leads to a higher sensitivity for all investigated volumes whereas the reduced false positive rate results in comparatively better specificity for the hybrid model. For the overall Jaccard overlapping index, it can be observed from Fig. 4.25c that the hybrid method outperforms the [17] model with a consistent higher index value. The complete statistical results are presented in Table 4.6 - 4.7.

Table 4.6 Statistical metrics (sensitivity, specificity and Jaccard Index) for volumes 00-08.

Metrics	Methods	3D CTA Volumes								
		DS00	DS01	DS02	DS03	DS04	DS05	DS06	DS07	DS08
Sens (%)	Hybrid	76.08	97.61	81.06	82.70	87.50	77.88	87.59	84.33	88.84
	Yang	70.49	62.34	52.54	71.43	66.31	60.49	49.27	54.62	55.73
	Obs1	53.43	99.85	74.01	84.62	66.44	64.67	54.09	57.41	57.41
	Obs3	75.10	93.79	85.00	88.01	86.13	80.31	89.37	84.07	87.18
Spec (%)	Hybrid	74.86	75.38	72.89	85.97	73.33	71.50	66.84	71.15	70.03
	Yang	71.49	82.59	59.15	45.53	75.97	66.85	37.68	64.98	63.49
	Obs1	59.50	70.49	71.39	78.26	72.63	71.45	66.89	69.57	70.46
	Obs3	75.07	78.81	73.75	81.95	80.04	75.72	81.68	77.30	79.86
Jaccard (%)	Hybrid	60.21	66.78	59.26	73.26	61.25	56.86	50.35	57.44	56.19
	Yang	55.43	58.49	47.18	39.55	57.61	50.14	47.52	49.29	48.25
	Obs1	46.60	58.13	56.02	66.82	55.42	54.10	50.07	51.48	51.86
	Obs3	60.04	71.18	58.99	68.55	60.43	58.72	62.34	58.57	56.04

Moreover, Fig. 4.26 represents the performance of two segmentation methods in the context of the mean human agreement of 3 human observers. It can be observed from the plot that the overall Jaccard index is dropped due to averaging against three manual

Table 4.7 Statistical metrics (sensitivity, specificity and Jaccard Index) volumes 10-18.

Metrics	Methods	3D CTA Volumes								
		DS09	DS10	DS11	DS12	DS13	DS14	DS15	DS16	DS17
Sens (%)	Hybrid	48.45	67.93	87.41	90.16	79.36	84.62	87.25	95.15	55.06
	Yang	53.74	62.07	70.40	73.52	69.37	68.04	48.62	69.25	55.00
	Obs1	48.91	52.72	72.79	74.47	72.64	70.08	64.90	51.93	61.34
	Obs3	65.20	58.17	73.06	81.05	84.02	79.23	83.12	83.24	54.38
Spec (%)	Hybrid	59.97	69.05	78.14	78.92	75.25	76.22	70.95	66.91	55.00
	Yang	48.14	46.28	44.42	88.40	76.54	79.64	41.63	70.68	55.00
	Obs1	41.81	57.73	84.01	86.85	82.31	81.15	65.88	55.88	71.45
	Obs3	69.19	62.49	86.96	94.12	83.39	77.70	75.09	79.76	64.10
Jaccard (%)	Hybrid	36.63	52.18	67.73	69.75	61.62	64.41	57.53	50.51	55.00
	Yang	36.84	38.22	39.61	68.64	59.23	60.54	44.38	54.31	55.00
	Obs1	35.40	46.12	65.75	68.49	64.63	62.49	49.16	45.36	53.43
	Obs3	51.15	46.49	67.56	62.42	59.25	63.50	57.44	52.01	48.03

annotations; however, the comparative performance of the proposed model remains superior to [17] model and shows a consistent inclination towards an inter-observer mean agreement. However, it can be observed from the plot of Fig. 4.26 that there occurs a considerable dip in Jaccard index value for CTA datasets 10 and 17 (for both segmentation methods as well as the inter-observer mutual agreement). This unexpected drop is related to the structural abnormalities of the coronary tree as shown in Fig. 4.27a. These aberrations in the coronary tree make segmentation challenging even for the manual observers, as Fig. 4.27b -4.27c shows a minimal agreement among three human experts.

4.10 Summary

In this chapter, we demonstrated an efficient coronary segmentation method with the help of qualitative and quantitative results. A limitation of the proposed method is the manual selection of the appropriate weight β for the global term, as the true boundary is surpassed occasionally due to high influence of the global force. Subsequently, in the CTA volume-based analysis, we evaluated different values for β from the normalized range [0, 0.01, 0.05, 0.10, 0.15, 0.25, 0.50, 0.75, 1.0] to derive an empirical evidence for best global weight. According to a series of experiments, the segmentation obtained with β less than 0.1 produces results similar to localization model of [16] due to a very less influence of global term, whereas setting β greater than 0.25 results in suppression of distal segments due to a very high influence of global term. This makes $\beta = 0.15, 0.25$ a feasible choice for effective segmentation of the coronary tree.

It should be noted that the fully automatic segmentation of the coronary tree has been a challenging problem so far and the current research is focused to minimize the human interaction. Several methods [139–141, 124, 142] have been proposed in recent years addressing the automatic and semi-automatic segmentation of coronary lumen with a motivation of stenosis detection; however, little attention has been paid on the negative remodelling of coronary vessels. From a clinical point of view, negative remodelling signals the presence of soft plaques which have been reported as most important indicator of heart attack and stroke [50]. Subsequently, the coronary tree segmented in this chapter will be used in the intensity-based investigation for detection and localization of non-calcified plaques in next chapter.

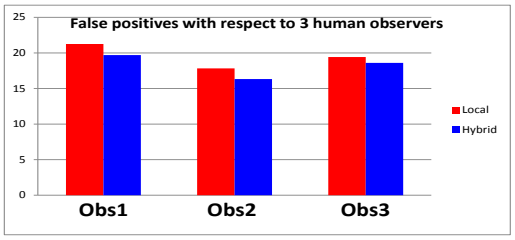

(a) DS5-FP

(b) DS5-Jaccard

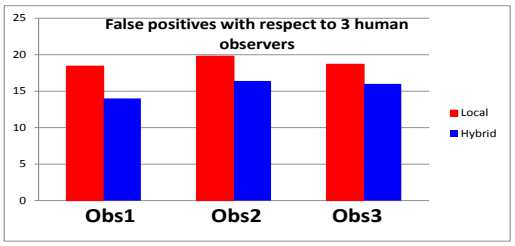

(c) DS15-FP

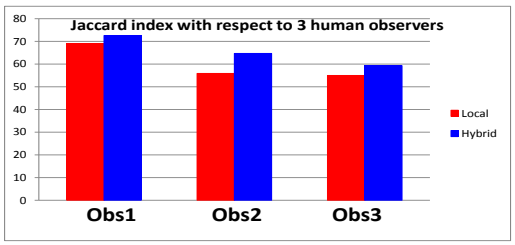

(d) DS15-Jaccard

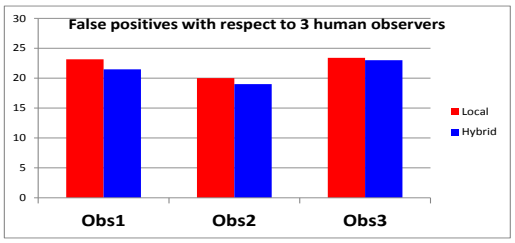

(e) DS13-FP

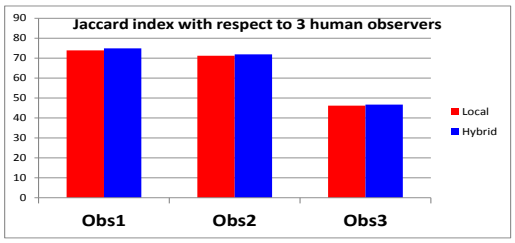

(f) DS13-Jaccard

Fig. 4.22 Segmentation accuracy of two methods with respect to three individual observers of Rotterdam dataset. Consistently low FP % and high Jaccard index value shows the advantage of hybrid model over the localization [16] method.

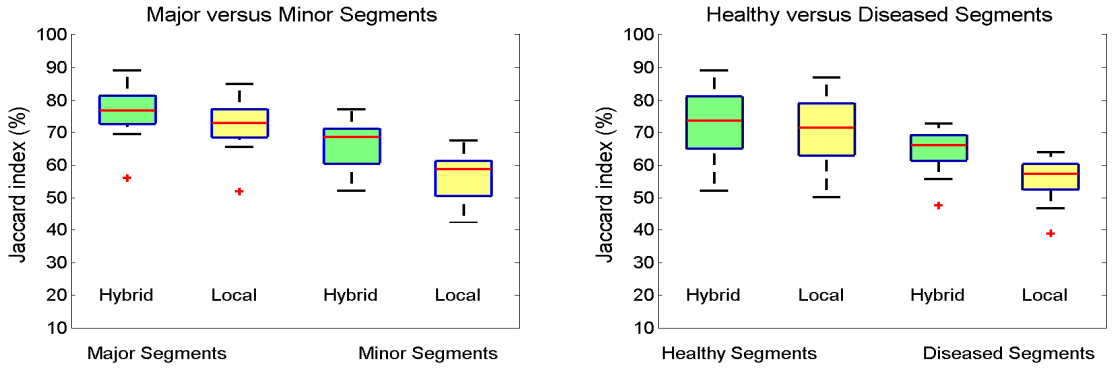

(a) Statistics for major - minor segments.

(b) Statistics for healthy - diseased segments.

Fig. 4.23 The mean performance of the hybrid model for complete Rotterdam CTA dataset in a clinical context. (a) shows higher accuracy for major segments in comparison to minor branches, similarly (b) shows higher accuracy for healthy segments in comparison to diseased branches.

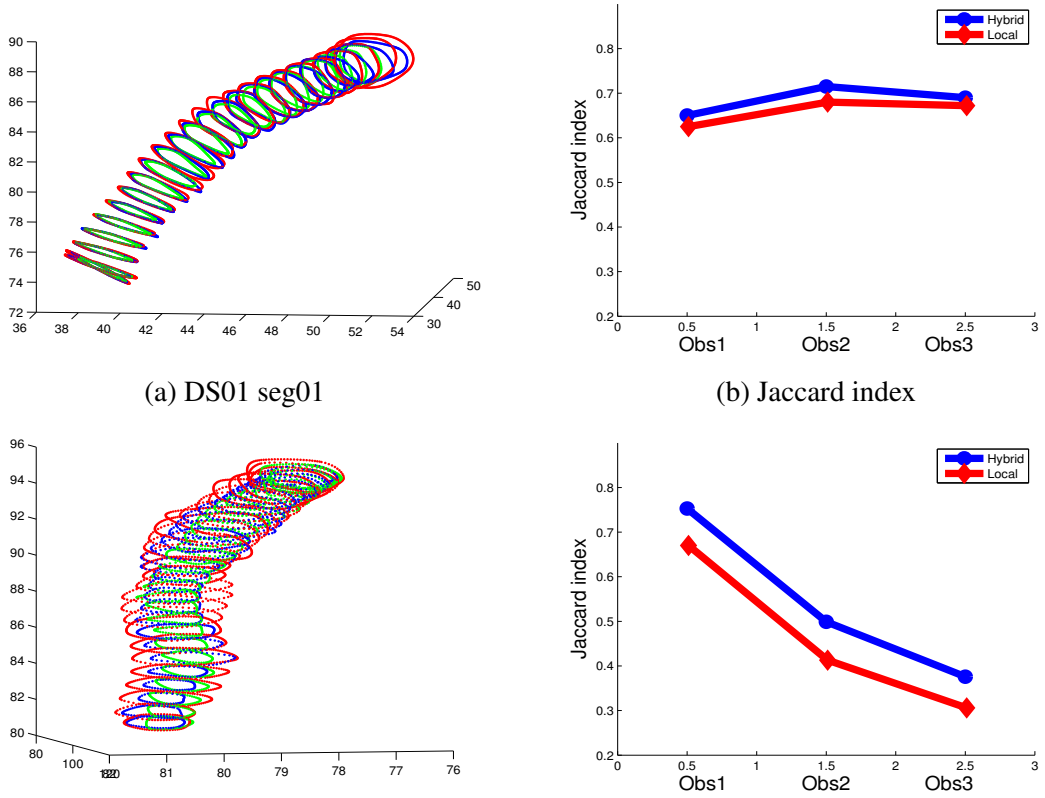

(a) DS01 seg01 (b) Jaccard index

(c) DS01 seg12 (d) Jaccard index

Fig. 4.24 Performance of two segmentation methods for different segment types. Good agreement among three manual observers (a) reflects the bright appearance of proximal segments. (b) the reduced agreement among three human observers due to the ambiguous appearance of distal segments. (c) and (d) represents the Jaccard index for two segmentation methods w.r.t three individual observers.

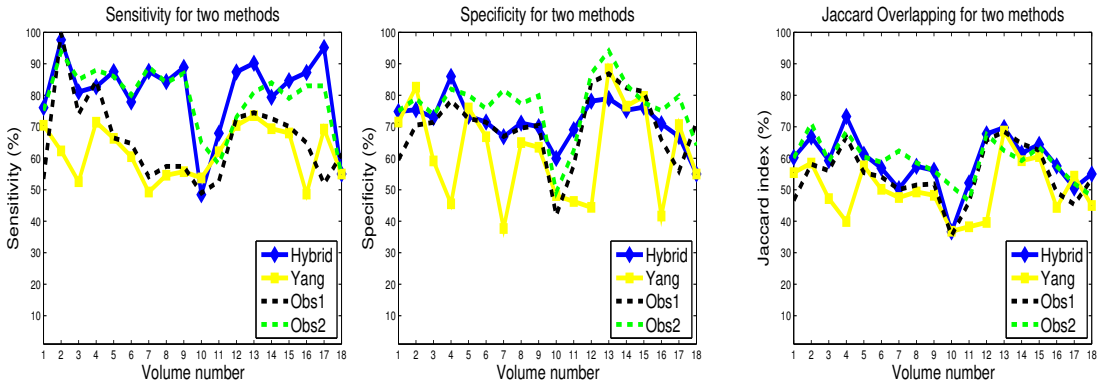

(a) Sensitivity (b) Specificity (c) Jaccard

Fig. 4.25 Segmentation result for [17] and the hybrid segmentation method with respect to observer 2 of the Rotterdam dataset.

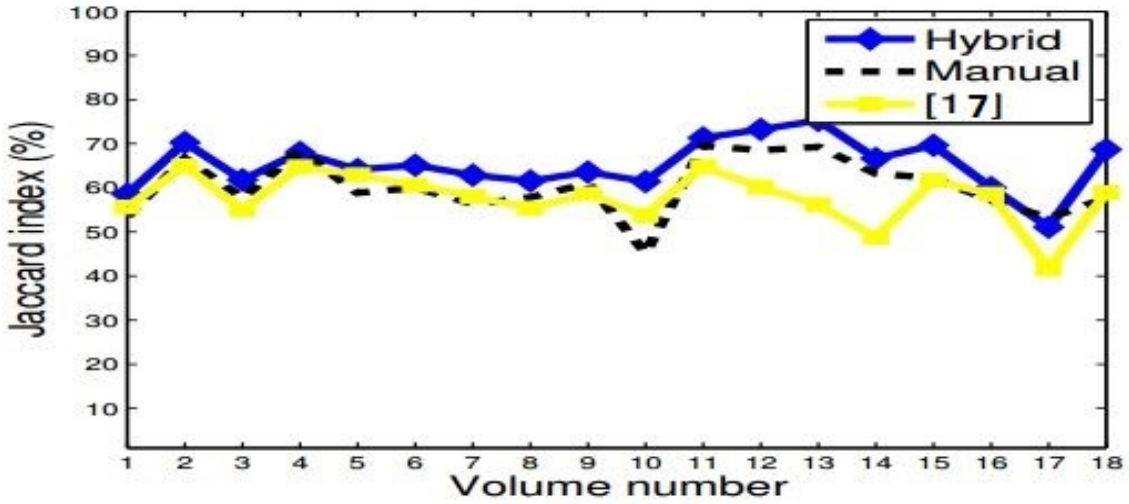

Fig. 4.26 Segmentation result for the mean human agreement, [17] and the proposed method with respect to the average of three observers.

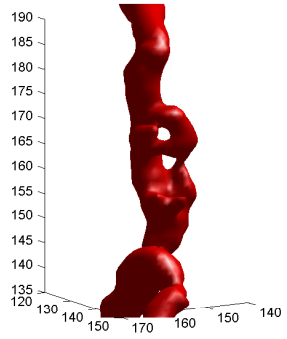

(a) Structural abnormality

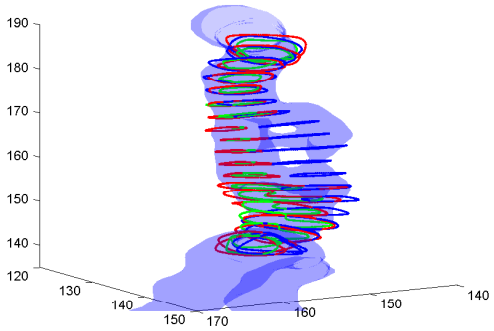

(b) Overlaid annotations

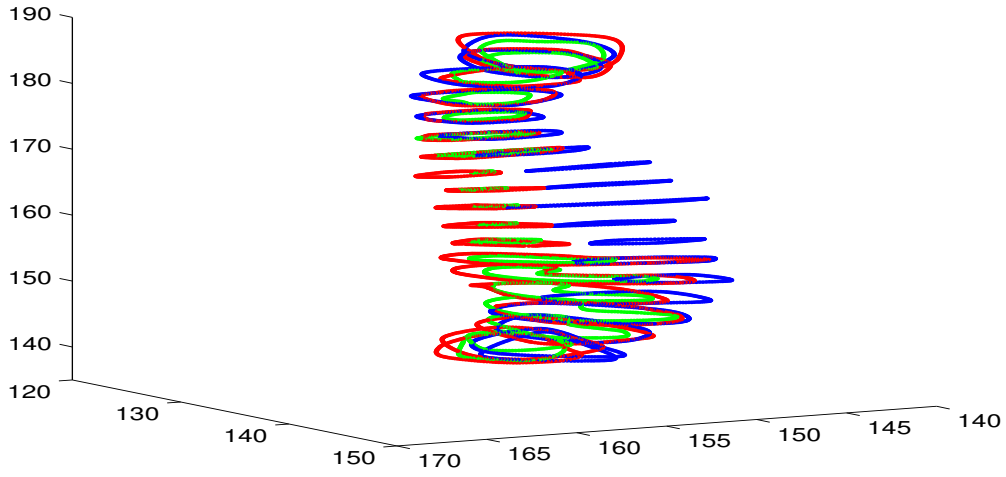

(c) Inter-observer agreement

Fig. 4.27 Illustration of the inconsistencies between manual observers. (a) A coronary structure with an aberration, which complicates segmentation. (b) Clinical annotations for lumen boundary for three observers (red, blue and green circles). (c) Magnification of the boundaries. Notice the inconsistent decision of the observers whilst delineating the lumen.

Chapter 5

Detection and Localization of Non-calcified Plaque Regions

5.1 Introduction

This chapter is focused on detection and localization of non-calcified plaques in the segmented coronary tree. The early detection of coronary plaques is crucial as future cardiac events can be avoided or at least delayed, by addressing the behavioural risk factors such as tobacco use, unhealthy diet and physical routine[24]. From a clinical point of view, calcified plaques represent the deposition of calcium inside coronaries, whereas Non-calcified plaques are formed due to the presence of lipids, fat and cholesterol. Moreover, the non-calcified plaques have been established as the most important indicator of acute coronary syndromes due to their fragile nature [50]. The risk of sudden rupture has made soft plaques threatening in a clinical context, i.e. for many individuals, sudden death becomes the first sign of soft plaque in contrast to calcified plaques which often lead to disease symptoms at early stages. It should be noted that calcified plaques can be identified easily in a CTA image based on the high intensity value, consequently numerous methods have been reported with a reasonable detection accuracy [105, 106, 143]. In contrast, non-calcified plaques (NCP) usually have a lower intensity value and quite close to nearby heart tissues that makes the detection problem challenging [33, 107, 144–146]. Moreover, the positive remodelling associated with NCP

(also termed as soft plaques) amplifies the detection challenge as the diameter-reduction based methods [105, 106, 143] fail to detect the presence of soft plaques. Consequently, the high morbidity rate associated with non-calcified plaques has provided the impetus for increased research on early detection of soft plaques to predict and avoid worst cardiac events.

In this chapter, we start with the centreline extraction of the coronary vasculature, followed with the detailed explanation of discrete radial profile based representation of the coronary segments. In the subsequent section, we explain the support vector machine (SVM) based analysis for detection and localization of non-calcified plaques. It is notable that along with Rotterdam CTA dataset (18 CTA volumes of Table 4.2), two additional datasets (12 CTA volumes obtained from Guy's and St. Thomas's hospital, London and 2CTA volumes obtained from Semmelweis University Budapest, Hungary) have been investigated in this experiment. After obtaining the respective coronary centrelines, the orthogonal cross-sections were computed for the second dataset and an expert was requested to label the cross sections as normal or pathological (soft plaque affected) using optimal window/level settings (W/L=800/300). Moreover, the classification for both CTA datasets was validated with the help of clinical quantitative coronary angiography (QCA) reports which was provided for two datasets.

Our contribution in this chapter is an efficient methodology for explicit detection and localization of the non-calcified plaques in clinical CTA. Accordingly, we demonstrate that the abnormal intensity drops resulting from soft plaque inside coronary vessels can be captured using concentric rings along the vessel centreline, which can be further employed for NCP detection. The proposed model differs from the anomaly detection methods of [113, 116] that the coronary tree is segmented in the first stage using a hybrid energy model from Chapter 4 which reveals radius variations along the length of vessels. Consequently, the radial information of the segment helps in tracing both positive and negative remodelling associated with the soft plaques. Furthermore, the plaque detection is performed using windowed statistics to uncover abnormalities in a relative context rather then evaluating individual cross sections as proposed in [116]. Experimental results demonstrate that the

proposed method achieves a good agreement (detection accuracy of 88.4% with respect to manual annotations) and results in-line with anomaly detection methods of [113], [116]. In addition, the proposed model approximates the position and length of the non-calcified plaques in the abnormal coronary segment with a good accuracy of 83.24% against manual annotations. We believe that detected plaque terminal points can be used to design a fully automated plaque quantification model as explained in Chapter 6. Likewise, Clouse's *et al.* [10] quantification can be automated using detected start and end positions for improved performance. It should be noted that the explicit detection of soft plaques is a challenging clinical problem. In this context, a number of local features proposed in [113] and [116] fail to detect fragile, low-intensity soft plaques; hence, the detection rate for non-calcified plaques is significantly lower then calcified plaque detections in [113] (i.e. 79.62% versus 94.05%).

5.2 Coronary Tree Skeletonization

The construction of the centreline from the segmented 3D coronary tree plays an important role in the plaque detection process. We extracted the vessel centrelines from the segmented tree using the sub-voxel thinning algorithm of Ultert *et al.* [147]. The accuracy of the obtained centrelines is evaluated by computing the mean distance (deviation error) with respect to the reference ground truth [118] as presented in Fig. 5.1. The visual comparison for the complete coronary vasculature is presented in the left column of Fig. 5.1, whereas the deviation error for individual segments (RCA, LCX, LAD and D1) is shown in the right column.

Moreover, statistical results showing the mean deviation for the coronary vasculature in the Rotterdam dataset is presented in Table 5.1. Accordingly, it can be observed from the table that the deviation error for the major coronary segments is less than one millimetre with respect to the reference centreline, except for dataset 09. The high deviation error in this dataset is related with the floating plaque inside RCA, which leads erroneous centrelines.

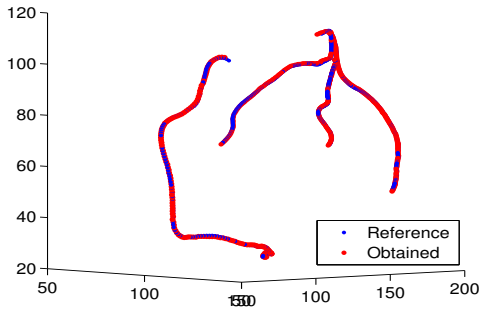

(a) Centrelines for DS02

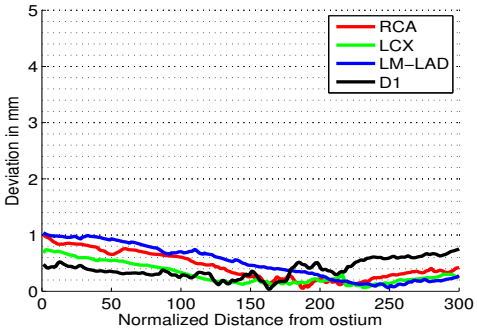

(b) CP deviation for DS02

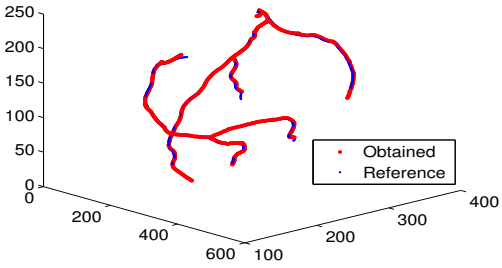

(c) Centrelines for DS08

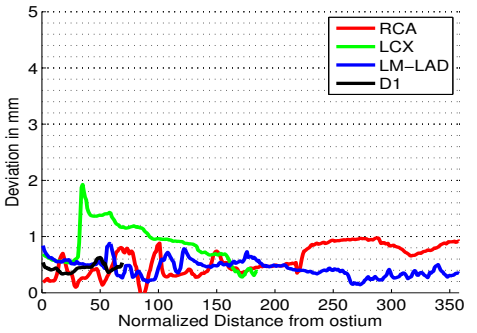

(d) CP deviation for DS08

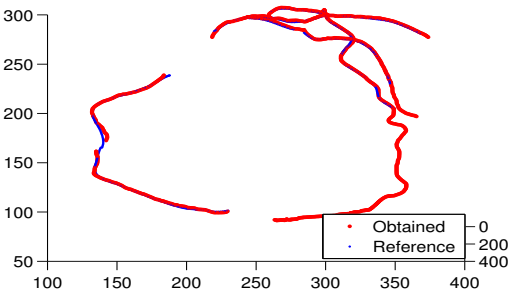

(e) Centrelines for DS09

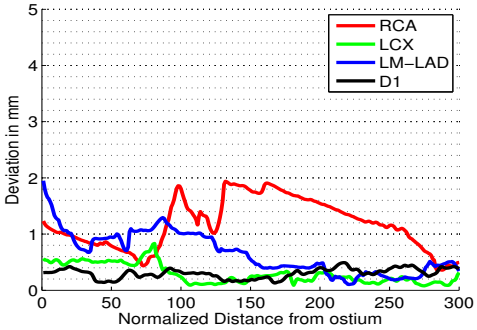

(f) CP deviation for DS09

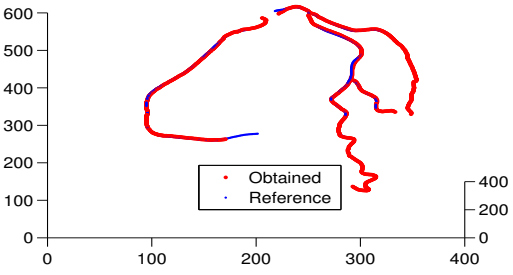

(g) Centrelines for DS12

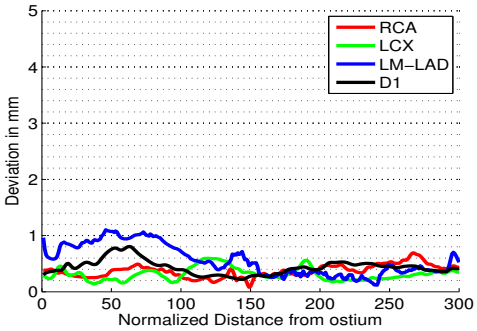

(h) CP deviation for DS12

Fig. 5.1 Accuracy of the coronary centreline with respect to the reference ground truth [18] for different CTA volumes. (Left column) obtained centreline overlaid with the ground truth centreline, (right column) mean deviation of the obtained centreline in millimeters. It can be observed that the coronary centreline has a mean deviation of about 1mm for the major segments.

Table 5.1 Centreline deviation in millimeters for coronary vasculature (for volume 00-17)

CTA Volume	Vascular Sections	Right Coronary Artery	Left Main Left Anterior Descending	Left Circumflex Artery	Diagonal Branch Artery
	AHA Segment No	{1,2,3,4,17}	{5,6,7,8}	{11,13,14,15}	{9,10,16}
DS00		0.298±0.11	0.384±0.14	0.320±0.11	0.286±0.06
DS01		0.301±0.14	0.590±0.24	0.425±0.08	0.612±0.16
DS02		0.504±0.15	0.304±0.11	0.539±0.21	0.475±0.09
DS03		0.407±0.15	0.311±0.11	0.407±0.15	0.359±0.08
DS04		0.355±0.09	0.314±0.15	0.410±0.16	0.447±0.06
DS05		0.421±0.20	0.413±0.18	0.368±0.12	0.381±0.09
DS06		0.383±0.18	0.365±0.14	0.418±0.11	0.380±0.06
DS07		0.375±0.14	0.45±0.17	0.63±0.20	0.511±0.23
DS08		0.557±0.26	0.412±0.13	0.885±0.35	0.439±0.07
DS09		1.180±0.44	0.651±0.37	0.290±0.17	0.301±0.08
DS10		0.449±0.12	0.551±0.12	0.435±0.19	0.000±0.00
DS11		0.722±0.19	1.271±0.47	0.350±0.17	0.381±0.11
DS12		0.368±0.11	0.560±0.27	0.314±0.11	0.435±0.13
DS13		0.351±0.17	0.304±0.14	0.467±0.09	0.339±0.11
DS14		0.497±0.21	0.284±0.14	0.363±0.11	0.368±0.11
DS15		0.470±0.21	0.345±0.14	0.498±0.12	0.262±0.10
DS16		0.000±0.00	0.000±0.00	0.000±0.00	0.000±0.00
DS17		0.421±0.18	0.305±0.20	0.409±0.13	0.410±0.08

5.3 Discrete representation of Coronary Segments

In the subsequent step, different branches of the coronary skeleton are labelled according to the 17-segment coronary model of the American Heart Association (AHA) [4]. The segment labelling is performed in this step as the plaque detection and quantification in this work is performed on a per-segment basis. Next, the respective centrelines are used to extract the orthogonal cross-sections to constitute the segment-wise cylindrical volume as illustrated in Fig. 5.2. The statistical representation for the segment-wise cylindrical volumes are explained in this section.

5.3.1 Mean Radial Profile

To investigate the intensity composition along the coronary segment, this work employed the notion of the mean radial profile. We observed that this representation is effective to identify the intensity abnormalities in 3D tubular vessels by comparing radial profiles of successive 2D cross sections along the vessel axis. To illustrate the advantage of mean radial profiles, we obtained 2D cross sections along the length of the segment by substituting respective

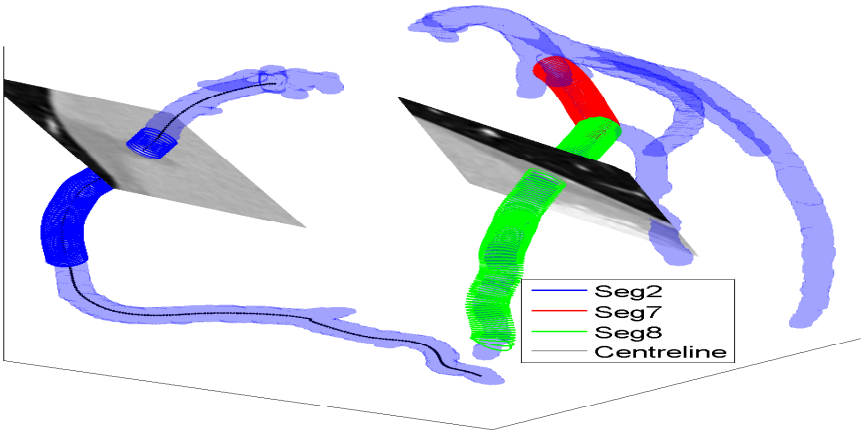

Fig. 5.2 Segmented coronary trees with overlaid centreline and two cross sectional planes. The centreline is overlaid in black for the right coronary artery, whereas blue, red and green represent the curved cylindrical approximations for coronary segments numbered 2, 7 and 8 respectively. A local cylinder with 6mm diameter well encompasses the coronary segments.

centreline points in Eq. 5.1.

$$\mathbf{n_{xyz}} \cdot (\mathbf{x} - \mathbf{c_{xyz}}) = 0, \tag{5.1}$$

where $\mathbf{c_{xyz}}$ represents a point at the centre of a planar patch and $\mathbf{n_{xyz}} = [n_x, n_y, n_z]^T$ represents the normal of the plane which is computed using successive points of the centreline to precisely follow the vessel orientation. In the subsequent step, we computed the respective radial profiles by sampling the obtained cross sections along concentric rings according to Eq. 5.2.

$$p[r,k] = \frac{\int_0^{2\pi} I(r,\theta,q_k)d\theta}{\int_0^{2\pi} d\theta}, \tag{5.2}$$

where q denotes the segment centreline and q_k defines the k_{th} cross section of the centreline, with $k = [1,...,N_s]$, where N_s is the total number of the cross sections in the coronary segment. Moreover, I represents the image intensity, $r = [1,...,6mm]$ defines the sampling radius, and θ defines the angle of a projecting ray. Fig. 5.3a shows the mean radial profiles for five sequential cross-sections (k=5, 10, 25, 40 and 45) of the coronary segment. It can be observed that the intensity is at its highest/maximum at the centre of a healthy cross section (i.e. k=5,

10, 40 and 45) and decreases outwards as a smooth function of distance. In contrast, the abnormal segments can be clearly differentiated based on an unexpected response of the mean radial profile. This deviation is visually illustrated in Fig. 5.3b where two cross-sections are displayed using optimal coronary display settings. High intensity in a normal cross section results in a bright appearance (top), whereas presence of low density material results in a darker appearance of the diseased cross section (bottom). Accordingly, this work employed the concept of mean radial profiles to compute the segment intensity response along the length of the segment.

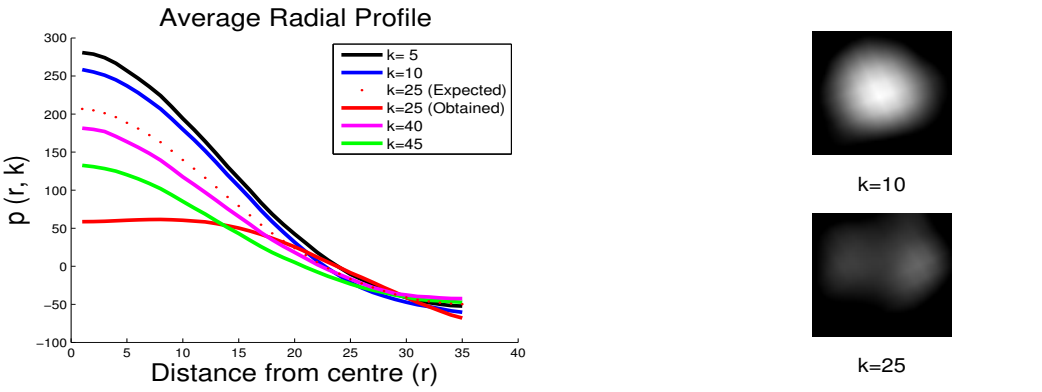

(a) Mean Radial Profiles

(b) Grey scale cross-sections

Fig. 5.3 Mean radial profile based intensity examination to detect abnormality in 3D vessel. (a) shows radial profiles for five sequential cross sections to detect composition abnormality, whereas (b) shows 2 cross-sections (normal and abnormal) using standard window level settings i.e. [w/l = 800/300].

5.3.2 Cylindrical Modelling of Coronary Segments

To effectively use the radial profiles in plaque detection, we approximated the individual coronary segments with a curved cylindrical model having a diameter of 6mm. The choice of a 6mm diameter is feasible as several studies [128], [139], [148] show that the maximum coronary diameter remains less than 6mm. Consequently, the circumference of our curved cylinder serves as an external boundary between the coronary vessel and the background. This is illustrated in Fig. 5.2 where three different coronary segments are mapped with respective curved cylindrical models. This method of segment approximation is superior to

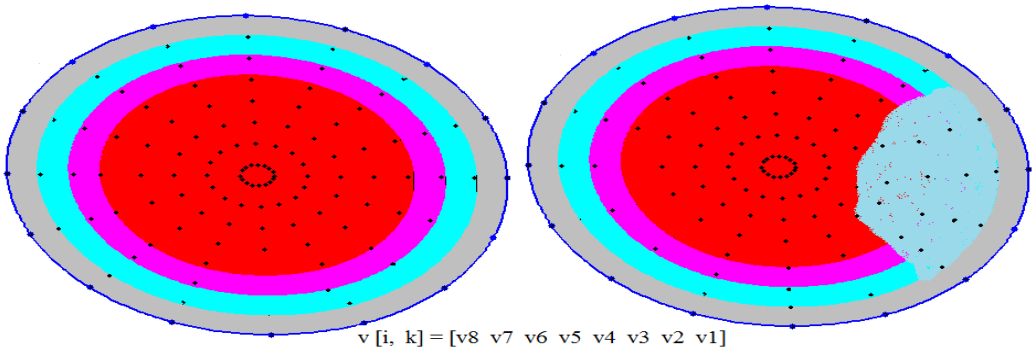

Fig. 5.4 A schematic representation of the intensity composition for normal and abnormal coronary cross sections. Left represents a normal cross section with adequate flow of blood, whereas right shows a plaque leading to blood obstruction. Moreover, the dots represent the discrete radial profiles obtained by sampling 8 concentric rings.

Clouse *et al.*'s [10] approach, where, a hard threshold of 0 Hounsfield units (HU) was used to cut off the vessel from the background. Nearby calcifications and image reconstruction artefacts often result in vessel borders that differ from 0 HU. Another advantage of our cylindrical approximation is that it allows a certain amount of flexibility in the centreline accuracy, as the mean response of the 6mm region can successfully model the segment intensity distribution by overcoming the slight perturbations in the centreline. Next, we used the approximated curved cylindrical model of respective coronary segments to obtain the radial profiles. However, in context of the computational robustness, this work used a discrete approximation of Eq. 5.2 to construct customized radial profiles along the length of the segment. To maintain a trade-off between the computational load and the radial profile accuracy, the discretization parameters are chosen as $\Delta r = 0.4mm$, $\Delta\theta = 22.5°$ and $\Delta q = 0.4mm$. The sampling interval of 0.4 mm is used for the radial and cylindrical axes due to the isotropic voxel size, whereas an angular spacing of 22.5° is used to project 16 rays onto the sampling plane. The chosen angular interval is fairly reasonable as the smaller interval leads to increased processing time without improving the performance. Accordingly, the customized radial profile is defined as expressed by Eq. 5.3.

$$v[ii,k] = \frac{1}{L}\sum_{t=1}^{L} I(r_{ii},\theta_t,q_k)\,\forall ii,k,\ ii = 1,...,8,\ k = 1,...N_s, \tag{5.3}$$

where q_k represents the k^{th} cross sectional of coronary segment and N_s defines the total number of points along the length of the segment. L denotes the total number of projected rays, which is set equal to 16 in this model and the respective projection angle is computed as $\theta_t = t\left(\frac{\pi}{8}\right)$. Moreover, ii denotes the concentric ring number formed at radius $r_{ii} = 0.4(9-ii)$ mm. This formulation of r_{ii} reveals that the outermost ring is labelled as v_1 and the innermost ring is denoted as v_8. This discrete approximation is illustrated in context of two cross sections in Fig. 5.4 where it is apparent that the outer four rings (v_1 to v_4) generally define the interface between lumen and external fat, while the inner four rings (v_5 to v_8) represent the contrast medium affected blood.

This fact is further demonstrated in Fig. 5.5 where the intensity response of eight concentric rings is plotted for the complete segment. It can be observed that irrespective of the segment composition, the inner four rings reflect the impact of the contrast medium in terms of high intensity, whereas the outer four rings represent comparatively lower HU values related to the external boundary of the vessel. Moreover, Fig. 5.5 shows that healthy segments lead to stable intensity responses for all the eight rings (see Fig. 5.5a) throughout the segment length, whereas the presence of low intensity (soft plaques) results in significant concavities for the inner four rings (see Fig. 5.5b). We observed that this considerable disparity in the stability of the four inner rings can be used to differentiate coronary segments into two classes i.e. normal and abnormal. Consequently, we derived the mean representation ($\mathbf{S}$) of the coronary segments by averaging the response of the four inner rings as expressed in Eq. 5.4. It should be noted that the segment mean representation $\mathbf{S}$ is based on the four inner rings, which minimizes the probability of erroneous plaque detection due to 6 mm circular approximation of distal segments.

$$S[k] = \frac{1}{4}\sum_{ii=5}^{8} v[ii,k],\ \forall k,\ k = 1...N_s. \tag{5.4}$$

To overcome the short term fluctuations in the mean representation of the coronary segments, this work applied finite impulse response filter using a moving window technique. Accordingly, the smoothed statistical representation of the coronary segment is obtained with

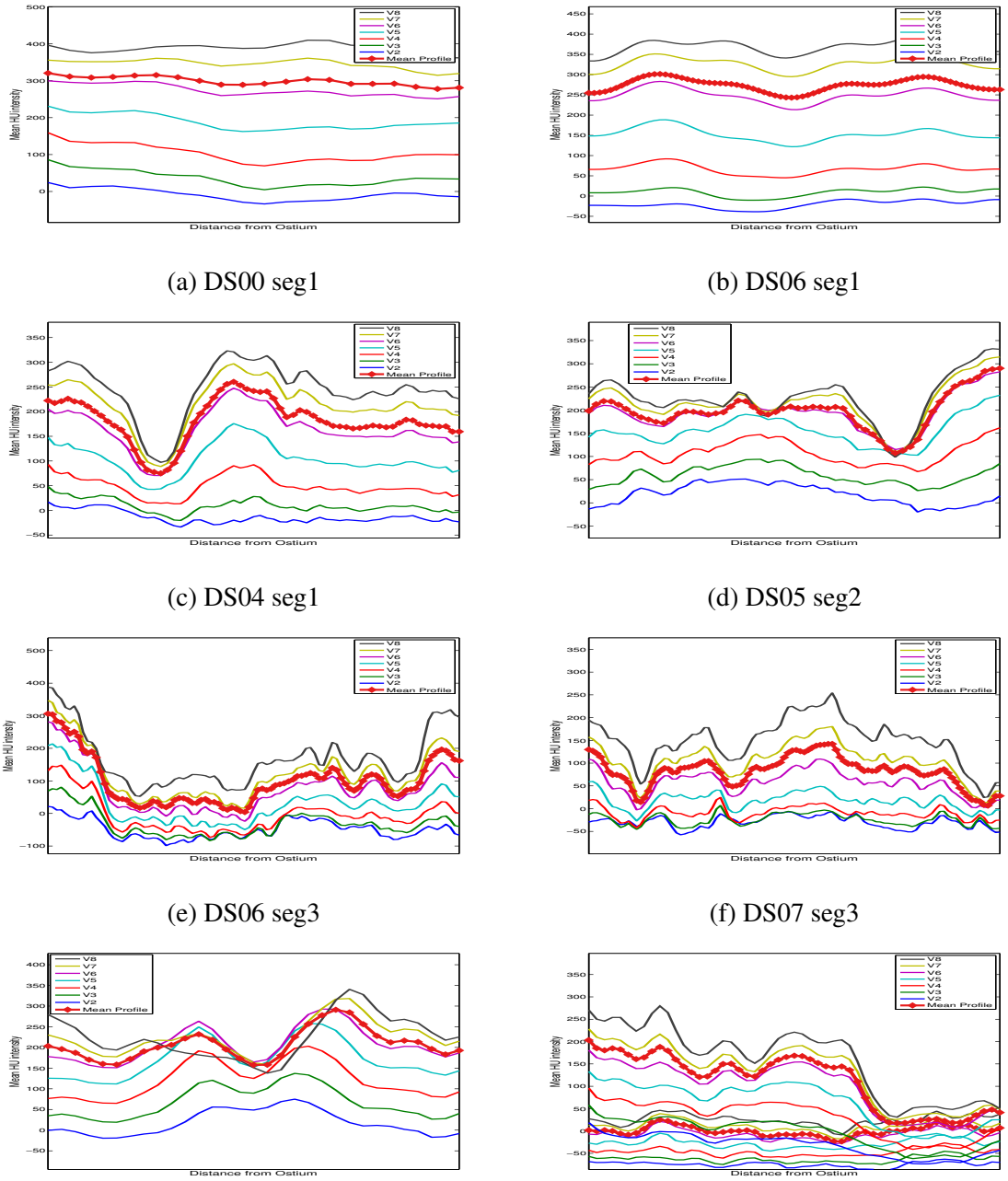

(a) DS00 seg1

(b) DS06 seg1

(c) DS04 seg1

(d) DS05 seg2

(e) DS06 seg3

(f) DS07 seg3

(g) DS09 seg2

(h) DS11 seg1

Fig. 5.5 Mean intensity response for 8 concentric rings (v_1 to v_8) along the length of segment. (a-b) represents two normal segments, whereas (c-h) shows six abnormal segments. It can be observed that the mid of the lumen, (v_8) exhibits high HU intensity, whereas a low value of (v_1) indicates a position away from the lumen centre. Moreover, the mean profile of the coronary segment is obtained by averaging the four inner rings (v_8) - (v_5).

the help of a moving mean and moving standard deviation operation as expressed in Eq. 5.5, where Sz i.e. the size of the moving window is set equal to 3.

$$\sigma_s[k] = \sqrt{\frac{1}{(2Sz+1)-1}\sum_{i=-Sz}^{Sz}(S[k+i]-\mu[k])^2},$$
$$\mu_s[k] = \frac{1}{2Sz+1}\sum_{i=-Sz}^{Sz}S[k+i],\ k=1,...,N_s. \tag{5.5}$$

In addition, we constructed the segment radius profile S_{rad} by computing the lumen radius from the segmented coronary tree, to take into account the remodelling impact along the length of the vessel. The radius along the segment is computed by detecting the vessel boundary on respective cross sections, as illustrated in the Fig. 5.6. It can be observed that the cross sections of the coronary segment representing the normal blood flow in the vessel (no plaque is present) appears approximately circular in shape leading to a consistent radius, whereas plaque related structural abnormalities can be traced by identifying shape deformations, which leads to inconsistent radius values.

It is notable that different coronary segments have variable length, as defined in the standard AHA coronary model (see Fig. 5.2 for a visual difference between segment 2, segment 7 and segment 8). We apportioned the variable length of individual segments at this stage with the help of spline interpolation to redefine the segments in terms of the fixed length characteristic functions $\mu_s^{'}$, $\sigma_s^{'}$ and $S_{rad}^{'}$ (each having 100 samples).

5.4 Non-Calcified Plaque Detection using SVM

5.4.1 Feature Based Representation for Coronary Segments

After obtaining the fixed length characteristic functions for coronary segments, we used an SVM classifier [149] to differentiate the plaque affected segments from the normal ones. An imperative pre-requisite for a learning-based classifier is the selection of appropriate features from the data. Ambiguous features failing to discriminate two classes effectively leads to poor accuracy, whereas distinctive features result in a promising classification. We

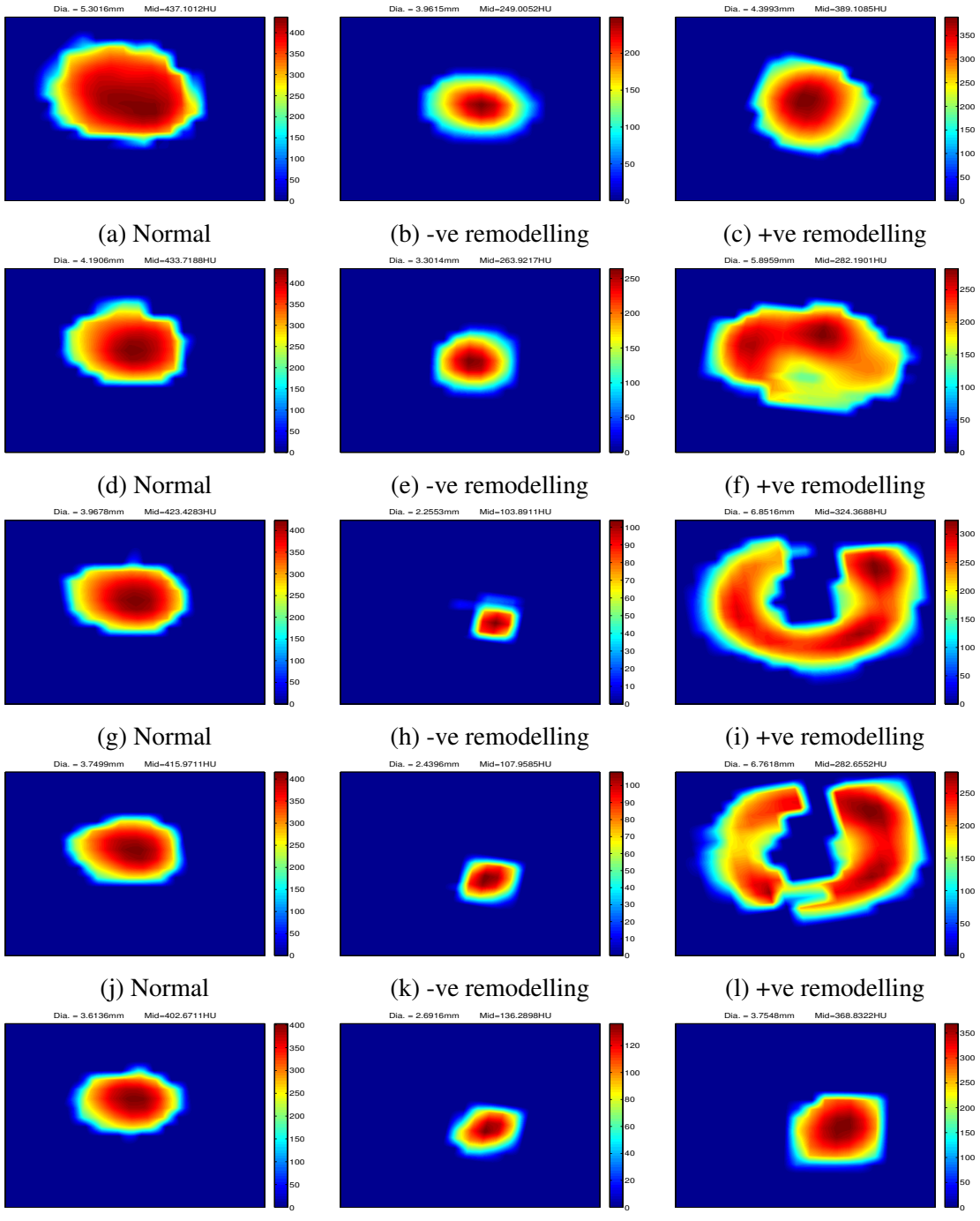

(a) Normal (b) -ve remodelling (c) +ve remodelling

(d) Normal (e) -ve remodelling (f) +ve remodelling

(g) Normal (h) -ve remodelling (i) +ve remodelling

(j) Normal (k) -ve remodelling (l) +ve remodelling

(m) Normal (n) -ve remodelling (o) +ve remodelling

Fig. 5.6 Radius computation using vessel cross sections. Left column represents consecutive cross sections from a normal coronary segment. Middle column shows consecutive cross-sections from a segment undergoing negative remodelling, whereas a segment showing positive remodelling of the vessel is shown using consecutive cross sections in right column. For abnormality detection, the approximate radius can be computed using circular approximation on respective cross-sections.

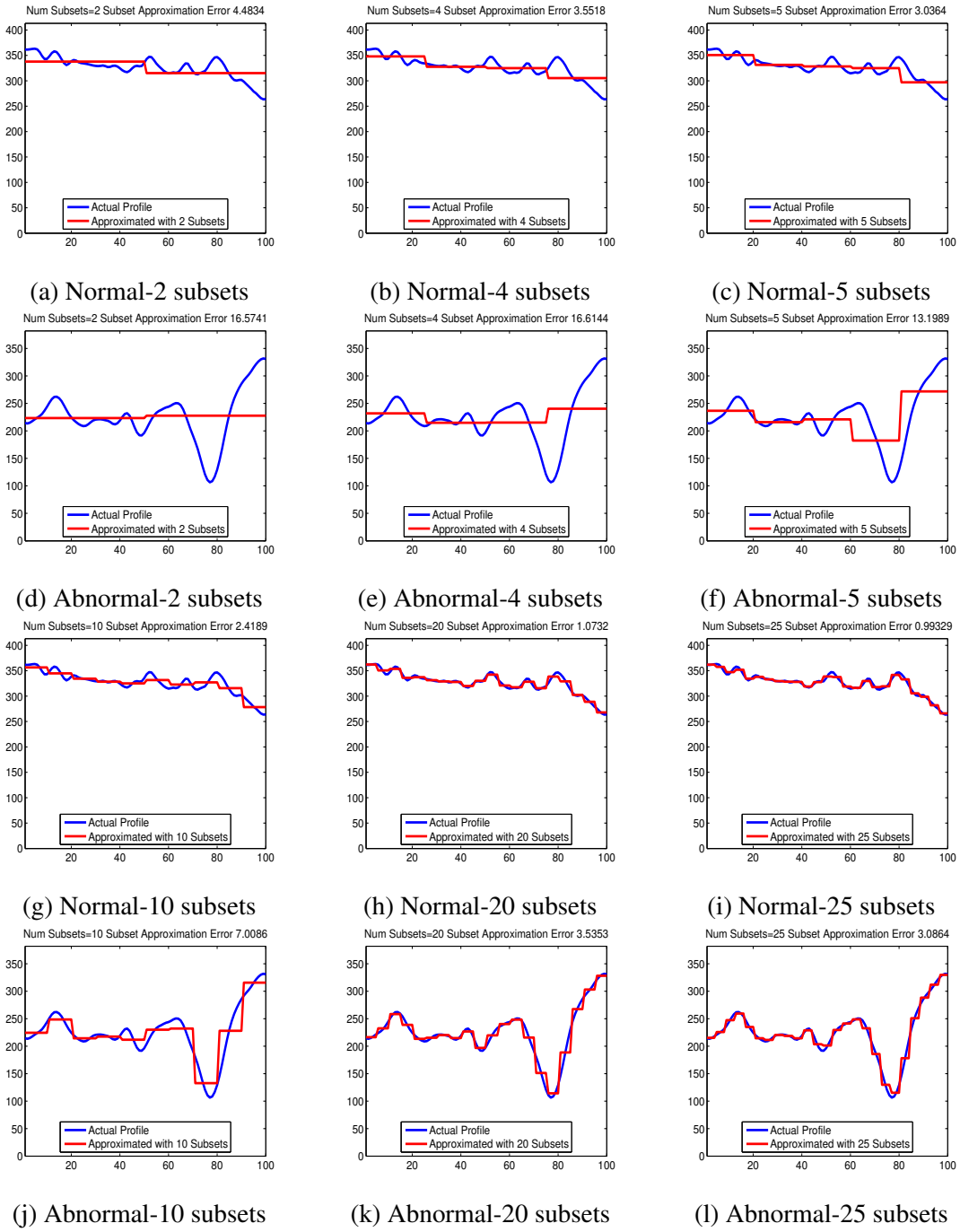

(a) Normal-2 subsets (b) Normal-4 subsets (c) Normal-5 subsets

(d) Abnormal-2 subsets (e) Abnormal-4 subsets (f) Abnormal-5 subsets

(g) Normal-10 subsets (h) Normal-20 subsets (i) Normal-25 subsets

(j) Abnormal-10 subsets (k) Abnormal-20 subsets (l) Abnormal-25 subsets

Fig. 5.7 Subset based signal representation to reduce the dimensions of the feature vector. It can be observed from a pair-wise comparison (row 1 versus row 2, row 3 versus row 4) that both normal and abnormal segments can be adequately represented using reduced subsets.

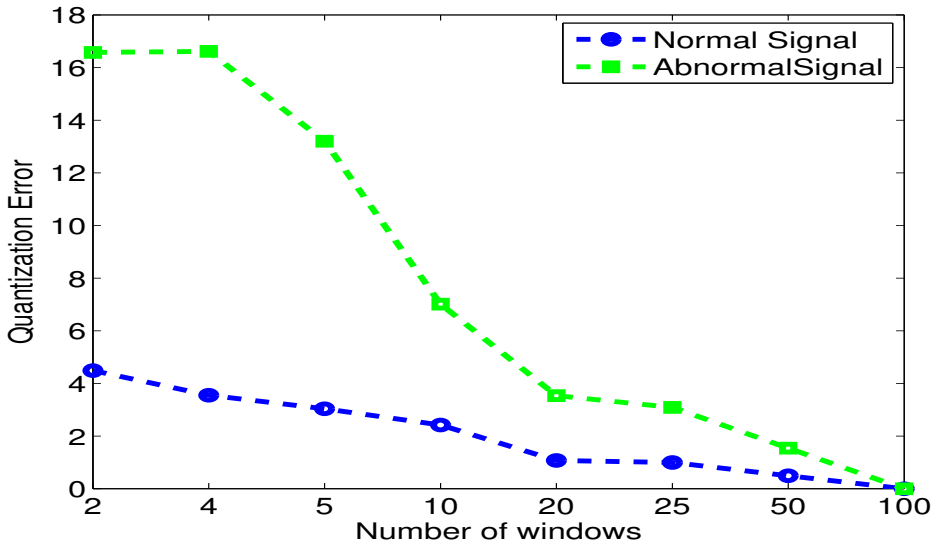

Fig. 5.8 Subset based signal representation to reduce the dimensions of the feature vector. It can be observed that both (normal and abnormal) segments can be adequately represented using 20 subsets.

identified the representative features of our data by analytical investigation before applying the SVM model to ensure the computational robustness. As the motive of this work is to detect plaque-based abnormalities along the length of the segment, we therefore, extracted the features by splitting the characteristic functions $\mu_s^{'}$ and $\sigma_s^{'}$ into m windows as expressed in Eq. 5.6.

$$f_{\mu}[m] = \sum_{n=1}^{5} \mu_s^{'}[n+5(m-1)], \forall m = 1,2,...,20,$$
$$f_{\sigma}[m] = \sum_{n=1}^{5} \sigma_s^{'}[n+5(m-1)], \forall m = 1,2,...,20. \tag{5.6}$$

The windowed, or sub-set based statistics, can effectively reveal the relative changes along the length of the segment; however, the selection of m is critical, as it serves as a trade-off between the the approximation error and the feature vector dimensions. To select the optimal number of windows, we investigated the relationship between m and segment approximation accuracy, as shown in Fig. 5.7. It can be observed that the quantization error is inversely proportional to the number of windows, i.e. an increase in m leads to improved

approximation of the segment profile s. Thus, to maintain a balance between the accuracy and the feature vector size, we defined the number of windows (m) equal to 20. The choice of 20 windows is reasonable, as both normal and abnormal segments show that the approximation error becomes steady at $m = 20$ as plotted in Fig. 5.8. Accordingly, Fig. 5.9 demonstrates the discriminative capability of the extracted windowed features (f_μ and f_σ) to distinguish the intensity patterns of two classes (see Fig. 5.9a - 5.9d).

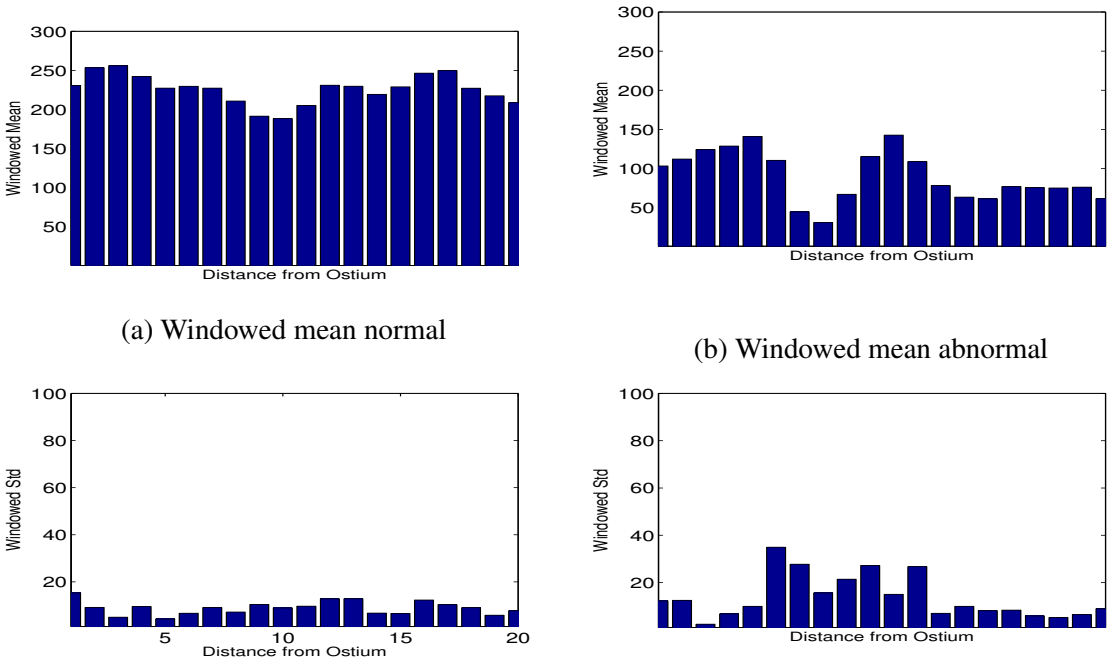

(a) Windowed mean normal

(b) Windowed mean abnormal

(c) Windowed deviation normal

(d) Windowed deviation abnormal

Fig. 5.9 Graphical representation for segment representative features. (a, c) define a normal segment having stable mean and standard deviation, whereas (b, d) represent a soft plaque effected segment.

Furthermore, two additional parameters, namely: mid-lumen intensity f_{mid} and mean radius f_{rad} are added to improve the performance of the SVM classifier. The mid-lumen intensity through the vessel is acquired by modelling the intensity response of the innermost concentric ring v_8 through the length of the vessel as expressed in Eq. 5.7, whereas the mean radius f_{rad} encoding the vessel remodelling impact is approximated in terms of m windows

using radial profile $S^{'}_{rad}$ as expressed in Eq. 5.8.

$$f_{mid}[m] = \frac{1}{5}\sum_{n=1}^{5} v_8[n+5(m-1)], \forall m = 1,2,...,20. \tag{5.7}$$

$$f_{rad}[m] = \frac{1}{5}\sum_{n=1}^{5} S^{'}_{rad}[n+5(m-1)], \forall m = 1,2,...,20. \tag{5.8}$$

Fig. 5.10a - 5.10d demonstrate the advantage of the additional features. Apparently f_{mid} replicates the distribution pattern of f_{μ}; however, it encodes the mid-lumen behaviour (i.e. the concentration of the contrast medium) from ostium to the end of the segment. It should be noted that a plaque present in the segment orifice (or even in the preceding segment) will result in low HU intensity through the mid-lumen; hence, the segment should be classified as abnormal but the stable mean and variance may lead to an erroneous classification in terms of the normal region. In this context, the feature f_{mid} ensures that the classifier takes into account not only the intensity variations but the mid-lumen response of the segment for effective classification.

In general, the radius obtained along the length of the segment conveys useful information to the classifier as illustrated in Fig. 5.10c - 5.10d. It can be observed from Fig. 5.10c that the segment radius decreases smoothly as a function of orifice distance for normal segments, whereas the plaque effected segments undergo unexpected variations in radii due to the positive or negative remodelling in the plaque affected area (see Fig. 5.10d). This is further illustrated in Fig 5.11, in which it can be observed that the vessel boundary (red contours) suffer through compressions at three distinct points along the length. These compressions represent stenosis of varying degree (mild, moderate, severe) at respective locations. Hence, the impact of the vessel stenosis can be clearly conveyed to the classifier using radius f_{rad} (i.e. inset blue plot shows unexpected sharp dips for the stenosis regions). The statistical results illustrate that integration of the mid-lumen intensity and the segment radial information improves the classifier accuracy by approximately 11% as demonstrated in results section. Next, we concatenate four feature sets f_{μ}, f_{σ}, f_{mid} and f_{rad} to obtain a feature based representation $\mathbf{X}_n$ for respective coronary segments with dimensions [1 x 80].

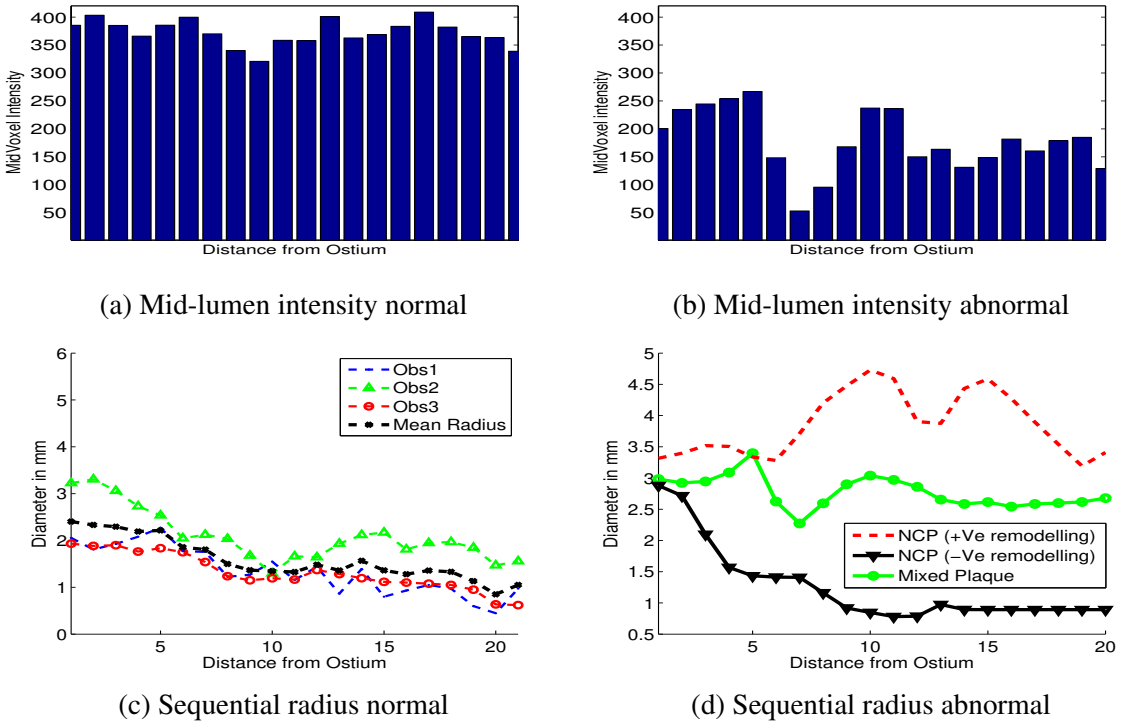

(a) Mid-lumen intensity normal

(b) Mid-lumen intensity abnormal

(c) Sequential radius normal

(d) Sequential radius abnormal

Fig. 5.10 Graphical representation for segment representative features. (a) defines mid-lumen intensity for a normal segment, whereas (b) shows the corresponding mid-lumen intensity in an abnormal segment. Moreover, (c) represents the vessel radius pattern for a normal segment, and (d) shows the radius obtained for three abnormal segments. It can be observed that normal segments is characterized with high mid-lumen intensity and smooth decreasing radius, whereas abnormal segment is related with low mid-lumen intensity and often suffers with unexpected radius variations (+ve, -ve and hybrid vessel remodelling).

5.4.2 SVM Classification Framework

For an SVM based classification, our data consists of N feature vectors of the form $\mathbf{X}_n$ and the associated binary labels Y_n, defining the class of the vector as either normal or diseased. The mathematical representation for classification data is as follows:

$$D = \left\{ (\mathbf{X}_n, Y_n) \,|\mathbf{X}_n \subseteq R^{dims}, Y_n \subseteq \{0,1\} \right\}_{n=1}^{N}. \tag{5.9}$$

where N is the number of samples for the classifier and $dims$ denotes the feature vector dimension i.e set equal to 80 in our work. The use of support vector machines in binary classification relies on quadratic optimization subject to linear constraints. The SVM model

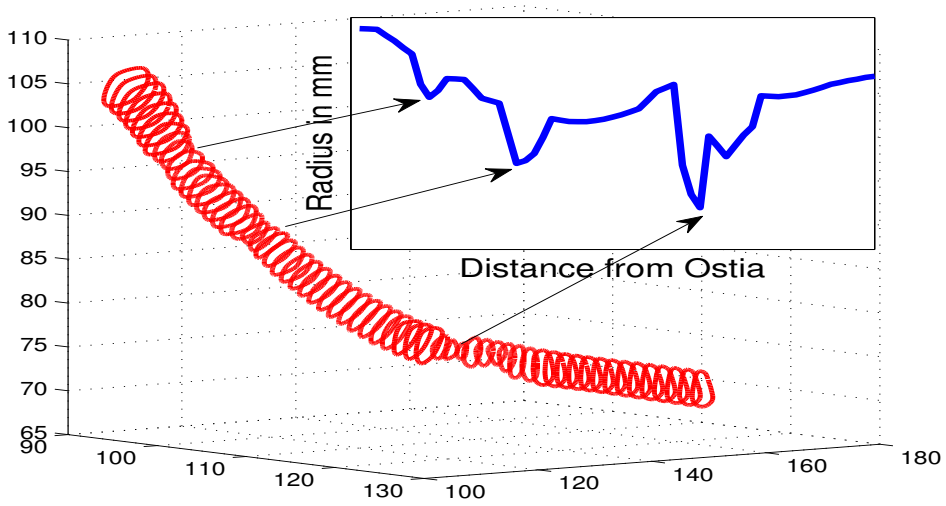

Fig. 5.11 Three-dimensional illustration of vessel stenosis. The coronary vessel is represented by boundary contours (red). The corresponding radius of each contour is displayed in the box as a solid blue line. Arrows point to three locations with stenosis of mild, moderate and severe degree respectively, as reflected in reduction of the radius.

finds an optimal hyperplane by minimizing the norm of weights for ideal segregation; however, a slack variable ε is often integrated to relax the constraints for a feasible solution as expressed in Eq. 5.10.

$$min\,|\mathbf{w}|^2 + P\sum_{n=1}^{N}\varepsilon_i, \tag{5.10}$$
$$subject\,to: Y_n\left(\mathbf{w}^T\mathbf{X_n} + b\right) \geq 1-\varepsilon_n,\ \varepsilon_n \geq 0,\ for\ n = 1,2,....N.$$

A penalty cost P regulates the influence of individual support vectors in the classification as high value of P leads to a hard margin, whereas a very small value allows for frequent violations of the constraints. After investigating values in the interval $\left[10^{-5}, 10^{5}\right]$, we defined $P = 10^0$ by adjusting the box-constraint parameter of the SVM classifier. Moreover, this work used a non-linear radial basis Gaussian kernel for mapping data into a higher space with sigma defined equal to *one*. Table 5.2 shows the detailed specification for SVM plaque detection model including features and the respective tuning parameters. Accordingly, the

SVM model classifies the test vector $\mathbf{X_n}$ into normal or diseased classes according to Eq. 5.11.

$$\hat{Y}(\mathbf{X}_n) = sgn\left(\mathbf{w}^T\mathbf{X}_n + b\right). \tag{5.11}$$

Table 5.2 SVM model for non-calcified plaque detection.

		Feature space & accuracy	
Parameter name	Parameter type	Intensity only	Intensity plus radius
Windowed mean	Discriminative feature	20	20
Windowed Deviation	Discriminative feature	20	20
Mid-lumen intensity	Discriminative feature	-	20
Windowed radius	Discriminative feature	-	20
SVM Kernel	Tuning parameter	RBF	RBF
Gaussian deviation [σ]	Tuning parameter	1	1
Penalty cost	Tuning parameter	10^0	10^0
Feature vector dimensions	N/A	[1x40]	**[1x80]**
Accuracy	N/A	77.8%	**88.4**%

5.5 Non-Calcified Plaque Localization in Abnormal Segments

Segments classified as "abnormal" are further investigated for precise position of the plaque in the vessel. The essence of the localization process is to identify unpredicted intensity dips in the mean radial profile of the coronary segment. For tracking valleys in the mean profile (S) of an abnormal segment, this work computed the intensity variation changes using a first order derivative. It should be noted from Fig. 5.12 that the relative slope (shown in blue) remains steady through the normal regions of the coronary segment, whereas the unexpected intensity value drop associated with soft plaques lead to a significant transition in the slope magnitude. In the subsequent step, we applied second order derivative analysis of Eq. 5.12 to identify the local extrema points. This computation is based on the idea that a valley region can be well characterized by pairs of adjacent maxima points as shown in Fig. 5.12.

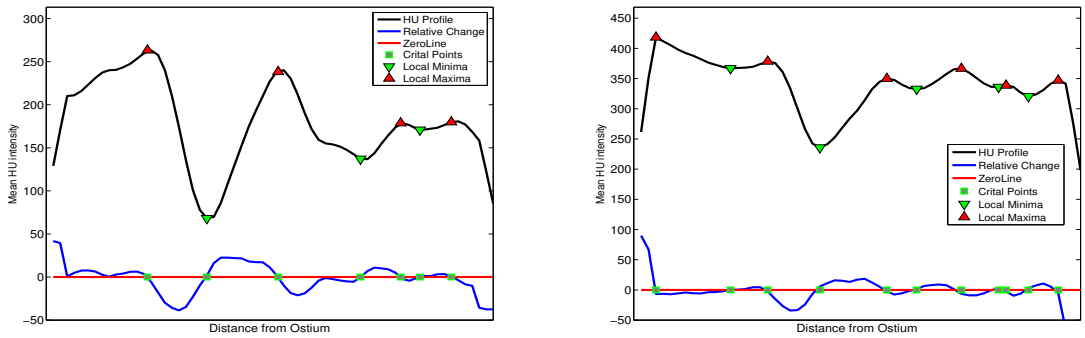

(a) DS04 seg2 (b) DS15 seg1

Fig. 5.12 Derivative based plaque localization in an abnormal segment. The black curve represents segment mean profile and the blue curve shows the relative change in mean profile. Moreover, red and green markers show the detected local extrema points.

After identifying the local extrema positions, we quantified the section-wise intensity drop by computing the sum of the relative slope between successive maxima points. This computation leads to the plaque affected section of the vessel, in terms of maximal depression. Consequently, two maxima, encompassing the maximal intensity drop are marked as the start and end positions of the lesion in the segment. To generalize the performance, an additional constraint was posed directly in terms of an intensity threshold of 50 HU to ensure that a low HU value inside the vessel was directly marked as plaque without requiring any additional evidence.

$$f^{''}(s) = \begin{cases} Minima\,at\ (s=p)\ \text{if}\ f^{'}(s)=0\,\&\,\frac{\partial^2 f}{\partial s^2} > 0, \\ Maxima\,at\ (s=p)\ \text{if}\ f^{'}(s)=0\,\&\,\frac{\partial^2 f}{\partial s^2} < 0. \end{cases} \tag{5.12}$$

5.6 Results

5.6.1 Plaque Detection Performance

Out of the available 32 CTA volumes, a total of 344 segments (200 normal, 144 abnormal) are extracted in the first stage for validation of the SVM classifier. As the focus of this work is non-calcified plaques, calcifications present in a neighbourhood are removed by assigning a mean value before extraction. In the subsequent stage, the mean discrete HU profiles

are generated for individual coronary segments. The performance of the SVM classifier is presented in Fig. 5.13 where Leave One Out (LOO) cross-validation shows promising results with a sensitivity of 93%. Furthermore, a positive predictive value (PPV) for the LOO validation is 86.4% and a negative predictive value (NPV) is 91.9% making the overall soft plaque detection accuracy equal to 88.4%.

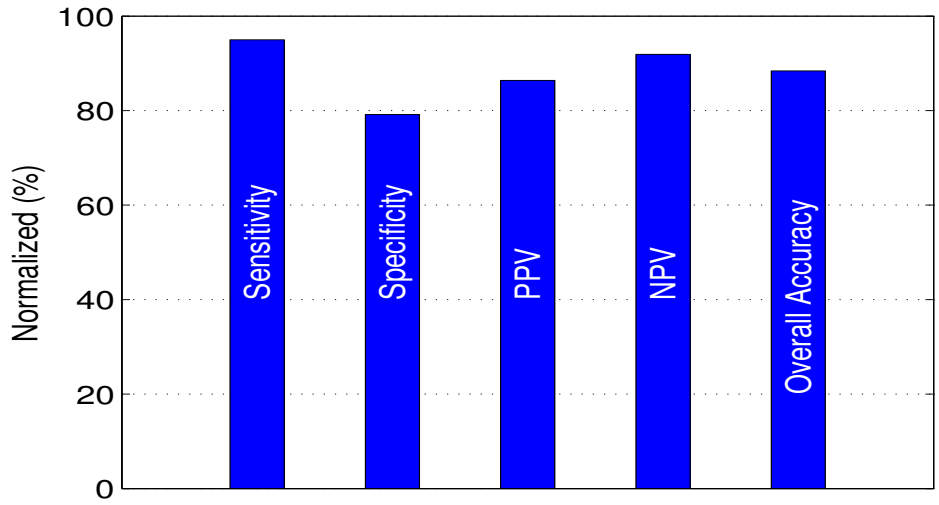

Fig. 5.13 Leave one out (LOO) validation for the SVM classifier. The overall accuracy (around 88.4%) shows the effectiveness of the plaque detection method.

Next, we used the trained SVM classifier to investigate the impact of feature vector dimensions on accuracy and the overall processing time. Accordingly, it has been observed that the windowed mean and deviation based 40 features lead to a classification accuracy of 77.8%, where the addition of mid-lumen f_{mid} and radius f_{rad} based features improved the classifier accuracy by approximately 11%. Moreover, the comparative analysis demonstrates that the further increase in the feature space dimensions shows only a marginal improvement in the classifier accuracy, while the computational time increases significantly. These results lead to the conclusion that the classifier performance becomes resistant to the feature vector dimensions at a certain point due to the redundancy of features.

In this context, we also experimented with the feature selection techniques to automatically select the optimal features in context of the plaque detection. However, based on the

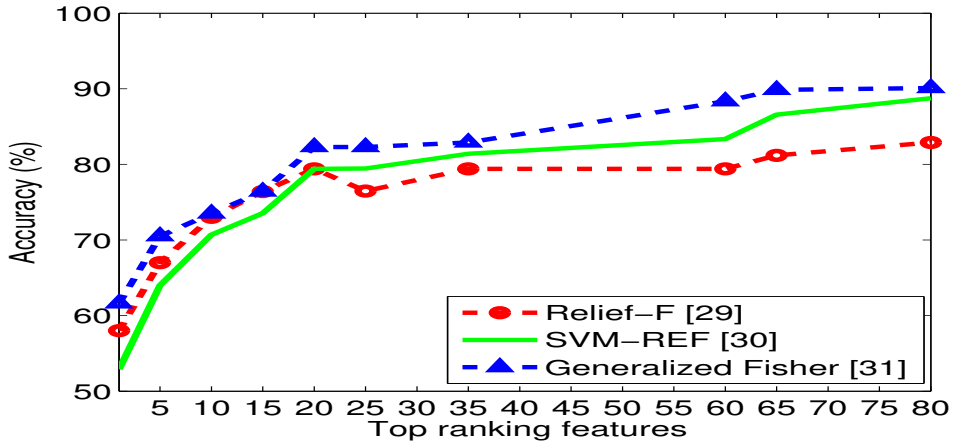

Fig. 5.14 Classification accuracy based on top ranking features for three different feature selection techniques. Fisher method [19] shows comparatively better accuracy due to correlated feature information.

fact that prior clinical knowledge has been employed to derive hand-crafted features in the context of non-calcified plaque detection, it is less likely that feature selection techniques will significantly reduce the dimensionality of the feature space. For the proof of concept, we compared three different feature selection techniques including Relief-F [150], recursive feature elimination [151] and Fisher [19] methods using a feature selection library [152]. To illustrate the efficiency of these methods this work performed the classification using top ranking features for three techniques as shown in Fig. 5.14. It can be observed that use of the top 5 features leads to a minimal accuracy for all three techniques, whereas an increased feature space lead to a continuous improvement in the accuracy of the classifier. This is due to the window-based nature of the features, as increased windowed statistics allows the classifier to make relatively improved decisions. From a comparative point of view, it can be observed from Fig. 5.14 that the Fisher method [19] achieves higher accuracy as it employs the correlation information to to rank the feature's discriminative power.

After computing the classifier performance on integrated dataset, we evaluated the efficiency of the classification model against three individual datasets to validate the reproducibility on generic CTA data. Accordingly, we extracted test segments individually from three datasets (66 from Rotterdam, 76 from St. Thomas and 36 from Semmelweis) and cross validation results are presented in Fig. 5.15. It can be observed that the individual classifica-

tion accuracy is consistent at around 85% across the data. Moreover, the classification results of Fig. 5.15 can be interpreted based on the fact that a “significant intensity dip" helps the classifier to achieve higher accuracy.

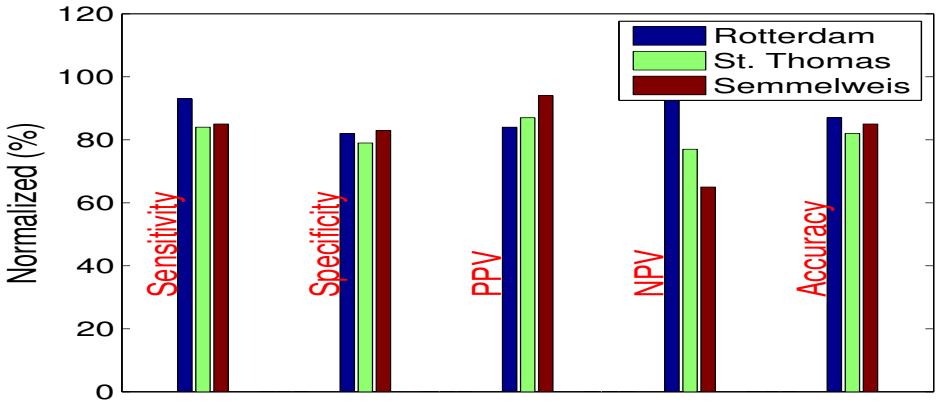

Fig. 5.15 Plaque detection results for three individual datasets using individual statistics and overall accuracy. It can be observed that SVM consistently achieves a plaque detection rate higher than 80%.

In this context, the high sensitivity of the Rotterdam data can be related to the presence of severe soft plaques in different coronary segments, whereas the lower accuracy for the Semmelweis CTA dataset reflects less test data and the absence of severe plaque instances. It should be noted that the detection of the immature (clinically graded as mild to moderate) soft plaque becomes extremely difficult due to uncertain intensity profiles.

After comparing individual results, this work also compared the outcome with plaque detection models of Wei *et al.* [112], Lankton *et al.* [99] and Tessmann *et al.* [113] to establish a correlation with the reported literature. It should be noted that the overall detection trend can be observed in Table 5.3 for different methods; however, a head to head comparison is not possible with [112] and [99] as the results are based on different quantitative metrics and datasets. For instance, the sensitivity reported by Lankton *et al.* [99] is achieved using volume based processing, whereas Wei *et al.* [112] used 2mm long plaque candidate regions. Moreover, the higher sensitivity reported in [113] is based on the fact a good detection rate for the calcified plaques improved the overall detection accuracy. It

is remarkable that specifically, in context of the explicit soft plaque detection, the reported accuracy for [113] is 79.62%.

Table 5.3 Plaque detection - Comparison with Literature.

NCP Detection	Four Different Methods			
	Proposed	Tessman	Lankton	Wei
Test Volumes	32	45	8	83
Classifier	SVM	AdaBoost	Energy Minimization	LDC
Target Plaques	Soft	Soft	Soft	Soft
FeaturesUsed	80	144	X	14
Dataset Used	UserDefined	UserDefined	UserDefined	UserDefined
Detection Target	Coronary Segments	Coronary Segments	Plaque Regions	Plaque Patches
Sensitivity	93	79.62	88	92

5.6.2 Plaque Localization Performance

SVM based identification of the abnormal segments is followed by the localization of the plaque inside the vessel segment. In this experiment, we used abnormal coronary segments of the Rotterdam CTA dataset only, as the manual ground truth for this dataset provides the start and end positions of the soft plaques along with the segment status. The plaque localization is illustrated in Fig. 5.16 where first and second order derivative analysis is used to highlight the intensity concavities. The proposed model achieved encouraging results as all substantial plaques are well localized; however, it slightly overestimates the plaque position due to numerical dependence on the second order extrema points as demonstrated in Fig. 5.16a - 5.16d.

The statistical accuracy for the plaque localization is evaluated by computing the Dice similarity index between the ground truth and the detected plaque locations. The total number of cross sections along the segment were represented using a binary vector where a *zero* denotes normal cross section and *one* reflects the abnormality. The ground truth vector is constructed using the start and end positions of the soft plaque from the manual ground truth annotations, whereas the obtained plaque vector is derived from our detected plaque positions. Fig. 5.17a demonstrates the efficacy of the plaque localization method with a mean Dice index of 83.2% with respect to the expert annotations. Moreover, Fig. 5.17b presents

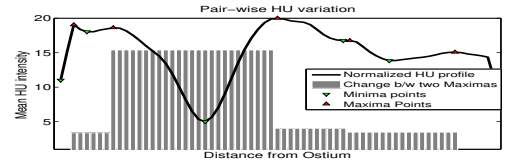

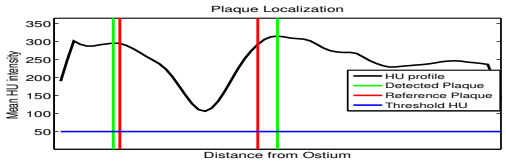

(a) DS04 seg1

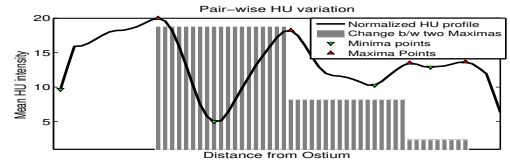

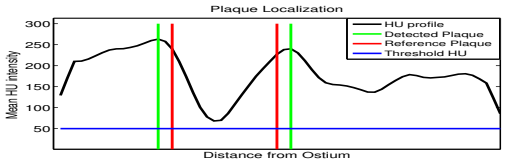

(b) DS04 seg2

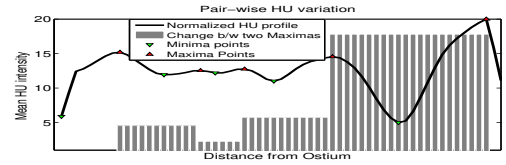

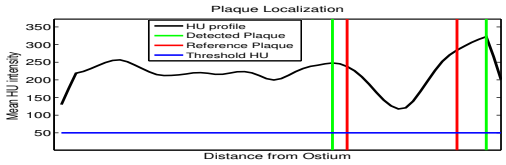

(c) DS05 seg2

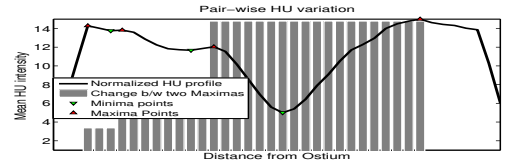

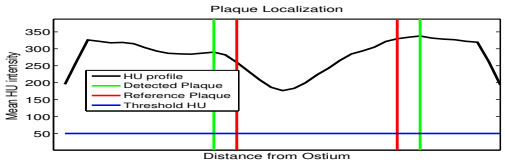

(d) DS15 seg2

Fig. 5.16 Plaque localization for four different abnormal segments of Rotterdam data. Green is the detected region and red is the manual expert based ground truth. It can be observed that the proposed method identifies the plaque region in the vessel with a slight over-estimation. For each figure (a-d), the first row shows the section-wise first order intensity change between consecutive maxima pairs, whereas the second row shows the detected plaque region.

the plaque length in millimeters where our obtained length is in correlation with the expert based length. However, a trend of slight over-estimation can be observed which is due to the numerical dependence on second derivative-based maxima points.

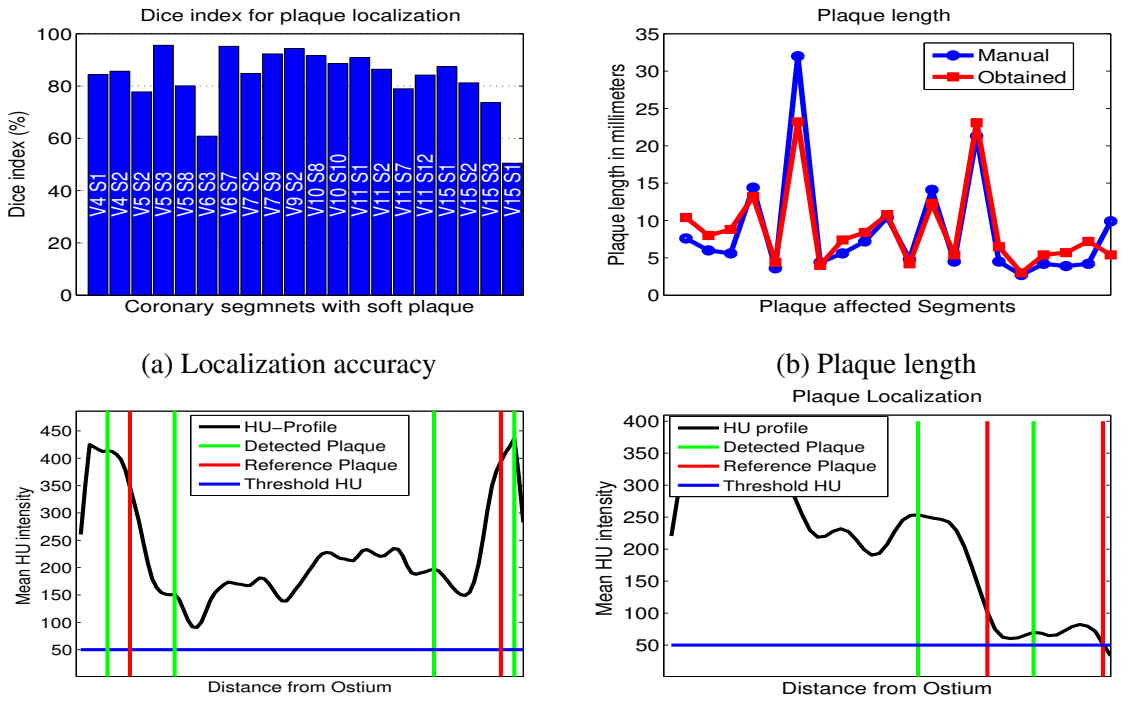

(a) Localization accuracy

(b) Plaque length

(c) DS06 seg3

(d) DS11 seg1

Fig. 5.17 Plaque localization performance. (a) shows the localization accuracy using Dice index (%) and (b) shows the plaque length with respect to the manual expert of Rotterdam. (c-d) shows particular cases where the proposed method fails in precise localization of plaque due to the relative decision made manually by human experts.

The shortcoming of the plaque localization method can also be observed in Fig. 5.17c - 5.17d as plaque length and Dice index both under perform for plaque effected segments of CTA volume 6 and 11. The mismatch for these two volumes occurred due to the unexpected length of the plaque (spanning over the complete segment) that leads clinician to make a relative decision. This is visually illustrated in Fig. 5.17c where the human observer selected the start and end positions of the plaque relative to the significant intensity drop and the complete intermediate region is marked as plaque, whereas the proposed model results in two individual plaque instances centred at the start and end of the actual plaque. Similarly, the larger plaques that span across multiple segments are identified individually as our model is operating on a per-segment basis.Extending the plaque detection and localization method to handle cases when the plaque spans the entire length of the segment is a subject of future work.

5.7 Summary

In this chapter, we formulated a simple yet efficient framework for detection and localization of the non-calcified coronary plaques. Based on abnormality detection, this model precisely located the position and approximate length of soft plaque which can be used in fully automated plaque quantification. The proposed model has been tested on three different datasets and has produced consistent results, demonstrating its reproducibility for generic CTA data. The overall accuracy of our plaque detection model is 88.4% against the manual observer ground truth with a sensitivity of 93% and specificity of 80%. Moreover, the Dice coefficient for plaque localization in diseased segments is 83.2% with respect to clinical annotations. This work compared the detection results with earlier studies and found a good agreement with the abnormality detection rate of Wei *et al.* [112], Lankton *et al.* [99] and Tessmann *et al.* [113]. It can be concluded that finding plaque affected segments is useful clinically, and could be used in a computer-aided detection system to alert a clinician to segments with suspected soft plaque.

The limitation of the plaque detection method is low detection rate for immature non-calcified plaques in the coronary tree. The immature non-calcified plaques does not exhibit the characteristic intensity deviations in the early stage, hence the segment profile based representation may overlook small intensity variations. However, all the developed substantial plaques are well detected by this method. Another possible limitation for the detection method is low performance for distal segments of the coronary tree. This is due to the fact that the vessel diameter becomes narrower in distal segments, consequently, the proposed concentric ring based representation of the segment may fail to model the true lumen. However, as mentioned in context of coronary tree segmentation, clinically significant lesions are usually identified in the main and proximal branches of the arteries, which can be well evaluated by the proposed detection model. Moreover, it should be noted that plaques present in the distal segments are less threatening as they lead to minimal muscular damage with no fatalities. Likewise, the limitations of localization method include an under-estimation of the long plaques in fully occluded segments. This limitation is based on the fact that the manual annotation of the plaque region is performed in a relative context of lumen and

the surrounding background. Especially, if there exist multiple low intensity lesions in a close proximity inside coronary segment, the human expert, in general demarcates the complete segment as plaque affected. In this context, the proposed method based on statistical evaluation of the segment leads to under-estimation with respect to manual ground truth.

Chapter 6

Segmentation and Quantification of Non-Calcified Plaques

6.1 Introduction

This chapter extends the plaque localization process for a more accurate estimation in terms of voxel-wise plaque segmentation. Based on the output of Chapter 5, where we identified the abnormal coronary segments along with the plaque terminal positions i.e. the start and end position of the non-calcified plaques, we derive voxel based features in this chapter for segmentation and quantification of the plaque. We start this chapter with a brief description of the coronary artery evaluation framework (a Matlab based framework designed in this work for visualization, analysis and expert based interactive demarcations) of the coronary vasculature. In the subsequent step, we describe the voxel-wise ground truth formulation for plaque, based on the boundary annotation of Rotterdam experts. This is followed by an inter-observer variability analysis, as three manual experts leads to a significant amount of agreement/dis-agreement for normal/abnormal segments of the coronary tree. The inter-observer variability is explained in this section as the segmentation results are compared with respect to three observers in the last section of this chapter. Next, we present an analysis of the vessel wall in context of the non-calcified plaques, as NCPs generally lead to compressed lumen and increased thickness of the vessel wall.

In the subsequent section, we explain the hand crafted voxel-wise features including 2-class posteriors, signed distance function, spatial neighbourhood information and bimodal histogram based customized fuzzy label. This is followed by support vector machine (SVM) based problem formulation of the voxel-wise classification, which is subsequently followed by experimental results. In the results section, we present the classifier performance using statistical metrics of Sensitivity, Specificity and Accuracy, as well as we present the plaque quantification results using Lumen and Plaque area metrics with respect to three manual observer. In addition, we used Bland-Altman plot to establish the correlation of obtained results with individual observer's approximations.

Our primary contribution in this chapter is an efficient methodology for precise quantification of the non-calcified plaques with a human-equivalent accuracy. To achieve this, we have an additional contribution, which is the design of an automated tool (Coronary Artery Evaluation Framework CAEF) for analysis and investigation of the segmented coronary tree. The CAEF framework allows the user to visualize the segmented coronary tree both in 2D and 3D space for a detailed investigation. Moreover, it allows user to construct customized visualization using maximum intensity projection, re-sampled oblique cross-section and multi-planar reformations for individual coronary segments. Moreover, the notable feature in CAEF is the provision of manual annotation, in which user can manually annotate the vessel components i.e. lumen and the plaque. It should be mentioned that CAEF can be used efficiently to construct expert based manual ground truth, which is often required in the quantification stage.

The second strength of this chapter is an efficient method for the vessel wall analysis in context of the non-calcified plaques in coronary tree. It is important to mention that the vessel-wall analysis alone can be used as a plaque-detection phenomena in the segmented coronary tree; however, we employed wall thickness in the plaque-quantification process in this research. The last contribution in this chapter is formulation of a SVM framework for voxel-wise plaque classification in segmented coronary tree. Experimental results demonstrate that the proposed method achieves a good agreement with human observers. It is important to mention that a number of studies [114, 153–162, 145] have been reported in context of

the non-calcified plaque quantification: however, the main focus in these studies was to demonstrate the capability of CTA imaging to capture the non-calcified plaque. Accordingly, non-calcified plaque lesions were manually selected in the first step, and plaque quantification results were compared with the outcome of ultrasound imaging to establish relation between two imaging modalities.

6.2 Ground Truth Construction

6.2.1 Interactive Framework

In context of qualitative and quantitative analysis of the coronary vasculature, we started with the "reference" ground truth formulation. Accordingly, we developed a Matlab based framework (Coronary Artery Evaluation Framework CAEF) for analysis, interpretation and manual annotation of the coronary vasculature. The designed framework allows user to visualize the segmented coronary tree both in 2D and 3D space as illustrated in Fig. 6.1. The extracted 3D surface is shown with planes overlaid at different locations along the length of coronary tree, whereas orthogonal (oblique cross sections), 2D curved planar and straightened curved planar images are obtained using the centreline of the coronary tree. Moreover, the CAEF framework allows the user to switch coronary segment according to AHA model [4] as well as user can perform manual adjustments in window and level setting for optimal visualization of grey scale images in a clinical context.

Fig. 6.2 illustrates the capability of the CAEF framework for differentiating calcified and non-calcified plaques in coronary vessels. The calcified deposition are easily discernible in the CTA due to high attenuation values, whereas the isolation of soft plaques is challenging due to ambiguous texture, however the CTA window setting can be customized to identify the soft plaques. This becomes evident in the figure as (left) displays a significant calcified plaque in the lumen and (right) shows a mixed plaque i.e. a non-calcified plaque in immediate vicinity of a calcification.

Fig. 6.3 demonstrates the user interaction in CAEF for manual annotation of the region of interest. Based on the optimal CTA display settings [23] and input from a qualified clinician,

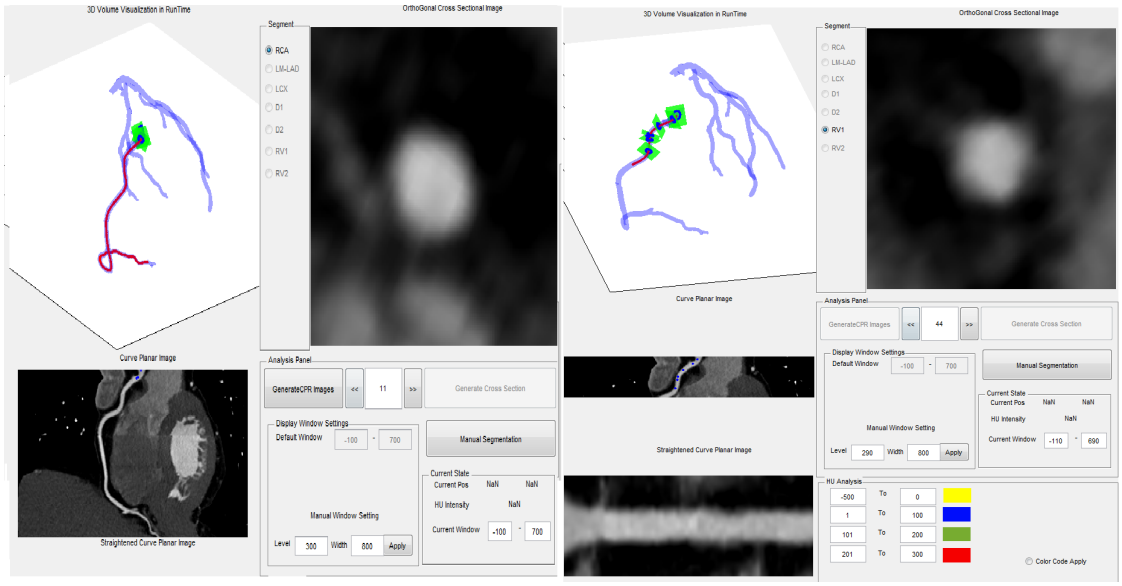

Fig. 6.1 Coronary visualization in CAEF. The basic visualization feature allows the coronary analysis using 3D surface, curved planar reconstructed images and cross sectional views.

CAEF can be used for manual demarcations of the coronary lumen, calcified and the non-calcified plaques. Accordingly, CAEF generates a spline interpolated based boundary using manually placed discrete points. Moreover, a pseudo-colour feature in Fig. 6.3 allows experts to isolate non-calcified plaques accurately using the customized intensity thresholds, since the visual evidence in the grey scale becomes ambiguous for non-calcified plaque effected regions. Accordingly, customized intensity thresholds can be used to effectively annotate the lumen and calcification present in the cross sections. The manual annotations (ground truth for region of interest) are stored in an internal database with appropriate component tag (lumen or plaque), and are used as the "reference" in the plaque quantification process. The use of an annotated boundary to segregate two components is illustrated in Fig. 6.4. It can be observed that user manually annotates the boundary for lumen (top row), and non-calcified plaque (middle row), and the CAEF combines the annotation to define the vessel.

In addition to visual analysis of segmented coronary tree and manual ground truth formation, the CAEF framework is capable of automatic quantification of the segmented tree with respect to the manual ground truth. Based on the dimensions of the manually defined ground truth (Rotterdam data provides 3D lumen boundary contours), subsequent processing

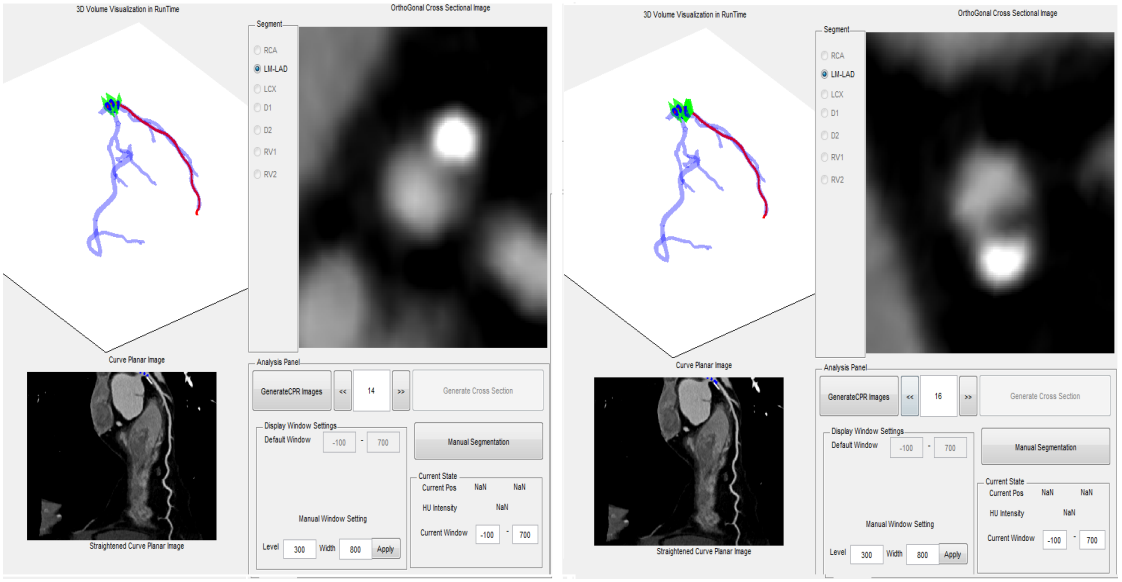

Fig. 6.2 Coronary plaque analysis in CAEF. Customized display settings (window/level preset) allows the visualization of calcified (bright) and non-calcified plaques (dull) appearance.

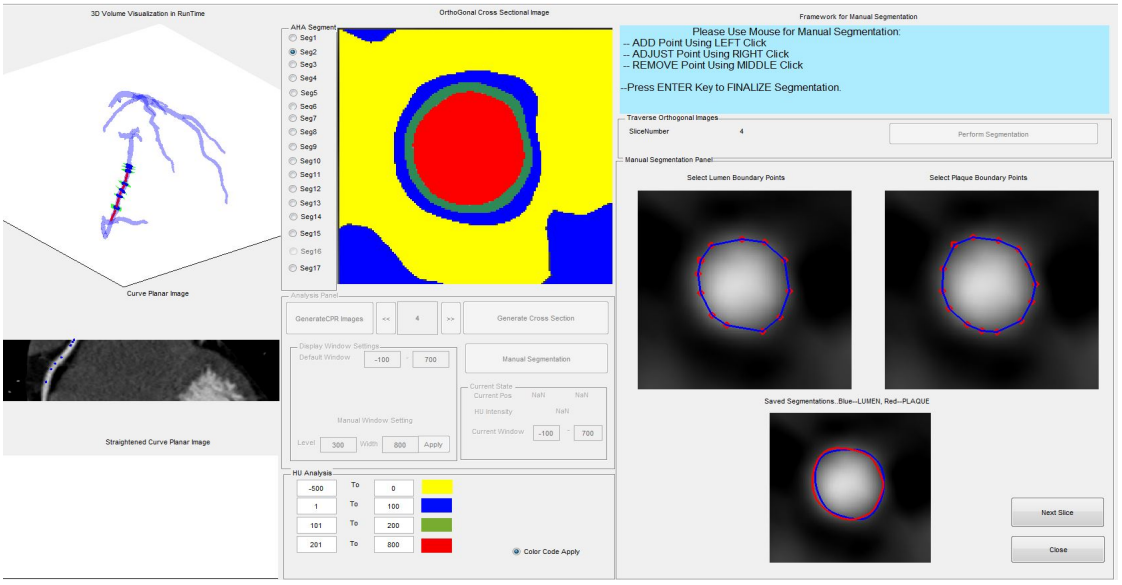

Fig. 6.3 Pseudo-color based coronary analysis and interactive lumen demarcation feature in CAEF.

is performed to quantify the automated segmentation against manual ground truth. In case of 3D space, the segmentation contours are projected first on a 2D plane and polygonal statistics are computed for individual plane across the length of segment. The similarity results are

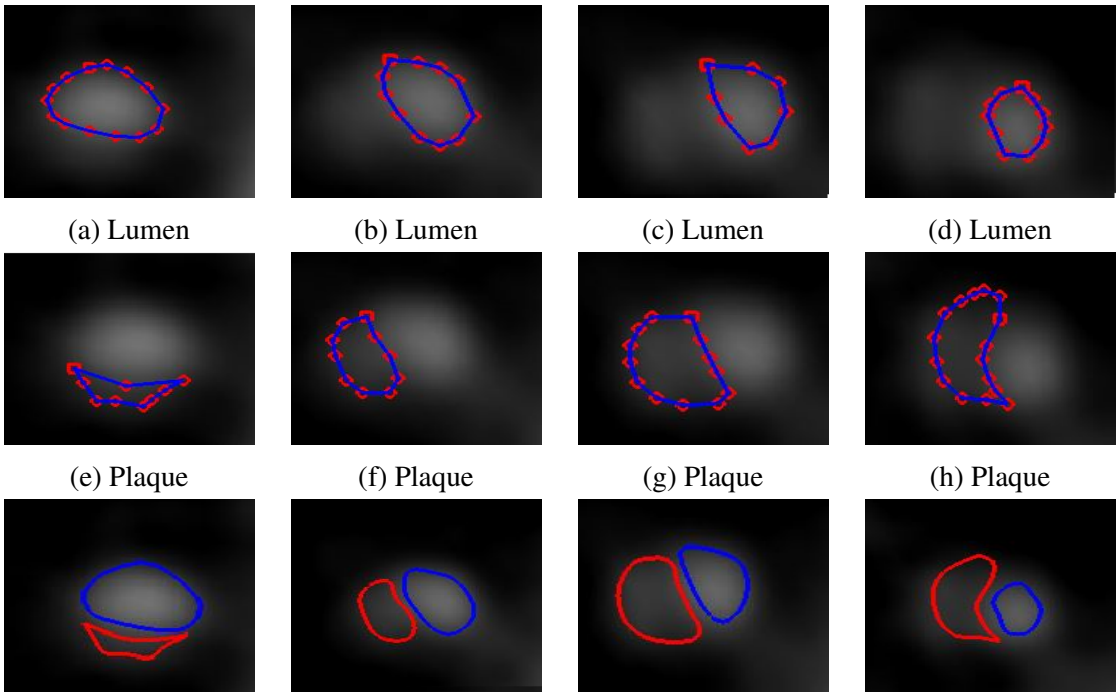

(a) Lumen (b) Lumen (c) Lumen (d) Lumen

(e) Plaque (f) Plaque (g) Plaque (h) Plaque

(i) Vessel (j) Vessel (k) Vessel (l) Vessel

Fig. 6.4 User based interactive annotation for lumen and plaque in sequential cross sections of the coronary vessel. The first row shows the user based boundary for lumen, the middle row shows the visually delineated plaque and the last row shows the overall vessel on respective cross section (combination of the lumen and plaque). Moreover, for first two rows the red points are control points for the spline, which is blue, whereas for the last row the blue curve defines the lumen boundary and red shows the delineated plaque in the last row.

presented using two similarity measures including *Dice* coefficient and the *Jaccard* similarity index on per-segment basis.

6.2.2 Rotterdam Data-based Annotations

Despite an interactive framework for the manual annotation of coronary vasculature, it becomes challenging to obtain the ground truth for a number of non-calcified plaque instances. This is based on the fact that the clinical experts have to spend a fair amount of time in the interactive investigation. Subsequently, we used the available lumen ground truth of the Rotterdam experts to derive the voxel-wise plaque ground truth indirectly as explained in this section. In the first step, we identified a number of soft plaque instances (segments) from the existing data for which the Rotterdam manual annotations are provided. It is

Table 6.1 Non-calcified plaque effected segments in the Rotterdam CTA data

Segment ID	Plaque Specifications			
	Segment Type	Plaque Type	Plaque Grading	Stenosis(%)
DS1 seg6	Proximal	Non-calcified	mild	20
DS2 seg6	Proximal	Non-calcified	mild	25
DS4 seg1	Proximal	Non-calcified	Severe	65
DS4 seg2	Proximal	Non-calcified	Moderate	51
DS5 seg2	Proximal	Non-calcified	Moderate	57
DS5 seg8	Distal	Non-calcified	Moderate	45
DS7 seg2	Proximal	Non-calcified	Severe	71
DS7 seg3	Proximal	Non-calcified	Moderate	41
DS9 seg2	Proximal	Non-calcified	Moderate	51
DS11 seg7	Proximal	Non-calcified	Mild	22
DS15 seg2	Proximal	Non-calcified	Moderate	53
DS15 seg3	Proximal	Non-calcified	Mild	22
DS15 seg14	Distal	Non-calcified	Moderate	45

important to mention that due to wide inter-patient variability, it is quite possible clinically that certain segments of the AHA-17 segment coronary model do not exist for a specific patient. Moreover, the manual demarcations of lumen boundary for all the existing segments are not required in general, as the distal segments are not associated with severe clinical threats. Hence, to maintain a balance between the manual annotation exercise and the clinical effectiveness of the study, the proximal segments of the coronary vasculature are generally investigated, as occlusion in proximal segments lead to fatal consequences in clinical practice. Accordingly, we identified the target segments from the Rotterdam CTA data i.e. the soft plaque effected segments having lumen boundary demarcations (in terms of 3D discreet contours) as defined in the Table 6.1.

The visual detection and manual demarcation of the non-calcified plaque is very challenging for human experts and often leads to significant inter-observer disagreement due to the ambiguous appearance of similar intensities in CTA volume. Consequently, the non-calcified plaque is generally estimated indirectly by exploiting relative deformations of lumen diameter in clinical practice. The lumen diameter variation is illustrated in Fig. 6.5a - 6.5b (top row) in which the lumen boundary undergoes significant diameter reductions during the length

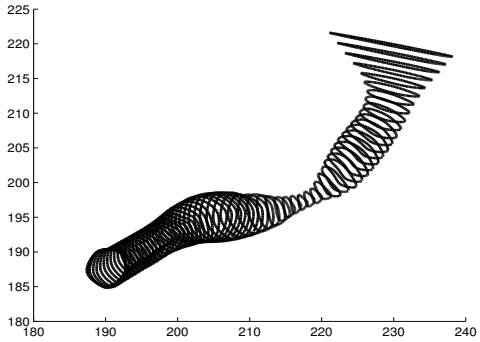

(a) DS4Seg1-lumen reduction

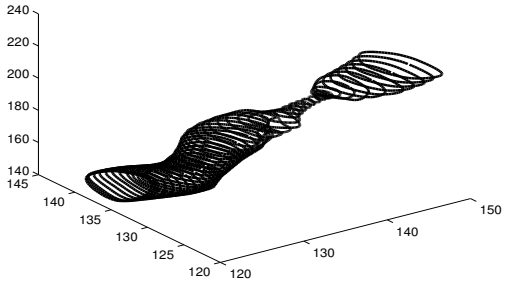

(b) DS7Seg2-lumen reduction

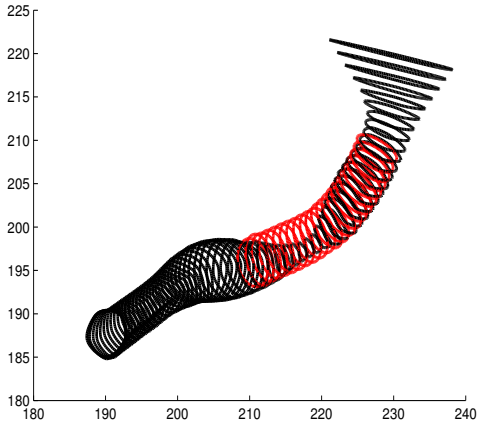

(c) DS4Seg1-ideal vessel

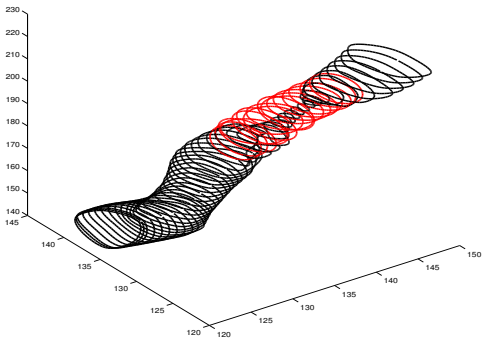

(d) DS7Seg2-ideal vessel

Fig. 6.5 Lumen boundary annotations for two non-calcified plaque effected coronary segments. Black contours represent manual annotations for lumen boundary in 3D space, (red) contours define "ideal" (plaque-free) vessel boundary for the plaque effected region of the coronary segment.

of the segment indicating non-calcified plaque instances at respective locations. Based on the fact that the plaque localization process of Chapter 5 leads to the precise position of the non-calcified plaque for respective coronary segments, we approximated the "ideal" vessel (red contours) for the plaque affected region using two "normal" cross sections (immediately before and after the plaque region) as shown in Fig. 6.5c -6.5d. In the subsequent step, the annotated lumen (black contour) is subtracted from the approximated ideal vessel (red contour) and the remaining voxels in the ideal region are identified/labelled as ground truth plaque voxels.

For mathematical representation (boundary based representation) of the coronary segment, we define a tubular model $T_{model}\left[CP, \theta'_{cs}\right]$, where CP denotes the centreline of the segment and θ'_{cs} defines the corresponding cross-section based information. Accordingly, the cross-section based information for complete segment is defined using an $[N_s]$ by $[m]$ array, where N_s represent the total number of points in the segment centreline and m denotes cross-section related parameters. For model based representation of vascular structures, a tubular model with circular cross-sections is frequently used [163–166, 9] in the literature. In the circular tube model, the cross sectional information θ'_{cs} for respective points of the centreline CP is presented using the centre and the diameter or radius information. However, vessels are elastic bodies which can accommodate local deformations of the lumen due to changes in the blood flow and intra-luminal pressure within the artery. Such deformations cannot be accurately represented using circular cross sections. Hence, we used an elliptical cross sectional tube model to approximate the vessel boundary which provides sufficient degrees of freedom to accommodate the potential deformations and facilitates accurate estimation of the vessel cross section.

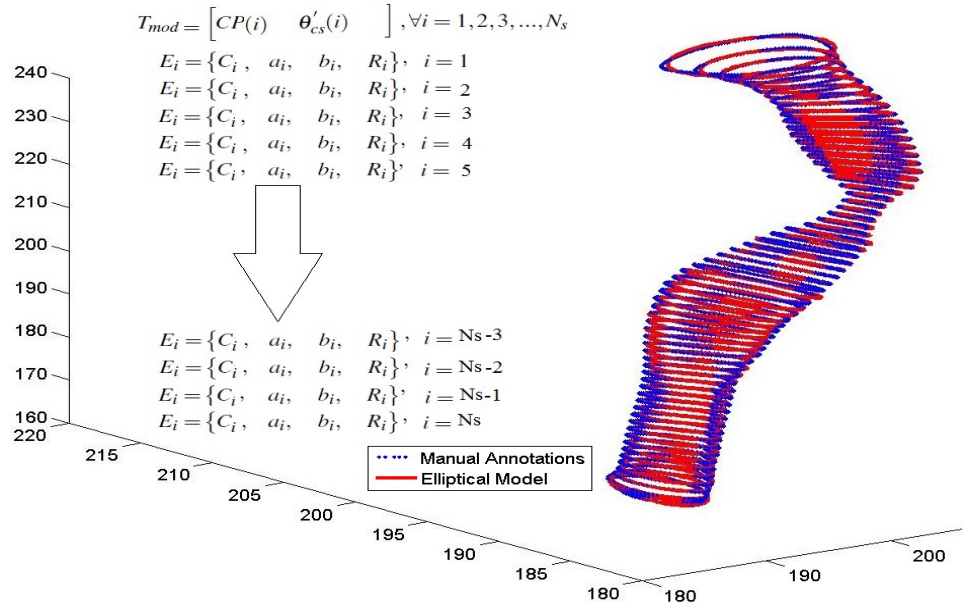

Fig. 6.6 Visual illustration for the tubular model of the coronary segment. The successive boundary contours along the length of the segment are defined using elliptical approximations.

The elliptical model based representation of the coronary segment is illustrated in Fig. 6.6. Accordingly, for the i^{th} point of the centreline CP, we define the parameter vector $\theta'_{cs}(i)$ using an ellipse model as $\left[\left\{a(i), b(i), C_{xyz}(i), R_{xyz}(i)\right\} \approx E_{xyz}(i)\right]$, where $a(i)$ and $b(i)$ represent the lengths of the major and minor axes of the current ellipse, $C_{xyz}(i)$ denotes the centre of the i^{th} ellipse of segment, and $R_{xyz}(i)$ defines orientation information for i^{th} ellipse in 3D space.

The mathematical formulation (parametric representation) for a 3-dimensional ellipse is expressed by Eq. 6.1, where E_{xyz} denotes circumference of the ellipse, C_{xyz} is the centre of the ellipse, a, b represent the lengths of the major and minor axes, respectively, R_{xyz} denotes the orientation information of the ellipse in 3D space and $t^{'}$ is the angular parameter varying between 0 to 2π. Moreover, the minimum distance of an arbitrary point, $P = [P_x, P_y, P_z]^T$ to the circumference of the ellipse can be found using Eq. 6.2.

$$E_{xyz} = \begin{bmatrix} Cx \\ Cy \\ Cz \end{bmatrix} + R_{xyz}. \begin{bmatrix} a.cos(t^{'}) \\ b.sin(t^{'}) \\ 0 \end{bmatrix}, \qquad where, R_{xyz} = R_1 R_2 R_3. \tag{6.1}$$

$$R1 = \begin{bmatrix} cos(\alpha) & sin(\alpha) & 0 \\ -sin(\alpha) & cos(\alpha) & 0 \\ 0 & 0 & 1 \end{bmatrix}, \qquad R2 = \begin{bmatrix} 1 & 0 & 0 \\ 0 & cos(\beta) & sin(\beta) \\ 0 & -sin(\beta) & cos(\beta) \end{bmatrix}, \qquad R3 = \begin{bmatrix} cos(\gamma) & sin(\gamma) & 0 \\ -sin(\gamma) & cos(\gamma) & 0 \\ 0 & 0 & 1 \end{bmatrix}.$$

$$distt = \min_{t} \mid P - E_{xyz} \mid^2 = \left| \begin{pmatrix} P_x \\ P_y \\ P_z \end{pmatrix} - \begin{pmatrix} C_x \\ C_y \\ C_z \end{pmatrix} - R_{xyz} \begin{pmatrix} acos(t^{'}) \\ bsin(t^{'}) \\ 0 \end{pmatrix} \right|^2. \tag{6.2}$$

For ellipse based modelling of the coronary segment, we approximated the manually annotated lumen boundaries using best fitting ellipses on respective cross sections of the coronary segment. Accordingly, the best fitting ellipse for lumen boundary contour on

respective cross section is obtained using non-linear least square fitting. Let

$$B_i = [(p_{1x}, p_{1y}, p_{1z}), (p_{2x}, p_{2y}, p_{2z}), (p_{3x}, p_{3y}, p_{3z}), ..., (p_{mx}, p_{my}, p_{mz})]^T,$$

be the manually annotated boundary points on i^{th} cross section (or can be obtained by slicing the vessel surface with the help of perpendicular plane at the i^{th} point of the centreline CP). Accordingly, the best fitting ellipse, for which the sum of the squares of the distances to the given points is minimum can be found by minimizing Eq. 6.3 as proposed in [6, 167].

$$\sum_{j=1}^{m} \left| \begin{pmatrix} p_{jx} \\ p_{jy} \\ p_{jz} \end{pmatrix} - \begin{pmatrix} C_x \\ C_y \\ C_z \end{pmatrix} - R_{xyz} \begin{pmatrix} acost_j \\ bsint_j \\ 0 \end{pmatrix} \right|^2 = min. \tag{6.3}$$

After obtaining the elliptical model $T_{model}\left[CP, \theta'_{cs}\right]$ of the coronary segment, we used two "normal" ellipses adjacent to the lesion region i.e (immediately before and after the plaque region) to derive the parameters for ideal ellipse (plaque-free vessel) through the plaque effected region as illustrated in Fig. 6.7. It should be noted that in order to model the ideal plaque-free vessel at i^{th} point of the centreline, we employed the ellipse orientation information from the current fitted ellipse i.e. $R_{xyz}(i)$, whereas the major-minor axis lengths for ideal ellipse are derived from two "normal" ellipses. This customized modelling for plaque-free ellipse ensures that the progression and local orientation of the vessel is retained at i^{th} point in 3D-space; however,the lumen diameter shrinkage associated with non-calcified plaque is reversed at current point.

Moreover, based on the fact that vessel tends to become narrower towards the distal segments, we computed the elliptical axes length for plaque effected region using Eq. 6.4. According to Eq. 6.4, the axes length for ideal vessel in the plaque effected region can be linearly interpolatedcomputed as a function of distance from start to end of the plaque region. Hence, the parametric variable f regulating the major-minor semi-axis length is computed as a ratio of distance from start of the plaque to the total length of the plaque region as

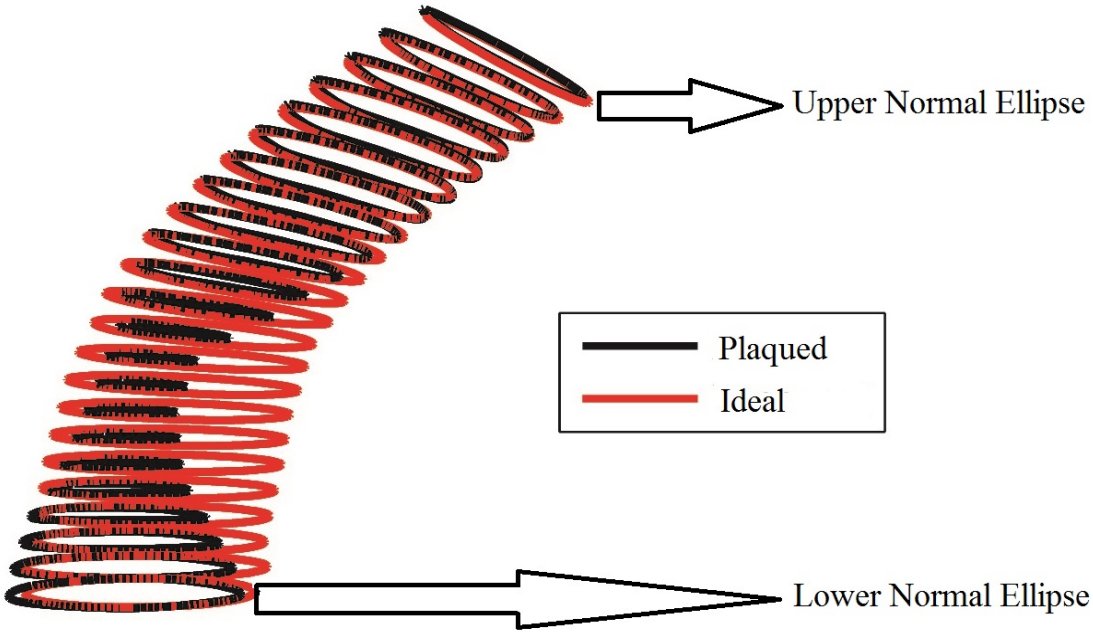

Fig. 6.7 Estimation of ideal vessel boundary for plaque effected region of coronary segment. Black contours represent manually annotated lumen boundary in the plaque effected region, red shows the estimated ideal (plaque-free) vessel boundary based on two normal (upper and lower) cross sections.

$f = \frac{d_i}{d_{total}}, \forall f \in [0,1].$

$$E_{xyz}(i) = \{a(i) \quad b(i), \quad C_{xyz}(i), \quad R_{xyz}(i)\}, \tag{6.4}$$

where

$$a_i = (1-f)a_s + fa_e,$$

$$b_i = (1-f)b_s + fb_e.$$

Here E_s and E_e represent two normal ellipses adjacent to the plaque region. Accordingly, $E_s = \{a_s \quad b_s, \quad C_{xyz}(s), \quad R_{xyz}(s)\}$ defines the upper normal ellipse i.e. immediately before the start of the non-calcified plaque and $E_e = \{a_e \quad b_e, \quad C_{xyz}(e), \quad R_{xyz}(e)\}$ represents the lower normal ellipse i.e. immediately after the end of the plaque region.

After deriving the ideal ellipses for the plaque effected region, we subtract the manually annotated lumen region, which results in "reference" ground truth plaque voxels. The process

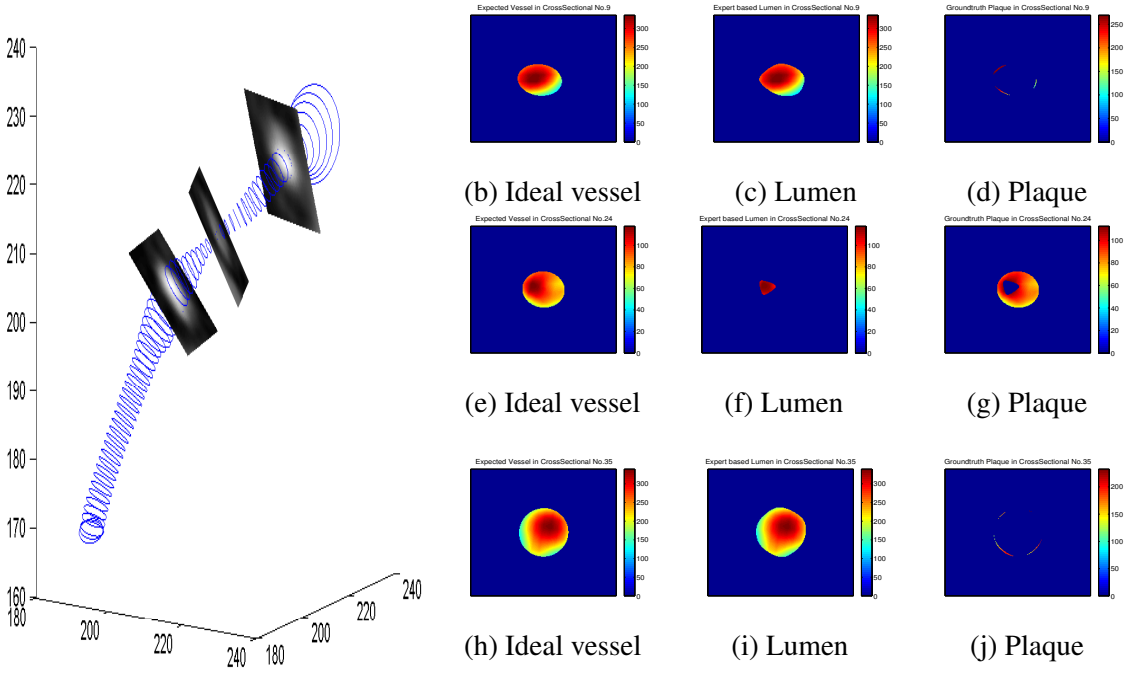

(b) Ideal vessel (c) Lumen (d) Plaque

(e) Ideal vessel (f) Lumen (g) Plaque

(h) Ideal vessel (i) Lumen (j) Plaque

(a) Lumen contours

Fig. 6.8 The ground truth estimation for plaque-effected cross-sections using lumen boundary annotations of manual expert. The top and bottom rows show two normal slices at the start and end of the plaque region, whereas the middle row represents a severely effected plaque cross section. The first column shows an ideal vessel, the middle column shows the manually annotated lumen and the right column shows derived plaque. The colorbar represent HU intensity for respective cross-section.

of obtaining plaque ground truth is further illustrated in Fig. 6.8 where lumen boundary contours are used effectively in plaque identification process. Fig. 6.8a shows expert based lumen boundary annotations for right coronary artery of CTA volume 4. It can be observed that due to the presence of a non-calcified plaque, the lumen shrinks in the proximal section and overcomes the diameter reduction after passing the plaque lesion. To estimate the "reference" plaque voxels for this segment, we started with the plaque localization methodology of Chapter 5 to identify the terminal positions of the lesion section. In the subsequent step, the ellipse representing two "normal" contours (immediate before and after the plaque) are used to compute the ideal vessel parameters for effected section. In the final

step, the annotated lumen is subtracted from the ideal vessel leading to isolated plaque voxels as illustrated in illustrated in Fig. 6.8b to 6.8j. The top and bottom row represents normal cross section, i.e. the normal plaque-free lumen is subtracted from the ideal vessel, whereas the middle row represents the case for a plaque effected lumen cross section. Moreover, the left column of the figure represents the ideal vessel at respective cross sections of the segment, the middle column shows the manually annotated lumen and the right column represents the remaining pixels to be interpreted as non-calcified plaque. It can be observed from the figure that lumen annotations are closely corroborating the expected vessel behaviour for two normal contours (top and bottom row), whereas the middle row the representing plaque effected contours appears significantly altered. Consequently, the right column demonstrates that a substantial plaque exists between the two normal cross-sections. To further validate this voxel detection method, we have added the colour bar in respective cross sectional images. It can be observed that for normal cross section (top, bottom) the colour bar assumes high intensity values reflecting the presence of contrast medium in the lumen, whereas the middle row shows significant low intensity reflecting the presence of low-density plaques. It is important to mention that the the 3D contours in this figure represent manual annotations of the Rotterdam framework experts; however, we can compute the soft plaque pixels for a generic vessel boundary by detecting surface intersection points on orthogonal planes (normal to the vessel centreline).

6.2.3 Inter-Observer Variability Statistics

The performance of our plaque segmentation algorithm is assessed by comparing our lumen-plaque results against the ground truth described in Section 6.2.2. To avoid biasing towards a specific human expert's opinion, the Rotterdam CTA data provides manual annotations from three independent experts for respective segments of the coronary tree. It should be noted that three observers are requested to perform lumen annotation using the same environment (i.e. identical orthogonal planes at a fixed distance along the segment) to ensure maximal correlation. Based on the fact that three different observers are performing the lumen annotation, a certain amount of variability is naturally expected. Accordingly, we performed

an inter-observer agreement analysis in this section to understand the inter-observer variability range for our plaque segmentation algorithm.

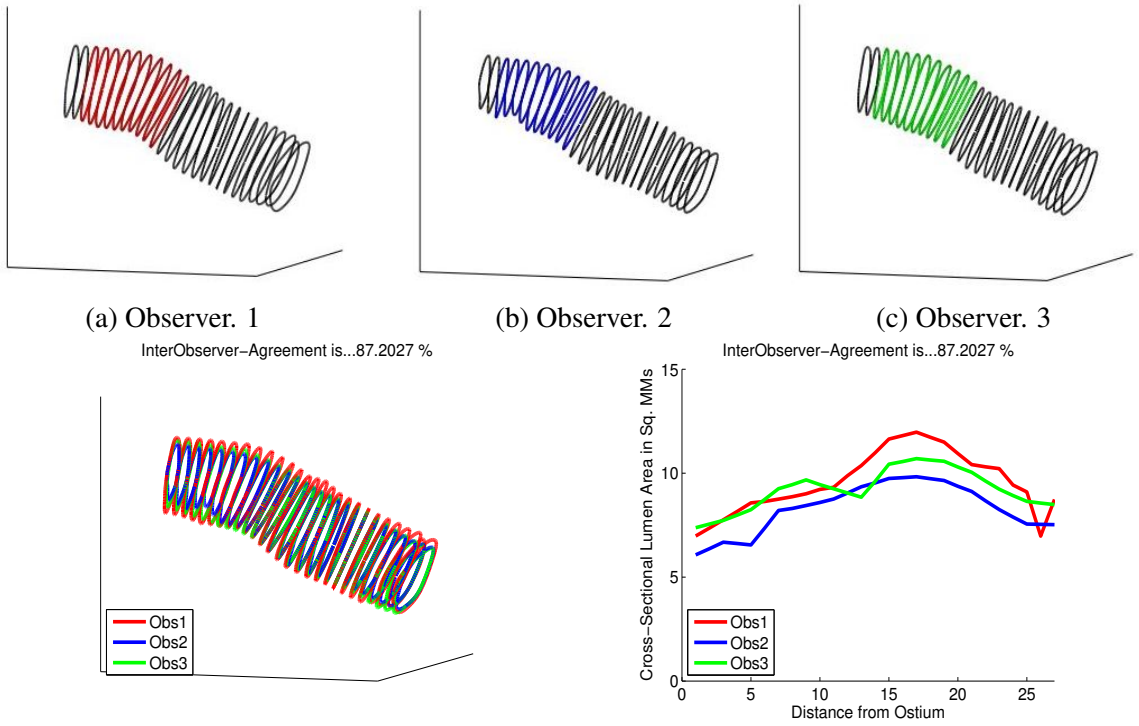

(a) Observer. 1 (b) Observer. 2 (c) Observer. 3

(d) Overlapped (e) Cross sectional lumen area

Fig. 6.9 The mutual agreement of three manual experts for a mild plaqued coronary segment. (a-c) reflects the lumen contours i.e. manual annotations by three experts in black colour, with plaque affected region shown in red, blue and green respectively (d) shows an overlap graph for relative visual comparison, whereas the cross sectional area for three experts is plotted in (e). A good correlation in the lumen area reflects a good agreement in vessel boundary annotations.

A detailed investigation of the manual annotation reveals that the mutual agreement among three observers is strongly dependent upon the segment location (proximal versus distal) and type of plaque (mild versus severe) present. In general, the proximal segments close to the aorta have large diameter as well as greater concentration of the contrast medium filled blood, whereas vessel diameter and contrast medium concentration decreases in the distal segments as a function of distance. Consequently, the proximal segments appear brighter, allowing the human observer to place sharp annotations of the lumen boundary, whereas an ambiguous appearance of the distal segments poses difficulty in true demarcation

of the lumen. Likewise the extent of the plaque also plays an important role in the visual demarcations, as a severe plaque demands a very careful annotation of the lumen boundary, whereas a mild plaque rarely causes a significant compression of the lumen. This segment based mutual agreement problem is visually illustrated in Fig. 6.9 (segment having a mild plaque) and 6.10 (segment having a severe plaque).

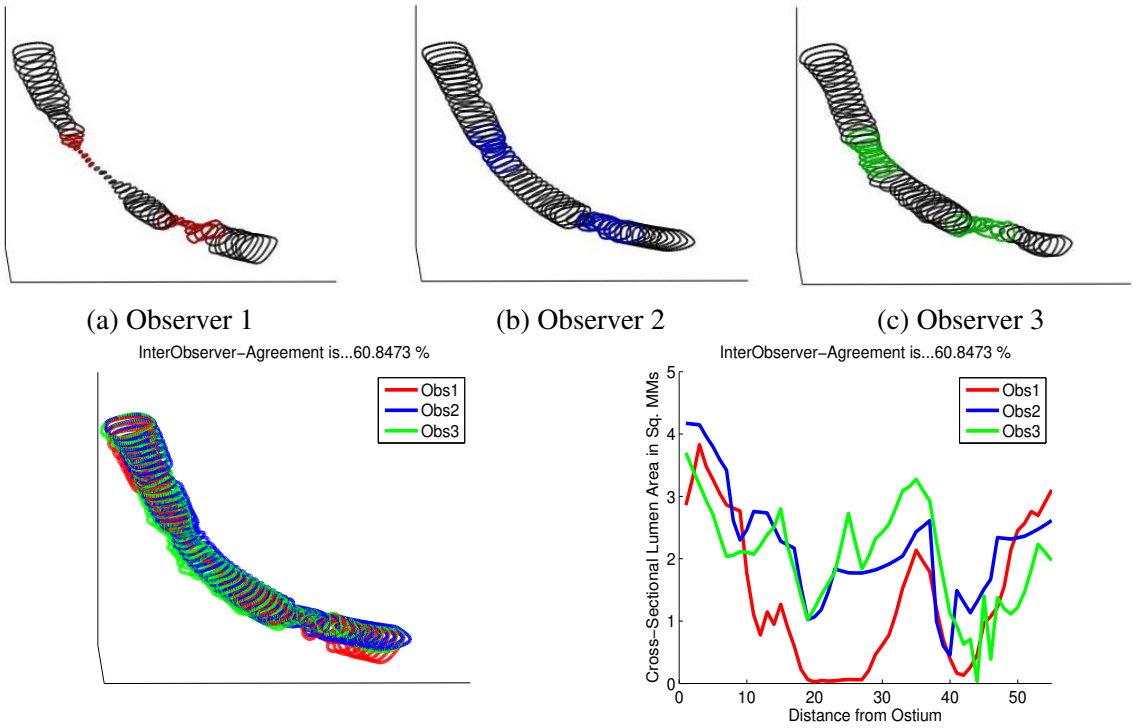

(a) Observer 1 (b) Observer 2 (c) Observer 3

(d) Overlapped (e) Cross sectional lumen area

Fig. 6.10 The mutual agreement of three manual experts for a severe plaqued coronary segment. (a-c) reflects the lumen contours i.e. manual annotations by three experts in black colour, with plaque affected region shown in red, blue and green respectively (d) shows an overlap graph for relative comparison, whereas the cross sectional area for three experts is plotted in (e). A high variability in the lumen area reflects a reduced agreement in vessel boundary annotations.

Fig. 6.9 represents the lumen demarcations for proximal segment (segment 6, CTA volume1, Rotterdam Data). The top row shows lumen boundary contours in black colour for three human experts, with colours (red, blue, green) representing the lesion region i.e. section effected with mild non-calcified plaque. It can be visually noted that three observers follow similar trend and there are no unexpected or sharp deviations in the lumen boundary through

out the segment. Moreover, the mild nature of the non-calcified plaque does not affect the mutual agreement in the lesion region and the exert based contours (red, blue and green) shows a reasonable correlation. This correlation of three observers is further investigated by overlaying three observations (see Fig. 6.9d) and cross-sectional area analysis (see Fig. 6.9e). It can be observed from Fig. 6.9e that the cross sectional lumen area remains static and close to each other for three observers through out the length of segment.

Likewise Fig. 6.10 represents the luminal demarcations for a distal segment (segment 3, CTA volume7, Rotterdam Dataset). Accordingly, the top row shows a significant variability in the lumen demarcations of three observers for a severely plaqued segment. Observer 1, annotates the affected lumen to a very narrow passage due to the potential plaque, whereas observer 2 and observer 3 have shown a reasonable lumen through the plaques effected section. This dis-agreement also becomes apparent in the cross-section based area plot (see Fig. 6.10e) in which observer 1 based lumen area touches almost zero-line for the plaque effected sections.

For a statistical comparison, we computed the Jaccard overlap percentage and area-wise mutual agreement of three manual observers as presented in Table 6.2. It can be noted from the table that proximal segment affected with mild non-calcified plaque, achieves higher mutual agreement in terms of both Jaccard overlap and the area-based correlation. In contrast, the distal segment affected with severe non-calcified plaque shows decreased Jaccard overlap as well as reduced area-correlation among independent observers. This inter-observer variability allows a certain degree of freedom for our plaque segmentation algorithm. This is based on the fact that, in principle, it is expected that the algorithm segmentation accuracy should fall within the range of three manual experts.

Table 6.2 Jaccard overlap and area based agreement for two segments

Expert pair	Overlap based agreement %		Area based agreement%	
	Mild	Severe	Mild	Severe
Obs (1 vs 2)	70.29	40.41	91.41	62.05
Obs (1 vs 3)	76.74	43.92	90.04	31.42
Obs (2 vs 3)	84.92	53.29	92.94	51.77

6.3 Vessel Wall Analysis for Healthy Vessels

The non-calcified plaque segmentation algorithm is based on the assumption that the input data (vessel) comprises of two components (i.e. blood lumen and the non-calcified plaque); however, the initial segmented tree violates this basic assumption. This is due to the fact that the vessel segmentation algorithm based on the hybrid energy model includes the vessel wall, i.e. the interface of the lumen with the background in the CTA. Hence, the vessel wall must be identified and removed in a pre-processing step before applying the non-calcified plaque segmentation algorithm. Accordingly, we started with the segmented coronary tree and computed the vessel wall thickness for normal segments using ray-projection technique in the respective CTA. In the subsequent step, the vessel wall (outer interface of the lumen with the CTA background) is removed from the segmented tree to investigate lumen and non-calcified plaques.

The wall thickness computation process starts with the cylindrical model of Section 5.2, in which the a coronary segment is approximated using 6 millimeters based cylindrical model (see Fig. 5.2 for cylindrical approximation of segment 2, 7 and 8). Based on the fact that 6-mm represents the maximum possible expansion (diameter) of coronary vessel, the background data is often included in the circular approximation. This phenomena is illustrated in the first column of Fig. 6.11 where the 6mm circle shows a dark black appearance around the circumference. This is followed by a homogeneous intensity distribution in a circular pattern around the centre of the circle, and then the lumen intensity remains stable and significantly higher in the middle passage. Accordingly, we used a three class Gaussian Mixture Model (GMM), followed with the Bayesian posterior's computation to classify the tubular segment voxels into three classes as illustrated in Fig. 6.11. It can be observed from the second column of the figure that background is generally well identified by "class-1" as first peak of the histogram corresponds to the low intensity regions that appears dark-black in the 6 mm circle of first column. Likewise, "class-2" defining vessel wall is represented in the middle column where a ring pattern circumscribing the lumen can be clearly visualized. Class-3 representing lumen is visually shown in column 4 of the figure where a stable pattern can be observed for normal cross sections along the length of the segment.

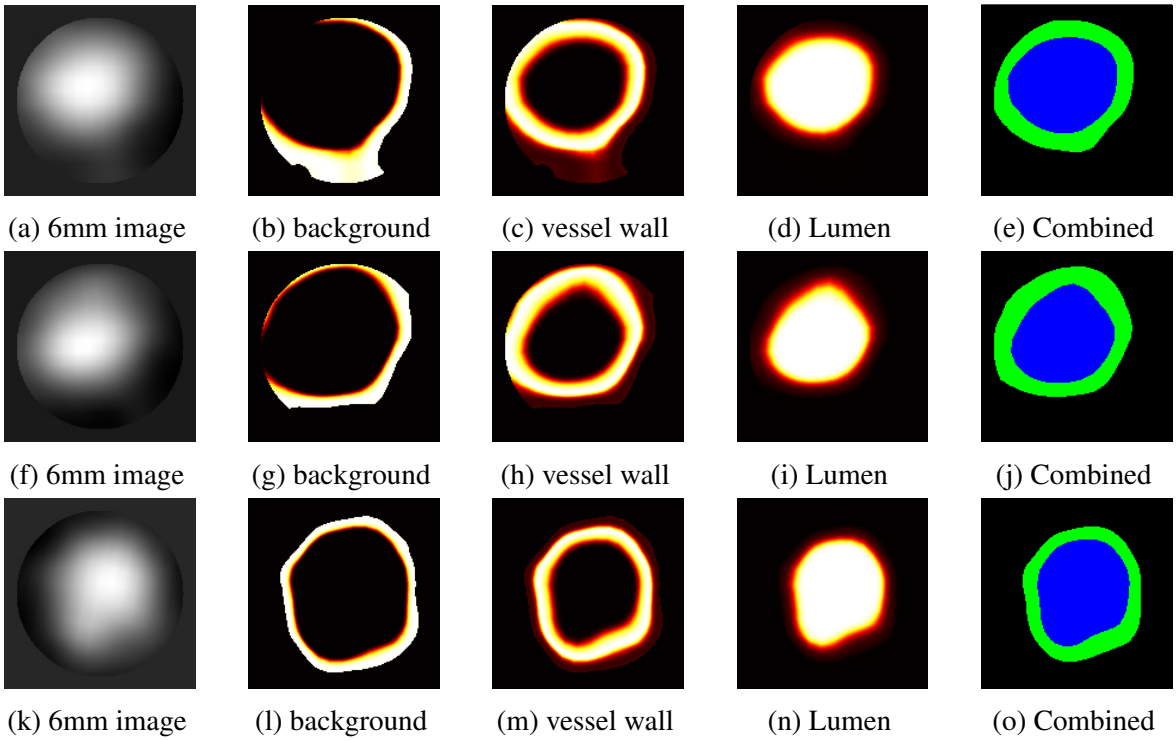

(a) 6mm image (b) background (c) vessel wall (d) Lumen (e) Combined

(f) 6mm image (g) background (h) vessel wall (i) Lumen (j) Combined

(k) 6mm image (l) background (m) vessel wall (n) Lumen (o) Combined

Fig. 6.11 Vessel wall analysis based on 3-class approximation of 6mm cylindrical model of DS4 seg1. The first column shows a 6mm region on the cross-sectional plane, the second column represents the background of vessel that comes inside 6mm, the next two columns shows the vessel wall and lumen respectively. These cross sections represent the normal section of the segment.

Interestingly, in case of an abnormal (plaque effected cross-section), the 3-class approximation reflects the abnormality in terms of deviation from the normal patterns of vessel wall and lumen. The non-calcified plaque in general assumes intensity value comparatively lower than the blood lumen and close to the myocardial tissues. Hence, our 3-class approximation assigns the existing non-calcified plaque voxels to "class-2" i.e. the vessel wall. Consequently, the vessel wall shows an unexpected increase in thickness for non-calcified plaque-effected sections with a significant reduction in lumen as illustrated in Fig. 6.12.

After identifying the vessel wall, we employed a ray-projection technique to compute the vessel wall thickness for the arterial cross section as illustrated in Fig. 6.13a - 6.13c. It should be noted that GMM based vessel wall leads to circular pattern of voxels around the lumen; however, the thickness varies around the circumference. Accordingly, the ray-projection method leads to a mean thickness value for the vessel wall. Based on the centre of the

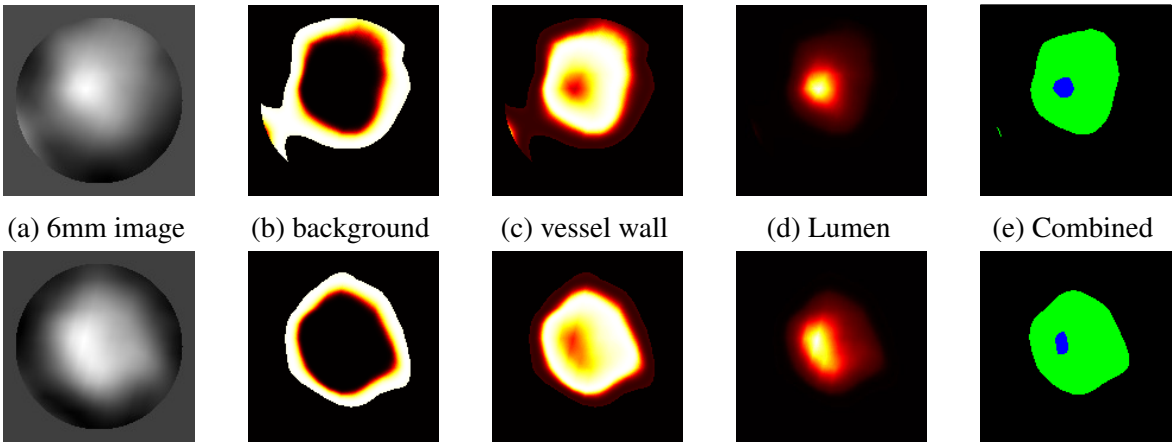

(a) 6mm image (b) background (c) vessel wall (d) Lumen (e) Combined

(f) 6mm image (g) background (h) vessel wall (i) Lumen (j) Combined

Fig. 6.12 Vessel wall analysis based on 3-class approximation of 6mm cylindrical model of DS4 seg1. The first column shows a 6mm region on the cross-sectional plane, the second column represents the background of vessel that comes inside 6mm, the next two columns show the vessel wall and lumen respectively. These cross sections represent the plaque affected section of the segment.

lumen, we projected 36 rays outward with an angular interval of 10 degrees and compute the ray-wise thickness of the vessel wall, which is averaged to define the wall thickness for respective cross section. The visual observation of Fig. 6.12 is statistically validated in Fig. 6.13c, i.e. the abnormal vessel wall leads to significantly high value for wall thickness. This phenomena is further illustrated using wall thickness plots for two plaque effected segments as shown in Fig. 6.13d and 6.14d. It can be observed that the lumen (black) remains stable as we move away from the orifice, with a stable wall thickness (red) along the length of the segment. However, the plaque effected region shows an unexpected reduction in lumen coupled with an unexpected increase in the wall thickness.

6.4 Features for Pixel-Based Segmentation

As the mean value for vessel wall thickness has been computed for the respective CTA volumes, the first step is to eliminate the vessel wall of the segmented coronary tree. This wall removal has been achieved by subtracting the wall voxels (average thickness equal to 0.65mm). After removing the vessel wall from the segmented tree, it is expected that the

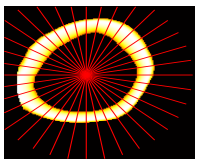

(a) Normal

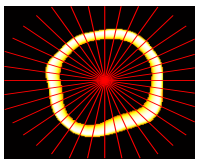

(b) Normal

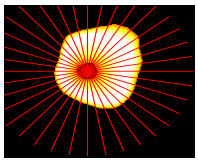

(c) Abnormal

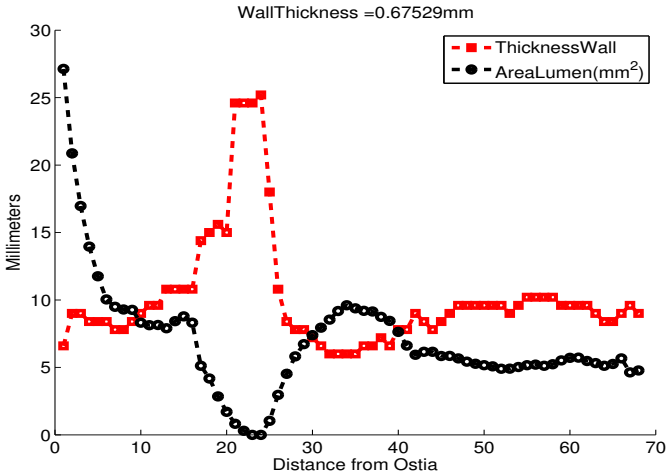

(d) Lumen area versus wall thickness plot

Fig. 6.13 Computation of the Vessel Wall thickness for coronary segment DS4 seg1. (a-c) shows the ray-projection to compute the mean thickness of the vessel wall, (d) represents the graphical comparison between lumen area and the normalized vessel wall thickness to reflect the anomalous lesion area. Cross sectional representing normal segment (a and c) leads to stable vessel wall, whereas abnormal cross section leads to expansion of the vessel wall based on low density soft plaques.

leftover is true lumen and non-calcified plaque (if any). Accordingly, we extract hand crafted discriminative features capable of differentiating voxels as lumen or non-calcified plaque. For voxel-wise discriminative features, we employed the spatial neighbourhood information, optimized 2-class GMM based posteriors, signed distance function, distance from the arterial orifice, pixel distance from the centreline and image histogram based customized fuzzy label as explained in this section.

6.4.1 Two-Class Posterior Probability

It is notable that the non-calcified plaques present inside coronary vasculature do not follow any particular shape or structure; hence, the use of shape-prior information is not very effective for NCP segmentation. Consequently, the extensively investigated feature in

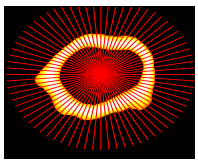

(a) Normal

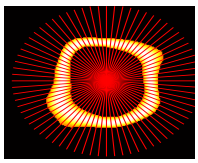

(b) Normal

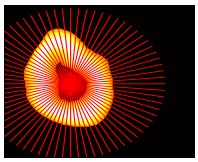

(c) Abnormal

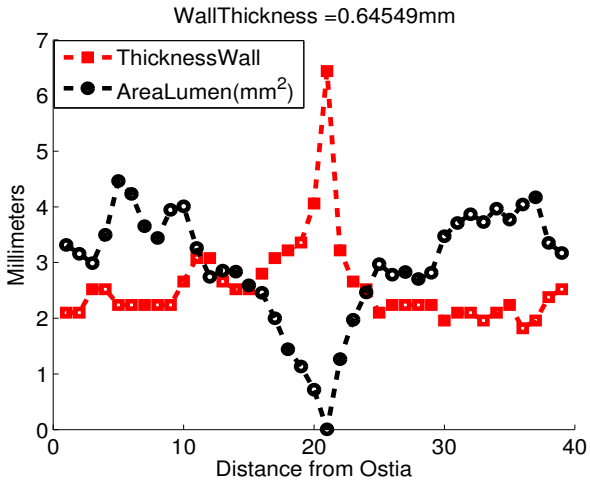

(d) Lumen area versus wall thickness plot

Fig. 6.14 Computation of the vessel wall thickness for coronary segment DS15 seg2. (a-c) shows the ray-projection to compute the mean thickness of the vessel wall, (d) represents the graphical comparison between lumen area and the normalized vessel wall thickness to reflect the anomalous lesion area. Cross sectional thickness representing normal segment (a and c) leads to a stable vessel wall thickness, whereas an abnormal cross section leads to expansion of the vessel wall based on low density soft plaques.

context of non-calcified plaque segmentation is the intensity distribution in the vessel, as the plaque region undergoes an unexpected drop relative to the normal blood HU distribution. To exploit the intensity fluctuation associated with the non-calcified plaques, we applied a two-class Gaussian Mixture Model (GMM) on the plaque effected section of the segmented vessel as illustrated in Fig. 6.15. Fig. 6.15a shows a plaque effected section of the coronary vessel, such that black contours define narrowed lumen, overlaid with the ideal vessel contours (red) for the lesion section. It can be observed from the figure that the lumen shrinks significantly leading to a certain amount of the non-calcified plaque in this region of vessel. In the subsequent step, we computed the intensity histogram for the plaque effected section with an expectation of two peaks representing plaque and lumen respectively as shown in Fig. 6.15b. Next, the bimodal intensity histogram of plaque effected section is approximated using a two-class Gaussian Mixture Model (GMM), followed with the application of the Expectation

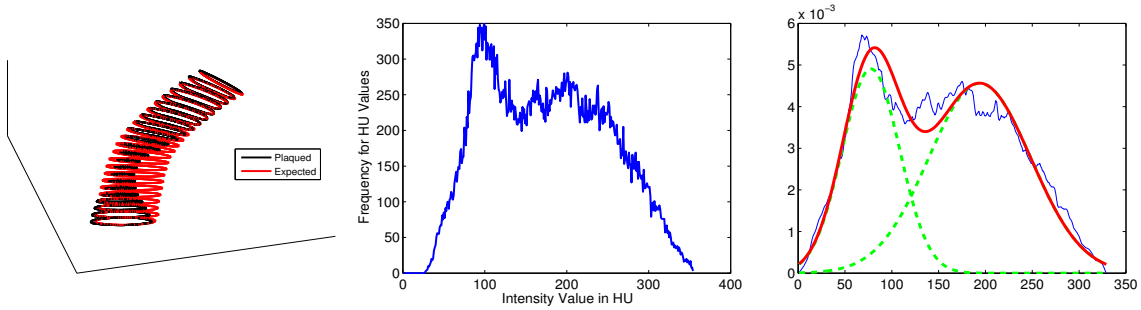

(a) Plaque effected section (b) Intensity histogram (c) 2-class GMM

Fig. 6.15 Two-class approximation for the plaque effected section of the coronary segment DS4 seg1. (a-b) shows the plaque effected boundary and respective bimodal intensity histogram, (c) represents two class Gaussian Mixture Model and respective HU intensity peaks. In (a), black contours define the narrowed lumen and red contours define the ideal vessel for the lesion section.

Maximization (EM) algorithm for optimal representation of two classes. Fig. 6.15c shows the GMM approximation, with the first class defining low density non-calcified plaque and second class representing the blood lumen.

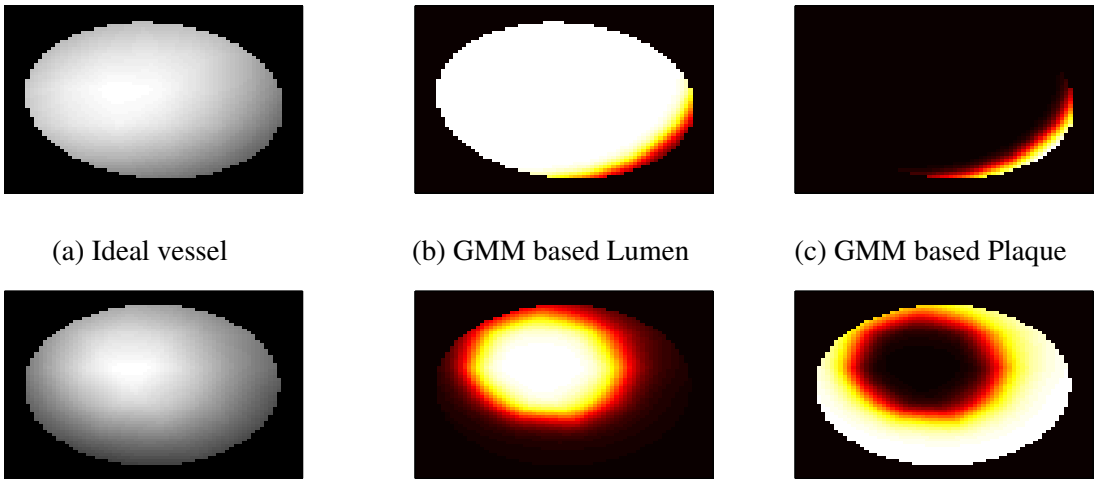

(a) Ideal vessel (b) GMM based Lumen (c) GMM based Plaque

(d) Ideal vessel (e) GMM based lumen (f) GMM based plaque

Fig. 6.16 Estimation for lumen and plaque using two-class GMM for DS4 seg1. The top row represents a normal cross-section, i.e. at the immediate start of the non-calcified plaque region, and the second row represents the cross-section in the mid of plaque region. The left column shows a 2D intensity based cross-section of the coronary vessel, whereas the middle and the right columns respectively show the two-class GMM based lumen and non-calcified plaque.

After obtaining the EM based optimal distribution parameters, we used a Bayesian modelling approach to compute the posterior probabilities for the two classes respectively as represented in Fig. 6.16. The left column represents the cross sectional view for an ideal vessel (plaque free vessel), the middle and right columns represents two-class GMM based lumen and the plaque voxels respectively. It can be observed that top row (start of the plaque) shows the two-class lumen close to the ideal vessel with a minimal plaque, however the second row reflecting the middle of the plaque region shows significantly reduced lumen along with an expanded plaque. Moreover, the relative position of the lumen and plaque validates the clinical fact that non-calcified plaque generally sticks with the vessel walls leading to Napkin Ring signs [168].

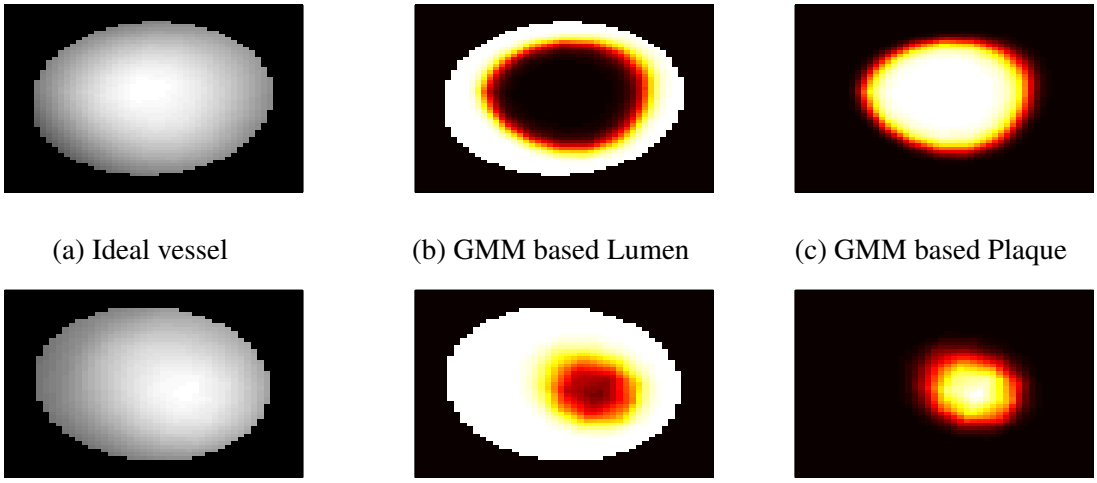

(a) Ideal vessel (b) GMM based Lumen (c) GMM based Plaque

(d) Ideal vessel (e) GMM based lumen (f) GMM based plaque

Fig. 6.17 Estimation for lumen and plaque using two-class GMM for DS9 seg2. The top row represents a normal cross-section, i.e. at the immediate start of the non-calcified plaque region, and the second row represents the cross-section in the mid of plaque region. The left column shows a 2D intensity based cross-section of the coronary vessel, whereas the middle and the right columns respectively show the two-class GMM based lumen and non-calcified plaque.

In contrast, the two-class GMM model for the plaque affected segment of DS9 shows poor performance as illustrated in Fig. 6.17. The first column shows the ideal vessel for two cross-section, the second column represents GMM-based lumen and the third column shows non-calcified plaque respectively. For the top row i.e. the normal cross-section, it is

expected that the lumen should fill the expected vessel boundary with minimal plaque on the outer circumference; however Fig. 6.17b - 6.17c shows that lumen voxels are pushed towards vessel boundary with plaque residing in the centre of cross section. Likewise, the abnormal cross-section of second shown in second row demonstrates a similar response of the two-class GMM. This ambiguous response of two-class GMM for certain plaque affected segments emphasises the need of additional investigation for quantification of the total non-calcified plaque. Subsequently, we derive additional features including spatial neighbourhood response, customized fuzzy label and a number of distance measures as defined here.

6.4.2 Signed Distance Function

In addition to the two-class GMM based posteriors, we derived an additional feature "Compound Distance" based on the ground truth lumen and the ideal vessel boundary. As illustrated in Fig. 6.7, the ideal vessel boundary can be overlaid on the lumen annotations of the human experts, which leads to the plaque estimation in the affected region. This visual demonstration can be represented mathematically using a signed distance function, i.e. use of lumen boundary based distance metric to differentiate the lumen and plaque inside the vessel. In principle, when there is no plaque, the annotated lumen overrides the ideal vessel boundary with a consistent (+ve) distance sign. In contrast, the presence of the plaque leads to a narrower lumen boundary inside vessel leading to bi-directional distances, i.e. positive for the inward lumen voxels and negative for the outer plaque region voxels.

In a mathematical context, the signed distance function (or oriented distance function) of a set Ω_s determines the distance of an arbitrary point $\mathbf{x}$ from the boundary of Ω_s as expressed by Eq. 6.5. The $\pm$ sign in Eq. 6.5 indicates the relative position of the arbitrary point i.e. whether $\mathbf{x}$ is inside or outside the Ω_s. The function assumes positive value for the points inside Ω_s and decreases in value as $\mathbf{x}$ approaches the boundary, where the signed distance function becomes zero. Likewise, the function of Eq. 6.5 assumes increasing magnitude as the point moves away from the boundary; however, the distance sign becomes negative to

reflect the outward positioning of the points.

$$Sdf(\mathbf{x}) = \begin{cases} +d(\mathbf{x}, \partial\Omega_s) & if \mathbf{x} \in \Omega_s, \\ -d(\mathbf{x}, \partial\Omega_s) & if \mathbf{x} \in \Omega_s^c, \end{cases} \tag{6.5}$$

where $\partial\Omega_s$ denotes the boundary of Ω_s. Accordingly, we constructed a signed distance function (SDF) such that the distance on the lumen boundary is zero, the distance from boundary to inward lumen in positive and distance from the lumen boundary to ideal vessel boundary is assigned a negative sign along with the Euclidean distance as the magnitude. This signed distance based interpretation of the voxels can certainly help the SVM classifier in improving the accuracy, since the classifier learns the voxel's characteristics in the training stage. The advantage of employing the signed distance function is illustrated in Fig. 6.18 where normal and plaque-effected cross sections are visualized.

Fig. 6.18 shows two normal cross-sections (i.e. immediately before and after the plaque region) in the first row (a, b), whereas an abnormal cross section from the mid of the plaqued region is presented in the second row (c). Moreover, the *blue* contour represents the "reference" ground truth lumen and the *magenta* contour denotes the ideal vessel boundary for the respective cross section. It can be observed from Fig. 6.18a-6.18b that, for normal cross-sections of the vessel, the "reference" ground truth lumen overlaps the ideal vessel boundary, and the distance map shows positive distances towards the inner lumen. However, for an abnormal cross section of the vessel, the "reference" ground truth lumen (blue) appears significantly compressed with respect to the ideal vessel boundary (magenta) as illustrated in Fig. 6.18c. Accordingly, the shrinkage of the lumen leads to the outward distance (negative distance) with respect to the lumen boundary. Moreover, to justify the effectiveness of the signed distance function, we have presented the applicable colour maps for respective signed distance distance functions. It can be observed from the respective colour bars that normal cross-sections employ positive values (i.e. lumen only), whereas abnormal cross-section employs both positive and negative values, reflecting the presence of non-calcified plaques.

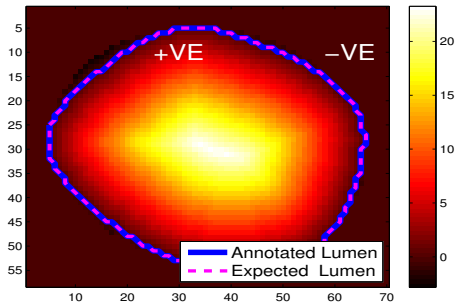

(a) Normal cross-section immediately before plaque

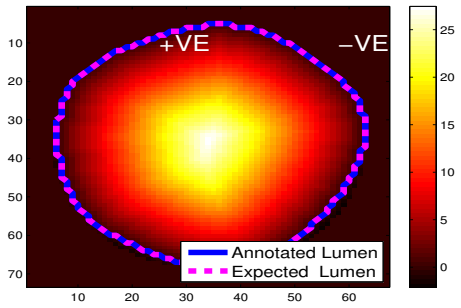

(b) Normal cross-section immediately after plaque

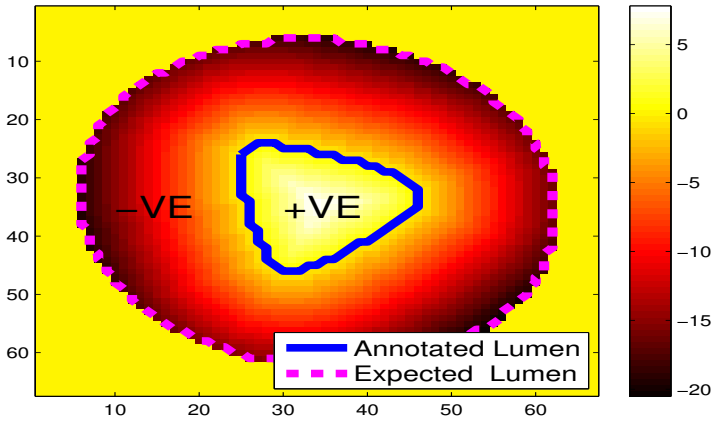

(c) Plaque effected cross-section

Fig. 6.18 Use of signed distance function (SDF) to discriminate the lumen and the plaque. (a, b) represents two normal cross-section i.e. at the start and end of the plaque region, whereas (c) represents a cross-section from the mid of the non-calcified plaque region. For a normal cross-section (a, b), the lumen (blue) overrides the ideal vessel boundary (magenta) with all (+ ve) distances, whereas for an abnormal cross-section (c), the lumen (blue) becomes significantly narrower than the vessel boundary (magenta) leading to (-ve) distances.

6.4.3 Spatial Neighbourhood Information

Along with the intensity based investigation, spatial neighbourhood information (connectivity) is generally employed in object detection algorithms. The neighbourhood of a pixel can be used effectively for operations such as morphology, edge detection, median filter, etc. Many computer vision algorithms allow the user to employ an arbitrary (3 by 3, or 5 by 5 square, circular or disk) neighbourhood for optimized performance; however, the neighbourhood selection is generally application dependent, i.e. neighbourhood weights

employed for sharpening an image may not work at all for smoothing and vice versa. Neighbourhood processing algorithms typically create a new image by computing new pixel value as a function of not only the corresponding old pixel value, but also its neighbouring old pixel values. This phenomena allows the user to overcome unexpected spikes by normalizing the output with respect to the regional response of the input image.

In image processing and image recognition, pixel connectivity is the way in which pixels in two-dimensional (or voxels in three-dimensional) images relate to their neighbours and the neighbourhood around a pixel/voxel is termed as "window" or "mask". The non-zero entries in a "convolution kernel" form one kind of neighbourhood; however, the non-zero values are chosen according to the nature of the task. For a simple two-dimensional image, a middle pixel can have a maximum of *eight* neighbouring pixels, which increases to 26 neighbours in 3-dimensional space since a 3D voxel is surrounded by the two additional planes. This spatial neighbourhood structuring is illustrated in Fig. 6.19, where a central voxel (red) is surrounded by its 26 neighbouring voxels. The purple voxels connected with green lines represent the *eight* neighbours on the same plane, whereas grey voxels connected by magenta lines denotes two additional planes.

The spatial neighbourhood based information can play an important role in differentiating plaque voxels from the lumen i.e. the SVM classifier can employ the neighbourhood behaviour of a particular voxel to label as one of two possible classes. As an example, we consider a particular voxel in 3D space along with its 26 neighbouring voxels. If the majority of the neighbours are labelled as “lumen”, there is a high probability of being lumen for the current voxel. Likewise, if the majority of the neighbours belong to “plaque” class, more likely it is that the current voxel also represents “plaque”. Hence, the neighbourhood based information can effectively help to improve the performance of the SVM classifier.

6.4.4 Fuzzy Labelling

As the intensity composition is the major indicator of the non-calcified plaques in coronary vasculature, we derived an additional "fuzzy label" feature based on the image intensity to differentiate the two classes. This intensity based feature is derived using bimodal

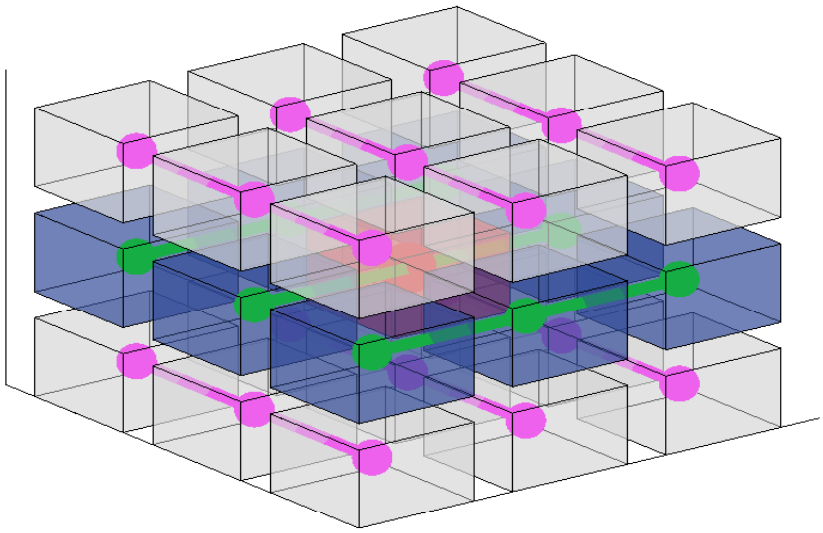

Fig. 6.19 Neighbourhood processing for a reference voxel. The reference voxel (red) along with local neighbours in 3D space, blue cubes represents 8-neighbours and grey cubes represent remaining neighbours to form a total of 26 neighbours in 3D space.

histogram of the plaque effected region as shown in Fig. 6.20, which reflects the expectation maximization based distribution parameters for two classes. We employed the two peaks of the histogram to derive a customized fuzzy label as a function of distance from the bimodal peaks. For mathematical computation of the fuzzy label, we let μ_p and μ_l represent the peak HU value for plaque and lumen classes respectively such that $\mu_l > \mu_p$. Accordingly, the fuzzy label at current location (i, j, k) is computed as expressed by Eq. 6.6.

$$F_{label}(i,j,k) = \begin{cases} 0 & \text{if } I(i,j,k) =\leq \mu_p, \\ 1 & \text{if } I(i,j,k) =\geq \mu_l, \\ \frac{I_{i,j,k}-\mu_p}{\mu_l-\mu_p} & \text{otherwise,} \end{cases} \tag{6.6}$$

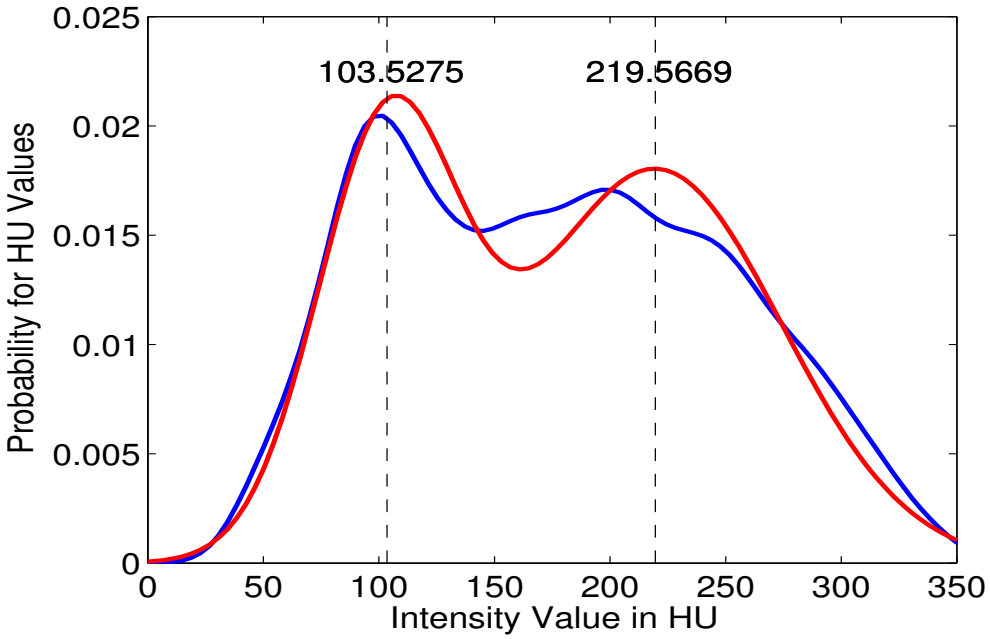

Fig. 6.20 Class-wise HU intensity peaks for lumen and plaque based on 2-class approximation of plaque affected region of the coronary segment DS4 seg1.

where, the current voxel intensity $I(i,j,k)$ is derived using $[3x3x3]$ square neighbourhood window of Eq. 6.7 to suppress possible noise and unexpected spikes.

$$I_{i,j,k} = \frac{1}{27}\left\{\sum_{mx=-1}^{1}\sum_{my=-1}^{1}\sum_{mz=-1}^{1} I(i+mx, j+my, k+mz)\right\}. \tag{6.7}$$

According to Eq. 6.6, when the current voxel intensity is less than or equal to first peak of the histogram, a constant value of *zero* is assigned. Similarly, for the values greater than or equal to the second peak of histogram, a fixed label of *one* is assigned. However, voxels assuming the intermediate values are labelled as a function of the difference between two peaks. A voxel value close to the first peak is more likely to be a part of the plaque, whereas a voxel falling close to the second peak is comparatively a stronger candidate of the lumen class.

The effectiveness of the fuzzy label is graphically illustrated in Fig. 6.21 where three cross sectional slices are presented. The first row represents orthogonal cross sections at three different locations of the segment, overlaid with the ideal vessel boundary, whereas the second row shows corresponding fuzzy labels based on Eq. 6.6. The greyscale images are processed

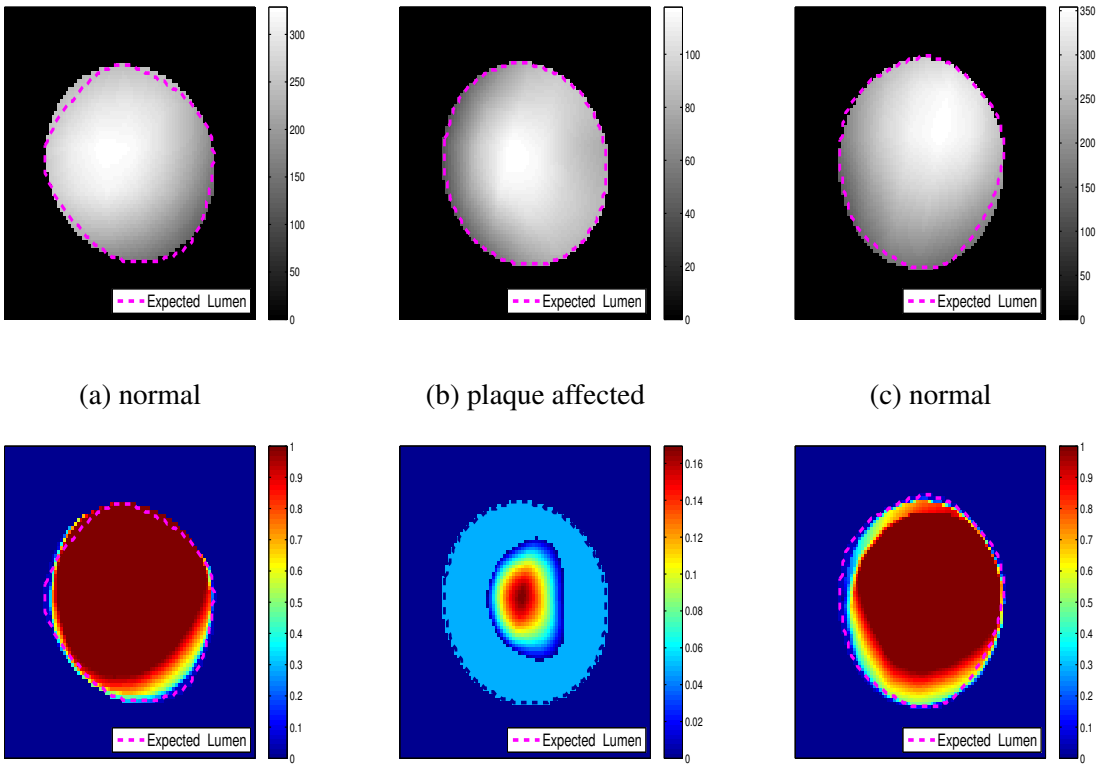

(a) normal (b) plaque affected (c) normal

(d) normal (e) normal (f) normal

Fig. 6.21 Voxel-wise fuzzy labelling bimodal histogram of the plaque affected section of the coronary segment DS4 seg1. The fuzzy value close to *zero* represents the likelihood of plaque, whereas value close to *one* represents the lumen.

in a first step to ensure that the background (anything outside the ideal vessel boundary *magenta* color) is suppressed. Apparently, the three greyscale images appear normal due to similar visual appearance; however, the first and third columns represent normal plaque-free cross-sections and the middle column shows a cross-section from a plaque affected region. The intensity based non-calcified plaque of the middle column can be easily identified using the fuzzy label function of the second row. For a meaningful interpretation of the fuzzy label display, the colour bar has been appended along with the images. It can be observed that the fuzzy label for normal cross sections (left and right column) assumes higher values throughout the vessel boundary, indicating that all the intensity values are centred around the second peak of the histogram and there is no plaque present. In contrast, the fuzzy label display of the middle column shows that majority of the voxels in the ideal vessel boundary

assumes low values (inclined towards zero), except few central voxels. Consequently, low fuzzy values reflect the presence of low intensity values centred around the first peak of the histogram i.e. non-calcified plaque with a significantly reduced lumen.

6.4.5 Distance Functions

After deriving intensity based features for effective differentiation of plaque from the lumen voxels, we employed some prior knowledge in the context of the clinical interpretation of the non-calcified plaques. In general, the concentration of the contrast medium decreases in the distal segments of the coronary tree i.e. the lumen voxel intensity decreases as the blood flows away from the orifice. Accordingly, the low intensity voxels of the distal segments should not be confused as plaque by the SVM classifier. Therefore, an additional input in the feature space is the distance of the current plane from the ostium of the segment. Subsequently, the plane voxels are replicated with the distance metric before using voxel-wise classifier. Likewise, based on clinical knowledge, we expect NCPs to be inclined towards the walls of the vessel. In context of the voxel-wise segmentation, we employed an additional feature i.e. the distance of the voxel from the centreline of the vessel as expressed by Eq. 6.8. Accordingly, the central voxels are assigned low distance values and outer voxels assume higher distance measures. It should be noted that the derived features do not operate or yield productive results in stand-alone, but an appropriate combination of different features allows the SVM classifier to learn the lumen and plaque patterns accordingly.

$$D3d(i,j,k) = \sqrt{(C_x - i)^2 + (C_y - j)^2 + (C_z - k)^2}. \tag{6.8}$$

6.5 Voxel-wise Classification

The use of a SVM for voxel-wise classification is explained in this section. It should be noted that the voxel-wise classification of non-calcified plaque is a challenging task as it becomes complex to derive discriminative features due to limited information. Consequently, features employed in this work are driven in a first (preprocessing) step to represent the specific

voxel in the context of its neighbourhood for optimal differentiation of plaque effected voxels from the normal ones. In total, we have computed *eight* features to be used in the SVM classifier including voxel intensity, fuzzy label, two-class posterior probability, spatial neighbourhood based voxel function and a variety of distance functions (distance from vessel ostium, distance from the ground truth lumen and distance from the centreline). In the subsequent step, we concatenate individual discriminative features to derive a N-by-$dims$ feature space for the SVM classifier as expressed by Eq. 6.9, where $X_n^{'}$ defines the feature vector for an individual voxel and $Y_n^{'}$ defines the associated binary label. Here, N is the number of SVM samples (voxels) and $dims$ represent the feature vector dimension for the SVM classifier. Accordingly, the total samples N is set equal to the number of voxels in respective segment and the dimension of the feature space $dims$ is set equal to number of hand crafted features i.e. *eight*.

$$D^{'} = \left\{ \left(\mathbf{X}_n^{'}, Y_n^{'} \right) | \mathbf{X}_n^{'} \subseteq R^{dims}, Y_n^{'} \subseteq \{0,1\} \right\}_{n=1}^{N}, \tag{6.9}$$

where $X_n^{'}$ represents the features described above. The SVM model finds an optimal hyperplane by minimizing the norm of weights for ideal segregation of input data into two classes as expressed by Eq. 5.10. The penalty cost P regulating the influence of individual support vectors is defined equal to $P = 10^0$. It is important that a high value of P leads to hard margin with strict classification criteria, whereas very small value allows frequent violations of the constraints. Moreover, we used a non-linear radial basis Gaussian kernel for mapping data into a higher dimensional space with sigma defined equal to *one*. Table 6.4 shows the detailed specification for SVM plaque segmentation model including features and the respective tuning parameters.

For training of the SVM classifier, we employed the voxels of the non-calcified plaque affected segments of Table 6.3, using respective feature vectors and the corresponding binary labels. As the vessel wall already has been removed for the segmented coronary tree, therefore the binary labels represent two possible states of the voxel (*zero*=lumen, *one*=non-calcified plaque). After training the SVM model on the plaque affected segments

Table 6.3 Non-calcified plaque effected segments in the Rotterdam CTA data

Segment ID	Plaque Specifications		
	Segment Type	Plaque Grading	Voxels
DS1 seg6	Proximal	mild	201*201*31
DS2 seg6	Proximal	mild	201*201*45
DS4 seg1	Proximal	Severe	201*201*68
DS4 seg2	Proximal	Moderate	201*201*64
DS5 seg2	Proximal	Moderate	201*201*61
DS5 seg8	Distal	Moderate	201*201*85
DS7 seg2	Proximal	Severe	201*201*50
DS7 seg3	Proximal	Moderate	201*201*90
DS9 seg2	Proximal	Moderate	201*201*36
DS11 seg7	Proximal	Mild	201*201*55
DS15 seg2	Proximal	Moderate	201*201*65
DS15 seg3	Proximal	Mild	201*201*90
DS15 seg14	Distal	Moderate	201*201*80

of particular CTA volumes, we evaluated the SVM performance on a per-segment basis as detailed in Results section. It is important to mention that the SVM model trained using the laque affected segment of a particular CTA volume, performs well for the remaining segments of the particular volume; however, it under-performs for coronary segments coming from other CTA volumes. This leads to the conclusion that SVM training is required using at least one coronary segment of a particular CTA volume before investigating remaining segments unless a generalized SVM model is designed.

6.6 Results

The performance of the SVM classifier is evaluated using classification metrics including true positive (TP), true negative (TN), false positive (FP), false negative (FN) respectively. True positive refers to a lumen voxel identified as normal (lumen) by the SVM classifier, whereas false negative status refers to a lumen voxel identified as abnormal (plaque) by the classifier model. Likewise, true negative refers to a plaque voxel identified as abnormal (plaque) by the SVM classifier, whereas false positive refers to a plaque voxel identified as normal (lumen)

Table 6.4 SVM model for voxel-wise plaque segmentation.

	Specifications for feature space	
Parameter name	Parameter type	dimension/value
2-class posterior probability	Discriminative feature	2
Signed distance function	Discriminative feature	1
Spatial neighbourhood	Discriminative feature	1
Fuzzy label	Discriminative feature	1
Distance functions	Discriminative feature	3
SVM Kernel	Tuning parameter	RBF
Gaussian deviation [σ]	Tuning parameter	1
Penalty cost	Tuning parameter	10^0
Feature vector dimensions	N/A	[1x8]

by the classifier model. For a meaningful interpretation of the classification statistics, we employed the computed metrics (TP, FP, FN and TN) to derive sensitivity, specificity and the accuracy metrics as expressed by Eq. 6.10

$$Sensitivity = \frac{TP}{(TP+FN)}, \qquad Specificity = \frac{TN}{(TN+FP)},$$
$$Accuracy = \frac{TP+TN}{(TP+TN+FP+FN)}. \tag{6.10}$$

6.6.1 Classification Statistics for Volume-Specific SVM Model

Before computing the mean accuracy of the SVM classifier with respect to the manual annotations of non-calcified plaques, we performed a 10-fold cross validation of the SVM model for respective plaque effected segments. Accordingly, the total number of samples (voxels) in plaque effected segments are divided into *ten* groups using random indexing method in Matlab. In the subsequent step, *nine* groups are used to train the SVM model and remaining *one* group is used as the test data. Subsequently, results are validated against ground truth labels as presented in Table. 6.5. This evaluation was extended by employing additional samples (voxels) from other segments of the same coronary tree. It has been observed that the increase in sample space leads to similar validation results with mean values of 92.40%, 83.70% and 91.16% for sensitivity, specificity and accuracy respectively;

however, the training and validation time significantly increases with each additional segment (on average, one segment leads to an addition of 201 by 201 by 50 voxels). Moreover, the consistent performance across different sample sizes is based on the fact that additional voxels come from same coronary tree, i.e. the SVM model is well aware of intensity characteristics of two classes due to training on plaque effected segments of specific CTA volume.

Table 6.5 10-Fold cross validation performance of SVM classifier.

Segment	Classification Statistics		
	Sensitivity%	Specificity%	Accuracy%
DS1 seg6	94.11	88.23	93.30
DS2 seg6	93.50	87.59	92.61
DS4 seg1	92.04	87.30	91.45
DS4 seg2	91.95	83.33	90.72
DS5 seg2	93.56	82.19	91.92
DS5 seg8	90.49	86.41	89.86
DS7 seg2	93.72	86.95	92.78
DS7 seg3	91.95	78.94	90.01
DS9 seg2	90.66	82.35	89.13
DS11 seg7	90.90	81.08	89.49
DS15 seg2	93.89	80.64	92.21
DS15 seg3	92.06	86.95	91.37
DS15 seg14	92.30	76.08	90.29
Mean	92.40	83.70	91.16

After performing the 10-fold cross-validation for the voxel-wise SVM classifier, we obtained the qualitative and quantitative results with respect to the human observers. The quantitative performance of the SVM based plaque segmentation algorithm is presented in Table 6.6, which shows mean performance against three manual experts. It can be observed from the table that, for the majority of the plaque affected segments, the SVM classifier delivers very good performance in terms of sensitivity, specificity and the overall accuracy. However, at certain occasions the performance drops in terms of the specificity, i.e. the plaque voxels are misclassified for certain instance. This misclassification can be related to the mild and unstable nature of the non-calcified plaque, i.e. the intensity drop is not significant enough to force the classifier to label the voxel correctly as plaque.

6.6.2 Classification Statistics for Generalized SVM Model

The classification results presented in Section 6.6.1 shows impressive performance for the voxel-wise SVM model; however; the model requires training on at least one plaque affected segment of the coronary tree to produce optimal classification results on the remaining segments of the respective tree. This limitation is associated with the fact that the different CTA volumes exhibit different behaviour in terms of contrast medium based blood intensity as illustrated in Table. 4.4. Since hand-crafted features used in the SVM classification process employ either direct intensity information or intensity distribution based explicit features, the inter-patient intensity variability becomes problematic in clinical practice. For instance, SVM model trained on a CTA volume having high concentration of the contrast medium, may classify the normal voxels of another volume as plaque-effected due to lower intensity; even if the second volume has overall low intensity due to the less dose of contrast medium or patient heart-beat.

To minimize the impact of the inter-patient intensity variability, we used the idea of generic SVM model (i.e. applicable across the CTA dataset). Accordingly, we performed normalization of the CTA data in a pre-processing step to represent all volumes in a fixed HU range [0-255]. Based on the normalized range, the intensity values lower than *zero* are mapped towards *zero*, whereas intensities greater than 255 are shifted toward the higher end of the normalized intensity range. Moreover, the intermediate values are adjusted to retain the true response of the image as illustrated in Fig.6.22.

The figure presents the effectiveness of the intensity normalization process for two CTA volumes i.e. the first row presents a case for CTA volume 01 and the second row justifies the normalization process for CTA volume 04. A side by side comparison of the CTA axial images reveal that despite of the intensity transformation, the axial image conveys complete information i.e. without any major artefacts in visual appearance (see Fig. 6.22a & 6.22c for CTA volume 01 and Fig. 6.22e & 6.22g for CTA volume 04).

Statistically, the overall behaviour of an image is presented using the intensity histogram. Before illustrating the effectiveness of the intensity normalization in context of the SVM classifier, we first compare the histogram of two original CTA volumes. It can be observed

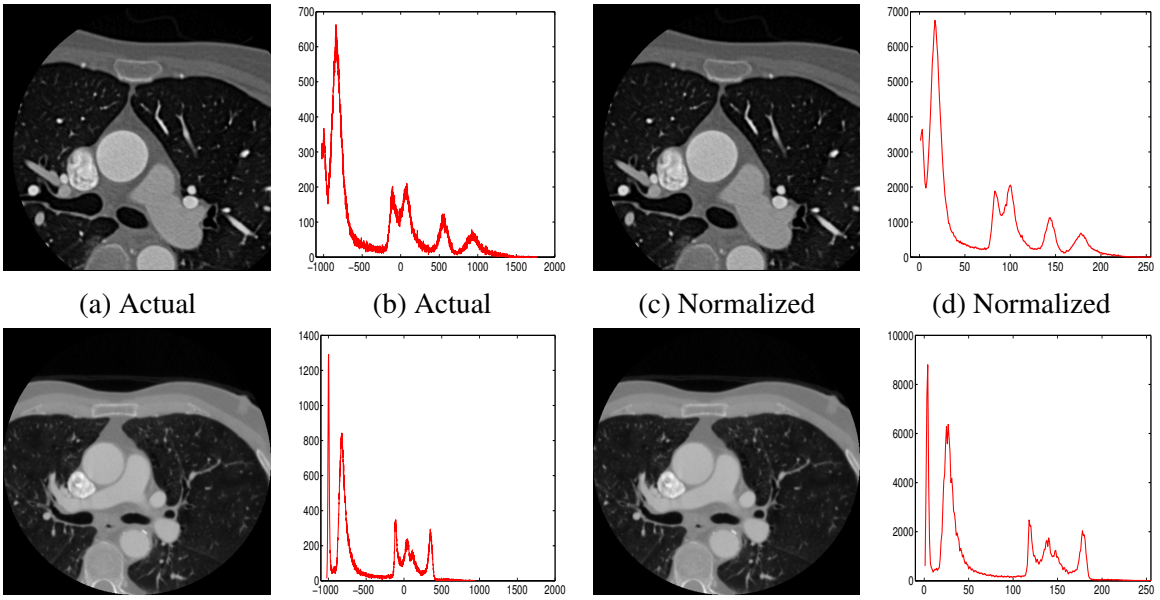

(a) Actual (b) Actual (c) Normalized (d) Normalized

(e) Actual (f) Actual (g) Normalized (h) Normalized

Fig. 6.22 Intensity range normalization in CTA. The top and bottom row show CTA volume 01 and 04 respectively. It can be observed that the intensity normalization shifts the overall distribution into a fixed range of [0, 255]. However, the image information is retained adequately as shown by visual images for actual and normalized volumes.

from the two histograms that there exists a significant variability in the intensity distribution for two CTA volumes, i.e. multi-modal histogram of volume 01 shows lumen peak intensity centred around 900 HU (Fig. 6.22b), whereas histogram of volume 04 defines the lumen peak intensity centred around 450 HU (Fig. 6.22f). From a clinical point of view, two intensity peaks define the normal lumen distribution in respective CTA volumes, however the SVM model trained for CTA volume 01 may interpret low intensity of CTA volume 04 as non-calcified plaques. Consequently, we transformed respective intensities in a normalized range of [0, 255] to minimize the impact of absolute voxel value in the SVM classification. It can be observed from the transformed histograms that the distribution of the intensity has been mapped into normalized range for two CTA volumes (see Fig. 6.22d and 6.22d). Subsequently, plaque affected segments from different normalized volumes were used in retraining of the volume-specific SVM model to obtain a generic SVM model for greater reproducibility i.e. for application across the CTA dataset. From a theoretical point of view, the generic classifier should perform well for all CTA volumes in the dataset; however,

the practical performance is marginally decreased due to the loss of information during normalization process.

Table 6.6 Volume-specific SVM model.

Segment	Classifier performance statistics		
	Sensitivity%	Specificity%	Accuracy%
DS1 seg6	99.62	97.75	99.60
DS2 seg6	99.96	83.37	99.01
DS4 seg1	99.98	93.73	99.18
DS4 seg2	99.86	78.48	97.76
DS5 seg2	98.25	97.22	98.11
DS5 seg8	99.41	72.97	97.60
DS7 seg2	99.93	97.88	99.81
DS7 seg3	99.96	75.93	99.71
DS9 seg2	94.61	90.89	93.02
DS11 seg7	99.99	71.28	99.53
DS15 seg2	99.95	87.53	98.83
DS15 seg3	99.99	51.65	99.06
DS15 seg14	X	YY	ZZ
Mean	99.34	83.45	98.45

Table 6.7 Generic SVM model.

Segment	Classifier performance statistics		
	Sensitivity%	Specificity%	Accuracy%
DS1 seg6	88.74	80.66	88.54
DS2 seg6	90.26	80.31	89.20
DS4 seg1	88.07	83.74	87.42
DS4 seg2	89.17	85.06	88.66
DS5 seg2	88.99	81.58	87.79
DS5 seg8	87.97	81.43	86.96
DS7 seg2	89.43	80.06	87.81
DS7 seg3	83.44	76.03	82.04
DS9 seg2	88.29	92.64	90.29
DS11 seg7	90.26	71.89	87.52
DS15 seg2	89.41	82.31	88.79
DS15 seg3	89.09	83.35	88.73
DS15 seg14	X	YY	ZZ
Mean	88.59	81.59	87.86

The performance of the generic SVM classifier based on normalized intensity is presented in this section. For this experiment, the train and test data for the SVM classifier comes from multiple plaque-effected segments of different CTA volumes. It is important to mention that due to a fixed intensity range, the normal lumen in all CTA volumes is defined using high intensity (inclined towards 255), whereas the non-calcified plaque in all volumes are represented using intermediate value on a scale of [0, 255]. After selecting appropriate number of sample voxels (collection of plaque and normal voxels from different segments of different CTA volumes), we performed 10-fold cross-validation test. According to the results, the performance is lower than the response of the volume-specific SVM classifier with a mean sensitivity, specificity and accuracy equal to 88.54%, 79.62% and 86.25% respectively.

In the subsequent step, we evaluated the performance of the generic SVM classifier with respect to manual observers for plaque affected segments as presented in Table 6.7. In this experiment, the generic SVM model was used to segregate lumen-plaque voxels in plaque affected segments. It can be observed from Table 6.7 that the overall performance of the classifier (sensitivity, specificity and accuracy) has dropped in comparison to the response of the volume-specific SVM model of Table 6.6. This is based on the fact that SVM model for Table 6.6 was trained/tested specifically for respective CTA volumes, hence

testing achieves higher accuracy for the plaque affected segments of respective volumes and an under-performance for other CTA volumes. In contrast, the SVM model for Table 6.7 has been trained on normalized data coming from multiple CTA volumes, hence testing achieves a reasonable accuracy for the plaque effected segments of different CTA volumes.

6.6.3 Lumen/Plaque Area Metrics

In this section, we present the performance of plaque segmentation algorithm with respect to three independent experts of the Rotterdam framework. For every plaque-affected instance of Table 6.1 we present here both qualitative and quantitative results using lumen and segmented plaque area metrics. This plaque area computation is based on the fact that the total plaque burden can be a more important indicator than the stenosis degree in coronary arteries as proposed in [169]. Accordingly, we start with the visual demonstration (Fig. 6.23a - 6.23c) of "reference" ground truth lumen contours to justify the nature (extent) of the plaque present in the respective segments as it has been validated earlier that, for mild nature plaques, three independent observers show a good agreement for lumen boundary, whereas severely affected plaque leads to reduced agreement for the lumen boundary.

The lumen contour plot is followed with the cross-section based lumen and plaque area analysis as shown in Fig. 6.23d - 6.23e. For a comparative purpose, we overlay the output of our plaque segmentation algorithm (the lumen and plaque area obtained using the SVM classifier) with respect to three human experts. It can be observed that both lumen and segmented plaque area remains stable within the range of three human expert agreement, which makes our algorithm a fair choice for plaque segmentation. In addition to the visual comparison of the lumen-plaque area, we performed a statistical (quantitative) comparison using Bland-Altman plot as illustrated in Fig. 6.24. In this section, we compared the obtained lumen and plaque area with three independent observers with an expectation of good correlation with three observers respectively.

It is important to mention that for mild to moderate plaques, there is a good interobserver mutual agreement. Accordingly, the Bland-Altman plot for the segments affected with mild plaque shows a good correlation with the all three observers simultaneously due to

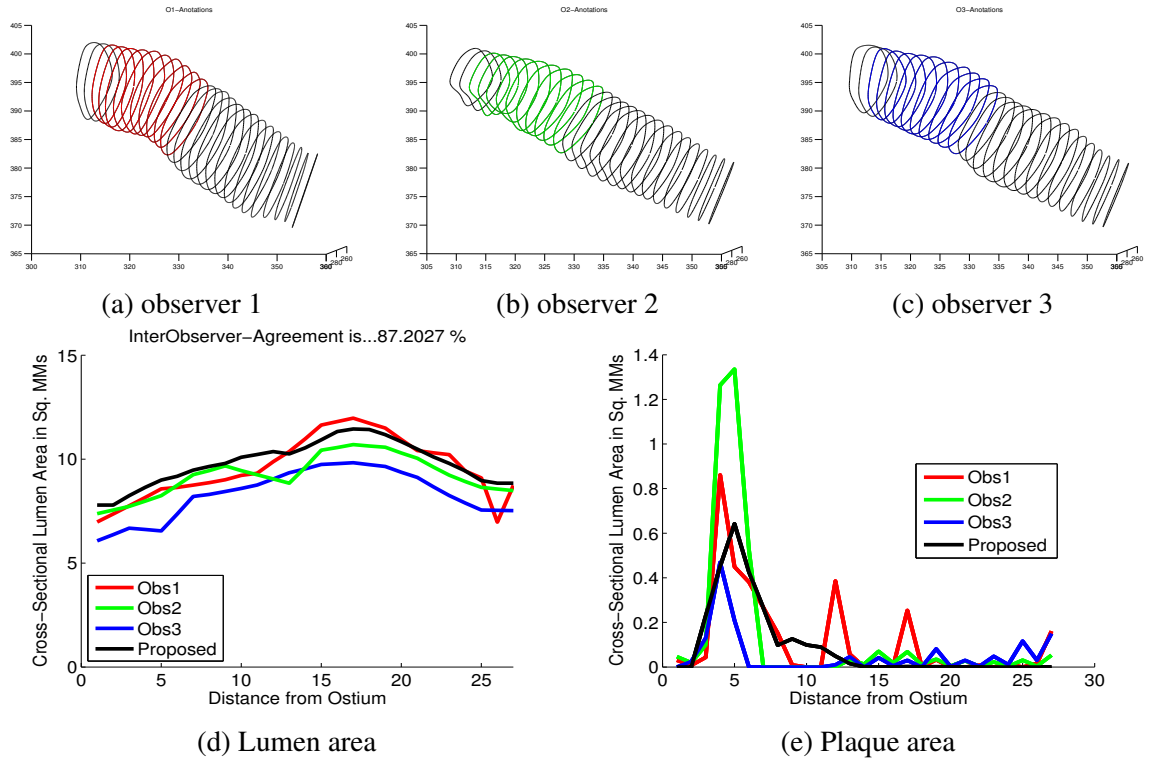

(a) observer 1 (b) observer 2 (c) observer 3

(d) Lumen area (e) Plaque area

Fig. 6.23 Lumen - plaque analysis w.r.t. manual observers for DS1 seg6. (a-c) lumen contours for three observers, (d-e) plots obtained cross-section based area for coronary lumen and non-calcified plaque respectively, with respect to annotations of three manual experts. Black is proposed method, whereas red, blue and green represent three observers.

consistency among the observers. In contrast, the severe plaques lead to reduced interobserver mutual agreement due to the ambiguity in visual demarcations. Hence, it becomes impossible for the segmented output to follow all three observers simultaneously. Consequently, the Bland-Altman plot for such cases demonstrate a good correlation with one or two observers while having bias towards others.

Likewise, Fig. 6.24 - A.12 show the plaque quantification performance of the proposed algorithm using lumen-plaque area statistics and the Bland-Altman plots. It can be observed from figures that the performance of the plaque quantification algorithm remains stable and within the approximate range of three human experts. An interesting case is shown in Fig. 6.31 - 6.32 which represents the floating non-calcified plaque in segment2 of dataset 09. It can be recalled from Chapter 4 (Fig. 4.27a - 4.27c) that the floating nature of the non-calcified plaque leads to reduced interobserver agreement and comparatively lower

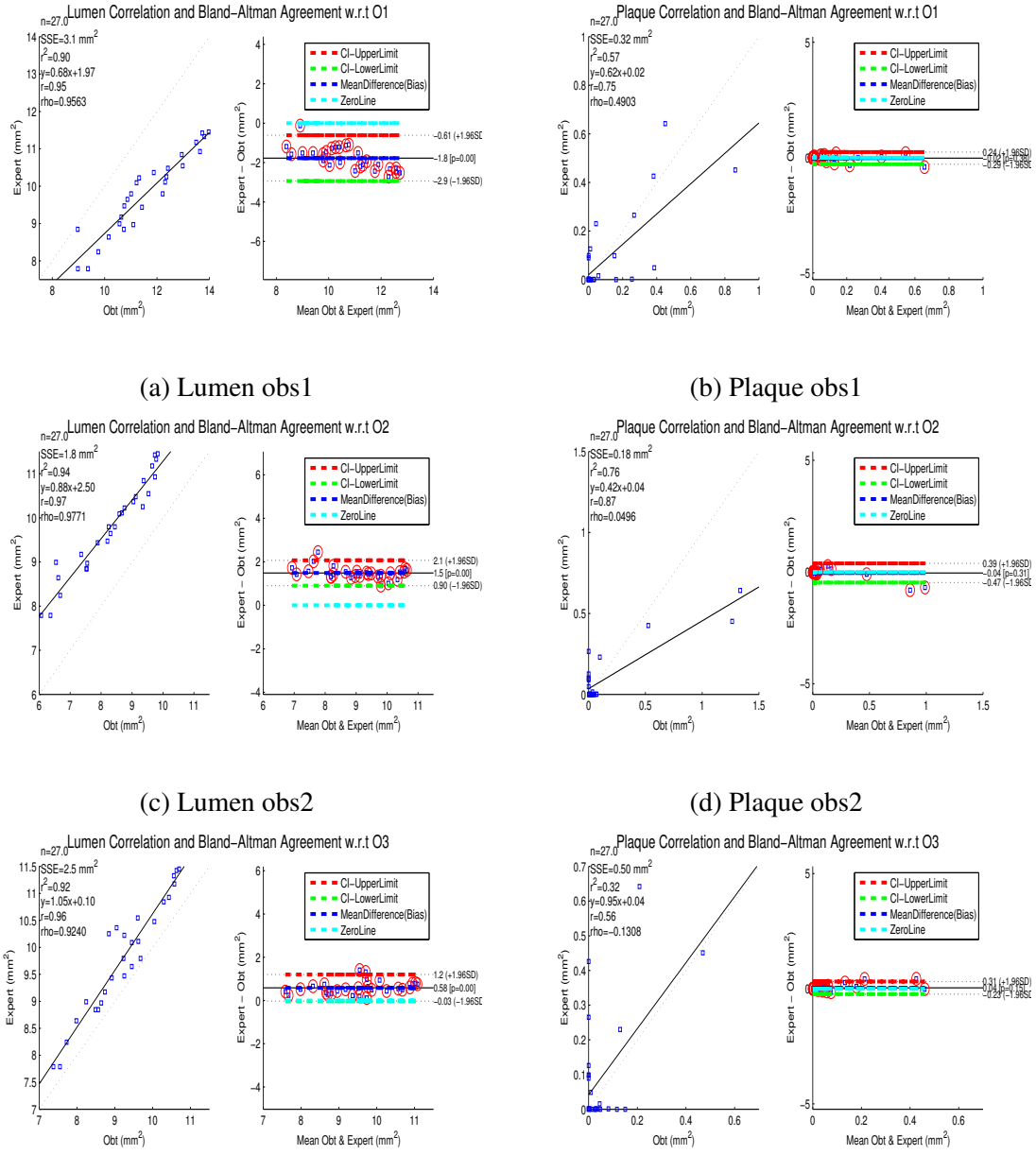

(a) Lumen obs1

(b) Plaque obs1

(c) Lumen obs2

(d) Plaque obs2

(e) Lumen obs3

(f) Plaque obs3

Fig. 6.24 Cross-section based analysis along the length of the segment with respect to three individual experts for DS1 seg6. Left (a, c, e) represents the obtained lumen area, whereas obtained plaque area is presented in right column (b, d, f). Both lumen and plaque area shows a good correlation and the Bland-Altman plots reflects an agreement within the 95% confidence interval.

segmentation accuracy for dataset 09. Consequently, the plaque quantification output shows a considerable shift against one or more human observers.

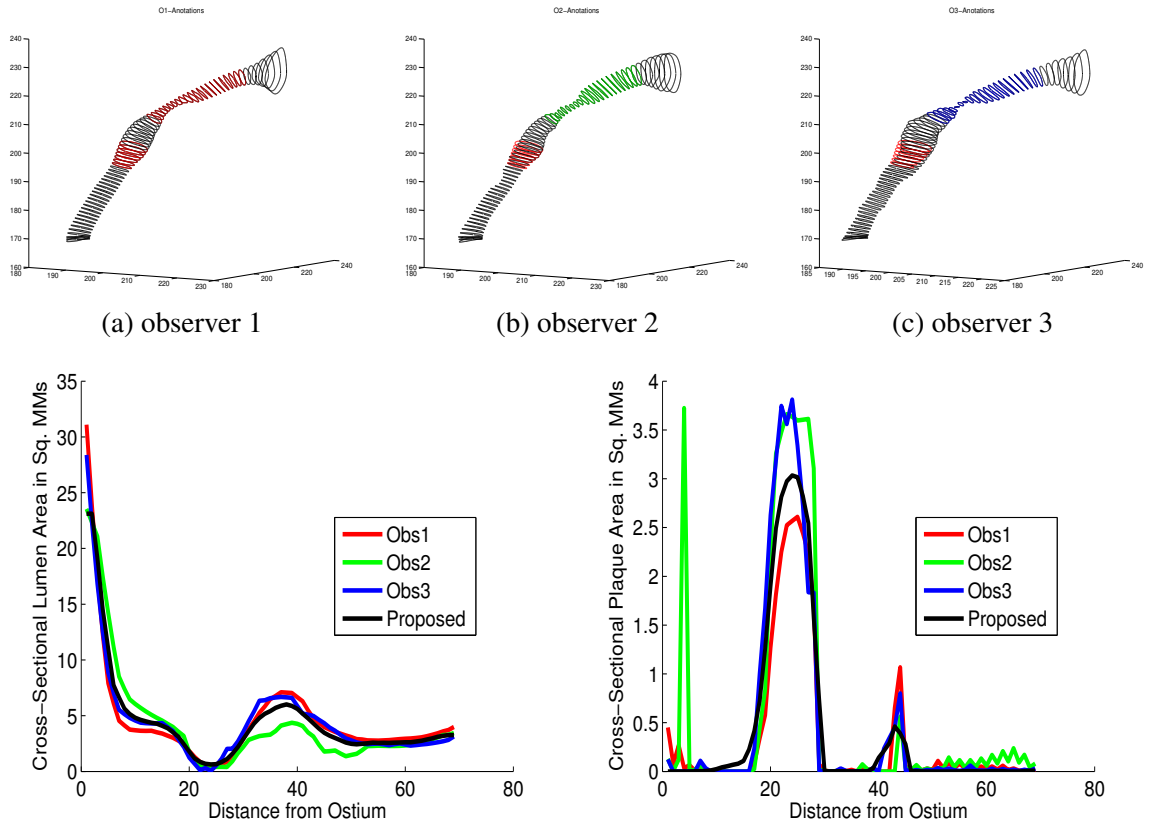

(a) observer 1 (b) observer 2 (c) observer 3

(d) Lumen area (e) Plaque area

Fig. 6.25 Lumen - plaque analysis w.r.t. manual observers DS4 seg1. (a-c) lumen contours for three observers, (d-e) plots obtained cross-section based area for coronary lumen and non-calcified plaque respectively, with respect to annotations of three manual experts. Black is obtained area, whereas red, blue and green represent three observers.

6.7 Summary

In this chapter, we performed voxel-wise quantification of coronary non-calcified plaque using support vector machines. Based on the normal coronary segments, we computed the vessel-wall thickness in a first step. In the subsequent step, we removed vessel wall from the segmented tree and employed a Gaussian Mixture Model to compute intensity based features. In the final step, the hand-crafted intensity based features are used to classify voxels into lumen or plaque. According to the experimental results, it is shown that the automated plaque segmentation method achieves an accuracy equivalent to the human experts with mean sensitivity, specificity and accuracy equal to 88.59% ,81.59% and 87.86%, respectively.

A limitation for the voxel-wise plaque quantification method is under-estimation of non-calcified plaque in mild-affected segments of the coronary tree. As the voxel-wise features employed in SVM classification relies on intensity distribution of two classes (lumen and the non-calcified plaques), the mild plaque voxels can be interpreted as lumen. Another limitation of the current method is dependence upon the accuracy of the plaque localization method. The plaque localization method of Chapter 5 leads to the start and end position of the non-calcified plaque, which leads to voxel-wise plaque ground truth. Accordingly, an erroneous plaque location can result in inaccurate quantification of non-calcified plaques.

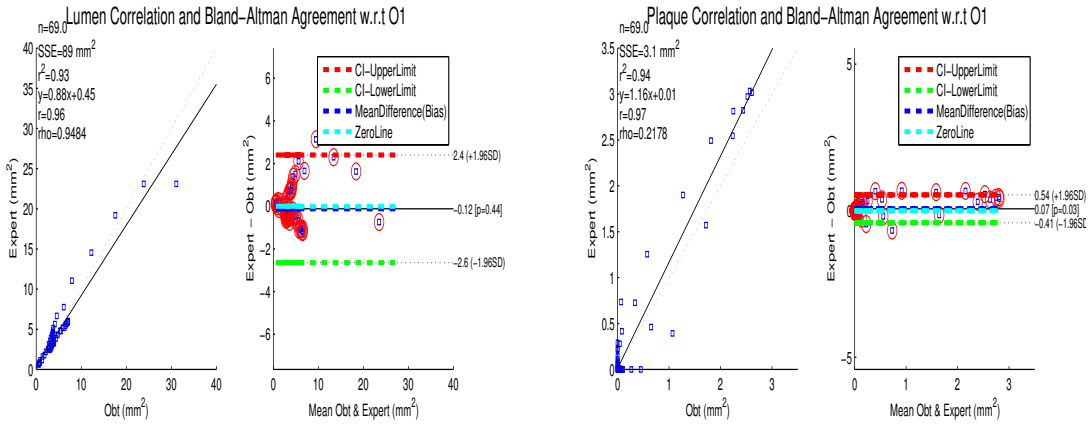

(a) Lumen obs1

(b) Plaque obs1

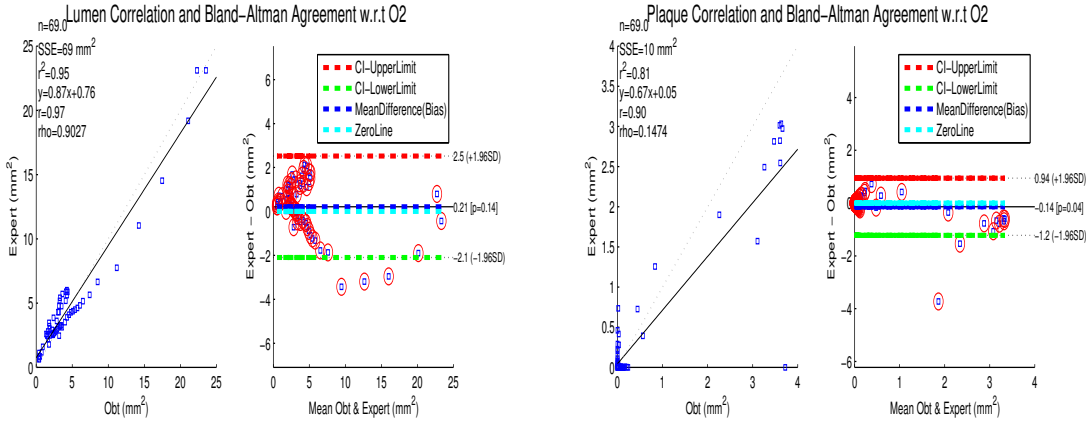

(c) Lumen obs2

(d) Plaque obs2

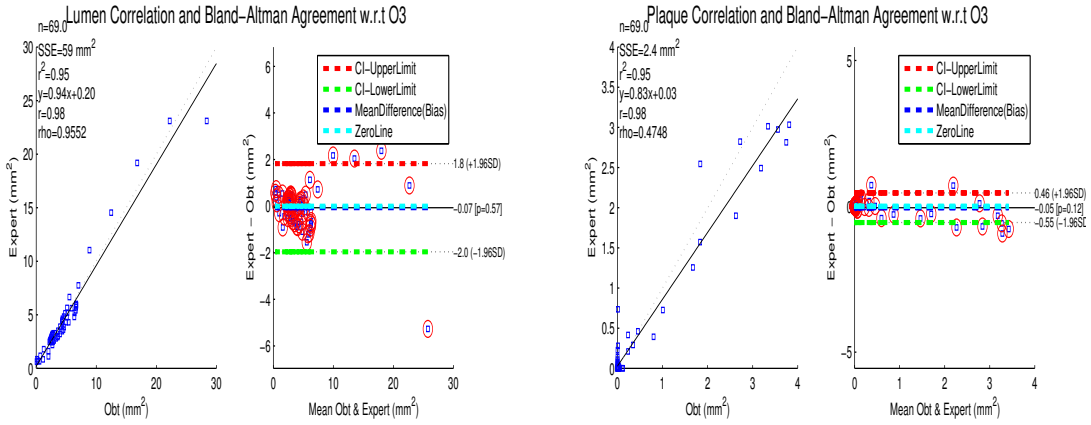

(e) Lumen obs3

(f) Plaque obs3

Fig. 6.26 Cross-section based analysis along the length of the segment with respect to three individual experts for DS4 seg1. Left (a, c, e) represents the obtained lumen area, whereas obtained plaque area is presented in right column (b, d, f). Both lumen and plaque area shows a good correlation and the Bland-Altman plots reflects an agreement within the 95% confidence interval.

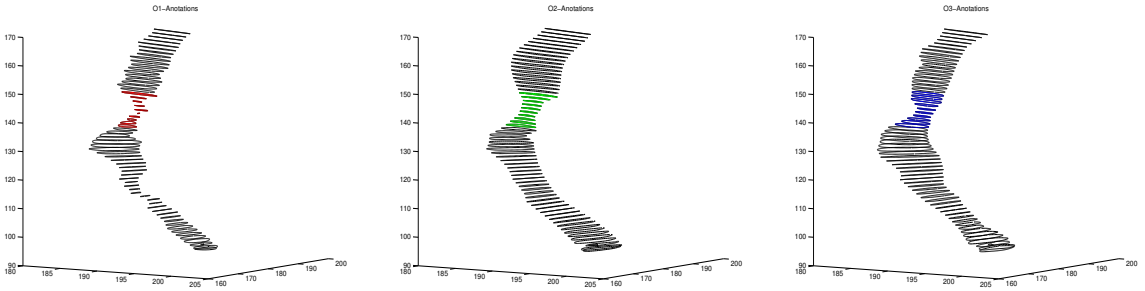

(a) observer 1 (b) observer 2 (c) observer 3

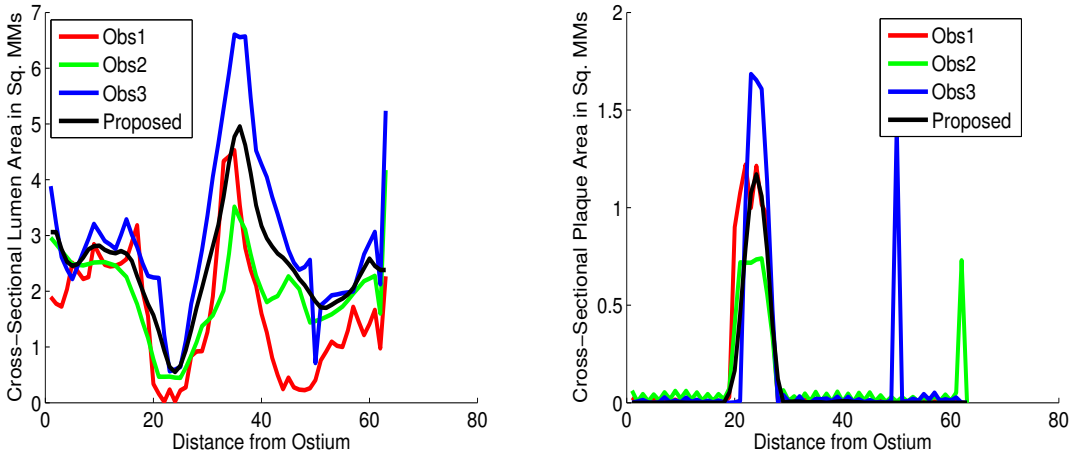

(d) Lumen area (e) Plaque area

Fig. 6.27 Lumen - plaque analysis w.r.t. manual observers for DS4 seg2. (a-c) lumen contours for three observers, (d-e) plots obtained cross-section based area for coronary lumen and non-calcified plaque respectively, with respect to annotations of three manual experts. Black is obtained area, whereas red, blue and green represent three observers.

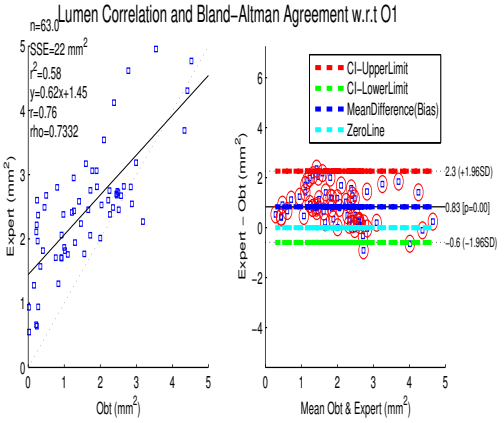

(a) Lumen obs1

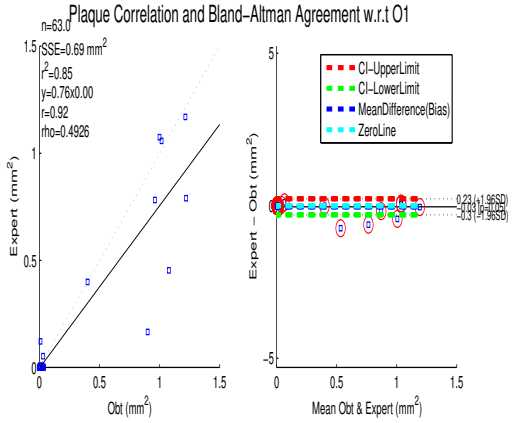

(b) Plaque obs1

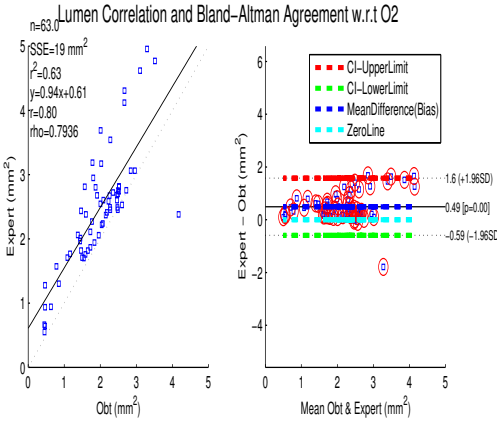

(c) Lumen obs2

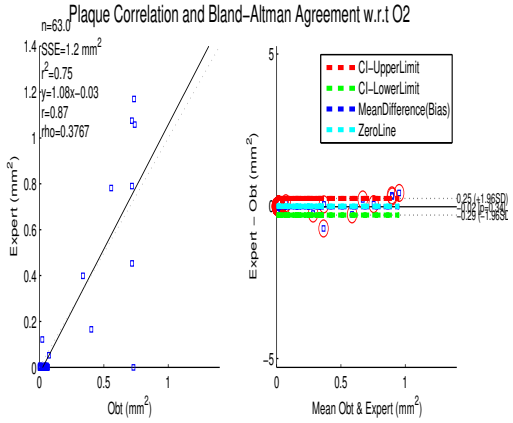

(d) Plaque obs2

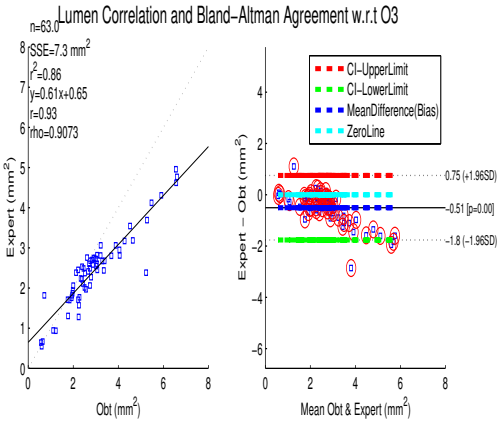

(e) Lumen obs3

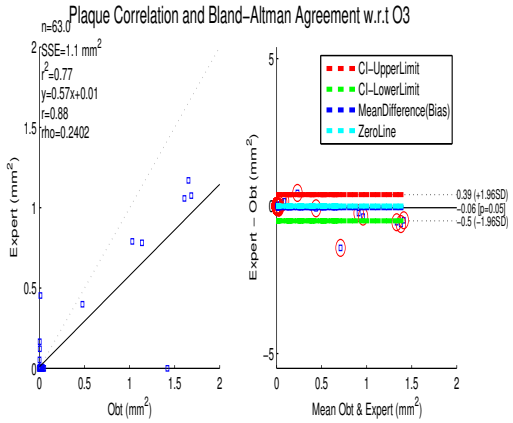

(f) Plaque obs3

Fig. 6.28 Cross-section based analysis along the length of the segment with respect to three individual experts for DS4 seg2. Left (a, c, e) represents the obtained lumen area, whereas obtained plaque area is presented in right column (b, d, f). Both lumen and plaque area shows a good correlation and the Bland-Altman plots reflects an agreement within the 95% confidence interval.

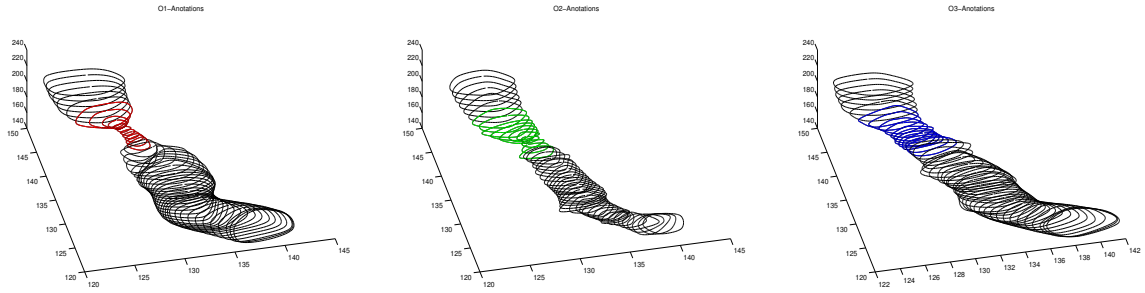

(a) observer 1 (b) observer 2 (c) observer 3

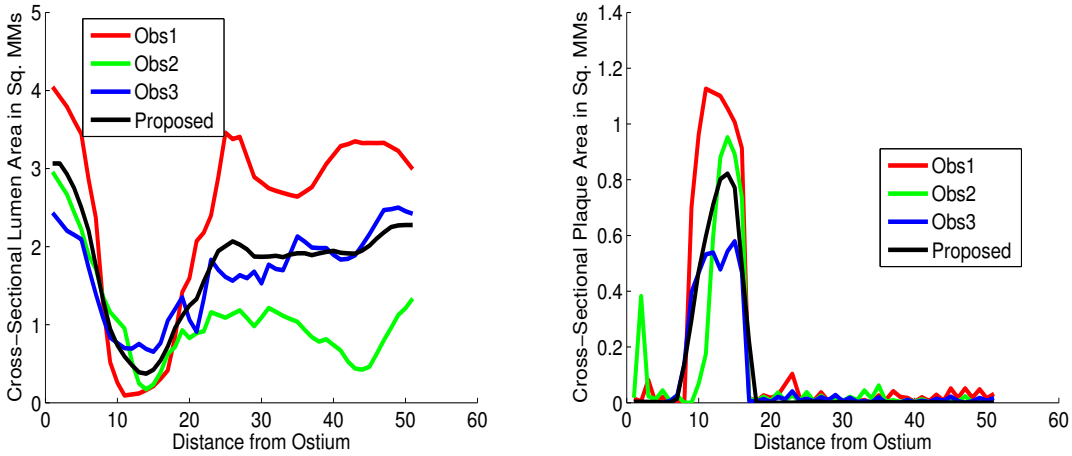

(d) Lumen Area (e) Plaque area

Fig. 6.29 Lumen - plaque analysis w.r.t. manual observers for DS7 seg2. (a-c) lumen contours for three observers, (d-e) plots obtained cross-section based area for coronary lumen and non-calcified plaque respectively, with respect to annotations of three manual experts. Black is obtained area, whereas red, blue and green represent three observers.

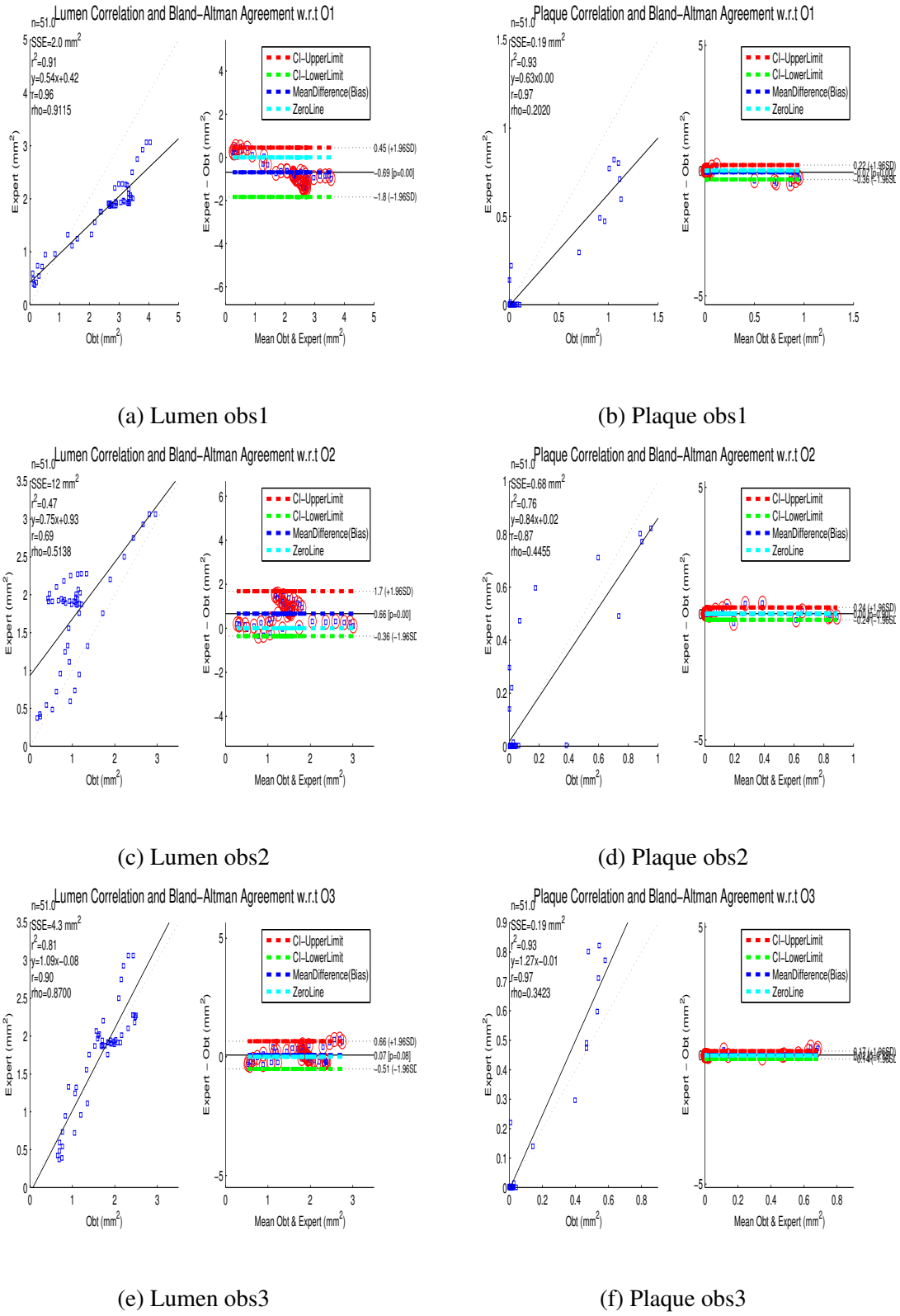

(a) Lumen obs1

(b) Plaque obs1

(c) Lumen obs2

(d) Plaque obs2

(e) Lumen obs3

(f) Plaque obs3

Fig. 6.30 Cross-section based analysis along the length of the segment with respect to three individual experts for DS7 seg2. Left (a, c, e) represents the obtained lumen area, whereas obtained plaque area is presented in right column (b, d, f). Both lumen and plaque area shows a good correlation and the Bland-Altman plots reflects an agreement within the 95% confidence interval.

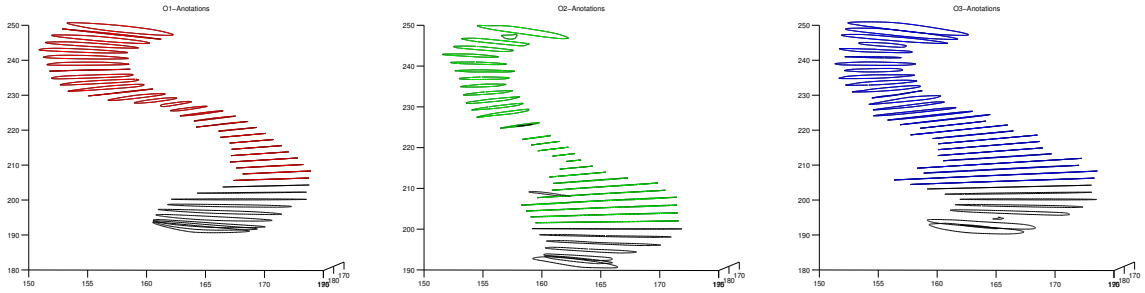

(a) observer 1 (b) observer 2 (c) observer 3

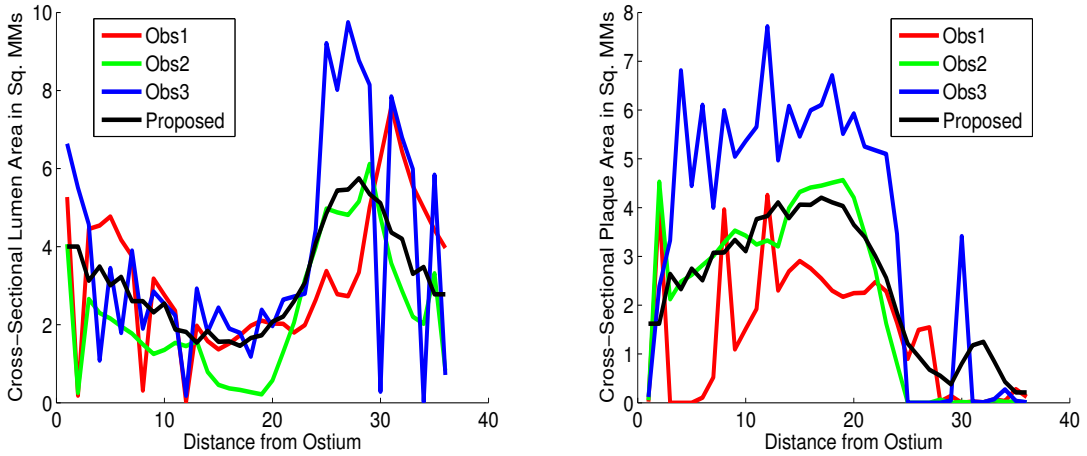

(d) Lumen area (e) Plaque area

Fig. 6.31 Lumen - plaque analysis w.r.t. manual observers for DS9 seg2. (a-c) lumen contours for three observers, (d-e) plots obtained cross-section based area for coronary lumen and non-calcified plaque respectively, with respect to annotations of three manual experts. Black is obtained area, whereas red, blue and green represent three observers.

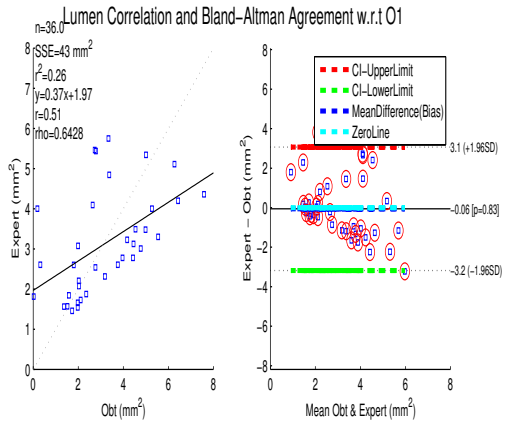

(a) Lumen obs1

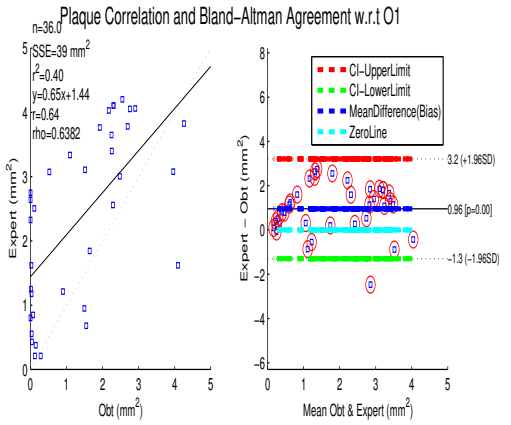

(b) Plaque obs1

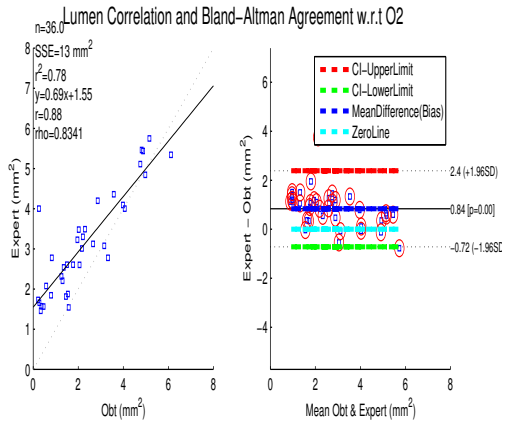

(c) Lumen obs2

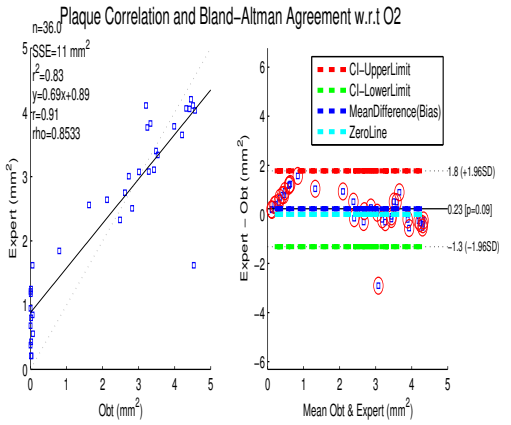

(d) Plaque obs2

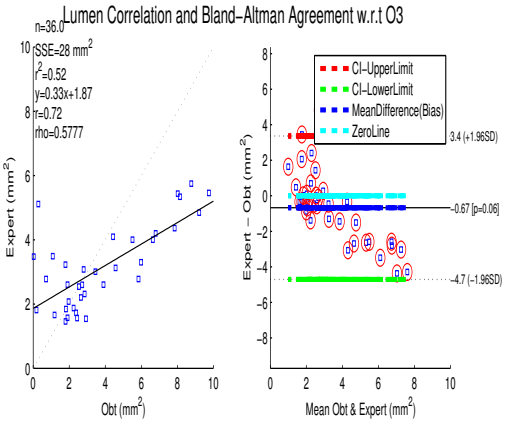

(e) Lumen obs3

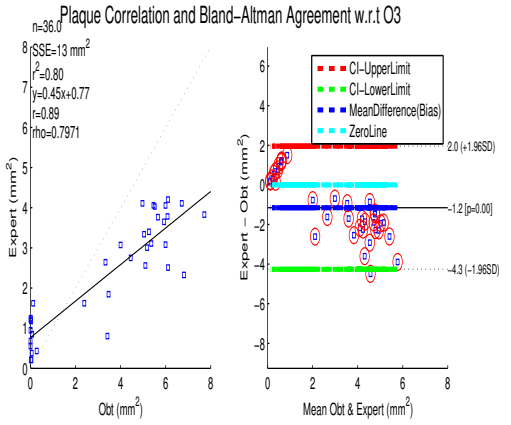

(f) Plaque obs3

Fig. 6.32 Cross-section based analysis along the length of the segment with respect to three individual experts for DS9 seg2. Left (a, c, e) represents the obtained lumen area, whereas obtained plaque area is presented in right column (b, d, f). Both lumen and plaque area shows a good correlation and the Bland-Altman plots reflects an agreement within the 95% confidence interval.

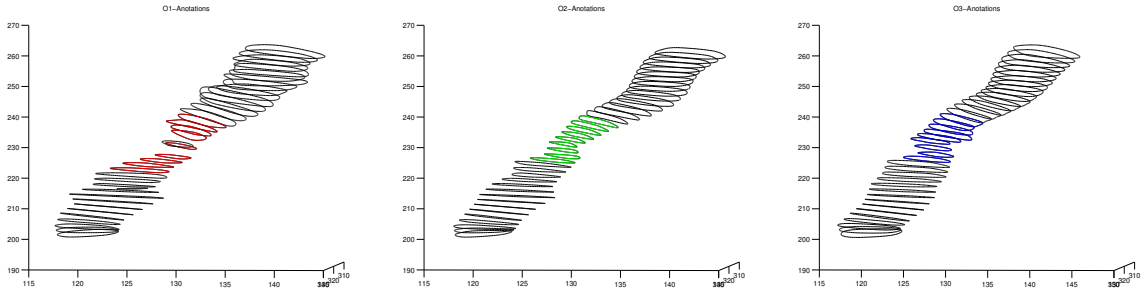

(a) observer 1 (b) observer 2 (c) observer 3

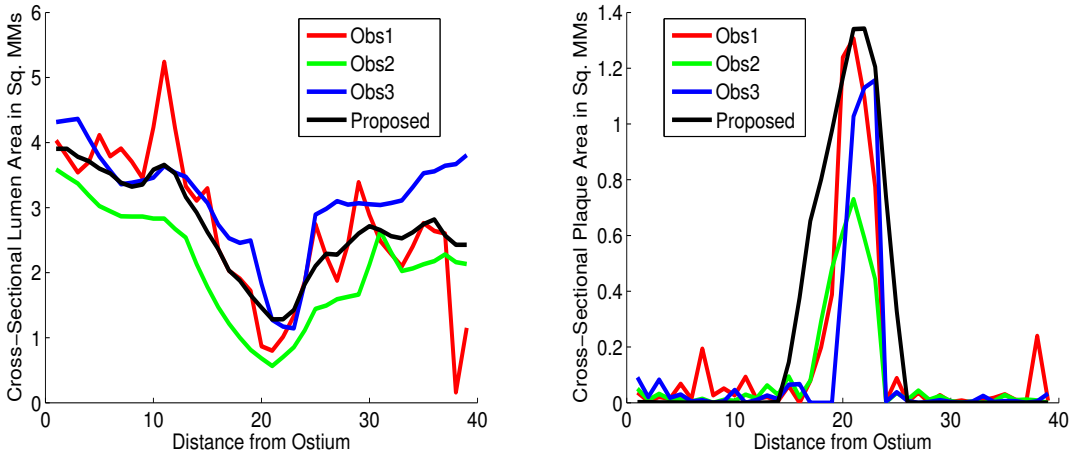

(d) Lumen area (e) Plaque area

Fig. 6.33 Lumen - plaque analysis w.r.t. manual observers for DS15 seg2. (a-c) lumen contours for three observers, (d-e) plots obtained cross-section based area for coronary lumen and non-calcified plaque respectively, with respect to annotations of three manual experts. Black is obtained area, whereas red, blue and green represent three observers.

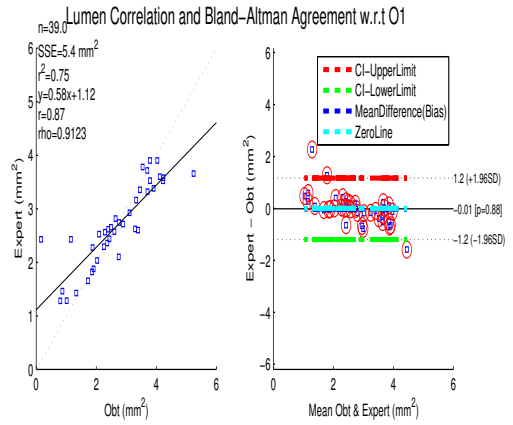

(a) Lumen obs1

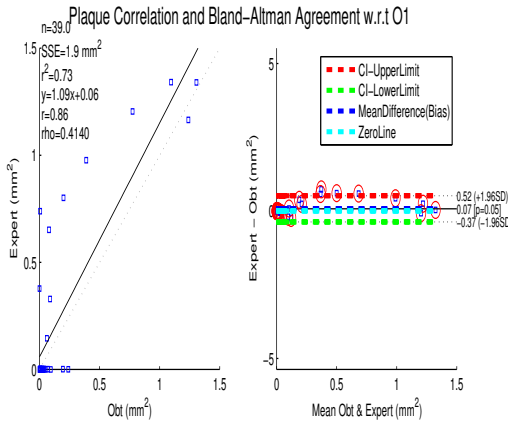

(b) Plaque obs1

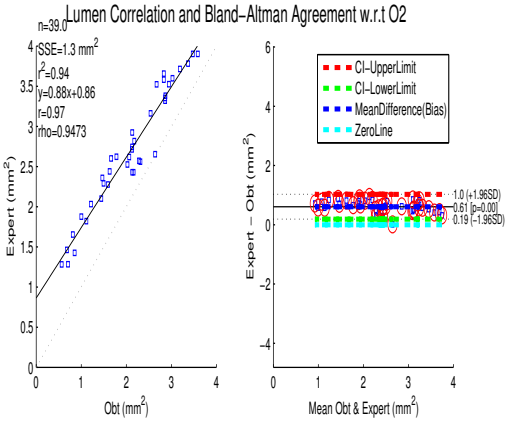

(c) Lumen obs2

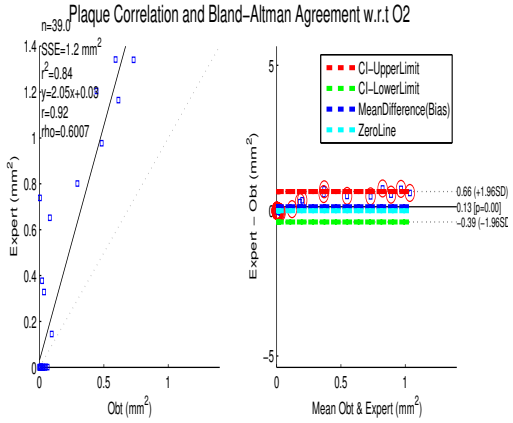

(d) Plaque obs2

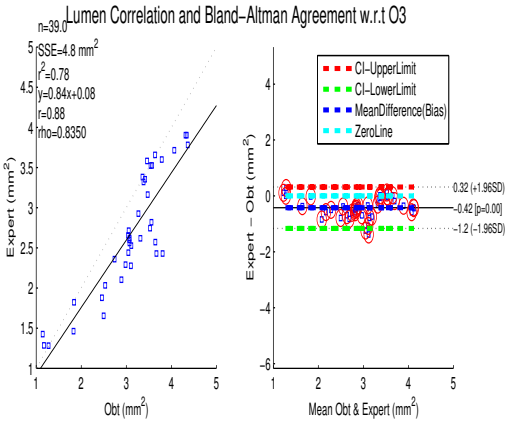

(e) Lumen obs3

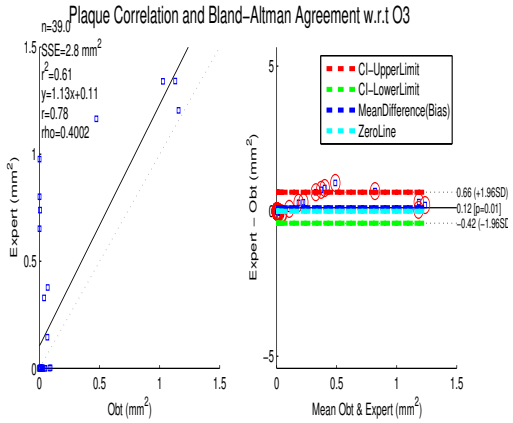

(f) Plaque obs3

Fig. 6.34 Cross-section based analysis along the length of the segment with respect to three individual experts for DS15 seg2. Left (a, c, e) represents the obtained lumen area, whereas obtained plaque area is presented in right column (b, d, f). Both lumen and plaque area shows a good correlation and the Bland-Altman plots reflects an agreement within the 95% confidence interval.

Chapter 7

Conclusion and Future Work

7.1 Introduction

This chapter concludes the proposed research and includes some recommendations for possible extensions of this work in future. The aim of this research has been the design of an automated system for detection, localization and quantification of non-calcified coronary plaques in cardiac CTA images, which could assist clinicians in the diagnosis of coronary heart disease.

It is important to mention that the explicit emphasis of this work is on the non-calcified plaques, since high intensity calcifications can be detected easily due to their bright appearance in CTA. In this context, this work has two main objectives. First, the development of an automated segmentation framework dedicated to the extraction of the coronary arteries in 3D contrast enhance coronary CT images. Second, the design of a reproducible plaque analysis method to detect, localize and quantify non-calcified plaque in the segmented coronary tree. The proposed framework is capable of producing a reliable estimation of the non-calcified plaques in the segmented coronary tree. Additionally, the proposed model can be operated in an automated fashion, which minimises the interaction from users and reduces the inter and intra-user variability in the quantification of non-calcified lesions.

Followed by this introduction, the remaining sections of this chapter are organised as follows: in section 7.2.1, we present the conclusions related to the coronary artery

segmentation techniques of Chapter 4. In section 7.2.2, the conclusions drawn from Chapter 5 are presented, i.e. algorithmic performance for detection and localization of non-calcified plaques. In the subsequent section, we present the voxel-wise plaque quantification method of Chapter 6. This is followed by a brief summary covering major contributions of this thesis. The possible extensions of this research and recommendations for future work are discussed in Section 7.5.

7.2 Conclusions

In context of the overall findings of the thesis, we present a brief chapter-wise conclusions in this section as follows:

7.2.1 Coronary Segmentation using Hybrid Image Energy

This chapter addresses the segmentation of coronary vasculature in 3D CTA volume. In the first part of this chapter, we demonstrated that adaptive modelling of the contrast medium intensity can considerably improve the accuracy of the coronary segmentation. In contrast, the use of a fixed intensity threshold across the dataset may decrease segmentation accuracy by capturing the nearby non-coronary segments or missing the distal parts of coronary tree. Subsequently, in the second part, we presented an efficient framework for image segmentation and demonstrated its efficacy for coronary delineation in a 3D CTA volume. In the proposed model, an image discontinuity model is combined with a localized active contour segmentation which achieves better overlap with manual annotations. The proposed method is less sensitive to the local optima problem which helps in reducing false positives as well as it allows a certain degree of freedom for initialization. The capability to address the variations in initial mask and localization radii simultaneously, makes our algorithm a feasible choice for the coronary segmentation. In the context of time complexity, we employed the sparse field method of Whitaker [77] to accurately evolve the curve using minimal representation.

A limitation of the proposed method is the manual selection of the appropriate weight β for the global term in hybrid energy formulation, as the true boundary is surpassed occasionally due to high influence of the global force. According to a series of experiments, the segmentation obtained with β less than 0.1 produces results similar to localization model of [16] due to very small influence of global term, whereas setting β greater than 0.25 results in suppression of distal segments due to very high influence of global term. This makes $\beta = [0.15 - 0.25]$ a feasible choice for effective segmentation of the coronary tree.

We also found that the Jaccard accuracy rates of the proposed method tend to decrease when approaching the distal and small segments of the arteries. However, clinically significant coronary lesions are usually identified in the main and proximal branches of the arteries, which can be well defined by the proposed model. Nevertheless, we can conclude that our technique is able to delineate the vessel boundaries in clinically important coronary segments with a level of variability similar to those obtained through manual segmentation. It should be noted that the fully automatic segmentation of the coronary tree has been a challenging problem so far and the current research is focused to minimize the human interaction. Several methods [139–141, 124, 142] have been proposed in recent years addressing the automatic and semi-automatic segmentation of coronary lumen with a motivation of stenosis detection; however, little attention has been paid to the negative remodelling of coronary vessels, which has been addressed in subsequent chapters of this thesis.

7.2.2 Detection and Localization of Non-calcified Plaque Regions

In this chapter, we proposed an efficient method for detection of the non-calcified plaques inside the segmented coronary tree using support vector machines (SVM). The innovative aspect of this work is statistical representation of coronary segments which leads to SVM based segregation of the abnormal segments. Moreover, this model precisely locates the position and approximate length of the non-calcified plaque in abnormal segment, which can be used in fully automated plaque quantification as explained in subsequent chapter. The overall accuracy of our plaque detection model is 88.4% against the manual observer ground truth with a sensitivity of 93.2% and specificity of 80.3%. Moreover, the Dice coefficient for

plaque localization in diseased segments is 83.2% with respect to clinical annotations. The proposed model was tested on three different CTA datasets individually and has produced consistent results, demonstrating its reproducibility for generic CTA data. In addition to manual ground truth comparison, we also compared our outcome with reported literature, and found very good agreement with plaque detection models of Wei *et al.* [112], Lankton *et al.* [99] and Tessmann *et al.* and [113].

The limitations of this work include an under-estimation of the long plaques in fully occluded segments and the low detection rate for the minor coronary segments due to the reduced diameter. This limitation is based on the fact that the manual annotation of the plaque region is performed in a relative context of lumen and the surrounding background. Especially, if there exist multiple low intensity lesions in a close proximity inside coronary segment, the human expert, in general demarcates the complete segment as plaque affected. Accordingly, the proposed method based on statistical evaluation of the segment leads to under-estimation with respect to manual ground truth. Another limitation of the proposed method is decreased detection rate for distal segments of the coronary tree. This is due to the fact that the vessel diameter becomes narrower in distal segments, consequently, the proposed concentric ring based representation of the segment fails to model the true lumen. However, as mentioned in context of coronary tree segmentation, clinically significant lesions are usually identified in the main and proximal branches of the arteries, which can be well evaluated by the proposed detection model. Moreover, it should be noted that plaques present in the distal segments are less threatening as they lead to minimal muscular damage with no fatalities.

7.2.3 Segmentation and Quantification of Non-Calcified Plaques

In this chapter, we extended the localization analysis for voxel-wise quantification of the non-calcified plaque in abnormal segments. We started with the formulation of voxel-wise ground truth using plaque positions detected in Chapter 5. In the subsequent step, vessel wall analysis was performed to compute the wall-thickness for normal coronary segments, which is found to be around 0.6mm for proximal segments. In the subsequent step, the plaque

effected region was investigated using a binary SVM classifier to differentiate lumen and non-calcified plaque voxels. Statistical quantification metrics shows a significant correlation with manual ground truth with a mean sensitivity, specificity, and accuracy of 88.59%, 81.59%, 87.86% respectively. After statistical evaluation of voxel-wise SVM classifier, we computed voxel based lumen and plaque area for respective segments and found a good agreement with respect to human experts.

7.3 Ethical Implications for the Automated Decision Framework

There is much emphasis in current Western healthcare systems on respect for autonomy; this is not to say that patients should be forced to make autonomous decisions (even if that were possible), but that they should be offered the tools needed for making such decisions [170]. A doctor cannot expect all her patients to have wide ranging clinical knowledge, and she must decide how much knowledge is required for a particular patient to be equipped to make a particular decision (paternalism). As the complexity of the medical condition increases the difficulty of giving the necessary information will increase; the range of treatments available, and the pros and cons of each may confuse patients. To avoid this, the doctor might decide that beneficence requires her to offer only a restricted range of treatment options that she deems most appropriate in the prevailing circumstances. It is important to mention that whatever balance is chosen between autonomy and paternalism, the patient trusts his doctor to decide what information he should receive, and to provide that information accurately. Where a decision support system (DSS) is involved in the process, it will have an important effect on the working of the doctor-patient relationship. Decision making in the doctor-patient relationship will inevitably be a balance between the patient's right to control his or her own life ("autonomy") and the doctor's duty to choose and prescribe the best course of treatment for the patient ("paternalism").

The design and implementation of DSSs should take into account the effect of the system on overall patient care. This research leads to a framework for automated diagnosis of the

non-calcified coronary plaques. In context of DSS, it can be used as an effective tool to enhance the clinician's diagnosis ability, however it does not suggest the possible care and medication. It is important to mention that the plaque analysis framework is designed merely as a diagnosis tool, able to detect the potential abnormalities; however, the interpretation of the results lie with the experienced cardiologist. The software will point out regions that are suspected of soft plaques, but the cardiologist will have the ultimate responsibility of analysing the data. In conclusion, the eventual incorporation of this plaque analysis tool into normal practice will depend on many factors, among them the most important is education of doctors regarding use and potential abuse. Moreover, the plaque detection accuracy of the software is around 88.4%, making the framework a reasonable diagnosis tool; however, the immature plaques may be missed in this framework at early stages. These undeveloped plaques does not pose severe clinical threat; however, for suspected patients, the clinician can advise a new CTA exam after a certain amount of time for investigation of possible false negatives.

7.4 Contributions of this Thesis

The contributions of this research, i.e., those that form the basis of the thesis, are to be found in two main areas, associated with the segmentation of the coronary vasculature and quantitative plaque analysis in the segmented tree, described in Chapters 4, 5 and 6, respectively. Specifically, the contributions of this thesis are summarised as follows:

We demonstrated that adaptive modelling of the contrast medium intensity can considerably improve the accuracy of the coronary segmentation. In contrast, the use of a fixed intensity threshold across the dataset may decrease precision by capturing the nearby non-coronary segments or missing the distal parts of coronary tree. The usefulness and originality of these contributions is reflected in the promising results validating a significant improvement in segmentation accuracy which have produced two journal publications [39, 40].

Moreover, we introduced a hybrid energy formulation that integrates the local intensity and a probability based global discontinuity map of the image. The proposed hybrid energy based model captures object boundaries accurately as the hybrid energy is less attracted to the local optima solutions. Accordingly, the hybrid energy provides robustness against the initialization and localization radius simultaneously. Furthermore, we introduced an auto-correction feature for the mask, which captures the emerging peripheries during the evolution process. The superiority of the proposed model is illustrated by comparing the segmentation performance against manual ground truth and the coronary segmentation model of Yang *et al.* [17]. This chapter leads to a journal publication [41].

After coronary tree segmentation, we extended our work for detection and localization of the non-calcified plaques using discrete radial profiles in clinical CTA. We demonstrated that the abnormal intensity drops resulting from soft plaque inside coronary vessels can be captured using concentric rings along the vessel centreline. Subsequently, we employed a machine learning framework (support vector machine) for segregating non-calcified plaque affected coronary segments from normal sections. The plaque detection is performed using the windowed statistics to uncover abnormalities in a relative context rather then evaluating individual cross sections as proposed in [116]. Experimental results demonstrate that the proposed method achieves a good agreement (detection accuracy of 88.4% with respect to manual annotations), and in-line with anomaly detection methods of [113], [116]. It should be noted that the explicit detection of the soft plaques is a challenging clinical problem. In this context, a number of local features proposed in [113] and [116] fails to detect the fragile low-intensity soft plaques; hence, the detection rate for the non-calcified plaques is significantly lower then the calcified plaque detections in [113] (i.e. 79.62% versus 94.05%). This chapter leads to two quality publications [42, 43].

7.5 Future Work

7.5.1 Automated Selection of Global Weight

Although the proposed hybrid energy formulation leads good results for coronary segmentation in clinical CTA; the selection of the global weight β is based upon an empirical investigation in this study. Accordingly, we evaluated different values for β from the normalized range $[0, 0.01, 0.05, 0.10, 0.15, 0.25, 0.50, 0.75, 1.0]$ to determine the best global weight. Subsequently, based upon a series of experiments, we observed that the segmentation obtained with β less than 0.1 produces results similar to localization model of [16] due to less influence of global term, whereas setting β greater than 0.25 results in suppression of distal segments due to very high influence of global term. A possible extension for this work could be the automatic selection of the global weight β with respect to the localization radii to fully automate the segmentation framework. A possible way is use of the machine learning to regress β based on hand-crafted features.

7.5.2 Quantification of Functional Significance of Atherosclerotic Lesions

Coronary CTA has strengths in excluding the presence of significant coronary diseases;however, it performs less well in terms of its positive predictive accuracy, often resulting in unnecessary catheterisation. This is mainly because coronary occlusions, with no significant effects on the function of coronary circulation, cannot be distinguished from those associated with a higher risk of developing myocardial ischemia by means of static coronary CT images. Fractional Flow Reserve (FFR), a technique measuring pressure differences between a stenotic artery and its normal proximal segments, is the current golden standard for diagnosis of myocardial ischemia [171].

Complications associated with the conventional invasive FFR procedure, however, restrict its application to a certain groups of patients with hypertension and hypercholesterolemia. Recent advances in image-based blood flow analysis have provided a non-invasive alternative

for the assessment of the functional significance of the coronary lesions. Preliminary research suggested that diagnostic results obtained from virtual FFR based on coronary CT angiograms have a high degree of correlation with conventional FFR [171]. Through the application of Computational Fluid Dynamics (CFD) in simulating blood flow in the cardiovascular system, haemodynamic parameters, such as velocity, stress/pressure as well as shear stress distribution, can be estimated in silico, which could provide the clinician with essential information in determining the associated risk for a patient. Functional information, obtained from a patient specific geometric model of the artery, may potentially enhance the diagnostic capability of standard coronary CT in high risk patients, without changing the imaging protocol. The framework presented in this thesis allows the construction of patient-specific models of coronary arteries, which in turn could be used as a starting point for analysing the fluid mechanical properties of blood flow in the coronary circulation.

7.5.3 Clinical Validation of the Proposed Segmentation Framework with Invasive Standards

In this research, the accuracy and capability of the proposed system was quantified by comparing the segmented arteries and non-calcified plaque with manual delineation respectively, which lacks validation with an invasive standard such as cardiac catheterisation or intravascular ultrasound. In order to determine the true clinical applicability of the proposed framework, a comparison of the diagnostic results obtained through the proposed algorithms with the actual diagnosis based on standard invasive procedure is required to carry out a per-vessel and per-patient basis.

7.5.4 Deep Learning Based Plaque Segmentation

Another possible extension of the current work can be replacement of the hand-crafted features with a convolutional neural network (CNN) to take maximal advantage of machine learning procedures; however, this requires a large repository of CTA data. We believe this

can serve as an important step forward towards the automated quantification of the soft plaques, which have been identified as the major reason of fatal cardiac events.

References

[1] National Lung Heart and Blood Institute. What Are the Signs and Symptoms of Coronary Heart Disease?, 2017.

[2] The Society of Thoracic Surgeons. Coronary Artery Diseasesigns and symptoms, 2017.

[3] Jesse Habets, Renee BA van den Brink, Ruben Uijlings, Anje M Spijkerboer, P Th M Willem, Steven AJ Chamuleau, and Ricardo PJ Budde. Coronary artery assessment by multidetector computed tomography in patients with prosthetic heart valves. *European radiology*, 22(6):1278–1286, 2012.

[4] Gilbert L Raff, Aiden Abidov, Stephan Achenbach, Daniel S Berman, Lawrence M Boxt, Matthew J Budoff, Victor Cheng, Tony DeFrance, Jeffrey C Hellinger, Ronald P Karlsberg, et al. Scct guidelines for the interpretation and reporting of coronary computed tomographic angiography. *Journal of cardiovascular computed tomography*, 3(2):122–136, 2009.

[5] Heart Research Institute. Heart Diseases, what is athreoscelerosis, 2017.

[6] Yin Wang. *Blood vessel segmentation and shape analysis for quantification of coronary artery stenosis in CT angiography*. PhD thesis, City, University of London, 2011.

[7] Paolo Pavone, Massimo Fioranelli, and David A Dowe. *CT evaluation of coronary artery disease*. Springer Science & Business Media, 2009.

[8] Herve Lombaert. Level set method:, explanation. Available at http://profs.etsmtl.ca/hlombaert/levelset/(2017/08/08).

[9] Peter J Yim, Juan J Cebral, Rakesh Mullick, Hani B Marcos, and Peter L Choyke. Vessel surface reconstruction with a tubular deformable model. *IEEE transactions on medical imaging*, 20(12):1411–1421, 2001.

[10] Melvin E Clouse, Adeel Sabir, Chun-Shan Yam, Norihiko Yoshimura, Shezhang Lin, Francine Welty, Pedro Martinez-Clark, and Vassilios Raptopoulos. Measuring noncalcified coronary atherosclerotic plaque using voxel analysis with mdct angiography: a pilot clinical study. *American Journal of Roentgenology*, 190(6):1553–1560, 2008.

[11] Felix Renard and Yongyi Yang. Image analysis for detection of coronary artery soft plaques in mdct images. In *2008 5th IEEE International Symposium on Biomedical Imaging: From Nano to Macro*, pages 25–28. IEEE, 2008.

[12] Ying Li, Wei Chen, Kaijun Liu, Yi Wu, Yonglin Chen, Chun Chu, Bingji Fang, Liwen Tan, and Shaoxiang Zhang. A voxel-map quantitative analysis approach for atherosclerotic noncalcified plaques of the coronary artery tree. *Computational and mathematical methods in medicine*, 20, 2013.

[13] P. Mirunalini and C. Aravindan. Automatic segmentation of coronary arteries and detection of stenosis. In *2013 IEEE International Conference of IEEE Region 10 (TENCON 2013)*, pages 1–4, Oct 2013.

[14] Dongjin Han, Nam-Thai Doan, Hackjoon Shim, Byunghwan Jeon, Hyunna Lee, Youngtaek Hong, and Hyuk-Jae Chang. A fast seed detection using local geometrical feature for automatic tracking of coronary arteries in cta. *Computer methods and programs in biomedicine*, 117(2):179–188, 2014.

[15] Alejandro F Frangi, Wiro J Niessen, Koen L Vincken, and Max A Viergever. Multiscale vessel enhancement filtering. In *International Conference on Medical Image Computing and Computer-Assisted Intervention*, pages 130–137. Springer, 1998.

[16] Shawn Lankton and Allen Tannenbaum. Localizing region-based active contours. *IEEE transactions on image processing*, 17(11):2029–2039, 2008.

[17] Yan Yang, Allen Tannenbaum, Don Giddens, and Arthur Stillman. Automatic segmentation of coronary arteries using bayesian driven implicit surfaces. In *2007 4th IEEE International Symposium on Biomedical Imaging: From Nano to Macro*, pages 189–192. IEEE, 2007.

[18] HA Kirisli and Michiel. Schaap. Standardized evaluation framework for evaluating coronary artery stenosis detection, stenosis quantification and lumen segmentation algorithms in computed tomography angiography. *Medical image analysis*, 17(8):859–876, 2013.

[19] Quanquan Gu, Zhenhui Li, and Jiawei Han. Generalized fisher score for feature selection. *arXiv preprint arXiv:1202.3725*, 2012.

[20] Véronique L Roger, Alan S Go, Donald M Lloyd-Jones, Emelia J Benjamin, Jarett D Berry, William B Borden, Dawn M Bravata, Shifan Dai, Earl S Ford, Caroline S Fox, et al. Heart disease and stroke statistics 2012 update. *Circulation*, 125(1):e2–e220, 2012.

[21] Gertrude Maatman. *High-Resolution Computed Tomography of the Paranasal Sinuses and Pharynx and Related Regions: Impact of CT identification on diagnosis and patient management*, volume 12. Springer Science & Business Media, 2012.

[22] Ella A Kazerooni and Barry H Gross. *Cardiopulmonary imaging*, volume 4. Lippincott Williams & Wilkins, 2004.

[23] Lois E Romans. *Computed tomography for technologists: Exam review*. Lippincott Williams & Wilkins, 2010.

[24] World Health Organization. Cardiovascular diseases CVDs, the global statistics. Available at http://www.who.int/mediacentre/factsheets/fs317/en/(2016/11/11).

[25] Jason M Tarkin, Marc R Dweck, Nicholas R Evans, Richard AP Takx, Adam J Brown, Ahmed Tawakol, Zahi A Fayad, and James HF Rudd. Imaging atherosclerosis. *Circulation research*, 118(4):750–769, 2016.

[26] Teruyoshi Kume, Takashi Akasaka, Takahiro Kawamoto, Nozomi Watanabe, Eiji Toyota, Yoji Neishi, Renan Sukmawan, Yoshito Sadahira, and Kiyoshi Yoshida. Assessment of coronary arterial plaque by optical coherence tomography. *The American journal of cardiology*, 97(8):1172–1175, 2006.

[27] Paul G Yock and Peter J Fitzgerald. Intravascular ultrasound: state of the art and future directions. *The American journal of cardiology*, 81(7):27E–32E, 1998.

[28] Peter J Fitzgerald, FG St Goar, Andrew J Connolly, Fausto J Pinto, Margaret E Billingham, Richard L Popp, and Paul G Yock. Intravascular ultrasound imaging of coronary arteries. is three layers the norm? *Circulation*, 86(1):154–158, 1992.

[29] Thomas Flohr and Bernd Ohnesorge. Multi-slice ct technology. In *Multi-slice and Dual-source CT in Cardiac Imaging*, pages 41–69. Springer, 2007.

[30] David C. Levin, Michael Savage, and David Fischman. Coronary CTA, a cost-effective alternative to cardiac catheterization for the evaluation of cad, study suggests. Available at https://www.sciencedaily.com/releases/2010/04/100421162617.htm(2016/12/07).

[31] Lars Husmann, Hatem Alkadhi, Thomas Boehm, Sebastian Leschka, Tiziano Schepis, Pascal Koepfli, Lotus Desbiolles, Borut Marincek, Philipp A Kaufmann, and Simon Wildermuth. Influence of cardiac hemodynamic parameters on coronary artery opacification with 64-slice computed tomography. *European Radiology*, 16(5):1111–1116, 2006.

[32] Alexander W Leber, Andreas Knez, Alexander Becker, Christoph Becker, Franz von Ziegler, Konstantin Nikolaou, Carsten Rist, Maximilian Reiser, Carl White, Gerhard Steinbeck, et al. Accuracy of multidetector spiral computed tomography in identifying and differentiating the composition of coronary atherosclerotic plaques: a comparative study with intracoronary ultrasound. *Journal of the American College of Cardiology*, 43(7):1241–1247, 2004.

[33] Sergio Waxman, Fumiyuki Ishibashi, and James E Muller. Detection and treatment of vulnerable plaques and vulnerable patients novel approaches to prevention of coronary events. *Circulation*, 114(22):2390–2411, 2006.

[34] Anne C Brisset, Brant E Isakson, and Brenda R Kwak. Connexins in vascular physiology and pathology. *Antioxidants & redox signaling*, 11(2):267–282, 2009.

[35] Sergio Waxman, Fumiyuki Ishibashi, and James E Muller. Global, regional, and national age-sex specific all-cause and cause-specific mortality for 240 causes of death, 1990-2013: a systematic analysis for the global burden of disease study 2013. *Lancet*, 385(9963):117–171, 2015.

[36] United Kingdom NHS. Coronary Heart Disease, statistics for united kingdom, 2016.

[37] Vitali Gorenoi, Matthias P Schönermark, and Anja Hagen. Ct coronary angiography vs. invasive coronary angiography in chd. *GMS health technology assessment*, 8, 2012.

[38] Sylvia Glasser, Steffen Oeltze, Anja Hennemuth, Christoph Kubisch, A Mahnken, Skadi Wilhelmsen, and Bernhard Preim. Automatic transfer function specification for visual emphasis of coronary artery plaque. In *Computer Graphics Forum*, volume 29, pages 191–201. Wiley Online Library, 2010.

[39] Muhammad Moazzam Jawaid, Ronak Rajani, Panos Liatsis, Constantino Carlos Reyes-Aldasoro, and Greg Slabaugh. Improved cta coronary segmentation with a volume-specific intensity threshold. In *Annual Conference on Medical Image Understanding and Analysis*, pages 207–218. Springer, 2017.

[40] Muhammad Moazzam Jawaid, Panos Liatsis, and Sanam Narejo. Automated extraction of the coronary tree by integrating localized aorta-based intensity distribution statistics in active contour segmentation. In *Developments of E-Systems Engineering (DeSE), 2015 International Conference on*, pages 83–87. IEEE, 2015.

[41] Muhammad Moazzam Jawaid, Ronak Rajani, Panos Liatsis, Constantino Carlos Reyes-Aldasoro, and Greg Slabaugh. A hybrid energy model for region based curve evolution-application to CTA coronary segmentation. *Computer Methods and Programs in Biomedicine*, 144C:189–202, 2017.

[42] Muhammad Moazzam Jawaid, Bhawani Shankar Chowdhry, and Greg Slabaugh. Automated framework for cta coronary segmentation and quantitative validation. In *Innovations in Electrical Engineering and Computational Technologies (ICIEECT), 2017 International Conference on*, pages 1–7. IEEE, 2017.

[43] Muhammad Moazzam Jawaid, Atif Riaz, Ronak Rajani, Constantino Carlos Reyes-Aldasoro, and Greg Slabaugh. Framework for detection and localization of coronary non-calcified plaques in cardiac cta using mean radial profiles. *Computers in Biology and Medicine*, 89(C):84–95, 2017.

[44] Vishy Mahadevan. Anatomy of the heart. *Surgery (Oxford)*, 26(12):473–476, 2008.

[45] Robert H Whitaker. Anatomy of the heart. *Medicine*, 38(7):333–335, 2010.

[46] Frank Henry Netter, Sharon Colacino, et al. *Atlas of human anatomy*. Ciba-Geigy Corporation, 1989.

[47] Robert Matthew Hay McMinn, Ralph T Hutchings, John Pegington, and Peter Abrahams. *A colour atlas of human anatomy*. Year Book Medical Publishers, 1988.

[48] Encyclopedia Wikipedia. Coronary artery disease, statistics and accociated risk factors in diagnosis, 2016.

[49] Thomas Thom, Nancy Haase, Wayne Rosamond, Virginia J Howard, John Rumsfeld, Teri Manolio, Zhi-Jie Zheng, Katherine Flegal, Christopher O'donnell, Steven Kittner, et al. Heart disease and stroke statistics–2006 update: a report from the american heart association statistics committee and stroke statistics subcommittee. *Circulation*, 113(6):e85, 2006.

[50] Renu Virmani, Allen P Burke, Andrew Farb, and Frank D Kolodgie. Pathology of the vulnerable plaque. *Journal of the American College of Cardiology*, 47(8s1):C13–C18, 2006.

[51] Ik-Kyung Jang, Brett E Bouma, Dong-Heon Kang, Seung-Jung Park, Seong-Wook Park, Ki-Bae Seung, Kyu-Bo Choi, Milen Shishkov, Kelly Schlendorf, Eugene Pomerantsev, et al. Visualization of coronary atherosclerotic plaques in patients using optical coherence tomography: comparison with intravascular ultrasound. *Journal of the American College of Cardiology*, 39(4):604–609, 2002.

[52] Christoph Kubisch, Sylvia Glaßer, Mathias Neugebauer, and Bernhard Preim. Vessel visualization with volume rendering. *Visualization in Medicine and Life Sciences II*, pages 109–132, 2012.

[53] Wisnumurti Kristanto, Peter MA van Ooijen, Marcel JW Greuter, Jaap M Groen, Rozemarijn Vliegenthart, and Matthijs Oudkerk. Non-calcified coronary atherosclerotic plaque visualization on ct: effects of contrast-enhancement and lipid-content fractions. *The international journal of cardiovascular imaging*, 29(5):1137–1148, 2013.

[54] Rafael C Gonzalez and Richard E Woods. Digital image processing prentice hall. *Upper Saddle River, NJ*, 2002.

[55] Nikhil R Pal and Sankar K Pal. A review on image segmentation techniques. *Pattern recognition*, 26(9):1277–1294, 1993.

[56] King-Sun Fu and JK Mui. A survey on image segmentation. *Pattern recognition*, 13(1):3–16, 1981.

[57] Robert M Haralick and Linda G Shapiro. Image segmentation techniques. *Computer vision, graphics, and image processing*, 29(1):100–132, 1985.

[58] Dzung L Pham, Chenyang Xu, and Jerry L Prince. Current methods in medical image segmentation. *Annual review of biomedical engineering*, 2(1):315–337, 2000.

[59] Hassana Grema Kaganami and Zou Beiji. Region-based segmentation versus edge detection. In *Intelligent Information Hiding and Multimedia Signal Processing, 2009. IIH-MSP'09. Fifth International Conference on*, pages 1217–1221. IEEE, 2009.

[60] James A Sethian et al. Level set methods and fast marching methods. *Journal of Computing and Information Technology*, 11(1):1–2, 2003.

[61] Stanley Osher and Ronald Fedkiw. *Level set methods and dynamic implicit surfaces*, volume 153. Springer Science & Business Media, 2006.

[62] Michael Kass, Andrew Witkin, and Demetri Terzopoulos. Snakes: Active contour models. *International journal of computer vision*, 1(4):321–331, 1988.

[63] Vicent Caselles, Ron Kimmel, and Guillermo Sapiro. Geodesic active contours. *International journal of computer vision*, 22(1):61–79, 1997.

[64] Tony F Chan and Luminita A Vese. Active contours without edges. *IEEE Transactions on image processing*, 10(2):266–277, 2001.

[65] Anthony Yezzi, Andy Tsai, and Alan Willsky. A fully global approach to image segmentation via coupled curve evolution equations. *Journal of Visual Communication and Image Representation*, 13(1):195–216, 2002.

[66] Chunming Li, Chiu-Yen Kao, John C Gore, and Zhaohua Ding. Implicit active contours driven by local binary fitting energy. In *2007 IEEE Conference on Computer Vision and Pattern Recognition*, pages 1–7. IEEE, 2007.

[67] John Canny. A computational approach to edge detection. *IEEE Transactions on pattern analysis and machine intelligence*, (6):679–698, 1986.

[68] Poonam Dhankhar and Neha Sahu. A review and research of edge detection techniques for image segmentation. *International Journal of Computer Science and Mobile Computing (IJCSMC)*, 2(7):86–92, 2013.

[69] Richard O Duda and Peter E Hart. Use of the hough transformation to detect lines and curves in pictures. *Communications of the ACM*, 15(1):11–15, 1972.

[70] Saburo Tsuji and Fumio Matsumoto. Detection of ellipses by a modified hough transformation. *IEEE transactions on computers*, (8):777–781, 1978.

[71] Huimin Lu, Yujie Li, Yingying Wang, Seiichi Serikawa, Bolong Chen, and Jinyi Chang. Active contours model for image segmentation: A review. In *The 1st International Conference on Industrial Application Engineering 2013 (ICIAE2013)*, 2013.

[72] Tim McInerney and Demetri Terzopoulos. Deformable models in medical image analysis: a survey. *Medical image analysis*, 1(2):91–108, 1996.

[73] Demetri Terzopoulos, Andrew Witkin, and Michael Kass. Constraints on deformable models: Recovering 3d shape and nonrigid motion. *Artificial intelligence*, 36(1):91–123, 1988.

[74] Vicent Caselles, Francine Catté, Tomeu Coll, and Françoise Dibos. A geometric model for active contours in image processing. *Numerische mathematik*, 66(1):1–31, 1993.

[75] Vicent Caselles. Geometric models for active contours. In *Image Processing, 1995. Proceedings., International Conference on*, volume 3, pages 9–12. IEEE, 1995.

[76] Ravi Malladi, James A Sethian, and Baba C Vemuri. Shape modeling with front propagation: A level set approach. *IEEE transactions on pattern analysis and machine intelligence*, 17(2):158–175, 1995.

[77] Ross Whitaker and David Breen. Level-set models for the deformation of solid objects. In *Proceedings of the Third International Workshop on Implicit Surfaces*, pages 19–35, 1998.

[78] Guopu Zhu, Shuqun Zhang, Qingshuang Zeng, and Changhong Wang. Boundary-based image segmentation using binary level set method. *Optical Engineering*, 46(5):050501–050501, 2007.

[79] Tony F Chan, B Yezrielev Sandberg, and Luminita A Vese. Active contours without edges for vector-valued images. *Journal of Visual Communication and Image Representation*, 11(2):130–141, 2000.

[80] Luca Antiga, Bogdan Ene-Iordache, and Andrea Remuzzi. Computational geometry for patient-specific reconstruction and meshing of blood vessels from mr and ct angiography. *IEEE Transactions on medical imaging*, 22(5):674–684, 2003.

[81] HAF Gratama van Andel, E Meijering, Aad van der Lugt, Henri A Vrooman, and Rik Stokking. Vampire: Improved method for automated center lumen line definition in atherosclerotic carotid arteries in cta data. In *International Conference on Medical Image Computing and Computer-Assisted Intervention*, pages 525–532. Springer, 2004.

[82] Monica Hernandez, Alejandro F Frangi, and Guillermo Sapiro. Three-dimensional segmentation of brain aneurysms in cta using non-parametric region-based information and implicit deformable models: Method and evaluation. In *International Conference on Medical Image Computing and Computer-Assisted Intervention*, pages 594–602. Springer, 2003.

[83] Yuanzhi Cheng, Xin Hu, Ji Wang, Yadong Wang, and Shinichi Tamura. Accurate vessel segmentation with constrained b-snake. *IEEE Transactions on Image Processing*, 24(8):2440–2455, 2015.

[84] Coert Metz, Michiel Schaap, Alina Van Der Giessen, Theo Van Walsum, and Wiro Niessen. Semi-automatic coronary artery centerline extraction in computed tomography angiography data. In *Biomedical Imaging: From Nano to Macro, 2007. ISBI 2007. 4th IEEE International Symposium on*, pages 856–859. IEEE, 2007.

[85] Jun Feng and Horace Ho-Shing Ip. A statistical assembled model for segmentation of entire 3d vasculature. In *Pattern Recognition, 2006. ICPR 2006. 18th International Conference on*, volume 4, pages 95–98. IEEE, 2006.

[86] L Flórez Valencia, Johan Montagnat, and Maciej Orkisz. 3d models for vascular lumen segmentation in mra images and for artery-stenting simulation. *IRBM*, 28(2):65–71, 2007.

[87] Stefan Wörz and Karl Rohr. A new 3d parametric intensity model for accurate segmentation and quantification of human vessels. *Medical Image Computing and Computer-Assisted Intervention–MICCAI 2004*, pages 491–499, 2004.

[88] S Olabarriaga, Marcel Breeuwer, and W Niessen. Minimum cost path algorithm for coronary artery central axis tracking in ct images. *Medical Image Computing and Computer-Assisted Intervention-MICCAI 2003*, pages 687–694, 2003.

[89] Brian Avants and James Williams. An adaptive minimal path generation technique for vessel tracking in cta/ce-mra volume images. In *Medical Image Computing and Computer-Assisted Intervention–MICCAI 2000*, pages CH402–CH402. Springer, 2000.

[90] Hua Li and Anthony Yezzi. Vessels as 4d curves: Global minimal 4d paths to extract 3d tubular surfaces. In *Computer Vision and Pattern Recognition Workshop, 2006. CVPRW'06. Conference on*, pages 82–82. IEEE, 2006.

[91] Onno Wink, Wiro J Niessen, and Max A Viergever. Fast delineation and visualization of vessels in 3-d angiographic images. *IEEE transactions on medical imaging*, 19(4):337–346, 2000.

[92] Delphine Nain, Anthony Yezzi, and Greg Turk. Vessel segmentation using a shape driven flow. *Medical Image Computing and Computer-Assisted Intervention–MICCAI 2004*, pages 51–59, 2004.

[93] Constantino C Reyes-Aldasoro. Retrospective shading correction algorithm based on signal envelope estimation. *Electronics letters*, 45(9):454, 2009.

[94] Thomas Brox and Daniel Cremers. On the statistical interpretation of the piecewise smooth mumford-shah functional. In *International Conference on Scale Space and Variational Methods in Computer Vision*, pages 203–213. Springer, 2007.

[95] David Mumford and Jayant Shah. Optimal approximations by piecewise smooth functions and associated variational problems. *Communications on pure and applied mathematics*, 42(5):577–685, 1989.

[96] Chunming Li, Chiu-Yen Kao, John C Gore, and Zhaohua Ding. Minimization of region-scalable fitting energy for image segmentation. *IEEE transactions on image processing*, 17(10):1940–1949, 2008.

[97] Jaeyoun Yi and Jong Beom Ra. A locally adaptive region growing algorithm for vascular segmentation. *International Journal of Imaging Systems and Technology*, 13(4):208–214, 2003.

[98] Juerg Tschirren, Eric A Hoffman, Geoffrey McLennan, and Milan Sonka. Intrathoracic airway trees: segmentation and airway morphology analysis from low-dose ct scans. *IEEE transactions on medical imaging*, 24(12):1529–1539, 2005.

[99] Shawn Lankton, Arthur Stillman, Paolo Raggi, and Allen Tannenbaum. Soft plaque detection and automatic vessel segmentation. In *12th International Conference on Medical Image Computing and Computer Assisted Intervention (MICCAI)*, pages 25–33. Springer Berlin Heidelberg, 2009.

[100] Haiyong Xu, Tingting Liu, and Guotao Wang. Hybrid geodesic region-based active contours for image segmentation. *Computers & Electrical Engineering*, 40(3):858–869, 2014.

[101] Yin Wang and Panos Liatsis. A fully automated framework for segmentation and stenosis quantification of coronary arteries in 3d cta imaging. In *Developments in eSystems Engineering (DESE), 2009 Second International Conference on*, pages 136–140. IEEE, 2009.

[102] Yin Wang and Panos Liatsis. An automated method for segmentation of coronary arteries in coronary ct imaging. In *Developments in E-systems Engineering (DESE), 2010*, pages 12–16. IEEE, 2010.

[103] Toshiro Kitagawa, Hideya Yamamoto, Norihiko Ohhashi, Tomokazu Okimoto, Jun Horiguchi, Nobuhiko Hirai, Katsuhide Ito, and Nobuoki Kohno. Comprehensive evaluation of noncalcified coronary plaque characteristics detected using 64-slice computed tomography in patients with proven or suspected coronary artery disease. *American heart journal*, 154(6):1191–1198, 2007.

[104] Arnon Blum and Menachem Nahir. Future non-invasive imaging to detect vascular plaque instability and subclinical non-obstructive atherosclerosis. *Journal of geriatric cardiology: JGC*, 10(2):178, 2013.

[105] Stefan C Saur, Hatem Alkadhi, Lotus Desbiolles, Gábor Székely, and Philippe C Cattin. Automatic detection of calcified coronary plaques in computed tomography data sets. In *International Conference on Medical Image Computing and Computer-Assisted Intervention*, pages 170–177. Springer, 2008.

[106] Gerd Brunner, Uday Kurkure, Deepak R Chittajallu, Raja P Yalamanchili, and Ioannis A Kakadiaris. Toward unsupervised classification of calcified arterial lesions. In *International Conference on Medical Image Computing and Computer-Assisted Intervention*, pages 144–152. Springer, 2008.

[107] Pal Maurovich-Horvat, Maros Ferencik, Fabian Bamberg, and Udo Hoffmann. Methods of plaque quantification and characterization by cardiac computed tomography. *Journal of cardiovascular computed tomography*, 3:S91–S98, 2009.

[108] Sadako Motoyama, Masayoshi Sarai, Hiroto Harigaya, Hirofumi Anno, Kaori Inoue, Tomonori Hara, Hiroyuki Naruse, Junichi Ishii, Hitoshi Hishida, Nathan D Wong, et al. Computed tomographic angiography characteristics of atherosclerotic plaques subsequently resulting in acute coronary syndrome. *Journal of the American College of Cardiology*, 54(1):49–57, 2009.

[109] Sushil Mittal, Yefeng Zheng, Bogdan Georgescu, Fernando Vega-Higuera, Shaohua Zhou, Peter Meer, and Dorin Comaniciu. Fast automatic detection of calcified coronary lesions in 3d cardiac ct images. *Machine Learning in Medical Imaging*, pages 1–9, 2010.

[110] B Michael Kelm, Sushil Mittal, Yefeng Zheng, Alexey Tsymbal, Dominik Bernhardt, Fernando Vega-Higuera, S Kevin Zhou, Peter Meer, and Dorin Comaniciu. Detection, grading and classification of coronary stenoses in computed tomography angiography. In *International Conference on Medical Image Computing and Computer-Assisted Intervention*, pages 25–32. Springer, 2011.

[111] JF Breen, PF Sheedy 2nd, RS Schwartz, AW Stanson, RB Kaufmann, PP Moll, and JA Rumberger. Coronary artery calcification detected with ultrafast ct as an indication of coronary artery disease. *Radiology*, 185(2):435–439, 1992.

[112] Jun Wei, Chuan Zhou, Heang-Ping Chan, Aamer Chughtai, Prachi Agarwal, Jean Kuriakose, Lubomir Hadjiiski, Smita Patel, and Ella Kazerooni. Computerized detection of noncalcified plaques in coronary ct angiography: Evaluation of topological soft gradient prescreening method and luminal analysis. *Medical physics*, 41(8):081901, 2014.

[113] Matthias Tessmann, Fernando Vega-Higuera, Dominik Fritz, Michael Scheuering, and Gunther Greiner. Multi-scale feature extraction for learning-based classification of coronary artery stenosis. In *SPIE Medical Imaging*, pages 726002–726002. International Society for Optics and Photonics, 2009.

[114] Harald Brodoefel, Christof Burgstahler, Adeel Sabir, Chun-Shan Yam, Faisal Khosa, Claus D Claussen, and Melvin E Clouse. Coronary plaque quantification by voxel analysis: dual-source mdct angiography versus intravascular sonography. *AJR. American journal of roentgenology*, 192(3):W84, 2009.

[115] Chuan Zhou, Heang-Ping Chan, Aamer Chughtai, Smita Patel, Lubomir M Hadjiiski, Jun Wei, and Ella A Kazerooni. Automated coronary artery tree extraction in coronary ct angiography using a multiscale enhancement and dynamic balloon tracking (mscardbt) method. *Computerized Medical Imaging and Graphics*, 36(1):1–10, 2012.

[116] Maria A Zuluaga, Isabelle E Magnin, Marcela Hernández Hoyos, Edgar JF Delgado Leyton, Fernando Lozano, and Maciej Orkisz. Automatic detection of abnormal vascular cross-sections based on density level detection and support vector machines. *International Journal of Computer Assisted Radiology and Surgery*, 6(2):163–174, 2011.

[117] Ingo Steinwart, Don R Hush, and Clint Scovel. Density level detection is classification. In *NIPS*, pages 1337–1344, 2004.

[118] Walsum Theo. The Great Challenge, coronary artery stenoses detection and quantification evaluation framework, 2016.

[119] Francois Lekien and J Marsden. Tricubic interpolation in three dimensions. *International Journal for Numerical Methods in Engineering*, 63(3):455–471, 2005.

[120] Guanyu Yang, Pieter Kitslaar, Michel Frenay, Alexander Broersen, Mark J Boogers, Jeroen J Bax, Johan HC Reiber, and Jouke Dijkstra. Automatic centerline extraction of coronary arteries in coronary computed tomographic angiography. *The international journal of cardiovascular imaging*, 28(4):921–933, 2012.

[121] W Gerald Austen, JE Edwards, RL Frye, GG Gensini, Vincent L Gott, Lawrence S Griffith, DC McGoon, ML Murphy, and BB Roe. A reporting system on patients evaluated for coronary artery disease. report of the ad hoc committee for grading of coronary artery disease, council on cardiovascular surgery, american heart association. *Circulation*, 51(4):5–40, 1975.

[122] Ivana Isgum, Bram van Ginneken, and Marco Olree. Automatic detection of calcifications in the aorta from ct scans of the abdomen 1: 3d computer-aided diagnosis. *Academic radiology*, 11(3):247–257, 2004.

[123] Cheng Hong, Christoph R Becker, U Joseph Schoepf, Bernd Ohnesorge, Roland Bruening, and Maximilian F Reiser. Coronary artery calcium: Absolute quantification in nonenhanced and contrast-enhanced multi–detector row ct studies 1. *Radiology*, 223(2):474–480, 2002.

[124] Brian Mohr, Saad Masood, and Costas Plakas. Accurate lumen segmentation and stenosis detection and quantification in coronary cta. In *Proceedings of 3D Cardiovascular Imaging: a MICCAI segmentation challenge workshop*, 2012.

[125] Andrzej Szymczak, Arthur Stillman, Allen Tannenbaum, and Konstantin Mischaikow. Coronary vessel trees from 3d imagery: a topological approach. *Medical image analysis*, 10(4):548–559, 2006.

[126] Yan Yang. *Image segmentation and shape analysis of blood vessels with applications to coronary atherosclerosis*. PhD thesis, Georgia Institute of Technology, 2007.

[127] Hrvoje Lusic and Mark W Grinstaff. X-ray-computed tomography contrast agents. *Chemical reviews*, 113(3):1641–1666, 2012.

[128] JT Dodge, B Greg Brown, Edward L Bolson, and Harold T Dodge. Lumen diameter of normal human coronary arteries. influence of age, sex, anatomic variation, and left ventricular hypertrophy or dilation. *Circulation*, 86(1):232–246, 1992.

[129] Imad Ghanem Shukri, Jawad Mohammed Hawas, Shilan Huseein Karim, and Issraa Khalil M Ali. Angiographic study of the normal coronary artery in patients attending ulaimani center for heart diseases. *European Scientific Journal*, 10(24), 2014.

[130] Cheemalapati Saikrishna, Sachin Talwar, Gurpreet Gulati, and Arkalgud Sampath Kumar. Normal coronary artery dimensions in indians. *Indian Journal of Thoracic and Cardiovascular Surgery*, 22(3):159–164, 2006.

[131] David C Gaze. Introduction to ischemic heart disease. In *Ischemic Heart Disease*. InTech, 2013.

[132] Anthony Yezzi, Andy Tsai, and Alan Willsky. A statistical approach to snakes for bimodal and trimodal imagery. In *Computer Vision, 1999. The Proceedings of the Seventh IEEE International Conference on*, volume 2, pages 898–903. IEEE, 1999.

[133] Li Wang, Lei He, Arabinda Mishra, and Chunming Li. Active contours driven by local gaussian distribution fitting energy. *Signal Processing*, 89(12):2435–2447, 2009.

[134] Li Wang, Chunming Li, Quansen Sun, Deshen Xia, and Chiu-Yen Kao. Active contours driven by local and global intensity fitting energy with application to brain mr image segmentation. *Computerized Medical Imaging and Graphics*, 33(7):520–531, 2009.

[135] Arthur P Dempster, Nan M Laird, and Donald B Rubin. Maximum likelihood from incomplete data via the em algorithm. *Journal of the royal statistical society. Series B (methodological)*, pages 1–38, 1977.

[136] Pietro Perona and Jitendra Malik. Scale-space and edge detection using anisotropic diffusion. *IEEE Transactions on pattern analysis and machine intelligence*, 12(7):629–639, 1990.

[137] Natick Massachusetts United States. The MathWorks, Inc. MATLAB, Release 2014b,, 2017.

[138] Paul Jaccard. Distribution de la flore alpine dans le bassin des dranses et dans quelques régions voisines. *Bull. Soc. Vaud. Sci. Nat.*, 37:241–272, 1901.

[139] Rahil Shahzad, Hortense Kirisli, Coert Metz, Hui Tang, Michiel Schaap, Lucas van Vliet, Wiro Niessen, and Theo van Walsum. Automatic segmentation, detection and quantification of coronary artery stenoses on cta. *The international journal of cardiovascular imaging*, 29(8):1847–1859, 2013.

[140] Yoshiro Kitamura, Yuanzhong Li, Wataru Ito, and Hiroshi Ishikawa. Coronary lumen and plaque segmentation from cta using higher-order shape prior. In *MICCAI*, pages 339–347. Springer, 2014.

[141] Felix Lugauer, Yefeng Zheng, Joachim Hornegger, and B Michael Kelm. Precise lumen segmentation in coronary computed tomography angiography. In *MICCAI Workshop on Medical Computer Vision*, pages 137–147. Springer, 2014.

[142] Chaolu Feng and Yang Hu. Segmentation of coronary artery using region based level set with edge preservation. *Journal of Medical Imaging and Health Informatics*, 6(7):1727–1731, 2016.

[143] Ivana Išgum, Annemarieke Rutten, Mathias Prokop, and Bram van Ginneken. Detection of coronary calcifications from computed tomography scans for automated risk assessment of coronary artery disease. *Medical physics*, 34(4):1450–1461, 2007.

[144] Matthew J Budoff. Prevalence of soft plaque detection with computed tomography, 2006.

[145] Christopher L Schlett, Maros Ferencik, Csilla Celeng, Pál Maurovich-Horvat, Hans Scheffel, Paul Stolzmann, Synho Do, Hans-Ulrich Kauczor, Hatem Alkadhi, Fabian Bamberg, et al. How to assess non-calcified plaque in ct angiography: delineation methods affect diagnostic accuracy of low-attenuation plaque by ct for lipid-core plaque in histology. *European Heart Journal–Cardiovascular Imaging*, 14(11):1099–1105, 2013.

[146] George Youssef and Matthew Budoff. Role of computed tomography coronary angiography in the detection of vulnerable plaque, where does it stand among others? *Angiology: Open Access*, 2013.

[147] Robert Van Uitert and Ingmar Bitter. Subvoxel precise skeletons of volumetric data based on fast marching methods. *Medical physics*, 34(2):627–638, 2007.

[148] Dr. Benteu Darius. Coronary arteries ? anatomy. Available at http://www.heartupdate.com/anatomyfunction/coronary-arteries-anatomy_218/(2016/11/22), 2016.

[149] Corinna Cortes and Vladimir Vapnik. Support-vector networks. *Machine learning*, 20(3):273–297, 1995.

[150] Huan Liu and Hiroshi Motoda. *Computational Methods of Feature Selection*. CRC Press, 2007.

[151] Isabelle Guyon, Jason Weston, Stephen Barnhill, and Vladimir Vapnik. Gene selection for cancer classification using support vector machines. *Machine learning*, 46(1-3):389–422, 2002.

[152] G. Roffo, S. Melzi, and M. Cristani. Infinite feature selection. In *2015 IEEE International Conference on Computer Vision (ICCV)*, pages 4202–4210, Dec 2015.

[153] Zhonghua Sun and Lei Xu. Coronary ct angiography in the quantitative assessment of coronary plaques. *BioMed research international*, 2014, 2014.

[154] Stephan Achenbach, Fabian Moselewski, Dieter Ropers, Maros Ferencik, Udo Hoffmann, Briain MacNeill, Karsten Pohle, Ulrich Baum, Katharina Anders, Ik-kyung Jang, et al. Detection of calcified and noncalcified coronary atherosclerotic plaque by contrast-enhanced, submillimeter multidetector spiral computed tomography. *Circulation*, 109(1):14–17, 2004.

[155] Paul Schoenhagen, E Murat Tuzcu, Arthur E Stillman, David J Moliterno, Sandra S Halliburton, Stacie A Kuzmiak, Jane M Kasper, William A Magyar, Michael L Lieber, Steven E Nissen, et al. Non-invasive assessment of plaque morphology and remodeling in mildly stenotic coronary segments: comparison of 16-slice computed tomography and intravascular ultrasound. *Coronary artery disease*, 14(6):459–462, 2003.

[156] Stephen Schroeder, Andreas F Kopp, Andreas Baumbach, Christoph Meisner, Axel Kuettner, Christian Georg, Bernd Ohnesorge, Christian Herdeg, Claus D Claussen, and Karl R Karsch. Noninvasive detection and evaluation of atherosclerotic coronary plaques with multislice computed tomography. *Journal of the American College of Cardiology*, 37(5):1430–1435, 2001.

[157] Tiziano Schepis, Mohamed Marwan, Tobias Pflederer, Martin Seltmann, Dieter Ropers, Werner G Daniel, and Stephan Achenbach. Quantification of non-calcified coronary atherosclerotic plaques with dual-source computed tomography: comparison with intravascular ultrasound. *Heart*, 96(8):610–615, 2010.

[158] H Brodoefel, C Burgstahler, M Heuschmid, A Reimann, F Khosa, A Kopp, S Schroeder, CD Claussen, and ME Clouse. Accuracy of dual-source ct in the characterisation of non-calcified plaque: use of a colour-coded analysis compared with virtual histology intravascular ultrasound. *The British journal of radiology*, 82(982):805–812, 2009.

[159] Damini Dey, Tiziano Schepis, Mohamed Marwan, Piotr J Slomka, Daniel S Berman, and Stephan Achenbach. Automated three-dimensional quantification of noncalcified coronary plaque from coronary ct angiography: comparison with intravascular us. *Radiology*, 257(2):516–522, 2010.

[160] Damini Dey, Victor Y Cheng, Piotr J Slomka, Ryo Nakazato, Amit Ramesh, Swaminatha Gurudevan, Guido Germano, and Daniel S Berman. Automated 3-dimensional quantification of noncalcified and calcified coronary plaque from coronary ct angiography. *Journal of cardiovascular computed tomography*, 3(6):372–382, 2009.

[161] T Pflederer, M Schmid, D Ropers, U Ropers, S Komatsu, WG Daniel, and S Achenbach. Interobserver variability of 64-slice computed tomography for the quantification of non-calcified coronary atherosclerotic plaque. In *RöFo-Fortschritte auf dem Gebiet der Röntgenstrahlen und der bildgebenden Verfahren*, volume 179, pages 953–957. © Georg Thieme Verlag KG Stuttgart· New York, 2007.

[162] Masato Otsuka, Nico Bruining, Niels C Van Pelt, Nico R Mollet, Jurgen MR Ligthart, Eleni Vourvouri, Ronald Hamers, Peter De Jaegere, William Wijns, Ron T Van Domburg, et al. Quantification of coronary plaque by 64-slice computed tomography: a comparison with quantitative intracoronary ultrasound. *Investigative radiology*, 43(5):314–321, 2008.

[163] Wilbur CK Wong and Albert CS Chung. Augmented vessels for quantitative analysis of vascular abnormalities and endovascular treatment planning. *IEEE transactions on medical imaging*, 25(6):665–684, 2006.

[164] Dong-Goo Kang, Dae Chul Suh, and Jong Beom Ra. Three-dimensional blood vessel quantification via centerline deformation. *IEEE Transactions on Medical Imaging*, 28(3):405–414, 2009.

[165] Alejandro F Frangi, Wiro J Niessen, Romhild M Hoogeveen, Theo Van Walsum, and Max A Viergever. Model-based quantitation of 3-d magnetic resonance angiographic images. *IEEE Transactions on medical imaging*, 18(10):946–956, 1999.

[166] Alejandro F Frangi, Wiro J Niessen, Paul J Nederkoorn, Jeannette Bakker, Willem P Th M Mali, and Max A Viergever. Quantitative analysis of vascular morphology from 3d mr angiograms: in vitro and in vivo results. *Magnetic Resonance in Medicine*, 45(2):311–322, 2001.

[167] Walter Gander, Gene H Golub, and Rolf Strebel. Least-squares fitting of circles and ellipses. *BIT Numerical Mathematics*, 34(4):558–578, 1994.

[168] Pál Maurovich-Horvat, Maros Ferencik, Szilard Voros, Béla Merkely, and Udo Hoffmann. Comprehensive plaque assessment by coronary ct angiography. *Nature Reviews Cardiology*, 11(7):390–402, 2014.

[169] Ryo Nakazato, Aryeh Shalev, Joon-Hyung Doh, Bon-Kwon Koo, Heidi Gransar, Millie J Gomez, Jonathon Leipsic, Hyung-Bok Park, Daniel S Berman, and James K Min. Aggregate plaque volume by coronary computed tomography angiography is superior and incremental to luminal narrowing for diagnosis of ischemic lesions of intermediate stenosis severity. *Journal of the American College of Cardiology*, 62(5):460–467, 2013.

[170] Alan Green. DSS:, ethical considerations for the development of decision support systems. Available at http://www.openclinical.org/docs/int/briefingpapers/greenEthics.pdf(2017/19/10).

[171] Pim AL Tonino, Bernard De Bruyne, Nico HJ Pijls, Uwe Siebert, Fumiaki Ikeno, Marcel vant Veer, Volker Klauss, Ganesh Manoharan, Thomas Engstrøm, Keith G Oldroyd, et al. Fractional flow reserve versus angiography for guiding percutaneous coronary intervention. *N Engl j Med*, 2009(360):213–224, 2009.

Appendix A

Lumen-Plaque Area Statistics

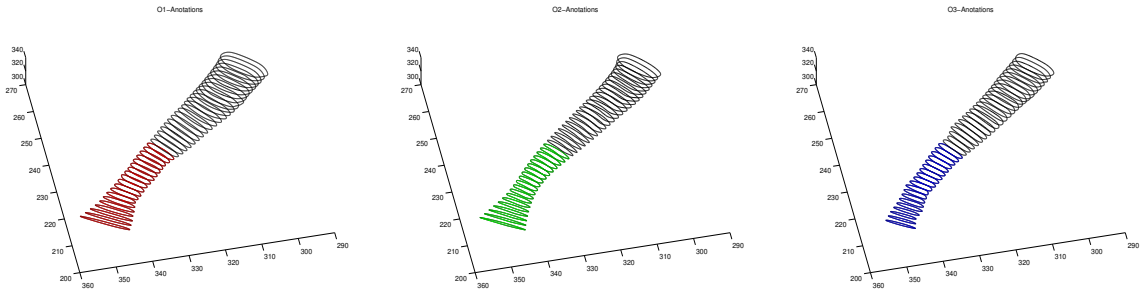

(a) observer 1 (b) observer 2 (c) observer 3

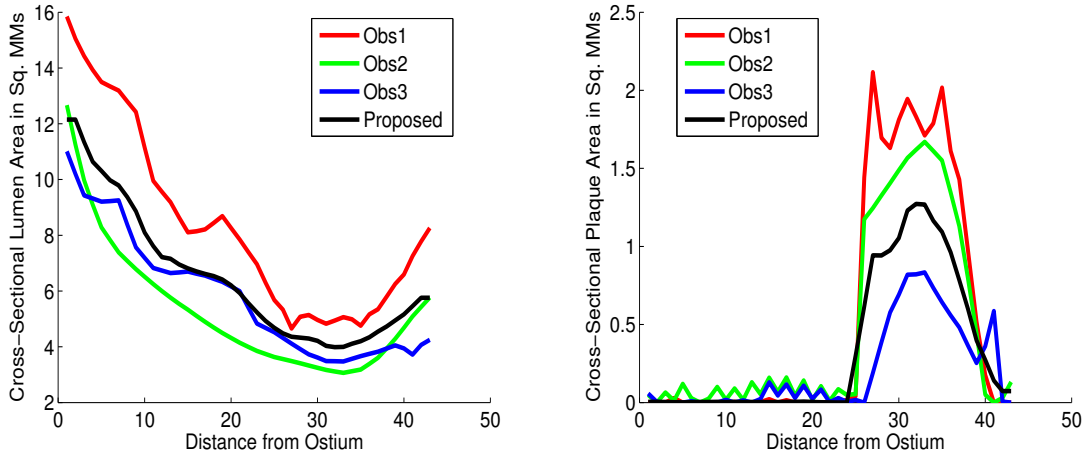

(d) Lumen area (e) Plaque area

Fig. A.1 Lumen - plaque analysis w.r.t. manual observers for DS2 Seg6. (a-c) lumen contours for three observers, (d-e) plots obtained cross-section based area for coronary lumen and non-calcified plaque respectively, with respect to annotations of three manual experts. Black is obtained area, whereas red, blue and green represent three observers.

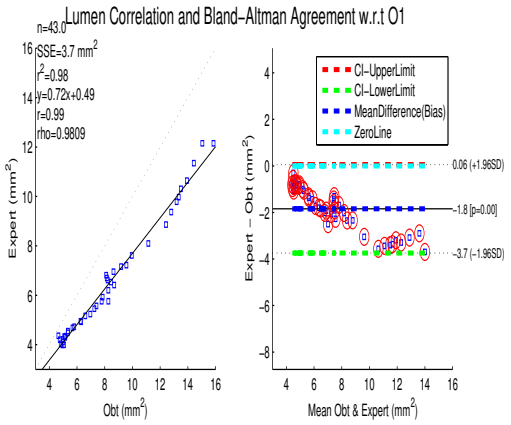

(a) Lumen obs1

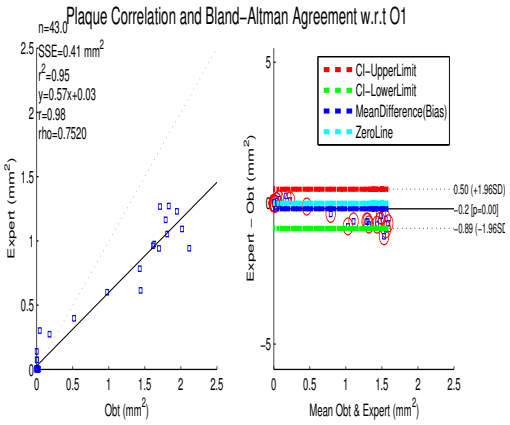

(b) Plaque obs1

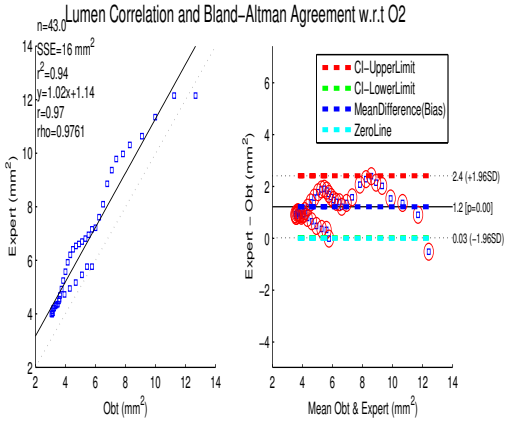

(c) Lumen obs2

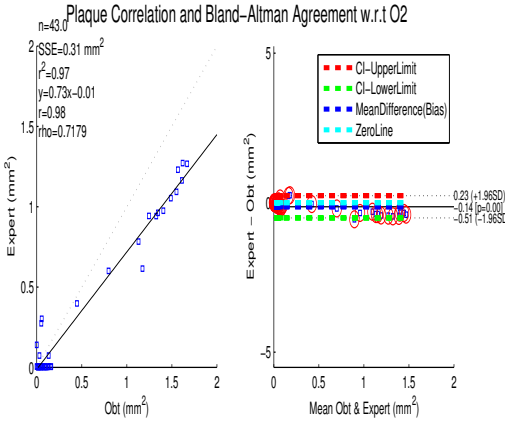

(d) Plaque obs2

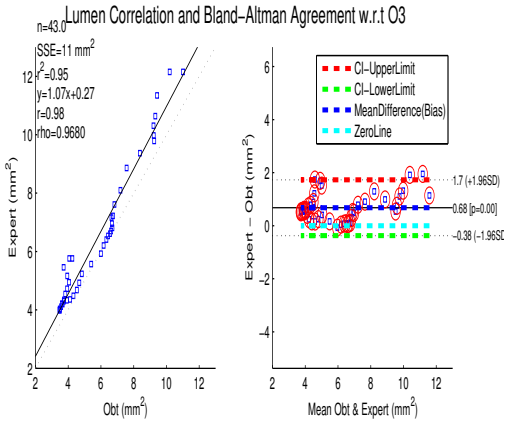

(e) Lumen obs3

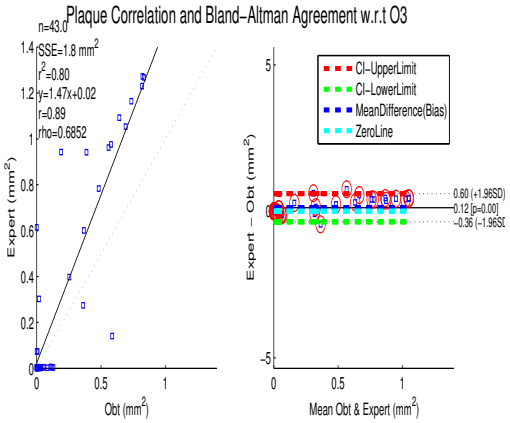

(f) Plaque obs3

Fig. A.2 Cross-section based analysis along the length of the segment with respect to three individual experts for DS2 seg6. Left (a, c, e) represents the obtained lumen area, whereas obtained plaque area is presented in right column (b, d, f). Both lumen and plaque area shows a good correlation and the Bland-Altman plots reflects an agreement within the 95% confidence interval.

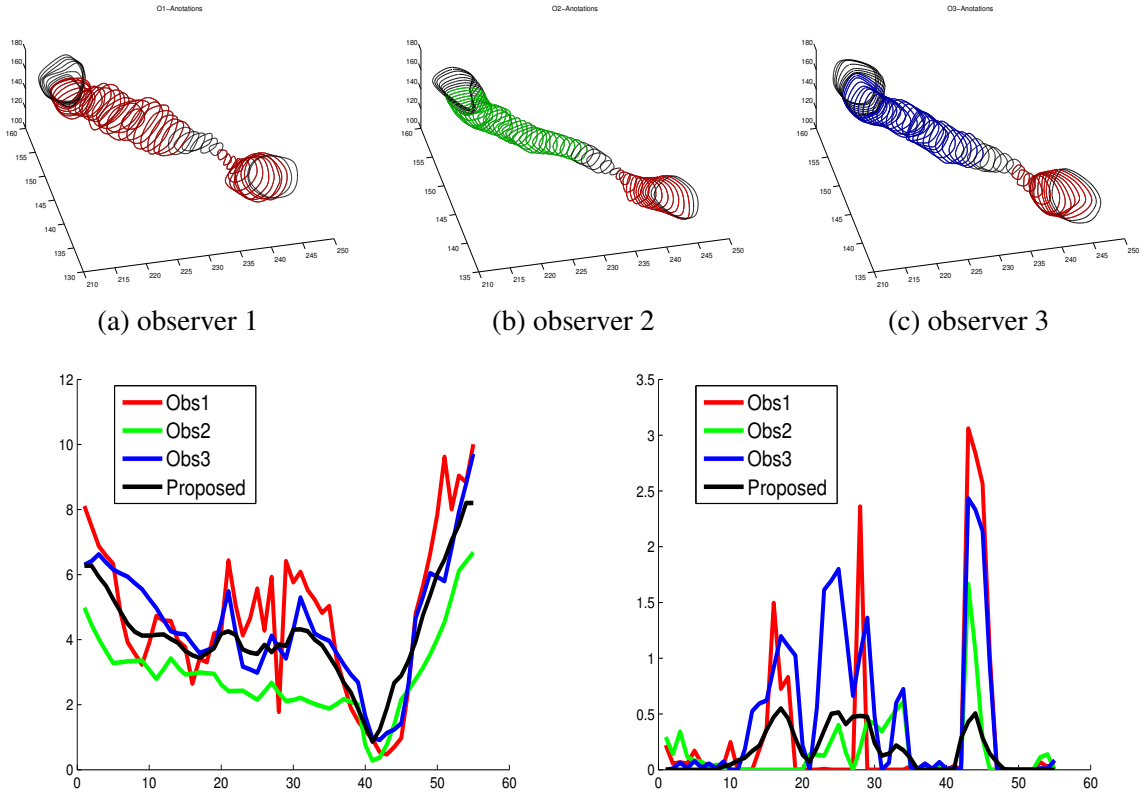

(a) observer 1 (b) observer 2 (c) observer 3

(d) Lumen area (e) Plaque area

Fig. A.3 Lumen - plaque analysis w.r.t. manual observers DS5 Seg2. (a-c) lumen contours for three observers, (d-e) plots obtained cross-section based area for coronary lumen and non-calcified plaque respectively, with respect to annotations of three manual experts. Black is obtained area, whereas red, blue and green represent three observers.

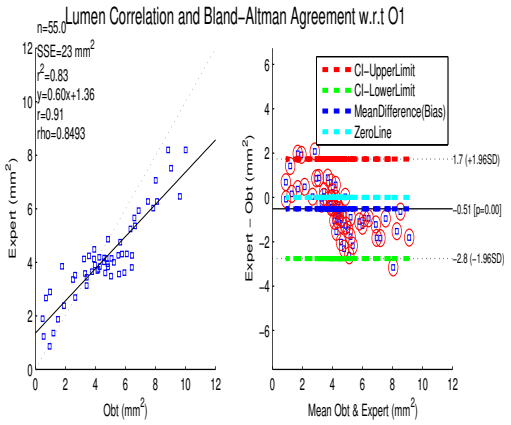

(a) Lumen obs1

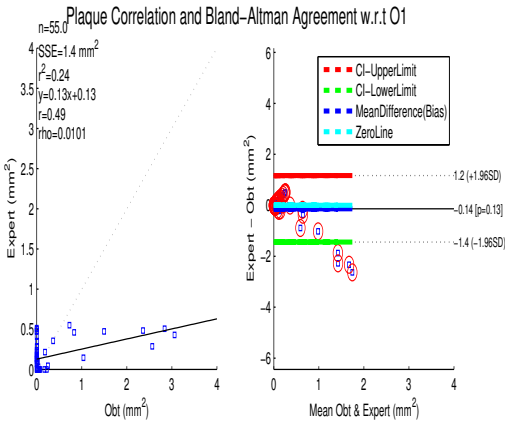

(b) Plaque obs1

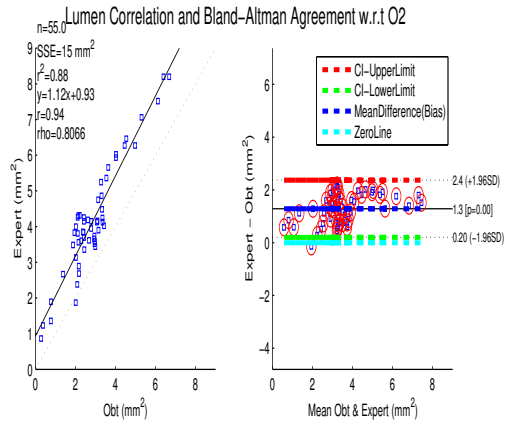

(c) Lumen obs2

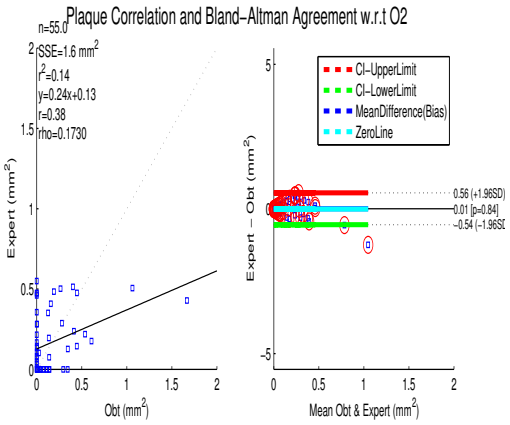

(d) Plaque obs2

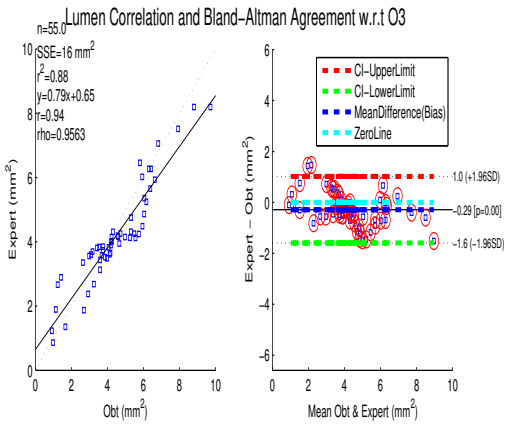

(e) Lumen obs3

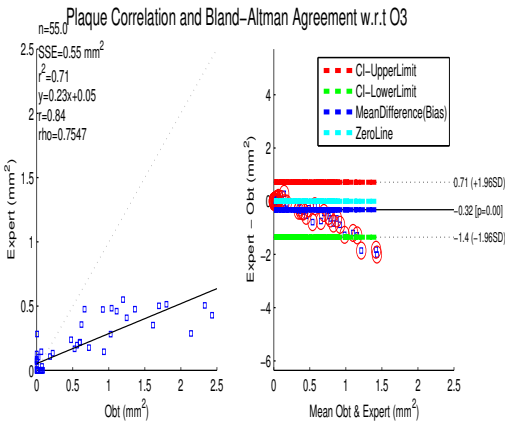

(f) Plaque obs3

Fig. A.4 Cross-section based analysis along the length of the segment with respect to three individual experts for DS5 seg2. Left (a, c, e) represents the obtained lumen area, whereas obtained plaque area is presented in right column (b, d, f). Both lumen and plaque area shows a good correlation and the Bland-Altman plots reflects an agreement within the 95% confidence interval.

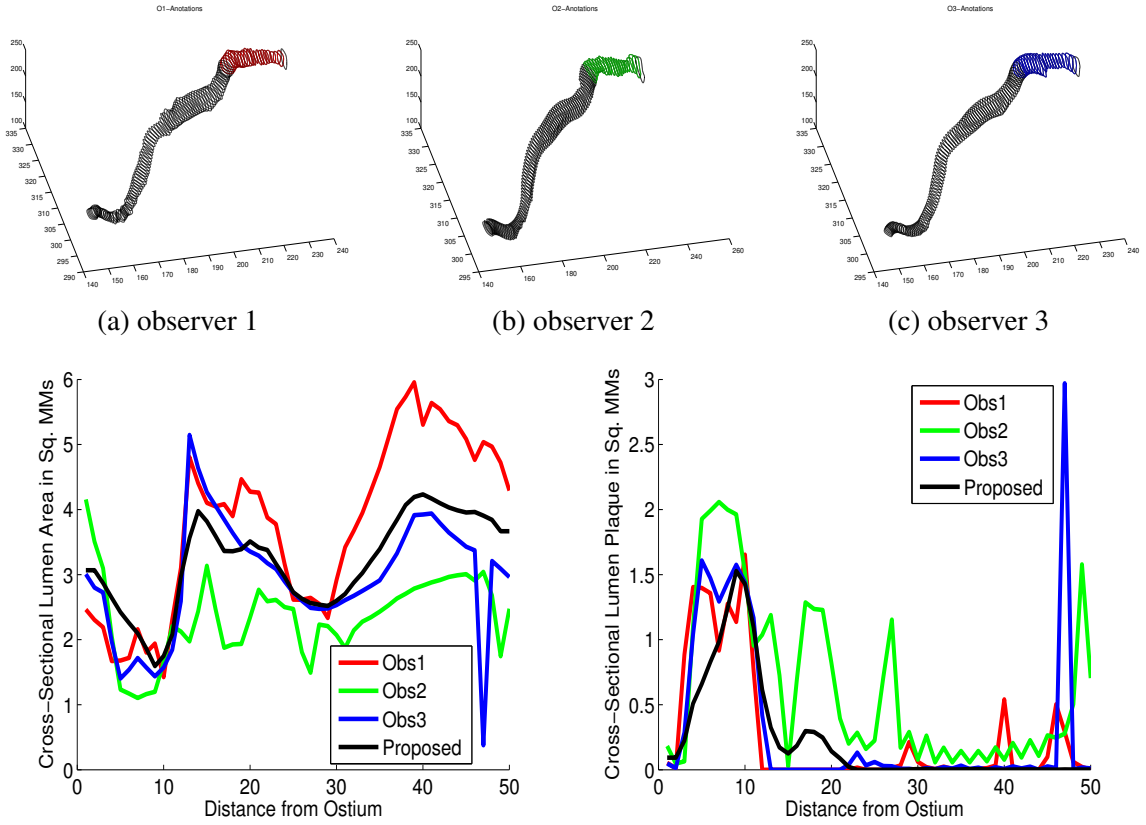

(a) observer 1 (b) observer 2 (c) observer 3

(d) Lumen area (e) Plaque area

Fig. A.5 Lumen - plaque analysis w.r.t. manual observers for DS5 Seg8. (a-c) lumen contours for three observers, (d-e) plots obtained cross-section based area for coronary lumen and non-calcified plaque respectively, with respect to annotations of three manual experts. Black is obtained area, whereas red, blue and green represent three observers.

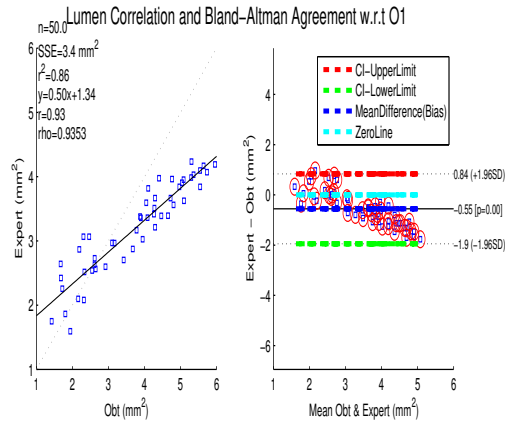

(a) Lumen obs1

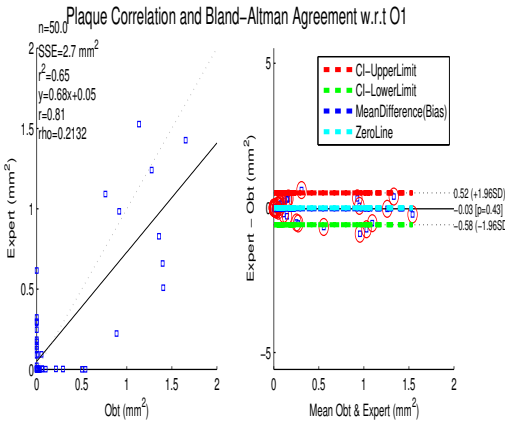

(b) Plaque obs1

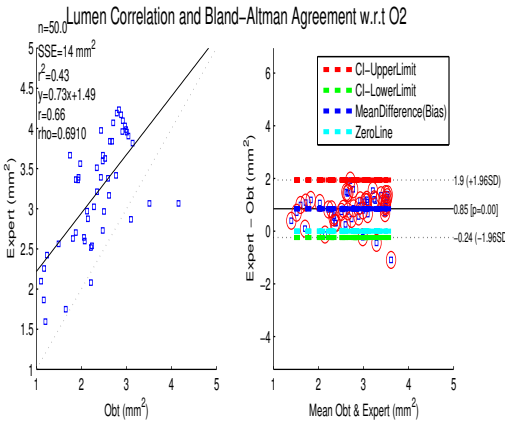

(c) Lumen obs2

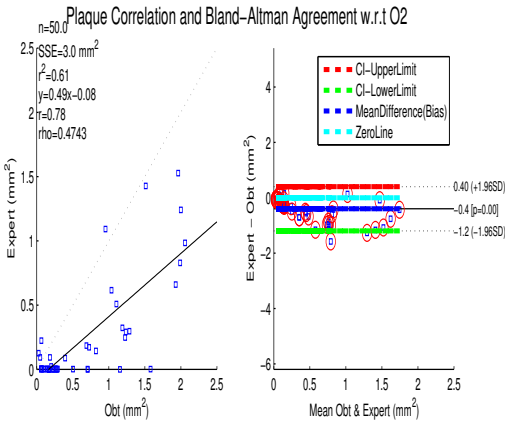

(d) Plaque obs2

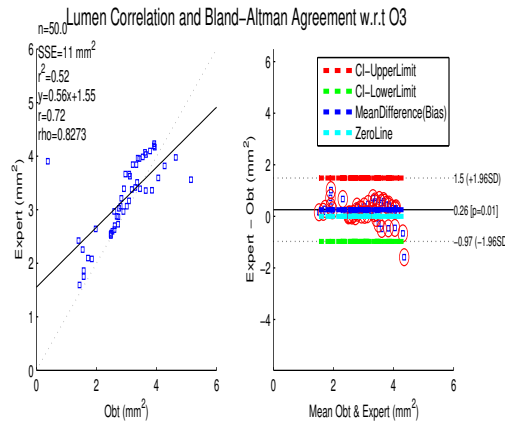

(e) Lumen obs3

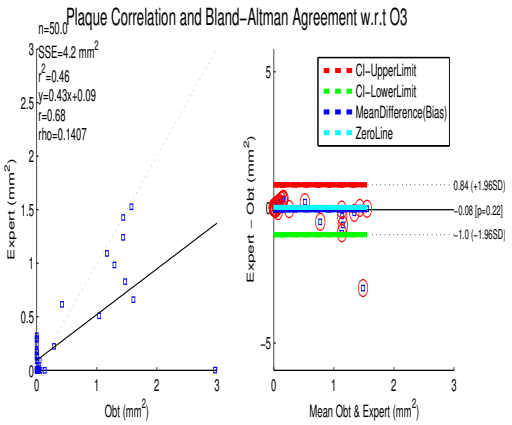

(f) Plaque obs3

Fig. A.6 Cross-section based analysis along the length of the segment with respect to three individual experts for DS5 seg8. Left (a, c, e) represents the obtained lumen area, whereas obtained plaque area is presented in right column (b, d, f). Both lumen and plaque area shows a good correlation and the Bland-Altman plots reflects an agreement within the 95% confidence interval.

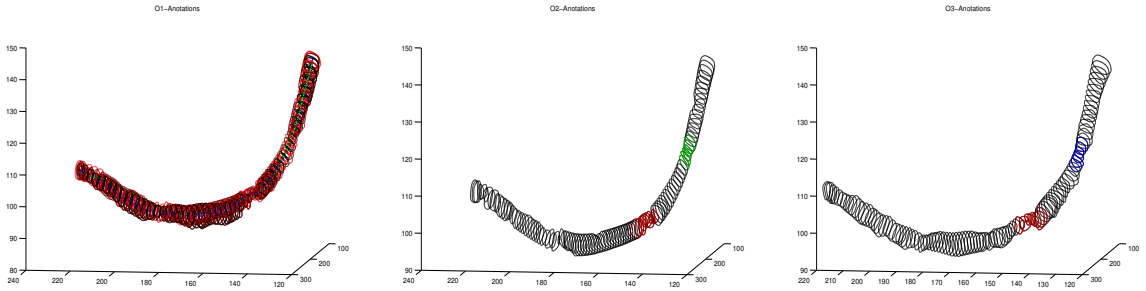

(a) observer 1 (b) observer 2 (c) observer 3

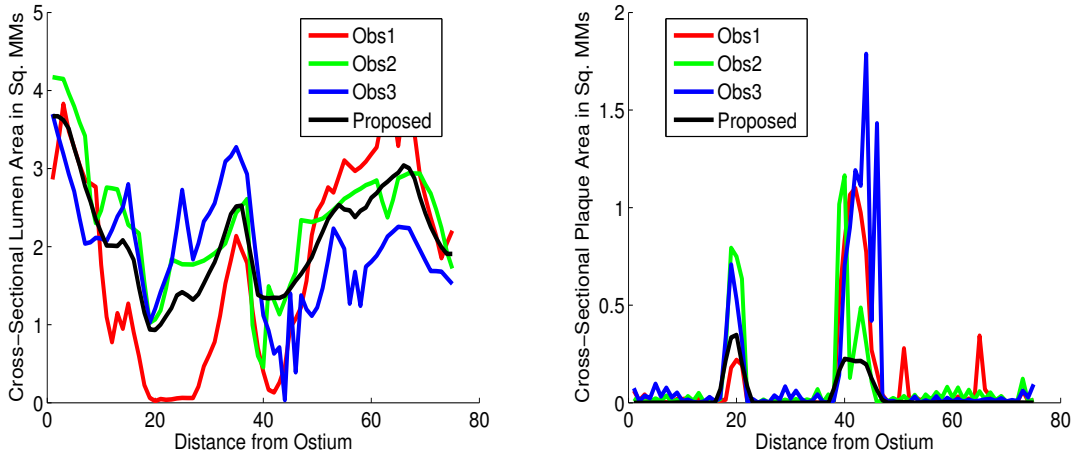

(d) Lumen area (e) Plaque area

Fig. A.7 Lumen - plaque analysis w.r.t. manual observers for DS7 Seg3. (a-c) lumen contours for three observers, (d-e) plots obtained cross-section based area for coronary lumen and non-calcified plaque respectively, with respect to annotations of three manual experts. Black is obtained area, whereas red, blue and green represent three observers.

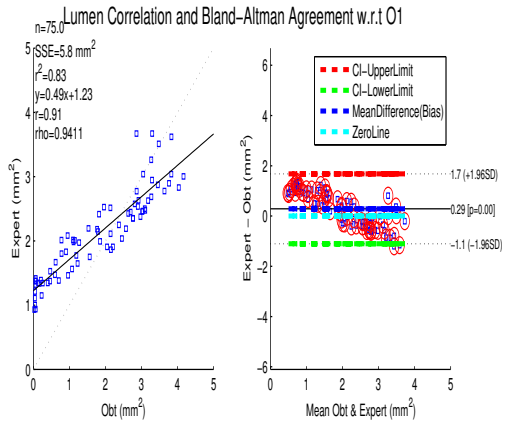

(a) Lumen obs1

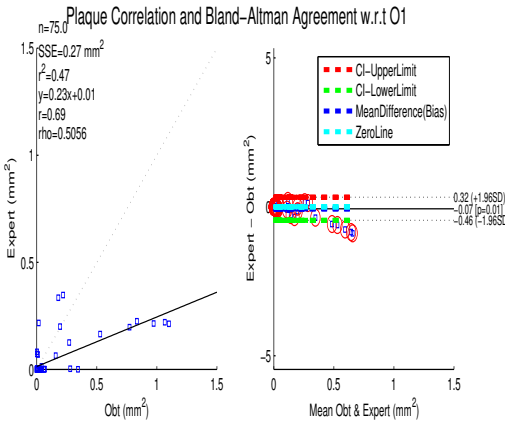

(b) Plaque obs1

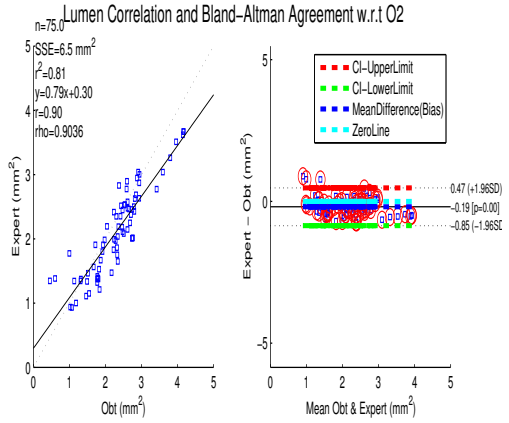

(c) Lumen obs2

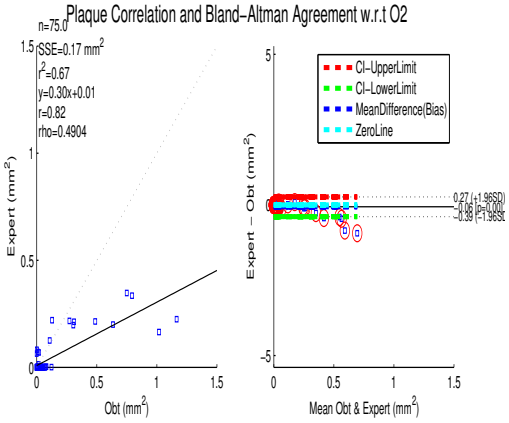

(d) Plaque obs2

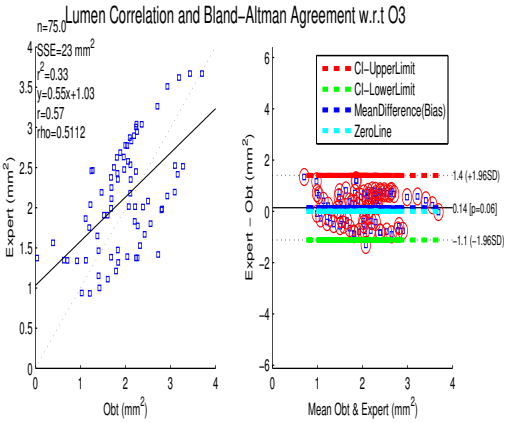

(e) Lumen obs3

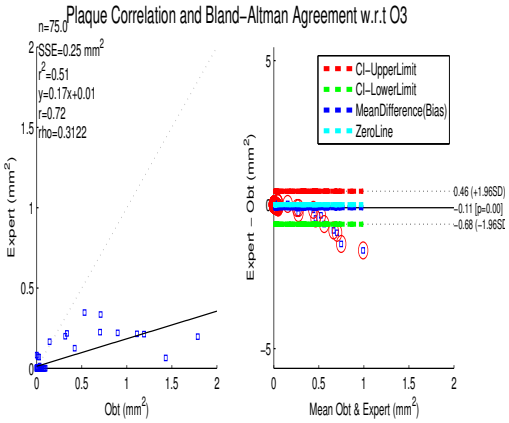

(f) Plaque obs3

Fig. A.8 Cross-section based analysis along the length of the segment with respect to three individual experts for DS7 seg3. Left (a, c, e) represents the obtained lumen area, whereas obtained plaque area is presented in right column (b, d, f). Both lumen and plaque area shows a good correlation and the Bland-Altman plots reflects an agreement within the 95% confidence interval.

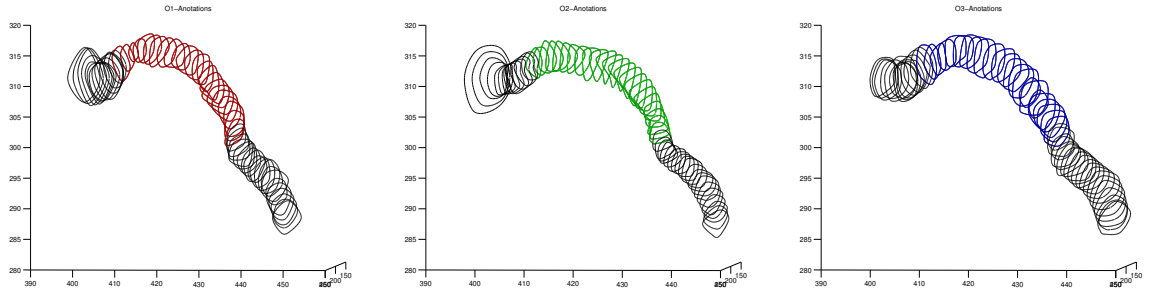

(a) observer 1 (b) observer 2 (c) observer 3

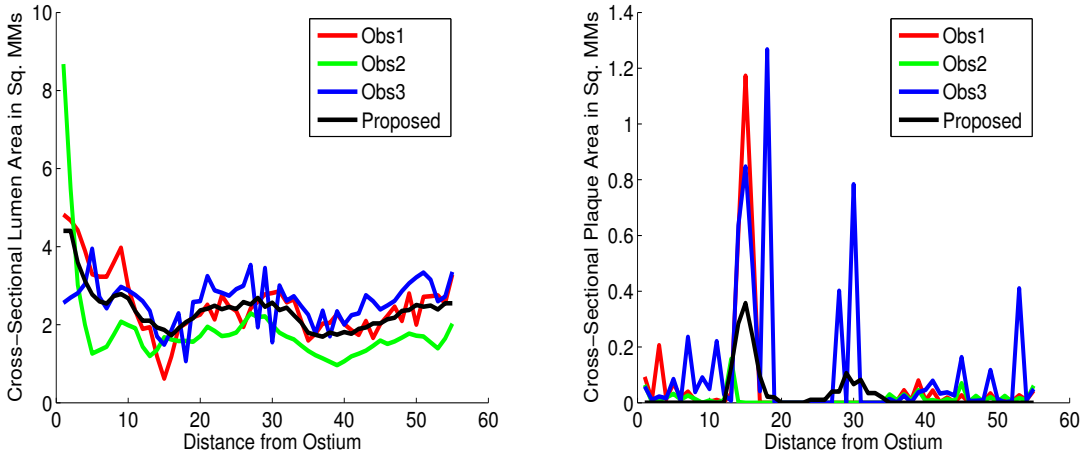

(d) Lumen area (e) Plaque area

Fig. A.9 Lumen - plaque analysis w.r.t. manual observers for DS11 Seg7. (a-c) lumen contours for three observers, (d-e) plots obtained cross-section based area for coronary lumen and non-calcified plaque respectively, with respect to annotations of three manual experts. Black is obtained area, whereas red, blue and green represent three observers.

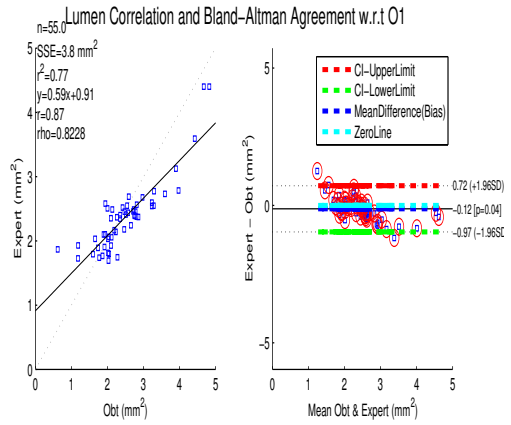

(a) Lumen obs1

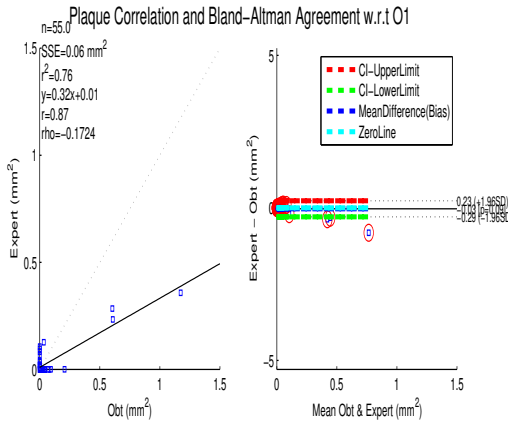

(b) Plaque obs1

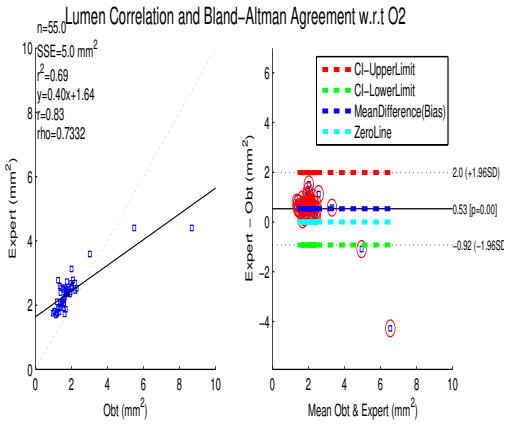

(c) Lumen obs2

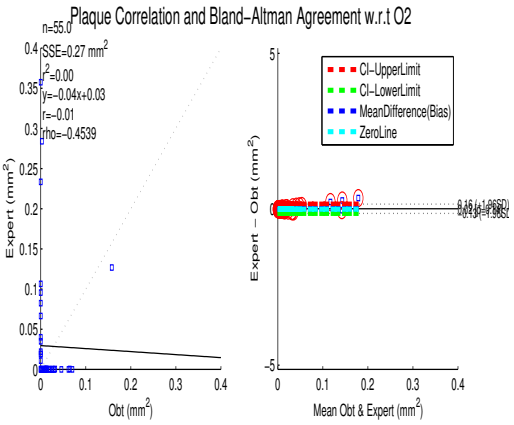

(d) Plaque obs2

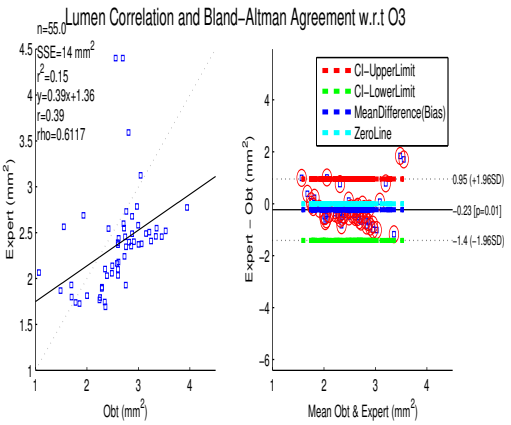

(e) Lumen obs3

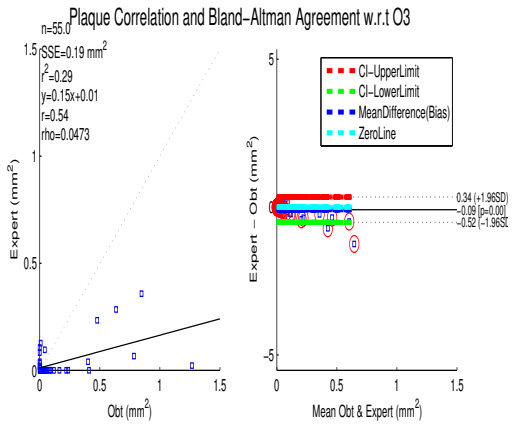

(f) Plaque obs3

Fig. A.10 Cross-section based analysis along the length of the segment with respect to three individual experts for DS11 seg7 . Left (a, c, e) represents the obtained lumen area, whereas obtained plaque area is presented in right column (b, d, f). Both lumen and plaque area shows a good correlation and the Bland-Altman plots reflects an agreement within the 95% confidence interval.

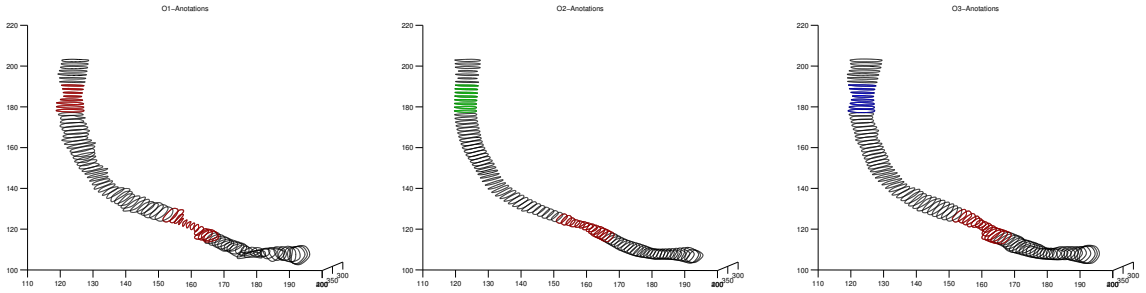

(a) observer 1 (b) observer 2 (c) observer 3

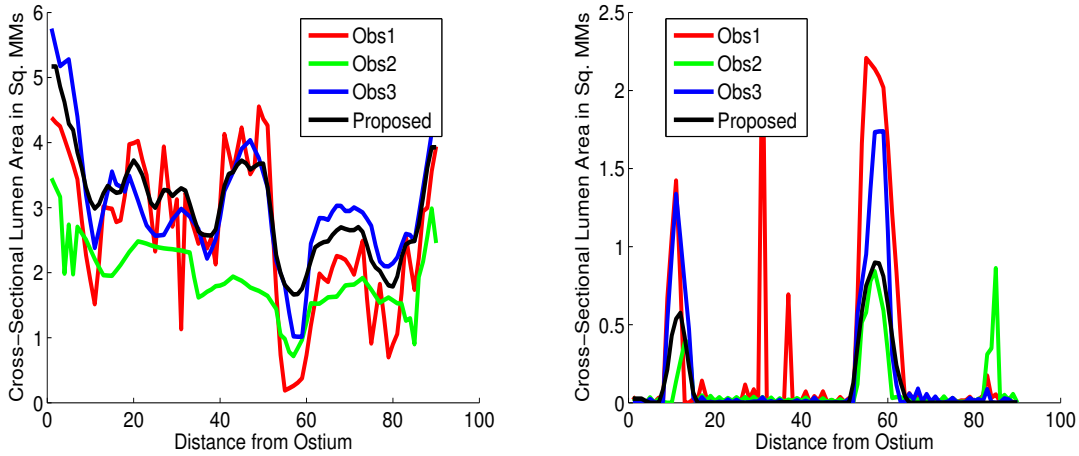

(d) Lumen area (e) Plaque area

Fig. A.11 Lumen - plaque analysis w.r.t. manual observers for DS15 seg3. (a-c) lumen contours for three observers, (d-e) plots obtained cross-section based area for coronary lumen and non-calcified plaque respectively, with respect to annotations of three manual experts. Black is obtained area, whereas red, blue and green represent three observers.

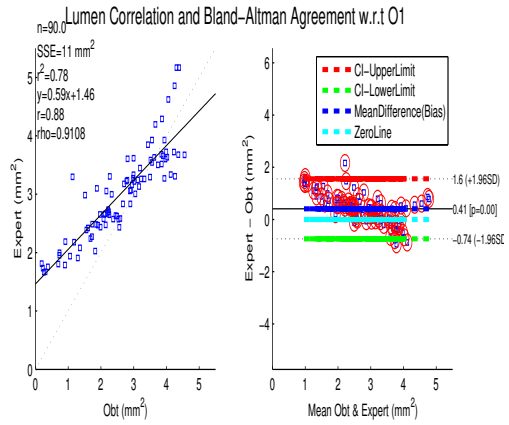

(a) Lumen obs1

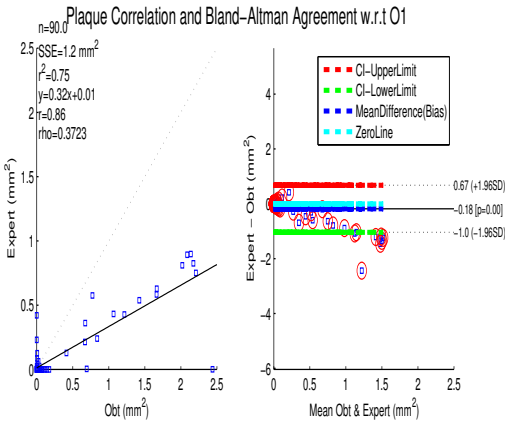

(b) Plaque obs1

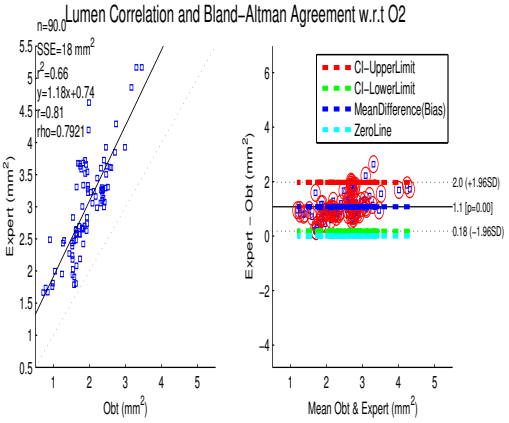

(c) Lumen obs2

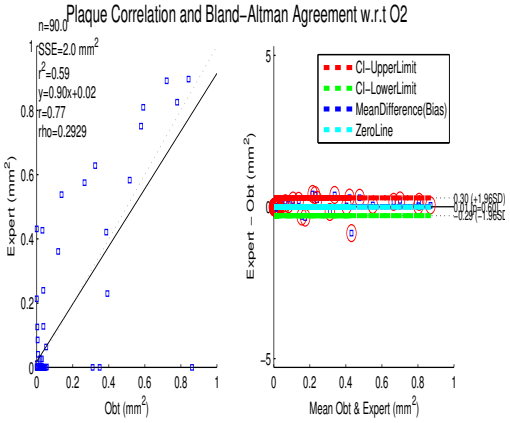

(d) Plaque obs2

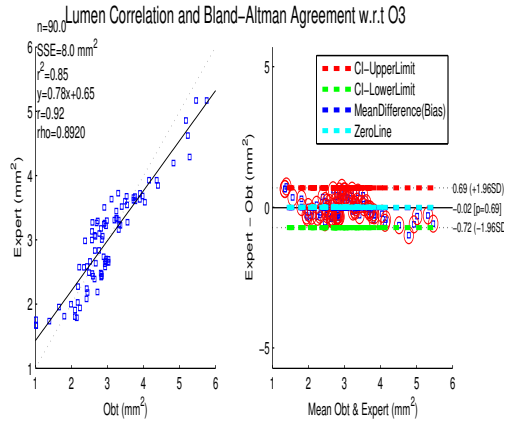

(e) Lumen obs3

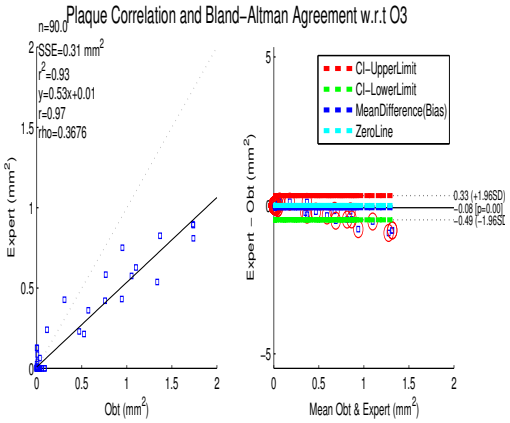

(f) Plaque obs3

Fig. A.12 Cross-section based analysis along the length of the segment with respect to three individual experts for DS15 seg3. Left (a, c, e) represents the obtained lumen area, whereas obtained plaque area is presented in right column (b, d, f). Both lumen and plaque area shows a good correlation and the bland-altman plots reflects an agreement within the 95% confidence interval.